UNIVERSITAT DE BARCELONA

# Crystalline and vibrational properties of kesterites

Mirjana Dimitrievska

University of Barcelona
Faculty of Physics

# Crystalline and vibrational properties of kesterites

Presented by:
Mirjana Dimitrievska

Thesis directors:
Dr. Victor Izquierdo-Roca and Prof. Alejandro Pérez-Rodríguez

Thesis tutor:
Prof. Blas Garrido Fernández

Thesis submitted October 2015 in the Doctorate Program
**of Physics of the University of Barcelona**

# Table of contents

**List of acronyms used in this work** ..... **1**

**Preface:** ***Publications and summary of the thesis*** ..... **3**

**Prefacio:** ***Publicaciones y resumen de la tesis*** ..... **15**

**Chapter 1:** ***Introduction*** ..... **27**

Thin film solar cells ..... 31

Raman scattering spectroscopy ..... 34

Objectives of the thesis ..... 38

**Chapter 2:** ***Fundamental properties of kesterites: Identification of vibrational modes*** ..... **39**

Multiwavelength excitation Raman scattering study of polycrystalline kesterite $Cu_2ZnSnS_4$ thin films ..... 46

Multiwavelength excitation Raman scattering of $Cu_2ZnSn(S_xSe_{1-x})_4$ ($0 \leq x \leq 1$) polycrystalline thin films: Vibrational properties of sulfoselenide solid solutions ..... 51

**Chapter 3:** ***Defect dynamics in kesterites: Classification, detection and effect on optoelectronic properties*** ..... **55**

Raman scattering crystalline assessment of polycrystalline $Cu_2ZnSnS_4$ thin films for sustainable photovoltaic technologies: Phonon confinement model ..... 68

Compositional paradigms in multinary compound systems: A case study of kesterites ..... 77

Influence of compositionally induced defects on the vibrational properties of device grade $Cu_2ZnSnSe_4$ absorbers for kesterite based solar cells ..... 85

Secondary phase and Cu substitutional defect dynamics in kesterite solar cells: impact on optoelectronic properties ..... 90

**Chapter 4:** ***Raman spectroscopy based methodologies for anion compositional assessment of kesterites and sulfo-selenide secondary phases*** ..... **101**

Raman scattering quantitative analysis of the anion chemical composition in kesterite $Cu_2ZnSn(S_xSe_{1-x})_4$ solid solutions ..... 109

Resonant Raman scattering of $ZnS_xSe_{1-x}$ solid solutions: role of S and Se electronic states ..... 118

**Chapter 5:** ***Conclusions*** ..... **127**

**References** ..... **132**

**Appendix:** ***Table of content graphics*** ..... **137**

# List of acronyms used in this work

AES – Auger electron spectroscopy

CZTS – $Cu_2ZnSnS_4$

CZTSe – $Cu_2ZnSnSe_4$

CZTSSe – $Cu_2ZnSn(S,Se)_4$

EDX – energy dispersive x-ray (spectroscopy)

EQE – external quantum efficiency

FF – fill factor

FWHM – full-width-at-half-max

$J_{sc}$ – short circuit current

IR – infrared

PCM – phonon confinement model

PV – photovoltaic

SEM – scanning electron microscopy

TCO – transparent conducting oxide

UV – ultraviolet

$V_{OC}$ - open circuit voltage

XPS – x-ray photoelectron spectroscopy

XRD – x-ray diffraction

XRF – x-ray fluorescence (spectroscopy)

ZnSSe – Zn(S,Se)

# Preface

*Publications and summary of the thesis*

The work presented in this thesis was carried out at the Catalonia Institute for Energy Research (IREC) in Sant Adria de Besos (Barcelona), Spain from 2013 to 2015, in the frame of Marie Curie Fellowship of the KESTCELLS project (FP7/2007-2013/ 316488). The main subject of the thesis is characterization of crystalline and vibrational properties of kesterite materials (CZTS, CZTSe and CZTSSe), which are used as light absorber layers in thin film photovoltaic devices.

Each chapter in the thesis is structured around several articles which are published in high impact peer-reviewed journals. According to the requirements for the Doctor of Philosophy in Physics at the University of Barcelona, this thesis is constituted of the following eight articles:

**M. Dimitrievska**, A. Fairbrother, X. Fontané, T. Jawhari, V. Izquierdo-Roca, E. Saucedo, and A. Pérez-Rodríguez, "Multiwavelength excitation Raman scattering study of polycrystalline kesterite $Cu_2ZnSnS_4$ thin films," **Appl. Phys. Lett.**, vol. 104, no. 2, p. 021901, (2014).

**M. Dimitrievska**, H. Xie, A. Fairbrother, X. Fontané, G. Gurieva, E. Saucedo, A. Pérez-Rodríguez, S. Schorr, and V. Izquierdo-Roca, "Multiwavelength excitation Raman scattering of $Cu_2ZnSn(S_xSe_{1-x})_4$ ($0 \leq x \leq 1$) polycrystalline thin films: Vibrational properties of sulfoselenide solid solutions," **Appl. Phys. Lett**., vol. 105, no. 3, p. 031913 (2014).

**M. Dimitrievska**, A. Fairbrother, A. Pérez-Rodríguez, E. Saucedo, and V. Izquierdo-Roca, "Raman scattering crystalline assessment of polycrystalline $Cu_2ZnSnS_4$ thin films for sustainable photovoltaic technologies: Phonon confinement model," **Acta Mater.**, vol. 70, pp. 272 – 280, (2014).

A. Fairbrother, **M. Dimitrievska**, V. Izquierdo-Roca, A. Pérez-Rodríguez, and E. Saucedo, "Compositional paradigms in multinary compound systems: A case study of kesterites," **J. Mat. Chem. A**, vol. 3, no. 18, p. 9451 (2015).

**M. Dimitrievska**, A. Fairbrother, E. Saucedo, A. Pérez-Rodríguez, and V. Izquierdo-Roca, "Influence of compositionally induced defects on the vibrational properties of device grade $Cu_2ZnSnSe_4$ absorbers for kesterite based solar cells," **Appl. Phys. Lett**., vol. 106, no. 7, p. 073903 (2015).

**M. Dimitrievska**, A. Fairbrother, E. Saucedo, A. Pérez-Rodríguez, and V. Izquierdo-Roca, "Secondary phase and Cu substitutional defect dynamics in

kesterite solar cells: impact on optoelectronic properties," **Sol. Energ. Mat. Sol. C.**, accepted (2015).

**M. Dimitrievska**, G. Gurieva, H. Xie, A. Carrete, A. Cabot, E. Saucedo, A. Pérez-Rodríguez, S. Schorr, and V. Izquierdo-Roca, "Raman scattering quantitative analysis of the anion chemical composition in kesterite $Cu_2ZnSn(S_xSe_{1-x})_4$ solid solutions" **J. Alloys Compd.**, vol. 628, pp. 464 – 470, (2015).

**M. Dimitrievska**, H. Xie, A. J. Jackson, X. Fontané, M. Espindola-Rodriguez, E. Saucedo, A. Pérez-Rodríguez, A. Walsh and V. Izquierdo-Roca, "Resonant Raman scattering of $ZnS_xSe_{1-x}$ solid solutions: role of S and Se electronic states," **Phys. Chem. Chem. Phys**, in press (2015). Doi: 10.1039/C5CP04498G.

The thesis is constituted of five chapters. At the beginning of each chapter there is a short summary of the most important results presented in the articles on which that chapter is based. After this, each chapter concludes with the full text of the included articles.

The first chapter is an introduction into photovoltaics, where the basic solar cell device structure and physics is explained, as well as the current state-of-the-art and challenges of the photovoltaic market and the possible solutions for the future. The main focus is then put on thin film photovoltaic solar cells, in particular those based in chalcogenide compounds, such as kesterites. Following this, an introduction into Raman scattering spectroscopy, as one of the main techniques used in the thesis, is presented. The physics and working principle of the regular and resonance Raman effect is explained, as well as advantages and disadvantages of applying this method for the characterization of polycrystalline thin films. Finally, the objectives of the thesis are presented.

The second chapter is centered in the characterization of the fundamental properties of kesterite compounds. This includes complete analysis and identification of all active Raman modes for polycrystalline CZTS and CZTSe thin films and their solid solutions using multi-wavelength excitation Raman spectroscopy methods. Frequency and symmetry assignment of the main Raman modes are obtained from the spectra measured under regular and resonance Raman conditions, and in different polarization configurations. Additionally, first principle simulations enabled calculation of normal displacements for each mode separately, which in return gave information about the type of atoms involved in each vibration. This chapter is concluded with two articles: "Multiwavelength excitation Raman scattering study of polycrystalline kesterite

$Cu_2ZnSnS_4$ thin films" and "Multiwavelength excitation Raman scattering of $Cu_2ZnSn(S_xSe_{1-x})_4$ ($0 \leq x \leq 1$) polycrystalline thin films: Vibrational properties of sulfoselenide solid solutions" in which detailed information about the results discussed in this chapter are presented.

The third chapter presents the defect dynamics in kesterite materials. This includes development of the methodologies for the identification of different types of defects and then exploring their effect on the optoelectronic properties. The first part of the chapter is based on explaining the phonon confinement effects in kesterites, which are dominant in the case where a high density of defects is present in the material. It is shown that these effects are evident in the asymmetrical broadening of the most intense Raman peaks, arising due to the activation of the non-center phonons caused by the loss of translational symmetry in the crystal. Simultaneous fitting of these peaks according to the phonon confinement model is used to determine the correlation length, a parameter which is shown to quantitatively indicate the crystal quality of the material. The second part of the chapter is focused on identification of the specific defect clusters, the formation of which is highly probable in these kinds of materials, according to theoretical simulations. Formation of defects is compositionally induced in the specially prepared combinatorial samples with lateral compositional gradients. These combinatorial samples were later made into solar cells, with about 200 devices per each sample. Systematic XRD, Raman and optoelectronic characterization of the samples was performed, with the aim of correlating the vibrational and optoelectronic properties with the changes of the absorber composition. This resulted in observation of the changes in the relative intensity of Raman peaks, which are then systematically analyzed in relation to the occurrence of different kinds of defect clusters involving $V_{Cu}$, $Zn_{Cu}$, $Zn_{Sn}$, $Cu_{Zn}$ and $Sn_{Zn}$ point defects, in order to analyze the vibrational origin of the different modes. Additionally, the effect of Sn-Se, Zn-Se and Cu-Se secondary phases on the optoelectronic properties is presented, with a special emphasis put on the presence of the secondary phases in the bulk or surface of the absorber. This chapter ends with the explanation of the influence of $[V_{Cu} + Zn_{Cu}]$ defect clusters on the open-circuit voltage. The chapter is based on four publications: "Raman scattering crystalline assessment of polycrystalline $Cu_2ZnSnS_4$ thin films for sustainable photovoltaic technologies: Phonon confinement model", "Compositional paradigms in multinary compound systems: A case study of kesterites", "Influence of compositionally induced defects on the vibrational properties of device grade $Cu_2ZnSnSe_4$ absorbers for kesterite based solar cells" and "Secondary phase and Cu substitutional defect dynamics in kesterite solar cells: impact on optoelectronic properties" which are presented at the end.

The fourth chapter is focused on application of Raman spectroscopy for the development of suitable methodologies for the anion compositional assessment of

kesterites and sulfo-selenide secondary phases. The first part of this chapter presents a general methodology that has been developed for the quantitative determination of anion composition of CZTSSe solid solutions using Raman spectroscopy. The methodology is based on the analysis of the integral intensity ratio of Raman bands sensitive to anion vibrations in relation to the anion composition of CZTSSe solid solutions. The methodology is calibrated using reference powder samples, and later validated by testing on different kinds of samples, including photovoltaic grade films with different compositions and films with different crystalline quality and the same composition. The second part of this chapter is dedicated to the Raman resonance scattering characterization of ZnSSe solid solutions, the most common secondary phase present in CZTSSe systems. Special focus is put on the Raman scattering intensities of the LO ZnS-like and ZnSe-like phonon modes, corresponding to vibrations of only S and Se ions, respectively, which proved to be significantly enhanced when excited with 325 nm excitation in the case of S vibrations, and with 455 nm in the case of the Se vibrations. This behavior is explained with the interaction of the excitation photons with the corresponding S or Se electronic states in the conduction band, and further confirmed by the first principle simulations. The chapter is concluded with the presentation of two publications: "Raman scattering quantitative analysis of the anion chemical composition in kesterite $Cu_2ZnSn(S_xSe_{1-x})_4$ solid solutions", and "Resonant Raman scattering of $ZnS_xSe_{1-x}$ solid solutions: role of S and Se electronic states", on which this chapter is based.

The final chapter of the thesis includes a summary and conclusion of the work.

Finally, the following papers, which are authored or co-author by Mirjana Dimitrievska, contributed to the preparation of this thesis, but are not included in the text:

**M. Dimitrievska**, H. Xie, G. Gurieva, X. Fontane, A. Fairbrother, R. Gunder, E. Saucedo, A. Perez-Rodriguez, S. Schorr, and V. Izquierdo-Roca, "Vibrational and structural properties of $Cu_2ZnSn(S_xSe_{1-x})_4$ ($0 \leq x \leq 1$) solid solutions," in *Photovoltaic Specialist Conference (PVSC)*, **2014 IEEE 40th**, pp. 0033-0036 (2014).

**M. Dimitrievska**, A. Fairbrother, V. Izquierdo-Roca, A. Perez-Rodriguez, and E. Saucedo, "Two ideal compositions for kesterite-based solar cell devices," in *Photovoltaic Specialist Conference (PVSC)*, **2014 IEEE 40th**, pp. 2307-2309 (2014).

H. Xie, **M. Dimitrievska**, X. Fontané, Y. Sánchez, S. López-Marino, V. Izquierdo-Roca, V. Bermúdez, A. Pérez-Rodríguez, E. Saucedo, "Formation and impact of secondary phases in Cu-poor Zn-rich $Cu_2ZnSn(S_{1-y}Se_y)_4$ ($0 \leq y \leq 1$) based solar cells", **Sol. Energ. Mat. Sol. C.,** vol. 140, p. 289 (2015).

M. Placidi, **M. Dimitrievska**, V. Izquierdo-Roca, X. Fontané, A. Castellanos-Gomez, A. Pérez-Tomás, N. Mestres, M. Espindola-Rodriguez, S. López-Marino, M. Neuschitzer, V. Bermudez, A.M Yaremko and A. Pérez-Rodríguez, "Multiwavelength excitation Raman scattering analysis of bulk and 2 dimensional $MoS_2$: Vibrational properties of atomically thin $MoS_2$ layers", **2D Mater.,** vol. 2, p. 035006 (2015).

G. Gurieva, **M. Dimitrievska**, S. Zander, A. Pérez-Rodríguez, V. Izquierdo-Roca, S. Schorr, "Structural characterisation of $Cu_{2.04}Zn_{0.91}Sn_{1.05}S_{2.08}Se_{1.92}$", **Phys. Status Solidi C**, vol. 12, pp. 588 – 591, (2015).

J. Márquez, M. Neuschitzer, **M. Dimitrievska**, R. Gunder, S. Haass, M. Werner, Y. Romanyuk, S. Schorr, N. Pearsall and I. Forbes, "Systematic compositional changes and their influence on lattice and optoelectronic properties of $Cu_2ZnSnSe_4$ kesterite solar cells". **Sol. Energ. Mat. Sol. C.,** accepted (2015).

J. M. Skelton, A. J. Jackson, **M. Dimitrievska**, S. K. Wallace, and A. Walsh, "Vibrational spectra and lattice thermal conductivity of kesterite-structured $Cu_2ZnSnS_4$ and $Cu_2ZnSnSe_4$," **APL Mat.**, vol. 3, no. 4, p. 041102 (2015).

L. Vauche, L. Risch, Y. Sánchez, **M. Dimitrievska**, M. Pasquinelli, T. Goislard de Monsabert, P.-P. Grand, S. Jaime-Ferrer, E. Saucedo, "8.2% $Cu_2ZnSnSe_4$ thin film solar cells from large area electrodeposited precursors", **Prog. Photovolt. Res. Appl.**, in press (2015). DOI: 10.1002/pip.2643

Y. Sanchez, M. Neuschitzer, **M. Dimitrievska**, M. Espindola-Rodriguez, J. Lopez-Garcia, V. Izquierdo-Roca, O. Vigil-Galan, and E. Saucedo, "High $V_{OC}$ $Cu_2ZnSnSe_4$/CdS:Cu based solar cell: Evidences of a metal-insulator-semiconductor (MIS) type hetero-junction," in *Photovoltaic Specialist Conference (PVSC)*, **2014 IEEE 40th**, pp. 0417-0420 (2014).

A. Fairbrother, L. Fourdrinier, X. Fontané, V. Izquierdo-Roca, **M. Dimitrievska**, A. Pérez-Rodríguez, and E. Saucedo, "Precursor stack ordering

effects in $Cu_2ZnSnSe_4$ thin films prepared by rapid thermal processing," **J. Phys. Chem. C**, vol. 118, no. 31, pp. 17291–17298 (2014).

## Contribution of the author to publications in the thesis

The author of this work, Mirjana Dimitrievska, has been responsible for the design and coordination of experiments, interpretation of the experimental results and theoretical modeling and calculations performed in this thesis. She has directly participated in the structural, vibrational and optoelectronic characterization of the samples. Additionally she has extensively worked on the theoretical simulations in order to develop models for the methodologies presented in this work. The author has coordinated the process of the preparation of absorbers and devices which were needed for the performance of the studies presented here.

**Chapter 2**

(1) M. Dimitrievska, et al, "Multiwavelength excitation Raman scattering study of polycrystalline kesterite $Cu_2ZnSnS_4$ thin films," **Applied Physic Letters**, vol. 104, no. 2, p. 021901, (2014).

Work was one of the most cited of the journal for period January-June 2015

Impact Factor (IF): 3.51

1st quartile in areas: Physics and Astronomy

This work is focused on the complete identification of Raman modes for the CZTS material using regular and resonance Raman spectroscopy. This article presents an important reference for future studies of these materials. In this work, Mirjana Dimitrievska was responsible for the measurements, interpretation of the experimental data and full writing of the manuscript.

(2) M. Dimitrievska, et al, "Multiwavelength excitation Raman scattering of $Cu_2ZnSn(S_xSe_{1-x})_4$ ($0 \leq x \leq 1$) polycrystalline thin films: Vibrational properties of sulfoselenide solid solutions," **Applied Physics Letters**, vol. 105, no. 3, p. 031913 (2014).

Impact Factor (IF): 3.51

1st quartile in areas: Physics and Astronomy

In this work, Raman spectroscopy and XRD were applied together in order to evaluate the crystal structure and the phonon modes of photovoltaic

grade CZTSSe kesterite thin films. This led to complete characterization of the structural and vibrational properties of these compounds. Part of this work Mirjana Dimitrievska has done at the Helmholtz Zentrum Berlin, where she had performed XRD characterization of the samples as well as the refinements of the patterns. She was also responsible for the coordination of the collaboration between the groups working at her host institute and HZB. Additionally, she had made the Raman characterization of the samples, done the interpretation of the experimental results, and was fully responsible for writing the manuscript.

**Chapter 3**

(3) M. Dimitrievska, et al, "Raman scattering crystalline assessment of polycrystalline $Cu_2ZnSnS_4$ thin films for sustainable photovoltaic technologies: Phonon confinement model," **Acta Materialia**, vol. 70, pp. 272 – 280, (2014).

Impact Factor (IF): 4.87

1st quartile in areas: Electronic, Optical and Magnetic Materials

This work explores the phonon confinement effects in the Raman spectra of polycrystalline CZTS thin films, which were prepared with different crystal quality. Mirjana Dimitrievska preformed the experimental characterization of the samples using Raman spectroscopy, SEM and XRD methods. She was also responsible for the interpretation of all experimental results. Additionally, for this work she has developed a theoretical model based on the phonon confinement effect for kesterite materials. The main objective of the model is quantitative estimation of the crystal quality from the Raman spectra. The model has been applied on several different types of kesterite samples, leading to successful estimation of the crystal quality. Mirjana Dimitrievska was also in charge of writing the manuscript and correlating all experimental data.

(4) A. Fairbrother, M. Dimitrievska, et al, "Compositional paradigms in multinary compound systems: A case study of kesterites," **Journal of Materials Chemistry A**, vol. 3, no. 18, p. 9451 (2015).

Impact Factor (IF): 7.44

1st quartile in areas: Chemistry; Materials Science; Renewable Energy

In this article, CZTSe thin films with lateral compositional gradients have been prepared and used for the fabrication of a high number of solar cells (approximately 200) with different absorber composition. These samples have been used for the combinatorial studies of optoelectronic properties, with the aim of narrowing the compositional range to produce higher performance devices as well as study fundamental properties of the materials. In that regard, Mirjana Dimitrievska was involved in the coordination of the production of the samples, as well as selecting the compositional intervals which would be interesting for this study. She has prepared and interpreted the data regarding the correlation among the optoelectronic properties and the absorber composition. Additionally, she has prepared and designed most of the figures for this article, and directly contributed to the writing of the manuscript.

(5) M. Dimitrievska, et al, "Influence of compositionally induced defects on the vibrational properties of device grade $Cu_2ZnSnSe_4$ absorbers for kesterite based solar cells," **Applied Physics Letters**, vol. 106, no. 7, p. 073903 (2015).

Impact Factor (IF): 3.51

1st quartile in areas: Physics and Astronomy

In this article, Mirjana Dimitrievska designed and coordinated an ambitious work which included experimental identification of the different defect clusters present in CZTSe compounds. The advanced characterization of the combinatorial samples by Raman spectroscopy led to identification of the effect of defect clusters on the peak features in the Raman spectra. This work is especially relevant because it shows for the first time the direct impact of defects on the Raman peaks of kesterites. This opens very interesting prospects for the use of Raman spectroscopy for the non-

destructive detection of structural defects in the absorber films. Mirjana Dimitrievska was responsible for measuring and interpreting Raman spectra of more than 200 samples with three excitation wavelengths. She was also in charge of writing the manuscript.

(6) M. Dimitrievska, et al, "Secondary phase and Cu substitutional defect dynamics in kesterite solar cells: impact on optoelectronic properties," **Solar Energy Materials & Solar Cells**, accepted (2015).

Impact Factor (IF): 5.76

1st quartile in areas: Electronic, Optical and Magnetic Materials; Renewable Energy

This article investigates the influence of point defects and secondary phases on the performance of CZTSe devices. Systematic Raman scattering, XRD and optoelectronic characterization of the combinatorial samples with nearly 200 cells per samples was made. These results are especially relevant for the kesterite community, particularly for the optimization of the device preparation processes, since it has been show that open-circuit voltage of solar cells can be tuned by adjusting the amount of Cu-substitutional defects present in the absorber. In this work, Mirjana Dimitrievska coordinated and designed the experiments, including the characterization of the samples, as well as the interpretation of the experimental data. She was also responsible for fully writing the manuscript.

**Chapter 4**

(7) M. Dimitrievska, et al, "Raman scattering quantitative analysis of the anion chemical composition in kesterite $Cu_2ZnSn(S_xSe_{1-x})_4$ solid solutions" **Journal of Alloys and Compounds**, vol. 628, pp. 464 – 470, (2015).

Impact Factor (IF): 2.72

1st quartile in areas: Materials Chemistry; Metals and Alloys, Mechanics of Materials

In this work, Mirjana Dimitrievska was responsible for the development of simple and non-destructive optical methodology for the quantitative measurement of [S] / ([S] + [Se]) anion composition in kesterite CZTSSe solid solutions by means of Raman spectroscopy. The methodology is based on the dependence of the integral intensity ratio of Raman bands sensitive to anion vibrations with the [S] / ([S] + [Se]) composition of the kesterite solid solutions. Mirjana Dimitrievska coordinated and designed the experiments for this work, which presents collaboration among three different scientific groups, two of which are based at IREC and one at Helmholtz Zentrum Berlin. Mirjana organized preparation of all samples, from which the reference powder samples were synthesized at Helmholtz Zentrum Berlin, while the rest were made at IREC. She was also completely responsible for all structural and vibrational characterization, interpretation of the data, and for writing of the manuscript.

(8) M. Dimitrievska, et al, "Resonant Raman scattering of $ZnS_xSe_{1-x}$ solid solutions: role of S and Se electronic states," **Physical Chemistry Chemical Physics**, in press (2015). Doi: 10.1039/C5CP04498G.

Work selected for back cover of the journal

Impact Factor (IF): 4.49

1st quartile in areas: Physics and Astronomy; Physical and Theoretical Chemistry

This article presents a collaborative work between IREC and the University of Bath, which was proposed, organized and coordinated by Mirjana Dimitrievska. The main objective of this study was to better understand the fundamental properties of ZnSSe solid solutions, which are the most common secondary phases in CZTSSe materials. All experimental characterization regarding the vibrational and structural properties, which included Raman and XRD measurements, was coordinated by Mirjana Dimitrievska. She has also performed the interpretation of the experimental data. Additionally she has designed the objectives for the theoretical simulations which were performed at University of Bath. Finally, she has made the correlation among the experimental and theoretical data, and fully prepared the manuscript.

None of these articles have been previously used by other co-authors for their doctoral thesis.

Barcelona, 21. 10. 2015.

Prof. Alejandro Pérez Rodríguez Dr. Victor Izquierdo-Roca

# Prefacio

## *Publicaciones y resumen de la tesis*

El trabajo presentado en esta tesis fue realizado en el Instituto de Investigación en Energía de Cataluña (IREC) en Sant Adrìa del Besòs (Barcelona), España, desde el año 2013 hasta el 2015 dentro del proyecto Marie Curie KESTCELLS (FP7/2007-2013/ 316488). El tema principal de la tesis es la caracterización de propiedades cristalinas y vibracionales de kesteritas (CZTS, CZTSe, CZTSSe), materiales que se utilizan como absorbedores de luz en dispositivos fotovoltaicos de capa delgada.

Cada capítulo de la tesis está estructurado en torno a varios artículos publicados en revistas de peer-review de alto impacto. De acuerdo con los requisitos para el Doctorado en Filosofía de Física en la Universidad de Barcelona, esta tesis está constituida por los siguientes ocho artículos:

**M. Dimitrievska**, A. Fairbrother, X. Fontané, T. Jawhari, V. Izquierdo-Roca, E. Saucedo, and A. Pérez-Rodríguez, "Multiwavelength excitation Raman scattering study of polycrystalline kesterite $Cu_2ZnSnS_4$ thin films," **Appl. Phys. Lett.**, vol. 104, no. 2, p. 021901, (2014).

**M. Dimitrievska**, H. Xie, A. Fairbrother, X. Fontané, G. Gurieva, E. Saucedo, A. Pérez-Rodríguez, S. Schorr, and V. Izquierdo-Roca, "Multiwavelength excitation Raman scattering of $Cu_2ZnSn(S_xSe_{1-x})_4$ ($0 \leqslant x \leqslant 1$) polycrystalline thin films: Vibrational properties of sulfoselenide solid solutions," **Appl. Phys. Lett**., vol. 105, no. 3, p. 031913 (2014).

**M. Dimitrievska**, A. Fairbrother, A. Pérez-Rodríguez, E. Saucedo, and V. Izquierdo-Roca, "Raman scattering crystalline assessment of polycrystalline $Cu_2ZnSnS_4$ thin films for sustainable photovoltaic technologies: Phonon confinement model," **Acta Mater.**, vol. 70, pp. 272 – 280, (2014).

A. Fairbrother, **M. Dimitrievska**, V. Izquierdo-Roca, A. Pérez-Rodríguez, and E. Saucedo, "Compositional paradigms in multinary compound systems: A case study of kesterites," **J. Mat. Chem. A**, vol. 3, no. 18, p. 9451 (2015).

**M. Dimitrievska**, A. Fairbrother, E. Saucedo, A. Pérez-Rodríguez, and V. Izquierdo-Roca, "Influence of compositionally induced defects on the vibrational properties of device grade $Cu_2ZnSnSe_4$ absorbers for kesterite based solar cells," **Appl. Phys. Lett**., vol. 106, no. 7, p. 073903 (2015).

**M. Dimitrievska**, A. Fairbrother, E. Saucedo, A. Pérez-Rodríguez, and V. Izquierdo-Roca, "Secondary phase and Cu substitutional defect dynamics in

kesterite solar cells: impact on optoelectronic properties," **Sol. Energ. Mat. Sol. C.**, accepted (2015).

**M. Dimitrievska**, G. Gurieva, H. Xie, A. Carrete, A. Cabot, E. Saucedo, A. Pérez-Rodríguez, S. Schorr, and V. Izquierdo-Roca, "Raman scattering quantitative analysis of the anion chemical composition in kesterite $Cu_2ZnSn(S_xSe_{1-x})_4$ solid solutions" **J. Alloys Compd.**, vol. 628, pp. 464 – 470, (2015).

**M. Dimitrievska**, H. Xie, A. J. Jackson, X. Fontané, M. Espindola-Rodriguez, E. Saucedo, A. Pérez-Rodríguez, A. Walsh and V. Izquierdo-Roca, "Resonant Raman scattering of $ZnS_xSe_{1-x}$ solid solutions: role of S and Se electronic states," **Phys. Chem. Chem. Phys**, in press (2015). Doi: 10.1039/C5CP04498G.

La tesis está estructurada en cinco capítulos. Cada capítulo comienza con un resumen de los resultados más importantes presentados en los artículos sobre los cuales se basa dicho capítulo. Después, cada capítulo concluye con el texto completo de dichos artículos.

El primer capítulo consiste en una introducción a la tecnología fotovoltaica. En ella se incluye la descripción de la estructura básica de un dispositivo fotovoltaico, los fundamentos físicos en los que se basa, el estado del arte y los desafíos que plantea el mercado fotovoltaico actual así como las posibles soluciones para el futuro. Seguidamente, el capítulo pasa a centrarse en los dispositivos fotovoltaicos de capa delgada, en particular en los basados en compuestos calcogenuros como las kesteritas. A continuación, se introduce la espectroscopia Raman, la técnica de caracterización principal utilizada en esta tesis. Se explican los fundamentos físicos del efecto Raman, tanto convencional como resonante, así como las ventajas y desventajas de la aplicación de este método para la caracterización de capas delgadas y policristalinas. Finalmente, se presentan los objetivos de la tesis.

El segundo capítulo se centra en la caracterización de las propiedades fundamentales de los compuestos de kesterita. Incluye un análisis e identificación completas de todos los modos activos de Raman de capas delgadas y policristalinas de CZTS, CZTSe y sus soluciones sólidas a través del empleo de métodos de espectroscopia Raman de excitación con múltiples longitudes de onda. La asignación de la frecuencia y la simetría de los principales modos Raman se obtiene a partir de los espectros realizados en condiciones convencionales y resonantes y utilizando distintas configuraciones de polarización. De manera adicional, simulaciones de primeros

principios permitieron el cálculo de los desplazamientos normales de cada modo. Estos cálculos proporcionan información sobre los tipos de átomos que participan en cada vibración. El capítulo finaliza con dos artículos en los que se presenta información detallada de los resultados discutidos a lo largo del mismo: "Multiwavelength excitation Raman scattering study of polycrystalline kesterite $Cu_2ZnSnS_4$ thin films" y "Multiwavelength excitation Raman scattering of $Cu_2ZnSn(S_xSe_{1-x})_4$ ($0 \leqslant x \leqslant 1$) polycrystalline thin films: Vibrational properties of sulfoselenide solid solutions".

El tercer capítulo trata la dinámica de los defectos en las kesteritas. Incluye el desarrollo de metodologías para la identificación de los diferentes tipos de defectos y el análisis del efecto que tienen en las propiedades optoelectrónicas. La primera parte de este capítulo explica los efectos del confinamiento de fonones en las kesteritas. Éstos son dominantes cuando el material presenta una alta densidad de defectos y se evidencian en el ensanchamiento asimétrico de los picos Raman más intensos. Este ensanchamiento es causado por la activación de fonones no céntricos originados por la pérdida de simetría traslacional en el cristal. Se han realizado ajustes simultáneos de los picos de acuerdo con el modelo de confinamiento de fonones para determinar la longitud de correlación. Se demuestra que este parámetro indica de forma cuantitativa la calidad cristalina del material. La segunda parte del capítulo está enfocada a la identificación de grupos específicos de defectos cuya formación es muy probable en este tipo de materiales de acuerdo con los cálculos teóricos. Se indujo la formación de defectos de manera composicional en muestras combinatorias con gradientes laterales de composición. Estas muestras fueron luego utilizadas para la fabricación de células solares con unos 200 dispositivos por muestra. Se realizó una caracterización sistemática por XRD, Raman y de las propiedades optoelectrónicas de las muestras con el fin de correlacionar las propiedades vibracionales y optoelectrónicas de los dispositivos con cambios en la composición del absorbedor. El resultado fue la observación de cambios en las intensidades relativas de los picos Raman. Éstos fueron analizados sistemáticamente en función de la presencia de diferentes grupos de defectos, incluyendo defectos puntuales de $V_{Cu}$, $Zn_{Cu}$, $Zn_{Sn}$, $Cu_{Zn}$ and $Sn_{Zn}$, para analizar el origen vibracional de los modos. Adicionalmente, se presenta el efecto de las fases secundarias de Sn-Se, Zn-Se y Cu-Se sobre las propiedades optoelectrónicas haciendo especial hincapié en la presencia de fases secundarias en el volumen ("bulk") o en la superficie del absorbedor. Este capítulo finaliza con una explicación sobre la influencia de los defectos [$V_{Cu}$ + $Zn_{Cu}$] en el voltaje de circuito-abierto de las células solares. El capítulo está basado en cuatro publicaciones que se adjuntan al final del mismo: "Raman scattering crystalline assessment of polycrystalline $Cu_2ZnSnS_4$ thin films for sustainable photovoltaic technologies: Phonon confinement model", "Compositional paradigms in multinary compound systems: A case study of kesterites", "Influence of

compositionally induced defects on the vibrational properties of device grade $Cu_2ZnSnSe_4$ absorbers for kesterite based solar cells" y "Secondary phase and Cu substitutional defect dynamics in kesterite solar cells: impact on optoelectronic properties".

El cuarto capítulo se centra en la aplicación de la espectroscopia Raman para el desarrollo de metodologías aptas para la estimación composicional de los aniones de kesteritas y otras fases sulfo-seleniuro. En la primera parte del capítulo se presenta una metodología general que fue desarrollada para la determinación cuantitativa de la composición de aniones de soluciones sólidas de CZTSSe utilizando la espectroscopia Raman. La metodología se basa en el análisis del ratio entre la intensidad integral de las bandas Raman sensibles a vibraciones de los aniones y la composición de aniones en soluciones sólidas de CZTSSe. La metodología fue calibrada utilizando muestras de referencia en polvo y validada a través de la comprobación de diferentes tipos de muestras, incluyendo capas de grado fotovoltaico con distintas composiciones y capas de la misma composición pero con diferencias en la calidad cristalina. La segunda parte del capítulo comprende la caracterización Raman en resonancia de soluciones sólidas de ZnSSe, la fase secundaria más común en sistemas de CZTSSe. Se pone una mayor atención en las intensidades Raman de los modos de fonones LO del tipo ZnS y ZnSe, correspondientes a vibraciones de S y Se puros, respectivamente, las cuales aumentan de manera significativa con la excitación de 325 nm, en el caso de vibraciones de S, y con 455 nm en el caso de vibraciones de Se. Este comportamiento se explica por la interacción de los fotones de excitación con los estados electrónicos correspondientes, de S o Se, en la banda de conducción. Esto ha sido confirmado, además, con simulaciones de primeros principios. El capítulo concluye con la presentación de dos publicaciones sobre las cuales está basado el mismo: "Raman scattering quantitative analysis of the anion chemical composition in kesterite $Cu_2ZnSn(S_xSe_{1-x})_4$ solid solutions", y "Resonant Raman scattering of $ZnS_xSe_{1-x}$ solid solutions: role of S and Se electronic states".

En el último capítulo de la tesis se incluyen un resumen del trabajo realizado y las conclusiones.

Por último, los siguientes artículos, en los cuales Mirjana Dimitrievska es autora o co-autora, han contribuido a la preparación de esta tesis pero no están incluidos en el texto:

**M. Dimitrievska**, H. Xie, G. Gurieva, X. Fontane, A. Fairbrother, R. Gunder, E. Saucedo, A. Perez-Rodriguez, S. Schorr, and V. Izquierdo-Roca, "Vibrational and structural properties of $Cu_2ZnSn(S_xSe_{1-x})_4$ ($0 \leqslant x \leqslant 1$) solid

solutions," in *Photovoltaic Specialist Conference (PVSC),* **2014 IEEE 40th**, pp. 0033-0036 (2014).

**M. Dimitrievska**, A. Fairbrother, V. Izquierdo-Roca, A. Perez-Rodriguez, and E. Saucedo, "Two ideal compositions for kesterite-based solar cell devices," in *Photovoltaic Specialist Conference (PVSC),* **2014 IEEE 40th**, pp. 2307-2309 (2014).

H. Xie, **M. Dimitrievska**, X. Fontané, Y. Sánchez, S. López-Marino, V. Izquierdo-Roca, V. Bermúdez, A. Pérez-Rodríguez, E. Saucedo, "Formation and impact of secondary phases in Cu-poor Zn-rich $Cu_2ZnSn(S_{1-y}Se_y)_4$ ($0 \leqslant y \leqslant 1$) based solar cells", **Sol. Energ. Mat. Sol. C.,** vol. 140, p. 289 (2015).

M. Placidi, **M. Dimitrievska**, V. Izquierdo-Roca, X. Fontané, A. Castellanos-Gomez, A. Pérez-Tomás, N. Mestres, M. Espindola-Rodriguez, S. López-Marino, M. Neuschitzer, V. Bermudez, A.M Yaremko and A. Pérez-Rodríguez, "Multiwavelength excitation Raman scattering analysis of bulk and 2 dimensional $MoS_2$: Vibrational properties of atomically thin $MoS_2$ layers", **2D Mater.,** vol. 2, p. 035006 (2015).

G. Gurieva, **M. Dimitrievska**, S. Zander, A. Pérez-Rodríguez, V. Izquierdo-Roca, S. Schorr, "Structural characterisation of $Cu_{2.04}Zn_{0.91}Sn_{1.05}S_{2.08}Se_{1.92}$", **Phys. Status Solidi C**, vol. 12, pp. 588 – 591, (2015).

J. Márquez, M. Neuschitzer, **M. Dimitrievska**, R. Gunder, S. Haass, M. Werner, Y. Romanyuk, S. Schorr, N. Pearsall and I. Forbes, "Systematic compositional changes and their influence on lattice and optoelectronic properties of $Cu_2ZnSnSe_4$ kesterite solar cells". **Sol. Energ. Mat. Sol. C.,** accepted (2015).

J. M. Skelton, A. J. Jackson, **M. Dimitrievska**, S. K. Wallace, and A. Walsh, "Vibrational spectra and lattice thermal conductivity of kesterite-structured $Cu_2ZnSnS_4$ and $Cu_2ZnSnSe_4$," **APL Mat.**, vol. 3, no. 4, p. 041102 (2015).

L. Vauche, L. Risch, Y. Sánchez, **M. Dimitrievska**, M. Pasquinelli, T. Goislard de Monsabert, P.-P. Grand, S. Jaime-Ferrer, E. Saucedo, "8.2% $Cu_2ZnSnSe_4$ thin film solar cells from large area electrodeposited precursors", **Prog. Photovolt. Res. Appl.**, in press (2015). DOI: 10.1002/pip.2643

Y. Sanchez, M. Neuschitzer, **M. Dimitrievska**, M. Espindola-Rodriguez, J. Lopez-Garcia, V. Izquierdo-Roca, O. Vigil-Galan, and E. Saucedo, "High $V_{OC}$ $Cu_2ZnSnSe_4$/CdS:Cu based solar cell: Evidences of a metal-insulator-semiconductor (MIS) type hetero-junction," in *Photovoltaic Specialist Conference (PVSC)*, **2014 IEEE 40th**, pp. 0417-0420 (2014).

A. Fairbrother, L. Fourdrinier, X. Fontané, V. Izquierdo-Roca, **M. Dimitrievska**, A. Pérez-Rodríguez, and E. Saucedo, "Precursor stack ordering effects in $Cu_2ZnSnSe_4$ thin films prepared by rapid thermal processing," **J. Phys. Chem. C**, vol. 118, no. 31, pp. 17291–17298 (2014).

**Contribución del autor a publicaciones de la tesis**

La autora de este trabajo, Mirjana Dimitrievska, ha sido responsable del diseño y la coordinación de los experimentos, la interpretación de los resultados experimentales, el modelado teórico y los cálculos realizados en esta tesis. La autora ha participado directamente en la caracterización estructural, vibracional y optoelectrónica de las muestras. Además, ha trabajado extensamente en las simulaciones teóricas desarrollando modelos para las metodologías presentadas en esta tesis. La autora ha coordinado el proceso de preparación de los absorbedores y dispositivos necesarios para realizar los estudios presentados en este documento.

**Capítulo 2**

(1) M. Dimitrievska, et al, "Multiwavelength excitation Raman scattering study of polycrystalline kesterite $Cu_2ZnSnS_4$ thin films," **Applied Physic Letters**, vol. 104, no. 2, p. 021901, (2014).

Este trabajo fue uno de los más citados durante el periodo enero-junio 2015

Factor de impacto (IF): 3.51

1$^{er}$ cuartil en las áreas: física y astronomía

Este trabajo se centra en la identificación completa de los modos Raman para el material CZTS utilizando espectroscopia Raman convencional y resonante. Este artículo representa una referencia importante para futuros estudios de estos materiales. En este trabajo, Mirjana Dimitrievska fue la responsable de las medidas, la interpretación de los datos experimentales y la escritura completa del manuscrito.

(2) M. Dimitrievska, et al, "Multiwavelength excitation Raman scattering of $Cu_2ZnSn(S_xSe_{1-x})_4$ ($0 \leqslant x \leqslant 1$) polycrystalline thin films: Vibrational properties of sulfoselenide solid solutions," **Applied Physics Letters**, vol. 105, no. 3, p. 031913 (2014).

Factor de impacto (IF): 3.51

1er cuartil en las áreas: física y astronomía

En este trabajo, la espectroscopia Raman y XRD fueron aplicadas conjuntamente para evaluar la estructura cristalina y los modos de fonones de capas delgadas de kesterita CZTSSe de grado fotovoltaico. De esta manera, se realizó una caracterización completa de las propiedades estructurales y vibracionales de estos compuestos. Una parte de este trabajo fue realizado por Mirjana Dimitrievska en el Helmholtz Zentrum Berlin, donde fue realizada la caracterización por XRD de las muestras y el refinamiento de los patrones. También fue responsable de la coordinación de la colaboración entre los grupos de su instituto de origen y el HZB. Además, realizó la caracterización por Raman de las muestras, la interpretación de los resultados experimentales y fue la responsable de la redacción del manuscrito.

**Capítulo 3**

(3) M. Dimitrievska, et al, "Raman scattering crystalline assessment of polycrystalline $Cu_2ZnSnS_4$ thin films for sustainable photovoltaic technologies: Phonon confinement model," **Acta Materialia**, vol. 70, pp. 272 – 280, (2014).

Factor de impacto (IF): 4.87

1er cuartil en las áreas: materiales electrónicos, ópticos y magnéticos

Este trabajo analiza los efectos de confinamiento de fonones en los espectros Raman de capas delgadas de CZTS policristalina sintetizadas con diferentes calidades cristalinas. Mirjana Dimitrievska realizó la caracterización experimental de las muestras empleando espectroscopia Raman, SEM y XRD. Fue también la responsable de la interpretación de los resultados experimentales. Adicionalmente, desarrolló un modelo teórico basado en el efecto de confinamiento de fonones para kesteritas en

este trabajo. El objetivo principal de este modelo es la estimación cuantitativa de la calidad cristalina a partir de los espectros Raman. Este modelo ha sido aplicado a varios tipos de muestras de kesterita consiguiendo una estimación correcta de la calidad cristalina. Mirjana Dimitrievska también fue la responsable de escribir el manuscrito y de correlacionar todos los datos experimentales.

(4) A. Fairbrother, M. Dimitrievska, et al, "Compositional paradigms in multinary compound systems: A case study of kesterites," **Journal of Materials Chemistry A**, vol. 3, no. 18, p. 9451 (2015).

Factor de impacto (IF): 7.44

1$^{er}$ cuartil en las áreas: química; ciencia de materiales; energías renovables

En este artículo, capas delgadas de CZTSe con gradientes laterales de composición fueron preparadas y utilizadas para la fabricación de un gran número de células solares (aproximadamente 200), cada célula con una composición diferente. Estas muestras fueron utilizadas para un estudio combinatorio de las propiedades optoelectrónicas con el objeto de reducir el rango composicional para la producción de dispositivos de alto rendimiento y para realizar un estudio de las propiedades fundamentales del material. A este respecto, Mirjana Dimitrievska fue involucrada en la coordinación de la producción de las muestras, además de en la selección de los intervalos composicionales de interés para el estudio. Preparó e interpretó los datos sobre la correlación entre las propiedades optoelectrónicas y la composición del absorbedor. Adicionalmente, preparó y diseñó la mayoría de las figuras del artículo y realizó contribuciones directas en la redacción del manuscrito.

(5) M. Dimitrievska, et al, "Influence of compositionally induced defects on the vibrational properties of device grade $Cu_2ZnSnSe_4$ absorbers for kesterite based solar cells," **Applied Physics Letters**, vol. 106, no. 7, p. 073903 (2015).

Factor de impacto (IF): 3.51

1$^{er}$ cuartil en las áreas: física y astronomía

En este artículo, Mirjana Dimitrievska diseñó y coordinó un ambicioso trabajo que incluye la identificación experimental de los diferentes grupos de defectos presentes en la kesterita CZTSe. La caracterización avanzada de las muestras combinatorias por espectroscopia Raman identificó los efectos de los grupos de defectos en las características de los espectros Raman. Este trabajo es particularmente relevante porque demuestra, por primera vez, el impacto directo de los defectos asociados con diferentes anomalías en los picos Raman de la kesterita. Esto abre posibilidades muy interesantes para el uso de la espectroscopia Raman para la detección no destructiva de los defectos estructurales en las capas del absorbedor. Mirjana Dimitrievska fue responsable de la medición e interpretación de los espectros Raman de más de 200 muestras con tres longitudes de onda de excitación. También fue responsable de la redacción del manuscrito.

(6) M. Dimitrievska, et al, "Secondary phase and Cu substitutional defect dynamics in kesterite solar cells: impact on optoelectronic properties," **Solar Energy Materials & Solar Cells**, accepted (2015).

Factor de impacto (IF): 5.76

1$^{er}$ cuartil en las áreas: materiales electrónicos, ópticos y magnéticos; energías renovables

Este artículo investiga la influencia de defectos puntuales y fases secundarias en el rendimiento de dispositivos de CZTSe. Una caracterización sistemática por Raman, XRD y de las propiedades optoelectrónicas de las muestras combinatorias de casi 200 células fue realizada en este trabajo. Estas muestras son muy relevantes para la comunidad de kesteritas, en particular para la optimización de procesos de fabricación de dispositivos, porque demuestran que el voltaje de circuito-abierto de las células solares se puede modificar ajustando la cantidad de defectos de sustitución de Cu presentes en el absorbedor. En este trabajo, Mirjana Dimitrievska coordinó y diseñó los experimentos, incluyendo la caracterización de las muestras y, además, la interpretó los datos experimentales. Fue responsable, también, de escribir el manuscrito.

**Capítulo 4**

(7) M. Dimitrievska, et al, "Raman scattering quantitative analysis of the anion chemical composition in kesterite $Cu_2ZnSn(S_xSe_{1-x})_4$ solid solutions" **Journal of Alloys and Compounds**, vol. 628, pp. 464 – 470, (2015).

Factor de impacto (IF): 2.72

1er cuartil en las áreas: química de materiales; metales y aleaciones; mecánica de materiales

En este trabajo, Mirjana Dimitrievska fue responsable del desarrollo de una metodología óptica sencilla y no destructiva para la medición cuantitativa de la composición de aniones [S] / ([S] + [Se]) en soluciones sólidas de kesterita CZTSSe. La metodología se basa en la dependencia del ratio entre la intensidad integral de las bandas Raman más sensibles a vibraciones de aniones y la composición de [S] / ([S] + [Se]) en soluciones sólidas de kesteritas. Mirjana Dimitrievska coordinó y diseñó los experimentos para este trabajo, lo cual requirió una colaboración entre tres grupos científicos: dos basados en IREC y uno en el Helmholtz Zentrum Berlin. Mirjana organizó la preparación de todas las muestras de las cuales las de referencia en polvo fueron sintetizadas en el Helmholtz Zentrum Berlin, mientras que las demás fueron fabricadas en IREC. También fue responsable de la caracterización estructural y vibracional, interpretación de los datos, y la redacción del manuscrito.

(8) M. Dimitrievska, et al, "Resonant Raman scattering of $ZnS_xSe_{1-x}$ solid solutions: role of S and Se electronic states," **Physical Chemistry Chemical Physics**, in press (2015). Doi: 10.1039/C5CP04498G.

Trabajo seleccionado para la portada interior de la revista

Factor de impacto (IF): 4.49

1er cuartil en las áreas: física y astronomía; química física y teórica

Este artículo presenta un trabajo de colaboración entre IREC y la Universitdad de Bath el cual fue propuesto, organizado y coordinado por Mirjana Dimitrievska. El objetivo principal de este estudio fue una mejor compresión de las propiedades fundamentales de las soluciones sólidas de

ZnSSe, la cual es la fase secundaria más común entre los materiales CZTSSe. Toda la caracterización experimental relacionada con las propiedades vibracionales y estructurales, lo cual incluye medidas de Raman y XRD, fue coordinada por Mirjana Dimitrievska. También realizó la interpretación de los datos experimentales. Adicionalmente, diseñó los objetivos para las simulaciones teóricas que fueron realizadas en la Universidad de Bath. Por último, realizó la correlación entre los datos experimentales y teóricos y preparo el manuscrito.

Ninguno de estos artículos ha sido utilizando previamente por los co-autores para su tesis doctoral.

Barcelona, 21. 10. 2015.

Prof. Alejandro Pérez Rodríguez Dr. Victor Izquierdo-Roca

# Chapter 1

*Introduction*

During the last decades the direct conversion of solar energy to electricity by photovoltaic (PV) cells has emerged from a pilot technology into one that produced more than 200 GW of electricity generating capacity in 2015, and it is projected to more than double or even triple between now and 2020.[1]

The rapid evolution of PV as an alternative means of energy generation is bringing it closer to the point where it can make a significant contribution to challenges posed by the rapid growth of worldwide energy demand and the associated environmental issues. Besides the main existing technology, which is based on silicon (Si), there is also fast development of new materials and fabrication technologies which significantly increase the potential application of this field. The PV industry, which was until recently based primarily on monocrystalline, polycrystalline, and amorphous Si, grew at an average annual rate of 50% during 2000–2010, and it is growing even faster in the recent years.[2] Even though this may seem like a very large number, PV installations are still supplying only < 1 % of all the world's power needs.[1] In order to scale this number to terawatts (TW) and reach the point at which the cost of PV power is equal to the price of grid electricity, it is necessary to increase individual cell efficiency and translate that to modules, as well as reduce the manufacturing expenses and increase the lifetime of the systems. This is why development of new materials is crucial for the future of PV.

The main working principle of solar cells is based on photovoltaic effect, in which separated photogenerated charge carriers are carried out through an external circuit.[2,3] An illustration of a working PV device in its most general form is shown in Figure 1.1. The device could be described as a system in which after absorption of a photon, an electron-hole pair is created, with the electron and hole staying in a high- and low-energy states, respectively. Normally, the electron and hole will recombine after some time, thus generating heat. In a PV solar cell however, a built in electric filed is used to separate the electron-hole pair before recombination.

In nearly all cells, especially those for the commercial use, the solar absorber is a semiconductor. If just one type of semiconductor is used, the common approach is to make a p-n junction with it. For that, the material needs to be "ambipolar", meaning that it can be doped to have either excess of electrons (n type) or excess of holes (p type). If p and n type materials are brought into contact so that they can reach electronic equilibrium, they form a junction (a diode or PV device), which can, because of the difference in electrochemical potential of the electrons between the p and n type regions, separate photogenerated carriers. Suitable external contacts then collect these photogenerated carriers and produce useful work (electric power) by the flow of current from high to low potential, through an external circuit. If the p and n type

semiconductors are made from the same material then the junction is termed a homojunction. If two different semiconductors are used, then these are termed as heterojunctions.

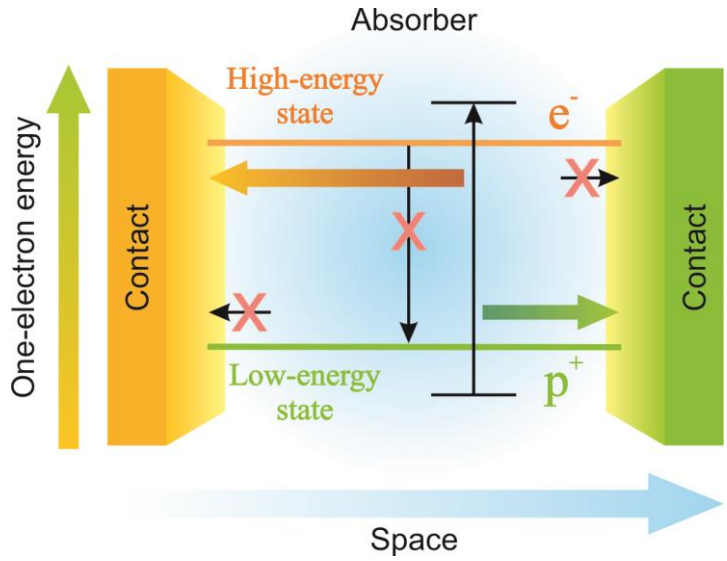


Figure 1.1 Basic working principles of a PV device

As mentioned previously, there is actually a wide variety of PV technologies, though all operate on the same mechanism described above. PV is frequently divided into three generations of technologies. These PV approaches are often named first-, second- and third-generation technologies, as illustrated in Figure 1.2.[2]

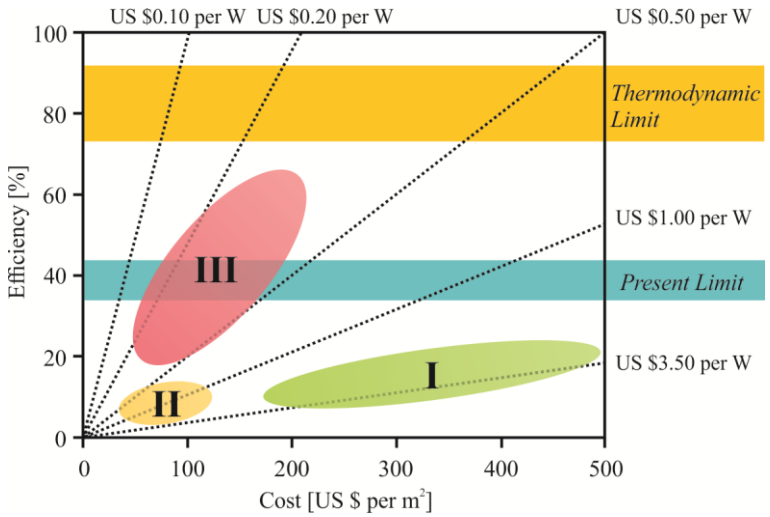


Figure 1.2 Cost efficiency analyses for I-, II- and III-generation PV technologies

The first generation technology is represented by the single-crystalline and multicrystalline Si-based modules. This is an already commercialized technology with research and optimization being developed for decades now. Unfortunately, silicon solar cells are slowly reaching their theoretical performance limit, so further improvements are becoming a challenge. Additionally, because silicon has an indirect band gap, which leads to a low absorption coefficient, relatively thick absorber layers (> 0.1 mm) are needed, which increases the cost and as well as the module weight making the layers unsuitable for flexible PV application. Nevertheless, the first generation technology constitutes about 90 % of the PV market, though it is slowly decreasing and giving way to second generation technologies.[1]

The second generation is based on thin film cells composed of a-Si:H, CdTe, chalcopyrite materials and even thin polycrystalline Si absorbers. Thin film cells are fabricated at low temperatures on low-cost substrates, such as glass or metal foils using suitable production techniques, rather than directly being cut as wafers from bulk materials. The main goal of this generation technology is to significantly reduce cost without making big loses in the efficiency, resulting in an overall reduction in the model cost per W. This is achieved by using direct band gap materials which are more efficient at absorbing light; leading to thin-film solar cells with absorber layers less than 5 μm thick. This in return significantly reduces the material usage for modules and is potentially compatible with flexible substrates. On the other side, the main drawbacks of these technologies include the use of relatively rare or toxic elements (In, Ga, Cd, Te, Ag). At the moment, these technologies account for about 10 % of the PV market, and are at early stage of commercialization when compared to the first generation technologies.

Third generation technologies exploit novel materials (like quantum dots), device designs and physical phenomena to significantly increase device efficiency and further lower production cost. Third-generation concepts have just begun to be investigated and have a long materials and development path ahead.

It should be mentioned that the boundary lines between these definitions are not so well defined and often blurred. For example, organic solar cells are thin films which could be potentially produced at very low cost, putting them in the second generation approach. However, their excitonic nature is relatively unexplored but might lead to new modes of energy harvesting, which are accounted in the third-generation approaches. Nevertheless, even with this blurring, the above mention characterization presents a very useful way to classify different PV technologies.

## Thin film solar cells

A typical cross section showing the device structure of thin film solar cells which, as mentioned before, belong to the second generation of photovoltaics, is illustrated in Figure 1.3. Usually thin film solar cells are heterojunction devices with a junction formed between a thin n-type buffer layer and a p-type absorber layer. Depending on the way of the light penetration in the solar cell, there are two possible configurations of device structures, usually referred as superstrate and substrate.[2] In the case of the superstrate configuration, the light enters through the glass on which the films making up the device are deposited, while in the substrate configuration the light enters from the face opposite of the substrate. Figure 1.3 shows a device which operates in the substrate configuration.

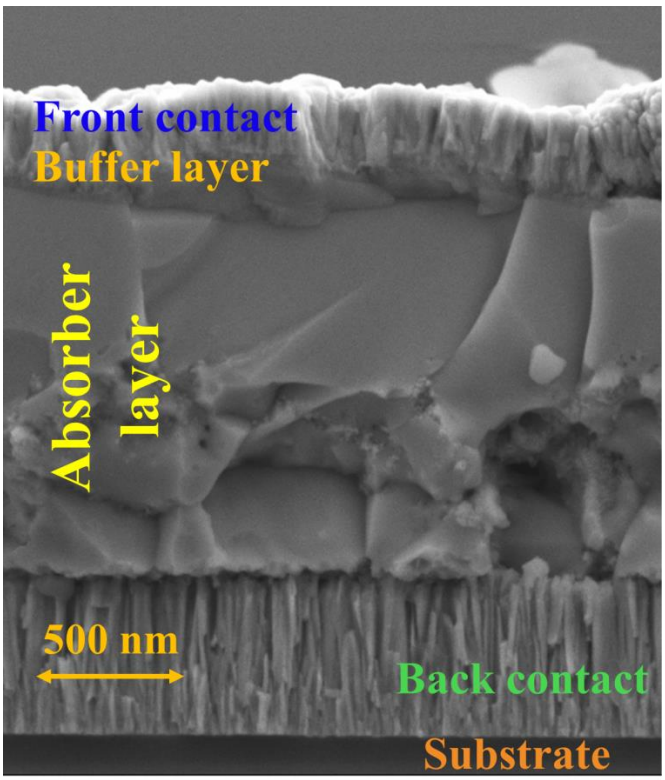


Figure 1.3 Cross section of a thin film (kesterite) solar cell device

Thin film solar cells typically consist of a transparent front contact, which is usually a transparent conducting oxide (TCO). These need to be made from low-cost, abundant elements, must have high conductivity and high transparency in the visible spectrum, and must allow easy electrical isolation of the device. This layer acts as a conduit for the photo-generated electrons, and transports them to the metal contacts.

Beneath this is an n-type buffer layer, usually less than 100 nm thick, which in conjunction with the p-type absorber, forms the p-n junction exploited for separation of the photo-generated charge carriers. The next lowest layer is the p-type semiconductor, which plays the role of absorbing the majority of incoming light, and is therefore referred as the absorber layer. Further down is the back contact layer which is usually a metal, but it may also be another semiconducting compound. And finally there is the substrate, which forms the basis of the solar cell, giving structural integrity to the entire device. The most commonly used substrate material is soda-lime glass because of its relatively low cost and the ease of working with a rigid substrate, but metal and polymer foils may also be used. Flexible substrates are of particular interest for low-weight applications, and for industrial roll-to-roll processing.

Chalcopyrite-based thin film solar cells have proved to be among the best performing devices from the second generation technology, with recently achieved conversion efficiencies above 21 % on the laboratory scale.[4] Many companies around the world are developing a variety of manufacturing approaches aimed at low-cost, high-yield, large-area devices process that try to maintain laboratory-level efficiencies in these systems. Unfortunately, materials challenges that exist in each of the layers and in the interaction between them make this accomplishment strenuous. One of the main problems for the long-term usage of this technology is abundance of the relatively rare elements like In and Ga. These metals are a by-product of other mining operations, which are mostly concentrated in a single country (China), raising concerns about mid- to long-term material supply.[5,6]

These factors have led to investigation of absorber layers based on more earth abundant materials such as kesterites ($Cu_2ZnSnS_4$, $Cu_2ZnSnSe_4$, and their solid solutions are the most common). Kesterites share many commonalities with chalcopyrites, and as such are viewed as a potential replacement in long-term production of PV modules.

Due to the abundance of all constituent elements (Cu, Zn, Sn, S and Se), kesterites are potentially a low cost, sustainable solution for multi-terawatt levels of PV deployment. At present, efforts are focused on bringing the power conversion efficiency of kesterite-based devices to commercially interesting levels, in the range of 15 – 20%, from the current record level of 12.6%.[7] For even the best solar cells, the main factor limiting the efficiency of the devices at present is the open-circuit voltage, which remains much lower than could be expected given the band gap of these materials. This has been mostly associated with electron-hole recombination in the bulk material that may be related to inhomogeneity in the distribution of Cu, Zn, and Sn.[8,9]

Kesterites, being a quaternary compound with additional number of elements relative to binary and ternary compounds, provide ample opportunities for material design, especially for the case of non-stoichiometric conditions, which are used for the production of the highest efficiency solar cells. Unfortunately, this also results in larger probability for formation of defects, either in intrinsic form (anti-sites and vacancies) or as secondary phases. Defect concentration is expected to have an important influence on the optical and electrical properties of these compounds, and therefore its knowledge is crucial for the optimization of these technologies in terms of device efficiency of solar cells with related absorbers. Additionally, fundamental properties of these materials need to be studied in more detail in order to solve the problems currently limiting the application of these technologies to the industrial level.

## Raman scattering spectroscopy

Raman spectroscopy is a vibrational spectroscopy technique based on the Raman effect and used for acquiring a unique chemical fingerprint of molecules. The Raman effect describes an inelastic light scattering process in which an incoming photon excites an electron in the material, creating excited electron-hole pair, which is then scattered on the lattice and falls back to the original state by emission of a photon (Figure 1.4).

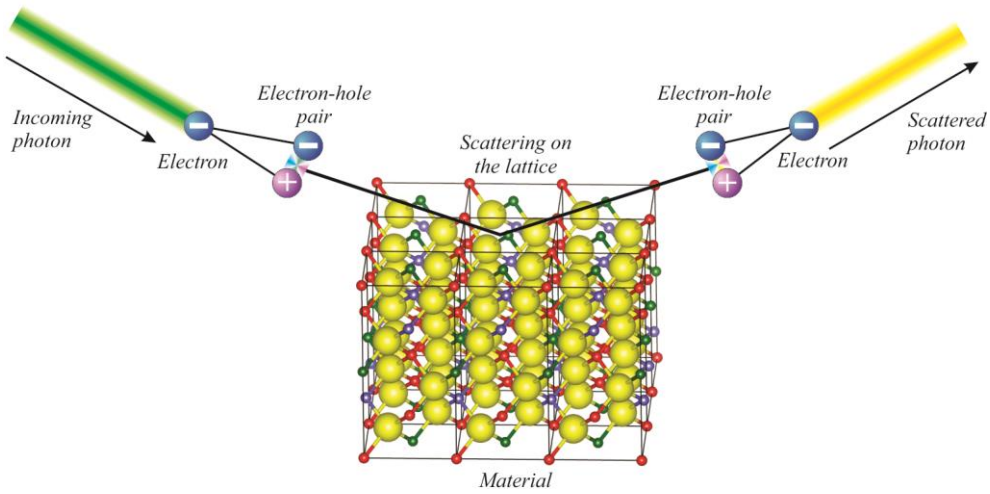


Figure 1.4 Illustration of the Raman scattering process which includes photon-electron and electron-lattice interaction.

According to the microscopic theory of the scattering process, the Raman effect can be separated into three steps.[10]

1) An incoming photon $\omega_i$ interacts with electron and creates an electron-hole pair. This state is referred to as the intermediate state $|n\rangle$ and the process is mediated by the electron-radiation Hamiltonian $H_{e-r}$ .
2) The electronic intermediate state $|n\rangle$ is scattered by the lattice, during which a phonon $\Omega$ is created and the intermediate state is converted into another intermediate state $|n'\rangle$. This process is mediated by the electron-phonon interaction and hence related to Hamiltonian $H_{e-ion}$ .
3) The electron-hole pair of the state $|n'\rangle$ decays radiatively, and a photon $\omega_s$ is emitted via $H_{e-r}$ .

According to Feynman's theory the Raman process can also be described by all possible permutations of the interactions described above. However, the order shown above gives the most important contribution to the scattering cross section. In the vicinity of electronic resonances the contributions of the other permutations are negligible. Figure 1.5 presents all six Feynman diagrams of Raman scattering process, with the first one indicating the process described before, and the other five are the possible permutations of the time order of the three vertices involved.

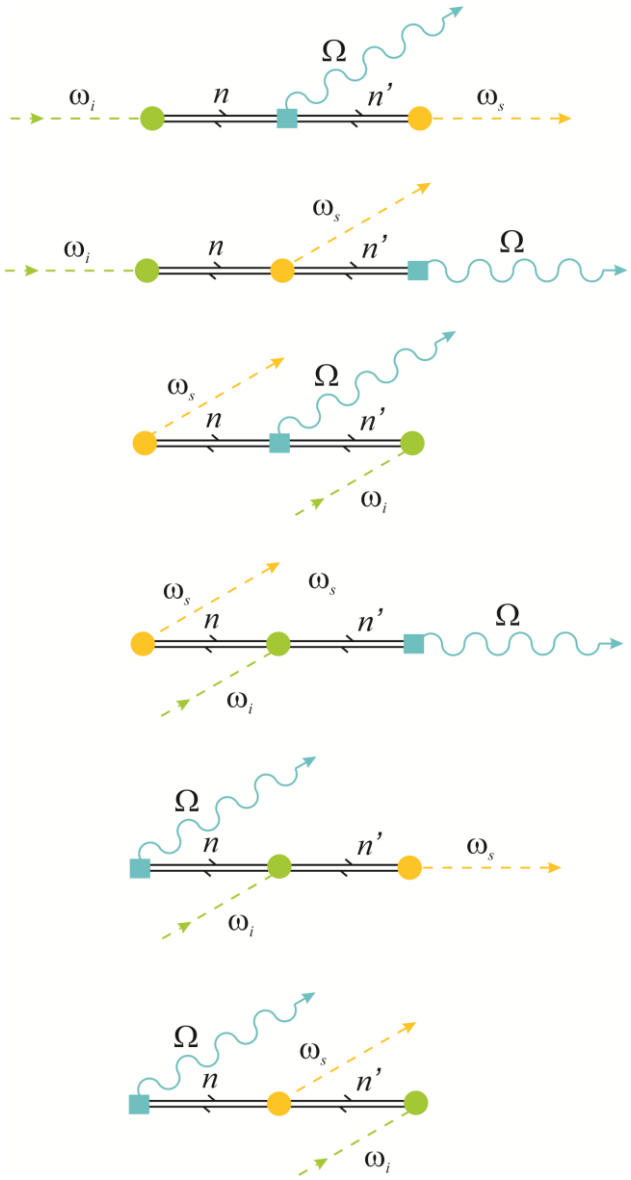


Figure 1.5 Feynman diagrams for the six scattering processes that contribute to one-phonon (Stokes) Raman scattering.

As a result from the time reversal invariance, the Feynman diagrams in Figure 1.5 can also be read from the right to the left, describing the anti-Stokes Raman process. In this case instead of creation, the phonon is annihilated and its energy is added to the energy of the incoming photon.

Using the Feynman diagrams presented in Figure 1.5, in which each vertex represents an interaction, and applying the Fermi's golden rule, the Raman scattering probability could be described by third order perturbation theory as given by equation (1.1).

$$P_{ph}(\omega_s)=\left(\frac{2\pi}{\hbar}\right)\left|\begin{aligned}&\sum_{n,n'}\frac{\langle i|\mathrm{H}_{eR}(\omega_i)|n\rangle\langle n|\mathrm{H}_{e-ion}|n'\rangle\langle n'|\mathrm{H}_{eR}(\omega_s)|i\rangle}{\left[\hbar\omega_i-(E_n-E_i)\right]\left[\hbar\omega_i-\hbar\omega_0-(E_{n'}-E_i)\right]}+\\&+\sum_{n,n'}\frac{\langle i|\mathrm{H}_{eR}(\omega_i)|n\rangle\langle n|\mathrm{H}_{eR}(\omega_s)|n'\rangle\langle n'|\mathrm{H}_{e-ion}|i\rangle}{\left[\hbar\omega_i-(E_n-E_i)\right]\left[\hbar\omega_i-\hbar\omega_s-(E_{n'}-E_i)\right]}+\\&+\sum_{n,n'}\frac{\langle i|\mathrm{H}_{eR}(\omega_s)|n\rangle\langle n|\mathrm{H}_{e-ion}|n'\rangle\langle n'|\mathrm{H}_{eR}(\omega_i)|i\rangle}{\left[-\hbar\omega_s-(E_n-E_i)\right]\left[-\hbar\omega_s-\hbar\omega_0-(E_{n'}-E_i)\right]}+\\&+\sum_{n,n'}\frac{\langle i|\mathrm{H}_{eR}(\omega_s)|n\rangle\langle n|\mathrm{H}_{eR}(\omega_i)|n'\rangle\langle n'|\mathrm{H}_{e-ion}|i\rangle}{\left[-\hbar\omega_s-(E_n-E_i)\right]\left[-\hbar\omega_s-\hbar\omega_i-(E_{n'}-E_i)\right]}+\\&+\sum_{n,n'}\frac{\langle i|\mathrm{H}_{e-ion}|n\rangle\langle n|\mathrm{H}_{eR}(\omega_i)|n'\rangle\langle n'|\mathrm{H}_{eR}(\omega_s)|i\rangle}{\left[-\hbar\omega_0-(E_n-E_i)\right]\left[-\hbar\omega_0-\hbar\omega_i-(E_{n'}-E_i)\right]}+\\&+\sum_{n,n'}\frac{\langle i|\mathrm{H}_{e-ion}|n\rangle\langle n|\mathrm{H}_{eR}(\omega_s)|n'\rangle\langle n'|\mathrm{H}_{eR}(\omega_i)|i\rangle}{\left[-\hbar\omega_0-(E_n-E_i)\right]\left[-\hbar\omega_0-\hbar\omega_s-(E_{n'}-E_i)\right]}\end{aligned}\right|^2$$
$$\times\delta(\hbar\omega_i-\hbar\omega_s-\hbar\omega_0) \qquad (1.1)$$

Here, $\hbar\omega_0$ is the energy of the created phonon, while $E_n$ and $E_{n'}$ are energies of the corresponding intermediate states, $|n\rangle$ and $|n'\rangle$, respectively.

The electronic states $|n\rangle$ and $|n'\rangle$ can be real or virtual states. In the case of regular Raman scattering, $|n\rangle$ and $|n'\rangle$ are virtual states. In contrast, if one of the states involved is a real state and the incoming or scattered photon meets the energy of the state, the scattering probability is in resonance, thus this process is referred to as resonant Raman scattering.

Under resonance conditions, the contributions of the non-resonant terms of the scattering probability could be regarded as constant. As the strongest contribution to the

scattering probability comes from the process described by the first Feynman diagram in Figure 1.5, the equation (1.1) could be significantly simplified. If it is assumed that the initial state is the ground state $|0\rangle$ with no electron-hole pairs excited and its energy is taken to be zero, and the intermediate state is $|n\rangle$ with energy $E_n$, then after summing over $\omega_s$ to remove the delta function, the equation (1.1) could be approximated as:

$$P_{ph}(\omega_s) = \left(\frac{2\pi}{\hbar}\right)\left|\frac{\langle 0|\mathrm{H}_{eR}(\omega_i)|n\rangle\langle n|\mathrm{H}_{e-ion}|n\rangle\langle n|\mathrm{H}_{eR}(\omega_s)|0\rangle}{[E_n - i\Gamma_n - \hbar\omega_i][E_n - i\Gamma_n - \hbar\omega_s]} + C\right|^2 \quad (1.2)$$

where C is a constant background. Additionally, in order to avoid the unphysical situation in which the denominator can become zero, it is necessary to assume that the intermediate state $|n\rangle$ has a finite lifetime $\tau_n$ due to the radiative and non-radiative decay processes. As a result the energy of the intermediate state $|n\rangle$ is defined as a complex energy $E_n - i\Gamma_n$, where $\Gamma_n$ is the damping constant which is related to the lifetime by $\Gamma_n = \hbar / \tau_n$.

Now it could be clearly seen that as the incoming or scattered photon energy is tuned to the energy of the intermediate state, the denominator in Eq. 1.2 becomes smaller, which then leads to the enhancement in the Raman scattering probability, and thus the resonance effects. Raman resonance effects in semiconductors may be achieved if the excitation energy approaches the band gap energy, or via the interaction of the incident photon with the exciton states or the impurity states. Raman resonance spectroscopy is especially useful for obtaining information on electron-phonon interaction, electron-radiation interaction and the electron band structure.

Both regular and resonance Raman spectroscopies present ideal characterization tools which are relatively simple and non-destructive, offer high resolution, give structural and electronic information, and are applicable at both laboratory and mass-production scales, which makes them highly suitable for the fundamental studies of materials.

## Objectives of the thesis

The main objective of this thesis is to provide detailed insights into the fundamental properties of kesterite materials, including pure quaternary CZTS and CZTSe compounds, and as well as their solid solutions, CZTSSe. The thesis is mainly focused on studying the structural and vibrational properties of kesterites principally using regular and resonant Raman spectroscopy techniques in correlation with other characterization methods. In view of this goal, some of the specific objectives of this thesis include:

- Complete analysis and identification of all active Raman modes for polycrystalline CZTS and CZTSe thin films and their solid solutions using multi-wavelength excitation Raman spectroscopy methods.
- Identification of the type of atoms involved within each vibrational mode.
- Investigation of the defect dynamics in kesterite materials, which includes development of methodologies for the experimental identification of different types of defects and exploration of their effect on the optoelectronic properties.
- Investigation of the phonon confinement effects in these materials and their effect on the Raman spectra. Development of methodologies for the assessment of crystal quality of kesterite samples.
- Application of Raman spectroscopy for the development of suitable methodologies for the anion compositional assessment of kesterites and sulfo-selenide secondary phases.
- Investigation of the role of the anion electronic states of kesterites and other types of sulfo-selenide materials in the resonant Raman scattering effects.

# Chapter 2

*Fundamental properties of kesterites:*

*Identification of vibrational modes*

The ground-state crystal structure of CZTS, CZTSe and CZTSSe materials is kesterite with space group $I\bar{4}$. The coordination environment of each metal and anion in the kesterite structure is close to tetrahedral, leading to a conventional unit cell which is analogous to a 1 × 1 × 2 supercell expansion of the zinc-blende structure. Each anion (S or Se) is surrounded by two Cu, one Zn, and one Sn atom (Figure 2.1), as required by local charge neutrality (or equivalently, the valence-octet rule).[11]

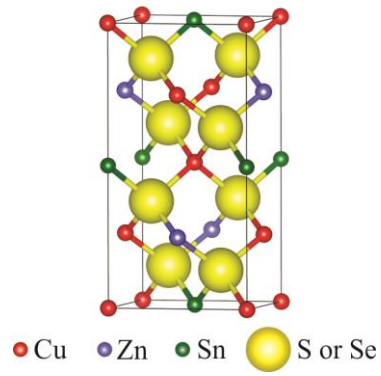


Figure 2.1 The kesterite structure

The highest performance devices based on kesterite absorbers are formed under non-stoichiometric compositions, which could promote disorder in the Cu and Zn occupancies.[12–14] To further complicate matters, a number of secondary binary and ternary phases can be formed by the same elements, which also adopt tetrahedral structures. Quantification of the degree of chemical disorder and disproportionation is difficult using standard laboratory X-ray diffraction, owing to the similar cross-sections of Cu and Zn, and the structural similarity of CZTS(Se) to its competing phases, e.g., ZnS(Se) and $Cu_2SnS(Se)_3$.[15] Raman spectroscopy, besides being a widely used tool for structural characterization, may also serve as a powerful technique for better characterization of the disorder effects and secondary phases in kesterites.[16–18] This is due to the fact that the frequency, shape, and spectral intensity of Raman modes are extremely sensitive to any structural changes of the material.

In order to achieve better device performance in solar cells based on CZTS, CZTSe and CZTSSe absorbers and to improve the application of Raman spectroscopy as a control method for assessment of crystalline quality and identification of secondary phases in these promising emerging semiconductors, it is necessary to obtain better knowledge of their vibrational properties.

Usually, experimental studies for determining the Raman peaks of kesterites are done with the use of green excitation (514.5 or 532.0 nm), which is standard in Raman spectroscopy. The main disadvantage of the standard excitation methods is the

observation of high number of Raman modes with relatively low intensity, which leads to difficulties in the determination of peak positions and phase identification. In contrast, resonance Raman methods allow measuring spectra, which are simpler in the sense that the number of observed independent modes is lower and at the same time, with several orders of magnitude higher intensity. This allows easier identification of the modes and facilitates their correlation with other properties, such as composition, impurities, defects, crystallinity, and electronic band structure.

Furthermore, identification of secondary phases in kesterite compounds in some cases cannot be done with the use of green excitation, but rather requires the use of different excitation wavelengths leading to near resonant excitation conditions for certain secondary phase compounds. For example, ultraviolet (UV) excitation (325 nm) allows very sensitive detection of ZnS which is the most expected secondary phase in Zn-rich and Cu-poor device grade CZTS layers, while blue excitation (457.8 nm) allows very easy identification of ZnSe in CZTSe layers.[19,21,22] Development of Raman scattering based procedures for detection of secondary phases in kesterites is of great interest, because of the high impact of these phases on the optoelectronic properties of the solar cells. While use of different excitation wavelengths allows identification of secondary phases, they can also induce changes in the intensities of the optical Raman modes of kesterites. For example, some Raman modes which could not be observed with standard excitation could appear with much higher intensity in the spectra measured under nonstandard excitations, and this might lead in some cases to misinterpretation with modes of secondary phases. Thus, it is important first to study the behavior of all Raman modes of kesterites in relation to different excitations, before applying this method for identification of secondary phases.

This chapter describes a complete analysis and identification of all active Raman modes for polycrystalline CZTS(Se) thin films and their solid solutions using multi-wavelength excitation Raman spectroscopy methods.

In general, IR and Raman spectroscopies probe only the modes at the Brillouin zone center (Γ point). In Mulliken notation, the irreducible representation of the optical Γ-point modes for kesterite is given as $\Gamma = 3A \oplus 6B \oplus 6E$. Here, the A and B modes are non-degenerate, while the E modes are doubly degenerate, resulting in the 21 optical modes expected for the eight-atom primitive cell (i.e., 3N-3). According to the selection rules for this crystal symmetry, all modes are Raman active, while only the B and E modes are IR active.

Based on the first principle simulations, normal displacements of each mode were calculated, resulting in the identification of which ions are involved within each vibration.[23] Normal displacements of the zone center modes are illustrated in Figure 2.2.

Based on this study, it was determined that the three A modes involve only anion vibrations, relative to fixed cations, whilst the B and E modes encompass both anion and cation vibrations. The B modes involve cation displacements along the *c* direction, while the E modes involve in-plane cation vibrations parallel to the *a* direction. From this it could be concluded that since A modes involve only anion vibrations, i.e. only negatively charged ions, thus they are labeled as non-polar modes (which is a reason why they are not IR active). On the other side B and E modes involve both cation and anion vibrations, labeling them as polar modes. B and E modes, due their polar character, will also experience TO/LO splitting. Additionally, greater resonant enhancement in the intensity of the polar Raman modes is expected when compared to the resonant enhancement of the intensity of non-polar Raman modes. This is due to the stronger Fröhlich electron-phonon interaction between the polar phonons and the electronic states.[10]

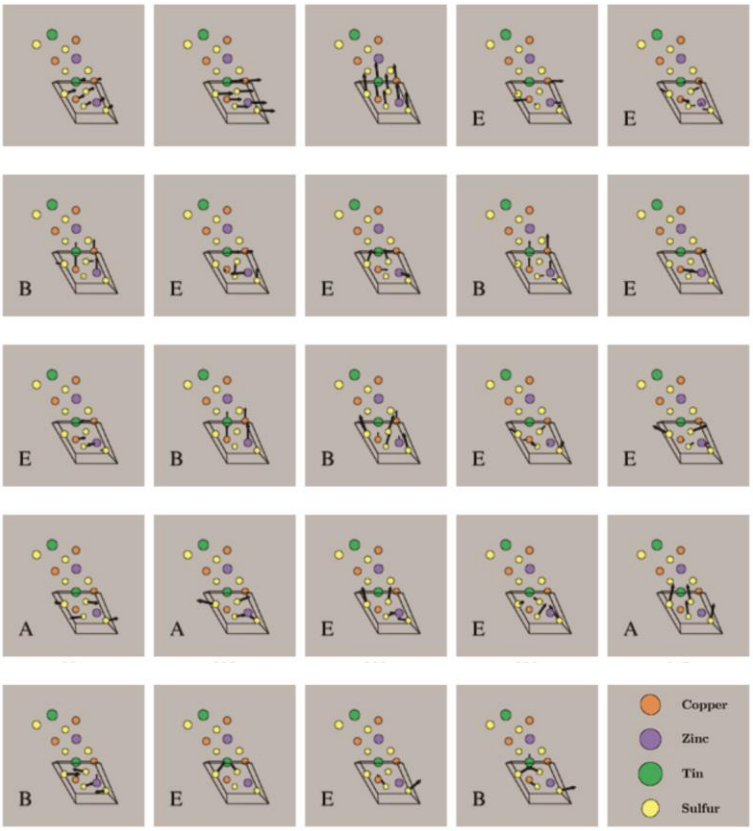


Figure 2.2 Normal displacements of the 24 Γ-point vibrational mode for the kesterite structure. The upper-case letter gives the irreducible representation (S4 point group). Note that the first three acoustic modes have zero frequency at the Γ-point. (Multimedia view) [URL: http://dx.doi.org/10.1063/1.4917044.1].

According to theoretical calculations for electronic band structure of kesterites done by Kumar and Persson the estimated energy, of the $\Gamma_1$ point (band gap energy) is 1.47 and 0.9 eV, while the energy of the $\Gamma_2$ point is around 3.50 and 3.0 eV, for CZTS and CZTSe, respectively.[24] Taking into the account the values of energies for $\Gamma_1$ and $\Gamma_2$ points, and comparing them with the available laser wavelengths, as illustratively shown on the electronic band structure diagram in Figure 2.3, it is expected that the resonant Raman conditions will be accomplished for the 830.0, 785.0, and 325.0 nm excitations in the case of CZTS. In contrast, the used excitation wavelengths are not considered as good conditions for resonance Raman scattering effects in case of CZTSe, except in the case of 830 nm excitation, where weak near resonance Raman effects are expected.

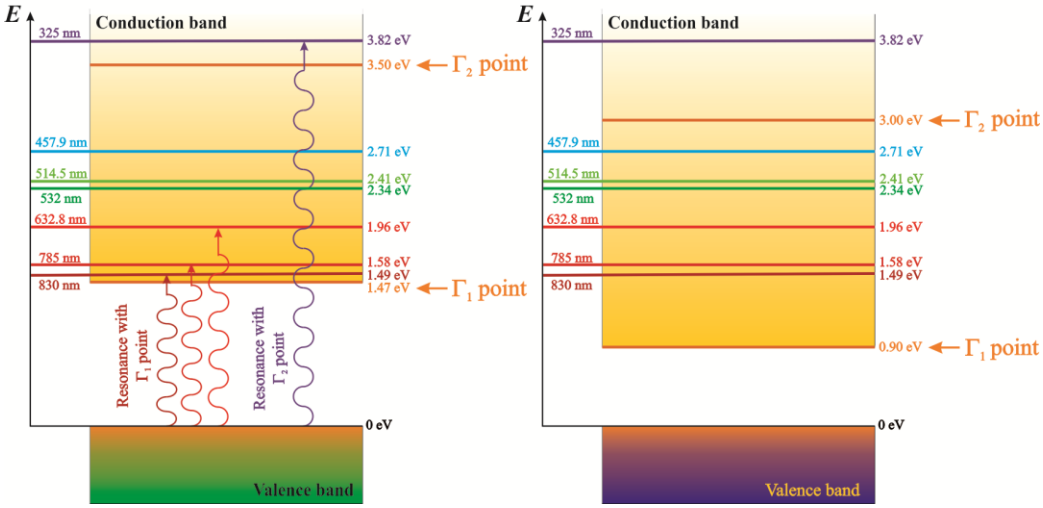


Figure 2.3 Schematic illustration of the electronic band structure in CZTS and CZTSe materials with special emphasis on the $\Gamma_1$ and $\Gamma_2$ points and different excitation wavelengths used in Raman spectroscopy.

Figure 2.4 presents the experimental Raman spectra of measured CZTS and CZTSe stoichiometric samples under different excitation wavelengths. Simultaneous fittings of spectra with Lorentzian curves have allowed identification of 18 and 17 peaks attributed to all optical modes which are expected according to the zone center phonon representation for CZTS and CZTSe, respectively. The symmetry assignment of Raman modes was done by comparing the experimentally obtained frequencies with the reported references as well as with polarization measurements done for these samples.[17]

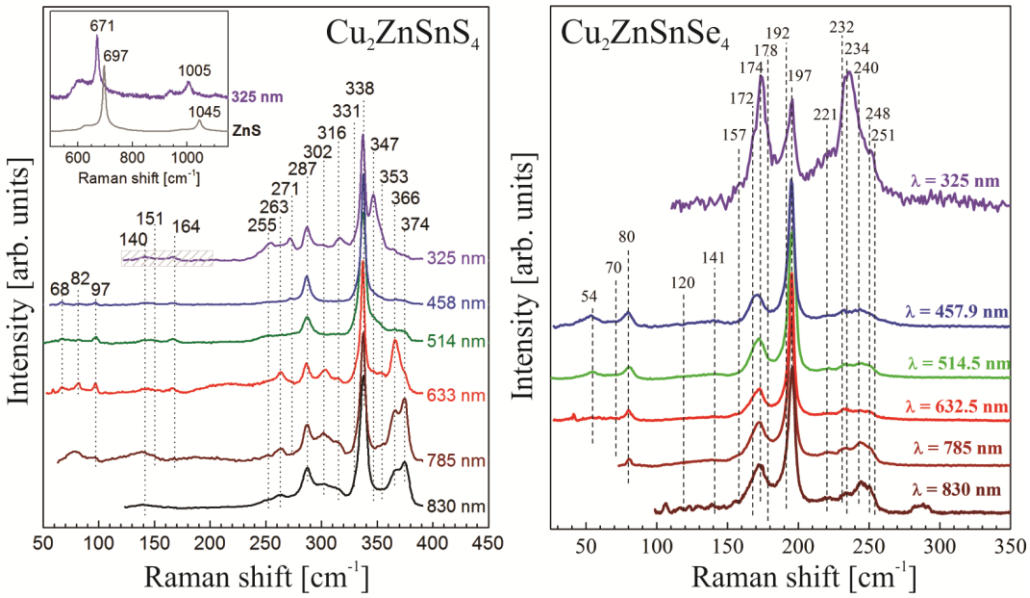


Figure 2.4 Raman spectra of stoichiometric polycrystalline CZTS and CZTSe thin film measured with different excitation wavelengths with indication of the characteristic peaks.

In contrast to CZTS and CZTSe, CZTSSe solid solutions have a more complex Raman behavior as seen in Figure 2.5 which presents Raman spectra of series of samples with different [S] / ([S] + [Se]) compositions measured with a 532 nm excitation wavelength. The Raman spectra of CZTSSe solid solutions are characterized by the presence of two dominant peaks in the high frequency region (280 – 400 $cm^{-1}$), and two dominant peaks in the low frequency region (170 – 205 $cm^{-1}$).[18,25] The peaks in the high frequency region are identified as CZTS-like peaks corresponding to A symmetry modes involving vibrations of only S ions, and the peaks in the lower frequency region are identified as CZTSe-like peaks corresponding to A symmetry modes involving vibrations of only Se ions. Furthermore, Raman spectra of solid solutions also show additional peaks in the intermediate frequency region (205 – 280 $cm^{-1}$). These peaks are attributed to vibrational modes which include vibrations from both S and Se atoms in the lattice, in contrast with CZTS-like or CZTSe-like peaks that involve vibrations of only one kind of anion. Detailed simultaneous fittings of the experimental spectra with Lorentzian curves and polarization measurements have allowed identification of 19 peaks with their symmetry assignments.[18] The positions of the peaks are in good accord with those calculated for these compounds from first principle simulations.[26]

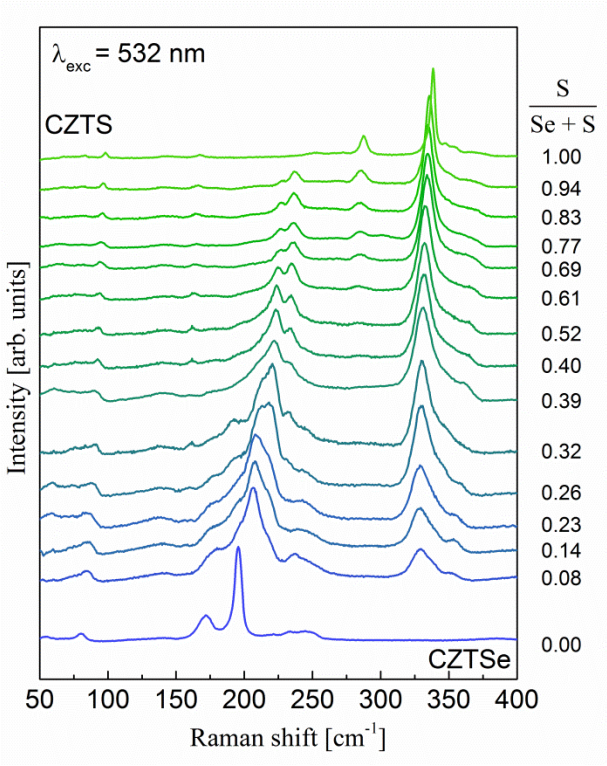


Figure 2.5 Raman spectra of polycrystalline CZTSSe solid solution thin films measured with a 532.0 nm excitation wavelength.

In conclusion, this chapter presents a summary of the vibrational properties of kesterite CZTS and CZTSe materials, as well as CZTSSe solid solutions based on simultaneous fittings of the Raman spectra measured with different excitation wavelengths and under different polarization configurations. This study has allowed identification of the positions and symmetry assignment of all Raman active vibrational modes expected in the case of this structure, resulting in the full vibrational characterization.

The chapter is concluded with two publications: "Multiwavelength excitation Raman scattering study of polycrystalline kesterite $Cu_2ZnSnS_4$ thin films" and "Multiwavelength excitation Raman scattering of $Cu_2ZnSn(S_xSe_{1-x})_4$ ($0 \leq x \leq 1$) polycrystalline thin films: Vibrational properties of sulfoselenide solid solutions" in which detailed information about the previously mentioned results are presented.

APPLIED PHYSICS LETTERS **104**, 021901 (2014)

# Multiwavelength excitation Raman scattering study of polycrystalline kesterite $Cu_2ZnSnS_4$ thin films

M. Dimitrievska,[1] A. Fairbrother,[1] X. Fontané,[1] T. Jawhari,[2] V. Izquierdo-Roca,[1,a)]
E. Saucedo,[1] and A. Pérez-Rodríguez[1,3]
[1]*Catalonia Institute for Energy Research (IREC), C. Jardins de les Dones de Negre 1, 08930 Sant Adrià del Besos, Barcelona, Spain*
[2]*Centres Científics i Technologies CCiTUB, Universitat de Barcelona, C. Lluis Sole i Sabarís 1, 08028 Barcelona, Spain*
[3]*IN2UB, Departament d'Electrònica, Universitat de Barcelona, C. Martí i Franquès 1, 08028 Barcelona, Spain*

(Received 8 October 2013; accepted 20 December 2013; published online 13 January 2014)

This work presents a complete analysis of all Raman active modes of $Cu_2ZnSnS_4$ measuring with six different excitation wavelengths from near infrared to ultraviolet. Simultaneous fitting of spectra allowed identification of 18 peaks from device grade layers with composition close to stoichiometry that are attributed to the 27 optical modes theoretically expected for this crystalline structure, including detection of 5 peaks not observed previously, but theoretically predicted. Resonance effects are assumed to explain the observed increase in intensity of weak modes for near infrared and ultraviolet excitations. These results are particularly relevant for experimental discrimination of Raman modes related to secondary phases. © *2014 AIP Publishing LLC*.
[http://dx.doi.org/10.1063/1.4861593]

Polycrystalline kesterite $Cu_2ZnSnS_4$ (CZTS) thin films have recently drawn much attention as being a promising candidate as an absorber layer in solar cell technologies,[1–3] and devices have already reached a conversion efficiency of 11.1% (Ref. 4) based on the related $Cu_2ZnSn(S,Se)_4$ compound. Optoelectronic properties of solar cells are strongly dependent on the structural properties, crystalline quality, and presence of secondary phases in the absorber layer.[5–8]

Raman spectroscopy is one of the most powerful tools for determining the crystalline structure and quality of semiconductor thin films, since the shape and position of Raman peaks are strongly influenced by the presence of defects in the material, either in the form of structural inhomogeneities or secondary phases.[9–12] In order to achieve better device performance in solar cells based on CZTS absorbers and to improve the usage of Raman spectroscopy as a control method for assessment of crystalline quality and identification of secondary phases in these promising emerging compound semiconductors, it is necessary to obtain better knowledge of their vibrational properties. Theoretical calculations on band structure, optical properties, and intrinsic defects have recently been reported.[13–16] First principle calculations done by Khare[17] and Gurel[18] have given theoretical predictions on the positions of all Raman active optical modes of the kesterite structure with the space group $I\bar{4}$ ($\Gamma = 3A \oplus 6B \oplus 6E$). The most detailed experimental study on this topic was done by Dumcencao,[19] where 14 of 27 Raman modes predicted for CZTS were identified. This included the first experimental report on the presence of a third A symmetry kesterite mode, which was deduced as a weak contribution from fitting of experimental spectra.

Usually, experimental studies for determining the Raman peaks of CZTS are done with the use of green excitation (514.5 or 532.0 nm), which is standard in Raman spectroscopy.[9,19,20] On the other hand, identification of secondary phases in CZTS in some cases cannot be done with the use of green excitation, but rather requires the use of different excitation wavelengths leading to near resonant excitation conditions for certain secondary phase compounds and they enable enhancement of their modes for more straightforward detection.[10] For example, ultraviolet (UV) excitation allows very sensitive detection of ZnS, which is the most expected secondary phase in Zn rich and Cu poor device grade CZTS layers.[21] Development of Raman scattering based procedures for detection of secondary phases in kesterite based compounds is of strong interest, because of the high impact of these phases on the optoelectronic properties of the solar cells. Detection of CZTS and secondary phases as ZnS by standard techniques such as x-ray diffraction is strongly compromised by the high level of overlapping of the main peaks in the diffractograms' characteristics for these phases.

While use of different excitation wavelengths allows identification of secondary phases, they can also induce changes in the intensities of the optical Raman modes of CZTS. For example, some Raman modes which could not be observed with standard excitation could appear with much higher intensity in the spectra measured under nonstandard excitations, and this might lead in some cases to misinterpretation with modes of secondary phases. Thus, it is important first to study the behavior of all Raman modes of CZTS in relation to different excitations, before applying this method for identification of secondary phases. First Raman spectra measured with different excitation wavelengths were reported in Ref. 12. Here, we perform a more detailed study of the whole spectral range where first order Raman CZTS modes are theoretically expected (from 50 $cm^{-1}$ up to

a)e-mail: vizquierdo@irec.cat. Tel.: + 34 933 562 615.

400 $cm^{-1}$), and we also extend the range of excitation wavelengths to the UV and near infrared (NIR) regions.

In this framework, this letter describes a complete analysis and identification of all active Raman modes for polycrystalline CZTS thin films using six different excitation wavelengths (325.0, 457.9, 514.5, 632.8, 785.0, and 830.0 nm). In principle, near resonance Raman effects are expected to be the main factors influencing changes in the Raman spectra of CZTS with the excitation wavelength. Tuning the incident laser to resonate with a strong electronic inter-band transition enables the enhancement of the Raman cross section, and vibrational modes associated with that particular transition exhibit an increase in intensity.[22]

According to theoretical calculations for electronic band structure of kesterites done by Kumar and Persson,[23] the estimated energy, for CZTS, of the $\Gamma_1$ point (band gap energy) is 1.47 eV, while the energy of the $\Gamma_2$ point is around 3.50 eV. Taking into account the values of energies for $\Gamma_1$ and $\Gamma_2$ points, the excitation wavelengths of 830.0, 785.0, and 325.0 nm, with corresponding energies of 1.49, 1.58, and 3.82 eV could be considered as good conditions for near resonance Raman scattering effects. In principle, increasing in intensity of the Raman modes because of near resonant excitation conditions is expected to take place especially for E and B symmetry modes, which are NIR active and have TO/LO splitting due to their polar character.[17,22] It is interesting to remark that these modes are only observed as very weak peaks in standard Raman scattering conditions, where the spectra are dominated by the two main A symmetry modes at 287 and 338 $cm^{-1}$, which are not NIR active.

For the present letter, CZTS thin films of photovoltaic grade with high crystalline quality were investigated. The samples were prepared by thermal treatment of metallic precursors made by DC-magnetron sputtering deposition onto soda-lime glass/Mo substrates. Prototype solar cell devices made with these films give promising efficiency values up to 5.5%. More details about precursor deposition, thermal processing, device fabrication, and characterization can be found elsewhere.[21] External quantum efficiency (EQE) measurements performed on these cells give a band gap estimation of 1.46 eV, close to the value calculated for the $\Gamma_1$ point energy. Compositional ratios of the as-annealed films were approximately $Cu/(Zn+Sn)=0.82$ and $Zn/Sn=1.24$. These non-stoichiometric composition conditions are typically required to achieve devices with reasonable efficiency.[8] These conditions inhibit formation of detrimental Cu-Sn-S ternary phases, although they might favour formation of the ZnS secondary phase. To remove this secondary phase from the surface of the films, a selective chemical etching for ZnS has been performed with a HCl solution.[24] After etching with this solution, the composition ratios change to values closer to a stoichiometric composition ($Cu/(Zn+Sn)=0.96$ and $Zn/Sn=1.09$). The spectra presented in this letter correspond to the as-etched sample. As previously reported,[21] Zn-excess remaining in the etched film tends to be mainly concentrated at the back contact region, and we can consider that the surface is free of ZnS. This is corroborated by Raman scattering measurements performed with UV excitation, as will be discussed later.

Raman scattering measurements were performed in back scattering configuration with a LabRam HR800-UV and T64000 Horiba-Jobin Yvon spectrometers. For the HR800-UV system, diode-pumped solid state lasers with wavelengths of 785.0 and 830.0 nm, and gas HeCd and HeNe lasers with wavelengths of 325.0 and 632.8 nm, respectively, were used for excitation. In this system, excitation and light collection were made through an Olympus metallographic microscope, with a laser spot size on the order of 1–2 $\mu$m (depending on the excitation wavelength). To avoid effects in the spectra related to potential microscopic inhomogeneities, the spot was rastered over an area of $30\times30\ \mu m^2$. Furthermore, the T64000 system works coupled with an ion-Ar+ laser, and measurements were made with 514.5 nm and 457.9 nm excitation lines, with a 100 $\mu$m spot size on the sample. In all cases, and to avoid the presence of thermal effects in the spectra, the power excitation density was around 50 $W/cm^2$. The first-order Raman spectrum of monocrystalline Si was measured as a reference before and after acquisition of each Raman spectrum, and the spectra were corrected with respect to the Si line at 520 $cm^{-1}$.

Figure 1 presents the experimental Raman spectra of measured CZTS sample under different excitation wavelengths. Simultaneous fittings of spectra with Lorentzian curves have allowed identification of 18 peaks attributed to the 27 optical modes, which are expected according to the zone center phonon representation. The position of each Raman peak, the excitation condition under which it is most intense, and symmetry assignment is presented in Table I.

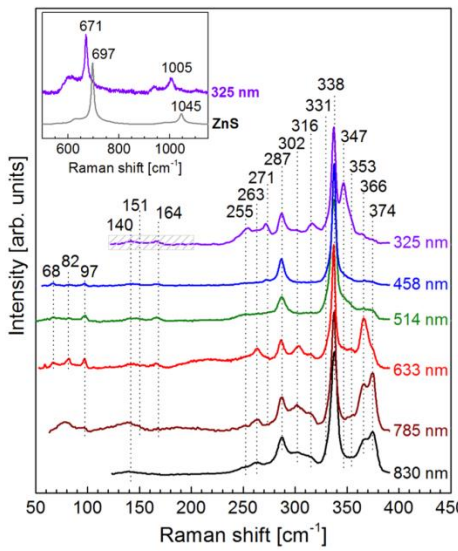


FIG. 1. Raman spectra of polycrystalline $Cu_2ZnSnS_4$ thin film measured with different excitation wavelengths with indication of the characteristic peaks. Dashed region presented in the spectrum measured with 325 nm wavelength corresponds to the region of strong attenuation originating from the Raman edge filter. Presence of Raman peaks in this region suggests strong enhancement of the modes expected in this spectral interval. Spectra are arbitrarily vertically shifted for more clarity. Inset shows the spectra measured in the 500–1150 $cm^{-1}$ region with 325 nm excitation wavelength from the $Cu_2ZnSnS_4$ thin film and a reference ZnS layer.

In addition, Table I also contains theoretical calculations[17,18] and previously reported experimental data.[9,19,20] The symmetry assignment of Raman modes was done by comparing the experimentally obtained frequencies with the reported references as well as with polarization measurements done for these samples. Inset in Figure 1 shows the Raman spectra measured with 325 nm excitation wavelength in the CZTS sample and in a reference ZnS sample, in the 500–1150 $cm^{-1}$ spectral range. The spectrum from the reference ZnS sample shows the peaks at 697 and 1045 $cm^{-1}$ corresponding to the second and third order peaks of the main ZnS Raman mode. Presence of these peaks is due to the existence of a quasi-resonant excitation of the main ZnS Raman mode at this excitation wavelength.[10] Absence of these peaks characteristic of the ZnS phase from the spectrum measured in the CZTS layer corroborates the absence in the surface region of this layer of a ZnS secondary phase. Additionally, the CZTS second (region between 550 and 750 $cm^{-1}$) and third (region between 900 and 1050 $cm^{-1}$) spectral regions are also observed in the spectrum, including the second and third order CZTS peaks at 670.9 and 1004.7 $cm^{-1}$, respectively.

Figure 2 shows a plot of the spectra measured with 325.0, 514.5 nm, 632.8, and 785.0 nm excitation wavelengths normalized to the intensity of the main peak at 337.5 $cm^{-1}$. Spectra measured with 325.0 nm are characterized by a strong increase in the relative intensity of the Raman peaks at 255.1, 271.1, 315.9, and 347.3 $cm^{-1}$ in relation to those from the spectra measured with standard 514.5 nm excitation. Similarly, relative intensity of peaks at 139.8, 150.7, 262.7, 366.6, and 374.4 $cm^{-1}$ increases for 785.0 nm excitation. These results agree with the expected enhancement in the intensity of CZTS polar vibrational modes taking into account the possible existence of a near resonant behavior. In addition, spectra measured with 632.8 nm also show an increase in the relative intensity of the peaks that are located at 81.5, 96.9, 262.7, and 366.6 $cm^{-1}$. This could be due to the existence also in this case of a near resonant excitation behavior, even if the energy is not so close to those of the $\Gamma_1$ and $\Gamma_2$ CZTS points.

TABLE I. Frequency (in $cm^{-1}$) of peaks from simultaneous fitting of Raman spectra measured with different excitation wavelengths, excitation condition under which the peak is best resolved, and proposed mode symmetry assignment. These are compared with theoretical predictions[17,18] and other reported experimental data.[9,19,20]

| This work | | Theoretical predictions | | | Experimental reported | | |
|---|---|---|---|---|---|---|---|
| $\lambda$[a] [nm] | RS[b] [$cm^{-1}$] | Sym[c] | RS[d] [$cm^{-1}$] | RS[e] [$cm^{-1}$] | RS[f] [$cm^{-1}$] | RS[g] [$cm^{-1}$] | IR[h] [$cm^{-1}$] |
| 633 | 67.8 | E | 79.2 E(TO/LO) | 82.2 E(TO/LO) | 66 | | 68 (IR) |
| 633 | 81.5 | B | 92.3 B(TO)/93.1 B(LO) | 87.8 B(TO)/88.2 B(LO) | 83 | | 86 (IR) |
| 633 | 96.9 | E/B | 101.4 E(TO/LO)/104.2 B (TO)/104.3 B(LO) | 99.3 B(TO/LO)/102.9 E(TO)/ 103.0 E(LO) | 97 | | |
| 785 | 139.8 | E | 166.1 E(TO) | 150.0 E(TO) | 143 | 143 E(TO) | 143 (IR) |
| 785 | 150.7 | E | 166.2 E(LO) | 150.5 E(LO) | | 145 E(LO) | |
| 325 | 164.1 | B | 179.6 B(TO)/179.9 B(LO) | 168.2 B(TO)/169.5 B(LO) | 166 | 160 B(TO) 162 B(LO) | 168 (IR) |
| 325 | 255.1 | B/E | 269.1 B(TO)/278.2 E(TO) | 237.9 B(TO)/247.8 E(TO) | 252 | 245 B(TO) 250 B(LO) 255 E(LO) | 255 (IR) |
| 633 | 262.7 | B | 285.1 B(LO) | 253.7 B(LO) | | | |
| 325 | 271.1 | E | 289.8 E(LO) | 254.8 E(LO) | 272 | | 293(IR) |
| 830 | 287.1 | A | 302.1 A | 281.7 A | 287 | 285 A | |
| 785 | 302.1 | A | 309.0 A | 270.0 A | | 306 A | |
| 325 | 315.9 | E | 309.7 E(TO)/ 314.1 E(LO) | 278.0 E(TO)/ 290.5 E(LO) | | | 316 (IR) |
| 325 | 331.9 | B | 332.7 B(TO)/ 336.1 B(LO) | 307.6 B(TO)/ 311.4 B(LO) | | | |
| 514 | 337.5 | A | 335.2 A | 338.5 A | 337 | 334 A | |
| 325 | 347.3 | E | 341.4 E(TO) | 351.1 E(TO) | 347 | 341 E(TO) 346 E(LO) | |
| 514 | 353.0 | B | 354.8 B(TO) | 357.0 B(TO) | 353 | 352 B(TO) 353 B(LO) | 351 (IR) |
| 633 | 366.6 | E | 353.3 E(LO) | 365.3 E(LO) | | | |
| 785 | 374.4 | B | 366.4 B(LO) | 373.6 B(LO) | | | |

[a] $\lambda$ is the excitation wavelength.
[b] RS is the Raman shift from this work.
[c] Sym is the symmetry proposed in this work.
[d] RS is the Raman shift reported in Ref. 17.
[e] RS is the Raman shift reported in Ref. 18.
[f] RS is the Raman shift reported in Ref. 9.
[g] RS is the Raman shift reported in Ref. 19.
[h] IR are the infrared absorption frequencies reported in Ref. 20.

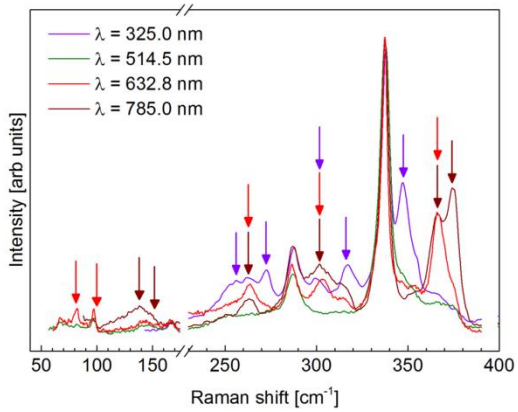


FIG. 2. Comparison between Raman spectra measured with standard green excitation (514.5 nm), and measurements made with 325.0, 632.8, and 785.0 nm excitation. The colored arrows indicate the excitation wavelength for which each particular band has the greatest increase in intensity.

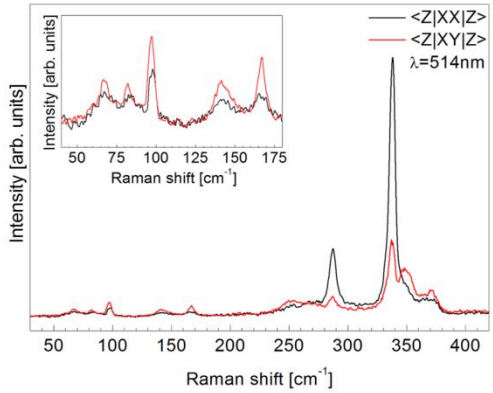


FIG. 3. Raman polarization measurements of $Cu_2ZnSnS_4$ done in parallel and perpendicular polarization configurations (excitation wavelength 514.5 nm).

In addition, these excitation conditions also allow observation of a well resolved peak at 302.1 $cm^{-1}$, that according to simulation data, has been identified as the third A symmetry mode from the CZTS kesterite phase.[19] Even though Dumcencao[19] already reported the existence of this mode, it is interesting to remark that in their work the presence of this mode was deduced from deconvolution of the experimental spectra, and the peak was not experimentally resolved in their spectra, as is done here.

In the case of the peak at 347.3 $cm^{-1}$ observed with UV excitation conditions, an increase in the intensity of a peak in this spectral region has previously been attributed to the presence of a ZnS secondary phase, because of the existence of a quasi-resonant excitation of ZnS in these measuring conditions.[10] However, experimentally, presence of this phase is also accompanied by the detection of the second order ZnS peak at 697 $cm^{-1}$ spectral region. Absence of this second order peak in the spectra from the samples analyzed in this work (as shown in the inset in Figure 1) supports its identification as a mode characteristic of the CZTS compound, unrelated to the presence of a ZnS secondary phase.

On the other hand, fitting of the spectra gives also a contribution at 331.9 $cm^{-1}$, which has been identified with a B symmetry mode, in agreement with the theoretical data. However, this is also close to a peak at 331 $cm^{-1}$, which has been related to the presence of local inhomogeneities with a high degree of disorder in the cation sublattice of CZTS, as reported by Fontané *et al.*[9] for bulk powder samples. More recent studies from single crystal bulk samples with different compositions[25] have identified this peak with the main $A_1$ symmetry mode from the disordered kesterite phase, which is characterized by a random distribution of Cu and Zn cations in the Cu-Zn planes. This leads to a change in the group symmetry to the stannite-like $I\bar{4}m2$. In contrast with the behavior shown in Figure 2, presence of this disordered kesterite phase in the bulk and single crystal samples reported in Refs. 9 and 25 is characterized by an intense and broad peak in this spectral region in the spectrum measured with 514.5 nm excitation. This suggests that conditions related to the growth of bulk samples, which typically involve higher temperature thermal treatments than those used for the synthesis of the device grade polycrystalline thin films, favor formation of this disordered phase when working under non-stoichiometric conditions.

Confirmation of proposed symmetry types could be done with comparison to polarized Raman spectra measurements for CZTS, as seen in Figure 3. According to Raman tensors for the space group $I\bar{4}$ (Ref. 17) and calculations of depolarization ratio for the polycrystalline films with random orientation, in the case of change in polarization conditions from parallel $\langle Z|XX|Z\rangle$ to perpendicular $\langle Z|XY|Z\rangle$ configurations, the intensity of all A modes would always decrease, while the intensity of all E modes would always increase. In case of B modes, their intensity could increase or decrease depending on their type. From the results shown in Figure 3, it can be seen that intensities of all peaks increase with the change in polarization, except for peaks in spectral region from 270 to 340 $cm^{-1}$, which decrease in intensity. This indicates that all A modes must be positioned in this region, which is in accord with the multiwavelength excitation results.

In conclusion, this work demonstrates the utility of multiwavelength excitation for the deeper vibrational characterization of device grade polycrystalline CZTS. In addition to allowing easier identification of 11 peaks previously observed with standard green excitation,[9,19,20] the analysis performed here also allows experimental observation and symmetry assignment of 5 Raman peaks characteristic for CZTS with positions at 262.7, 315.9, 331.9, 366.6, and 374.4 $cm^{-1}$, which were not previously experimentally reported, but are theoretically predicted. The symmetry assignment of these peaks is performed according to polarization measurements and the theoretical calculations done by Gurel *et al.*[17] and Khare *et al.*[18] This knowledge is especially relevant for the further development of multiwavelength Raman scattering based methodologies for detection of secondary phases, which is still required for further optimization of these technologies.

The research leading to these results has received funding from the People Program (Marie Curie Actions) of the European Union's Seventh Framework Program FP7/2007-2013/ under REA Grant Agreement No. 316488 (KESTCELLS), and from project KEST-PV (Ref. ENE2010-121541-C03-1) from the Spanish "Ministerio de Economia y Competitividad." Authors from IREC and IN$^2$UB belong to the M-2E (Electronic Materials for Energy) Consolidated Research Group and the XaRMAE Network of Excellence on Materials for Energy of the "Generalitat de Catalunya." E.S. thanks the Government of Spain for the "Ramon y Cajal" fellowship (RYC-2011-09212) and V.I. for the "Juan de la Cierva" fellowship (JCI-2011-10782) and A.F. thanks the Spanish Government for the FPU Fellowship (FPU12/05508).

[1]C. A. Wolden, J. Kurtin, J. B. Baxter, I. Repins, S. E. Shaheen, J. T. Torvik, A. A. Rockett, V. M. Fthenakis, and E. S. Aydil, J. Vac. Sci. Technol., A **29**, 030801 (2011).
[2]H. Katagiri, Thin Solid Films **480–481**, 426 (2005).
[3]T. Kato, H. Hiroi, N. Sakai, S. Muraoka, and H. Sugimoto, in *27th European PV Solar Energy Conference and Exhibition* (2013), p. 2236.
[4]T. Todorov, J. Tang, S. Bag, O. Gunawan, Y. Zhu, and D. Mitzi, Adv. Energy Mater. **3**, 34 (2013).
[5]S. Schorr, Sol. Energy Mater. Sol. Cells **95**, 1482–1488 (2011).
[6]A. Redinger, D. M. Berg, P. J. Dale, and S. Siebentritt, J. Am. Chem. Soc. **133**, 3320 (2011).
[7]S. Chen, X. G. Gong, A. Walsh, and S.-H. Wei, Appl. Phys. Lett. **96**, 021902 (2010).
[8]D. B. Mitzi, O. Gunawan, T. K. Todorov, K. Wang, and S. Guha, Sol. Energy Mater. Sol. Cells **95**, 1421 (2011).
[9]X. Fontane, V. Izquerdo-Roca, E. Saucedo, S. Schorr, V. O. Yukhymchuk, M. Ya. Valakh, A. Perez-Rodrigez, and J. R. Morante, J. Alloys Compd. **539**, 190 (2012).
[10]X. Fontané, L. Calvo-Barrio, V. Izquierdo-Roca, E. Saucedo, A. Pérez-Rodriguez, J. R. Morante, D. M. Berg, P. J. Dale, and S. Siebentritt, Appl. Phys. Lett. **98**, 181905 (2011).
[11]A.-J. Cheng, M. Manno, A. Khare, C. Leighton, S. A. Campbell, and E. S. Aydil, J. Vac. Sci. Technol., A **29**, 051203 (2011).
[12]P. A. Fernandes, P. M. P. Salome, and A. F. da Cunha, J. Alloys Compd. **509**, 7600–7606 (2011).
[13]S. Chen, X. G. Gong, A. Wals, and S. H. Wei, Phys. Rev. B **79**, 165211 (2009).
[14]C. Persson, J. Appl. Phys. **107**, 053710 (2010).
[15]A. Nagoya, R. Asahi, R. Wahl, and G. Kresse, Phys. Rev. B **81**, 113202 (2010).
[16]S. Chen, J. H. Yang, X. G. Gong, A. Walsh, and S. H. Wei, Phys. Rev. B **81**, 245204 (2010).
[17]T. Gurel, C. Sevik, and T. Cagin, Phys. Rev. B **84**, 205201 (2011).
[18]A. Khare, B. Himmetoglu, M. Cococcioni, and E. S. Aydil, J. Appl. Phys. **111**, 123704 (2012).
[19]D. Dumcenco and Y.-S. Huang, Opt. Mater. **35**, 419–425 (2013).
[20]M. Himmrich and H. Haeuseler, Spectrochim. Acta A **47**, 933 (1991).
[21]A. Fairbrother, X. Fontané, V. Izquierdo-Roca, M. Espíndola-Rodríguez, S. López, M. Placidi, L. Calvo-Barrio, A. Pérez-Rodríguez, and E. Saucedo, Sol. Energy Mater. Sol. Cells **112**, 97–105 (2013).
[22]P. Y. Yu and M. Cardona, *Fundamentals of Semiconductors*, 4th ed. (Springer, Berlin, 2010), p. 401.
[23]M. Kumar and C. Persson, Int. J. Theor. Appl. Sci. **5**(1), 1 (2013).
[24]A. Fairbrother, E. Gracia-Hemme, V. Izquierdo-Roca, X. Fontane, F. A. Pulgarin-Agudelo, O. Vigil-Gala, A. Perez-Rodrigez, and E. Saucedo, J. Am. Chem. Soc. **134**, 8018 (2012).
[25]M. Y. Valakh, O. F. Kolomys, S. S. Ponoaryov, V. O. Yukhymcuk, I. S. Babichuk, V. Izquierdo-Roca, E. Saucedo, A. Perez Rodrigez, J. R. Morante, S. Schorr, and I. V. Bodnar, Phys. Status Solidi (RRL) **7**, 258 (2013).

APPLIED PHYSICS LETTERS **105**, 031913 (2014)

# Multiwavelength excitation Raman scattering of $Cu_2ZnSn(S_xSe_{1-x})_4$ ($0 \le x \le 1$) polycrystalline thin films: Vibrational properties of sulfoselenide solid solutions

Mirjana Dimitrievska,[1] Haibing Xie,[1] Andrew Fairbrother,[1] Xavier Fontané,[1] Galina Gurieva,[2] Edgardo Saucedo,[1] Alejandro Pérez-Rodríguez,[1,3] Susan Schorr,[2,4] and Victor Izquierdo-Roca[1,a)]

[1]*Catalonia Institute for Energy Research (IREC), Jardins de les Dones de Negre 1 2pl., 08930 Sant Adrià del Besòs, Barcelona, Spain*

[2]*Helmholtz Centre Berlin for Materials and Energy, Department Crystallography, Hahn-Meitner-Platz 1, 14109 Berlin, Germany*

[3]*IN²UB, Departament d' Electrònica, Universitat de Barcelona, C. Martí i Franquès 1, 08028 Barcelona, Spain*

[4]*Institute of Geological Sciences, Freie Universität Berlin, Malteserstr. 74-100, 12249 Berlin, Germany*

(Received 10 June 2014; accepted 14 July 2014; published online 23 July 2014)

In this work, Raman spectroscopy and X-ray diffraction were applied together to evaluate the crystal structure and the phonon modes of photovoltaic grade $Cu_2ZnSn(S_xSe_{1-x})_4$ thin films, leading to a complete characterization of their structural and vibrational properties. Vibrational characterization has been based on Raman scattering measurements performed with different excitation wavelengths and polarization configurations. Analysis of the experimental spectra has permitted identification of 19 peaks, which positions are in good accord with theoretical predictions. Besides, the observation of $Cu_2ZnSnS_4$-like A symmetry peaks related to S vibrations and $Cu_2ZnSnSe_4$-like A symmetry peaks related to Se vibrations, additional Raman peaks, characteristic of the solid solution and previously not reported, are observed, and are attributed to vibrations involving both S and Se anions. © *2014 AIP Publishing LLC*. [http://dx.doi.org/10.1063/1.4891333]

Kesterite $Cu_2ZnSnS_4$ (CZTS) and $Cu_2ZnSnSe_4$ (CZTSe) compounds and their solid solutions $Cu_2ZnSn(S_xSe_{(1-x)})_4$ (CZTSSe) have attracted much attention due to their potential application in thin film solar cells as light absorber materials. In contrast with more mature thin film technologies based on $Cu(InGa)Se_2$ chalcopyrites, these compounds are only composed of earth abundant and non-toxic elements. So far the best devices are based on Se-rich CZTSSe absorbers, with the reported record efficiency of 12.6%.[1] Although devices based on CZTSSe solid solutions exhibit the highest solar cells efficiencies, their structural and vibrational properties have been studied considerably less than the ones corresponding to the quaternary CZTS and CZTSe counterparts.

To date the majority of studies reported on the CZTSSe compounds deal mainly with different synthesis processes and their influence on optoelectronic properties (solid state reaction,[2] co-evaporation,[3] sputtering deposition,[4] monograin molten-salt synthesis,[5] colloidal nanocrystal syntheses,[6] hydrazine,[1] and non-hydrazine based solution processing[7]). Several groups have also confirmed the ability to tune the bandgap of CZTSSe solid solutions by control of stoichiometry which allows for more versatile tuning of optical properties.[2–6] Systematic variation of the sulfur/selenium ratio allows the bandgap to be tuned from 1.4 to 0.9 eV, which greatly extends potential application of CZTSSe alloys in thin film photovoltaic devices, where a defined and controllable bandgap is required. Theoretical calculations, based on first principles simulations, of the band structure and optical properties of CZTSSe compounds have revealed that the mixed-anion alloys are highly miscible.[8] Furthermore, the composition dependence of structure and optical properties of CZTSSe powders has been experimentally investigated in Ref. 2, where a linear decrease of lattice parameters in accordance with Vegard's law was observed with the change in composition from S-rich to Se-rich samples. As for the vibrational properties, experimental determination of the main Raman scattering vibrational modes has been done in Refs. 2–6, where usually the two-mode behavior was attributed to the most intensive modes throughout the entire alloy concentration range. Additionally, weaker peaks were interpreted as secondary phases such as SnS, SnSe, ZnS, and ZnSe or Se.

In order to further develop CZTSSe thin film solar cells and achieve better device performance and higher efficiencies, a deeper knowledge on the fundamental and vibrational properties of these compounds and their impact on the optoelectronic parameters are required.

Herein Raman spectroscopy and X-ray diffraction (XRD) are applied together to perform a systematic study of the crystal structure and the phonon modes of the polycrystalline CZTSSe device grade layers (used for producing solar cells with up to 8.2% efficiency). This has allowed a detailed characterization of the structural and vibrational properties in the complete range of anion compositions of the solid solutions ($0 \le S/(S+Se) \le 1$). Furthermore, for better identification of Raman modes and their dependence on the anion composition Raman measurements with different excitation wavelengths from ultra-violet (UV) to near-infrared (NIR) regions are performed. NIR excitation conditions are used due to the expected increase in the intensity of the Raman modes because of near-resonant Raman effects. This is expected to take place, in

a)Email: vizquierdo@irec.cat

particular, for the polar modes of CZTS–like peaks, which are NIR active and are usually observed as very weak peaks in standard Raman scattering conditions.[9] The analysis of the experimentally obtained spectra has allowed observation of the existence of a more complex behavior than the two-mode behavior previously reported for these solid solutions.

CZTSSe device grade layers were synthesized on Mo coated soda-lime glass by annealing of Cu/Sn/Cu/Zn metallic multi-stacks, deposited by DC magnetron sputtering, under a S + Se + Sn atmosphere. Changing the mass of S and Se and the total pressure during the annealing, it was possible to tune the S-Se composition in the whole range, from pure CZTS to pure CZTSe.[4] The cationic ratios of Cu/(Sn + Zn) and Zn/Sn were kept constant between 0.75–0.80 and 1.16–1.22, respectively. As grown S-rich samples were submitted to an HCl etching[10] and Se-rich ones to a two stage $KMnO_4/H_2SO_4 + Na_2S$ (Ref. 11) etching with the aim to remove ZnS(Se) secondary phases potentially present at the surface of the absorbers. Raman scattering measurements performed with excitation conditions corresponding to resonant excitation of ZnS and ZnSe phases confirms the absence of these phases on the surface of the etched samples.[11,12]

Solar cells were fabricated with these layers as described in Ref. 4. Optoelectronic properties from the devices synthesized in this way gave efficiencies up to 8.2%. External quantum efficiency (EQE) curves were obtained using a PV300 Photovoltaic characterization system (Bentham Instruments).

Raman scattering measurements were performed in back scattering configuration with a LabRam HR800-UV and T64000 Horiba-Jobin Yvon spectrometers. For the HR800-UV system, diode-pumped solid state lasers with wavelengths of 785.0 and 532.0 nm and gas HeCd laser with wavelength of 325.0 nm were used for excitation. In this system, excitation and light collection were made through an Olympus metallographic microscope with a laser spot diameter of the order of 1–2 $\mu$m, depending on the excitation wavelength. To avoid effects in the spectra related to potential microscopic inhomogeneities, the spot was rastered over an area of $30 \times 30\ \mu m^2$. Furthermore, the T64000 system works coupled with an ion-Ar + laser, and measurements were made with 514.5 nm and 457.9 nm excitation lines, with a 100 $\mu$m spot size on the sample. In all cases, and to avoid the presence of thermal effects in the spectra, the power excitation density on the surface of the samples was around 50 W/cm$^2$. Under these experimental measurement conditions no thermal effects are observed in the spectra. This has been corroborated by the analysis of spectra measured with different excitation powers. The first-order Raman spectrum of monocrystalline Si was measured as a reference before and after acquisition of each Raman spectrum, and the spectra were corrected with respect to the Si line at 520 cm$^{-1}$.

XRD diffraction patterns were measured on PANalytical X'pert Pro MPD diffractometer with Cu−K$\alpha$-radiation ($\lambda = 1.54056$ Å) and a secondary graphite monochromator. Structural characterization of the thin films was carried out by grazing incidence XRD (GIXRD) with angles of 0.5°, 1°, 2°, and 5°. Refinements of the lattice constant values were carried out by Le Bail analysis using the FullProf[13] program with Thompson-Cox-Hastings pseudo-Voigt convoluted with axial divergence asymmetry profile function.[14]

The crystal structure of CZTSSe solid solutions was characterized by XRD measurements from which representative patterns of the 112 reflection are presented in Figure 1(a). The anion compositions of the samples were obtained based on the position of the 112 diffraction peak in comparison with the positions of this peak for the pure CZTS and CZTSe compounds. The systematic shift in peak position towards higher angles as the S/(S + Se) ratio increases correlates with the replacement of smaller S atoms with larger Se atoms. Furthermore, presence of a single and symmetric 112 diffraction peak in all measured diffractograms indicates that all samples are homogeneously alloyed rather than a mixture of CZTS and CZTSe phases.[15] The kesterite structure (space group $I\bar{4}$) was used as starting model for the refinement procedure, since it has been shown that both CZTS and CZTSe adopt a kesterite structure.[16] Additionally, lattice parameters $a$ and $c$ of the thin films were obtained as result of the Le Bail analysis. The dependence of lattice parameters on S/(S + Se) ratio is presented in the inset in Figure 1 and it is in good accordance with the Vergard's law.

In order to examine the compositional uniformity through the thickness of CZTSSe thin films, GIXRD measurements with 0.5°, 1°, 2°, and 5° angles were performed. Inset in Figure 1(b) presents diffractograms measured from S-rich and Se-rich samples. No significant shift in peak positions of the 112 reflection with the change in grazing incidence angles was observed. Additionally lattice parameters obtained from Le Bail analysis and presented in Figure 1(b), have proven to be constant for all grazing incidence angles. Furthermore, Raman measurements preformed on the front and back surface of the layers do not show changes in the

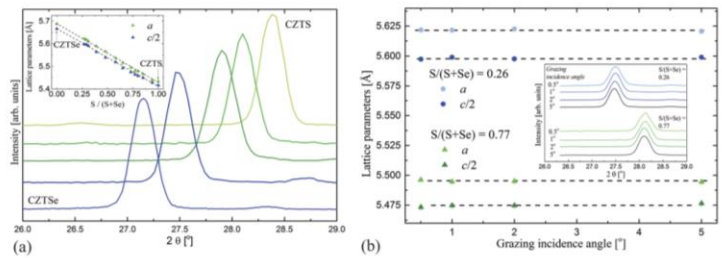


FIG. 1. (a) Representative XRD diffractograms centered at the 112 reflection kesterite peak measured for CZTSSe solid solutions. Inset: Lattice parameters on dependence of the anion S/(S + Se) composition ratio. (b) Lattice parameters in dependence of grazing incidence angles for two representative samples with 0.26 and 0.77 S/(S + Se) composition. Inset: Representative GIXRD diffractograms centered at the 112 reflection kesterite peak measured with 0.5°, 1°, 2°, and 5° angles for CZTSSe samples with 0.26 and 0.77 S/(S + Se) compositions.

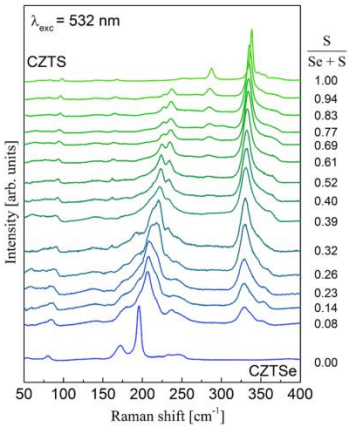


FIG. 2. Raman spectra of polycrystalline CZTSSe solid solution thin films measured with a 532.0 nm excitation wavelength.

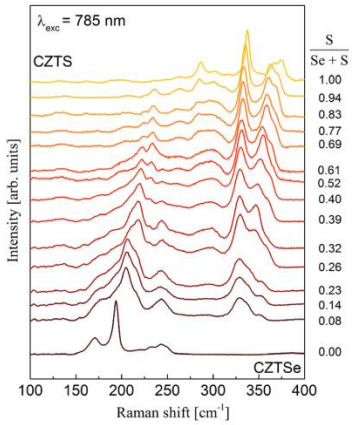


FIG. 4. Raman spectra of polycrystalline CZTSSe solid solution thin films measured with a 785.0 nm excitation wavelength.

shape and positions of Raman peaks. Raman measurements from the back region were made with the laser spot directly focused on the back surface of the layer from layers that were previously mechanically removed from the substrate.[17] This behavior strongly supports the absence of the significant changes in the S/(S + Se) composition through the thickness of the layers, thus the CZTSSe thin films used in this study could be considered uniform.

Irreducible representation of the kesterite structure with the space group $I\bar{4}$ ($\Gamma = 3A \oplus 6B \oplus 6E$) leads to the theoretical prediction of 27 active Raman modes, from which most have been experimentally detected for the CZTS and CZTSe compounds.[9,18] Usually, two dominant Raman peaks have been observed in this system and assigned to A symmetry modes. On the other hand, the CZTSSe compounds have a more complex behavior as seen in Figure 2, which presents Raman spectra of series of samples with different S/(S + Se) compositions measured with a 532 nm excitation wavelength.

Figure 3(a) presents the frequencies of the most intense Raman peaks of CZTSSe solid solutions plotted against composition. Note that Raman scattering is a surface sensitive technique (penetration depth of approximately ~100 nm in CZTSSe), which is why the surface anion compositions of the samples used for Raman characterization are calculated based on the Vergard's law applied on the bandgap energies which were determined from EQE measurements of solar cell devices based on these films. This is because the penetration depth of scattered light is similar to the expected width of the space charge region in the devices. Anion compositions obtained from the EQE measurements are in good agreement with the compositions obtained from the XRD measurements.

The Raman spectra of CZTSSe solid solutions are characterized by the presence of two dominant peaks in the higher frequency region (280–400 $cm^{-1}$) and two dominant peaks in the lower frequency region (170–205 $cm^{-1}$). The peaks in the higher frequency region are identified with CZTS-like peaks corresponding to A symmetry modes involving pure S vibrations,[9] and the peaks in the lower frequency region are identified with CZTSe-like peaks corresponding to A symmetry modes involving pure Se vibrations.[18,19] This apparently agrees with the existence of a two-mode behavior for these peaks, as previously reported in Refs. 2–6.

In addition, the Raman spectra from the solid solutions also show additional peaks in the intermediate frequency region (205–280 $cm^{-1}$). The observed additional peaks could not be attributed to secondary phases, because measurements with the 325.0 and 457.9 nm excitation wavelengths have demonstrated the absence of ZnS and ZnSe secondary phases or their alloys, which are resonant under these conditions.[11,12] Furthermore, the spectral contributions of Sn-(S,Se) phases are expected in the 50–220 $cm^{-1}$ interval,[20,21] which is not completely overlapping with the frequency interval of the observed additional peaks. Finally, the experimental conditions under which the samples were prepared, constituted of Zn-rich and

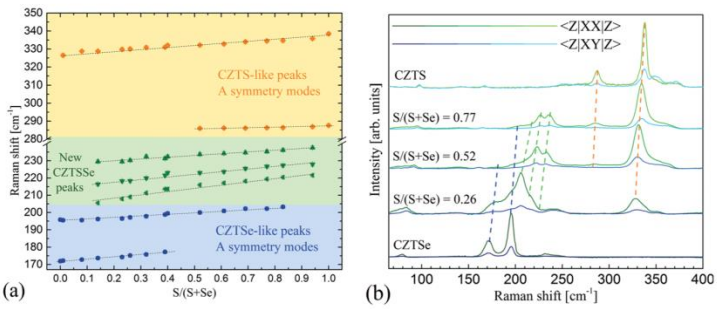


FIG. 3. (a) Variations of the frequencies of the most intense Raman peaks of CZTSSe solid solutions on dependence of S/(S + Se) anion composition ratio. (b) Raman polarization measurements of CZTSSe solid solutions done in parallel and perpendicular polarization configurations (excitation wavelength of 514.5 nm). Dashed lines are visual guide for the most intense Raman peaks positions presented in Figure 3(a).

Cu-poor conditions, are expected to inhibit formation of detrimental Cu-Sn-(S,Se) ternary phases and Cu-(S,Se) binary phases.[22] The absence of these phases is also confirmed by the XRD measurements. All this leads to the conclusion that the additional peaks are due to vibrational modes involving vibrations of both S and Se anions in the lattice. Accordingly, the vibrational spectrum from the solid solution is more complex than the previously reported two-mode behaviour. Similar behaviour in the Raman modes of alloys with the appearance of additional peaks was also observed in Cu-(S,Se) system.[23]

From Figure 3(a), all observed Raman modes shift monotonously with the variation of the composition and no splitting of peaks are detected. These results suggest that the observed Raman spectra of CZTSSe compounds of the intermediate compositions are able to be interpreted based on the kesterite type structure, which is in accordance with XRD results. As the cationic ratios were kept constant for all samples, it is expected that changes in the peak positions are caused mainly by the change in anion composition. Additional CZTSSe peaks in the interval of 205–280 $cm^{-1}$ show a higher dependency of frequency from the anion composition ratio than the CZTS-like and CZTSe-like ones, which indicates that they are attributable to vibrational modes which include vibrations from both S and Se atoms in the lattice, in contrast with CZTS-like or CZTSe-like peaks that involve vibrations of only one kind of anion. Furthermore, full-width-at-half-maximum (FWHM) of peaks from the solid solution are similar to those observed in the pure compounds, which indicates the absence of significant chemical disorder effects.[24] These results suggest the possible existence of fine ordering of anions in the structure, instead of the expected random distribution.

TABLE I. Frequency (in $cm^{-1}$) of peaks from simultaneous fitting of Raman spectra of CZTSSe solid solutions for different S/(S + Se) anion compositions measured with 532.0 and 785.0 nm excitation wavelengths. The proposed symmetries of the modes are determined based on polarization measurements, resonant Raman measurements, and comparison with the modes of the pure S and Se kieserite compounds reported in Refs. 9 and 18 (/ is assignment of the overlapped modes).

| Experimentally reported in Ref. 18 | | This work | | | | | | Experimentally reported in Ref. 9 | |
|---|---|---|---|---|---|---|---|---|---|
| S/(S + Se) = 0 | | S/(S + Se) = 0.26 | | S/(S + Se) = 0.52 | | S/(S + Se) = 0.77 | | S/(S + Se) = 1 | |
| RS[a] ($cm^{-1}$) | Sym[b] | RS[c] ($cm^{-1}$) | Sym[d] | RS[c] ($cm^{-1}$) | Sym[d] | RS[c] ($cm^{-1}$) | Sym[d] | RS[e] ($cm^{-1}$) | Sym[f] |
| | | 58.9 | E | 60.8 | E | 62.7 | E | 67.8 | E |
| | | 69.9 | B | 75.7 | B | 75.8 | B | 81.5 | B |
| 77 | B | 76.4 | B | 85.4 | B | 85.8 | B | | |
| 82 | E | 83.8 | E | 92.6 | E | 92.9 | E | 96.9 | E/B |
| 138 | E | 131.1 | E | 139.4 | E | 139.3 | E | 139.8 | E |
| | | 140.4 | | 146.3 | | 145.3 | | | |
| 157 | B | 153.7 | B | 163.0 | B | 162.9 | B | 164.1 | B |
| 170 | A | | | | | | | | |
| 174 | A | 175.0 | A | | | | | | |
| | | | | 176.0 | | 174.5 | | | |
| 178 | B | 180.8 | | | | | | | |
| 196 | A | 196.6 | A | 200.7 | A | 202.9 | A | | |
| | | 208.2 | A or B | 214.8 | A or B | 219.4 | A or B | | |
| | | 217.0 | A or B | 223.3 | A or B | 226.7 | A or B | | |
| 224 | E | | | | | | | | |
| 231 | E | | | | | | | | |
| | | 230.5 | A or B | 234.4 | A or B | 235.1 | A or B | | |
| 235 | B | 237.2 | B/E | 246.3 | B/E | 254.2 | B/E | 255.1 | B/E |
| 239 | B | 245.2 | B | 262.6 | B | 265.1 | B | 262.7 | B |
| 245 | B | | | | | | | | |
| 250 | B | | | | | | | | |
| | | | | | | | | 271.1 | E |
| | | | | 286.0 | A | 286.4 | A | 287.1 | A |
| | | 290.3 | A | 300.5 | A | 301.0 | A | 302.1 | A |
| | | | | | | | | 315.9 | E |
| | | | | | | | | 331.9 | B |
| | | 329.8 | A | 331.5 | A | 332.1 | A | 337.5 | A |
| | | 334.0 | B/E | 345.0 | B/E | 346.8 | B/E | 347.3 | E |
| | | | | | | | | 353.0 | B |
| | | 352.4 | B/E | 357.9 | B/E | 358.3 | B/E | 366.6 | E |
| | | | | | | | | 374.4 | B |

[a]RS is the Raman shift reported in Ref. 18.
[b]Sym is the symmetry reported in Ref. 18.
[c]RS is the Raman shift from this work.
[d]Sym is symmetry proposed in this work.
[e]RS is the Raman shift reported in Ref. 9.
[f]Sym is the symmetry reported in Ref. 9.

Raman polarization measurements performed on these layers (Figure 3(b)) show the same behavior for the additional peaks observed in the 205–280 $cm^{-1}$ region as that of CZTS-like and CZTSe-like A symmetry peaks. According to Raman tensors for the space group $I\bar{4}$ and calculations of depolarization ratio for the polycrystalline films with random orientation, with changes in polarization conditions from parallel $\langle Z|XX|Z\rangle$ to perpendicular $\langle Z|XY|Z\rangle$ configurations the intensity of all A modes would always decrease, while the intensity of all E modes would always increase. In case of B modes, their intensity could increase or decrease depending on their type. Assuming the existence of a kesterite crystalline structure for the alloys (in agreement with the XRD data) and the expected behavior of the modes with the change in polarization conditions, this indicates that these peaks are related to either A or B symmetry modes.[9]

In order to deepen understanding of the CZTSSe vibrational modes and to more clearly observe and resolve the peaks, Raman measurements with a 785 nm excitation wavelength were performed on the same set of samples. The Raman spectra measured on the films with different compositions are plotted in Figure 4. The intensity of the Raman peaks located at highest frequencies from the spectra of S-rich CZTSSe samples are enhanced in the case of 785 nm excitation due to the resonance Raman effects. This kind of behavior is attributed to the coupling of the excitation energy with the electronic energy bands at Γ point.[9] The selective enhancement of these peaks suggests that they can be attributed to polar modes, since this kind of behavior is expected only for those type of modes,[9] which again, assuming the kesterite structure, indicates that these peaks are related to B or E symmetry modes.

The detailed simultaneous fittings of the experimental spectra with Lorentzian curves and polarization measurements have allowed identification of 19 peaks. The positions of the peaks are in good accordance with those calculated for these compounds from first principle simulations.[8] The position of each Raman peak for the three representative samples with S/(S + Se) anion compositions of 0.26, 0.52, and 0.77 are presented in Table I. In this Table, the symmetry of the modes related to the different peaks is proposed based on the polarization and Raman scattering resonant measurements, and from the comparison with the previously reported experimental Raman modes from the CZTS[9] and CZTSe compounds.[18]

In conclusion, this work presents a complete vibrational characterization based on simultaneous fittings of the Raman spectra measured with different excitation wavelengths and under different polarization configurations, which allowed identification of 19 peaks. In contrast with previous reports on the existence of a two-mode behavior, a more complex behavior of the most intense peaks with the change in anion composition has been observed. The Raman spectra from the solid solution show dominant CZTS-like peaks in the higher frequency region (280–400 $cm^{-1}$), dominant CZTSe-like peaks in the lower frequency region (170–205 $cm^{-1}$), and additional peaks related to vibrations of both S and Se anions in the intermediate frequency region (205–280 $cm^{-1}$). These results provide a better insight in the fundamental properties of CZTSSe solar cells, and lead to an improved knowledge on their vibrational properties.

The research leading to these results has received funding from the People Program (Marie Curie Actions) of the European Union's Seventh Framework Program FP7/2007-2013/ under REA Grant Agreement No. 316488 (KESTCELLS). Authors from IREC and University of Barcelona belong to the M-2E (Electronic Materials for Energy) Consolidated Research Group and the XaRMAE Network of Excellence on Materials for Energy of the "Generalitat de Catalunya." A.F. thanks the Spanish Ministry of Economy and Competitiveness (MINECO) for the FPU Fellowship (FPU12/05508), V.I. for the "Juan de la Cierva" Fellowship (JCI-2011-10782), E.S. for the "Ramon y Cajal" Fellowship (RYC-2011-09212), and H.X. thanks support from the "China Scholarship Council" fellowship (CSC No. 201206340113).

[1]W. Wang, M. T. Winkler, O. Gunawan, T. Gokmen, T. K. Todorov, Y. Zhu, and D. B. Mitzi, Adv. Energy Mater. **4**, 1301465 (2014).
[2]J. He, L. Sun, S. Chen, Y. Chen, P. Yang, and J. Chu, J. Alloys Compd. **511**, 129 (2012).
[3]L. Grenet, S. Bernardi, D. Kohen, C. Lepoittevin, S. Noël, N. Karst, A. Brioude, S. Perraud, and H. Mariette, Sol. Energy Mater. Sol. Cells **101**, 11 (2012).
[4]A. Fairbrother, X. Fontané, V. Izquierdo-Roca, M. Espindola-Rodriguez, S. López-Marino, M. Placidi, J. López-García, A. Pérez-Rodríguez, and E. Saucedo, ChemPhysChem **14**, 1836 (2013).
[5]M. Grossberg, J. Krustok, J. Raudoja, K. Timmo, M. Altosaar, and T. Raadik, Thin Solid Films **519**, 7403 (2011).
[6]A. Singh, S. Singh, S. Levcenko, T. Unold, F. Laffir, and K. M. Ryan, Angew. Chem., Int. Ed. **52**, 9120 (2013).
[7]Y. Sun, Y. Zhang, H. Wang, M. Xie, K. Zong, H. Zheng, Y. Shu, J. Liu, H. Yan, M. Zhu, and W. Lau, J. Mater. Chem. A **1**, 6880 (2013).
[8]A. Khare, B. Himmetoglu, M. Cococcioni, and E. S. Aydil, J. Appl. Phys. **111**, 123704 (2012).
[9]M. Dimitrievska, A. Fairbrother, X. Fontané, T. Jawhari, V. Izquierdo-Roca, E. Saucedo, and A. Pérez-Rodríguez, Appl. Phys. Lett. **104**, 021901 (2014).
[10]A. Fairbrother, E. García-Hemme, V. Izquierdo-Roca, X. Fontané, F. A. Pulgarín-Agudelo, O. Vigil-Galán, A. Pérez-Rodríguez, and E. Saucedo, J. Am. Chem. Soc. **134**, 8018 (2012).
[11]S. López-Marino, Y. Sánchez, M. Placidi, A. Fairbrother, M. Espindola-Rodríguez, X. Fontané, V. Izquierdo-Roca, J. López-García, L. Calvo-Barrio, A. Pérez-Rodríguez, and E. Saucedo, Chem. - Eur. J. **19**, 14814 (2013).
[12]A. Fairbrother, X. Fontané, V. Izquierdo-Roca, M. Espíndola-Rodríguez, S. López-Marino, M. Placidi, L. Calvo-Barrio, A. Pérez-Rodríguez, and E. Saucedo, Sol. Energy Mater. Sol. Cells **112**, 97 (2013).
[13]J. Rodriguez-Carvajal and T. Roisnel, Physica B **192**, 55 (1993).
[14]L. W. Finger, D. E. Cox, and A. P. Jephcoat, J. Appl. Crystallogr. **27**, 892 (1994).
[15]P. M. P. Salomé, J. Malaquias, P. A. Fernandes, M. S. Ferreira, A. F. da Cunha, J. P. Leitão, J. C. González, and F. M. Matinaga, Sol. Energy Mater. Sol. Cells **101**, 147 (2012).
[16]S. Siebentritt and S. Schorr, Prog. Photovoltaics: Res. Appl. **20**, 512 (2012).
[17]S. Lopez-Marino, M. Placidi, A. Perez-Tomas, J. Llobet, V. Izquierdo-Roca, X. Fontane, A. Fairbrother, M. Espindola-Rodriguez, D. Sylla, A. Perez-Rodriguez, and E. Saucedo, J. Mater. Chem. A **1**, 8338 (2013).
[18]M. Guc, S. Levcenko, V. Izquierdo-Roca, X. Fontané, E. Arushanov, and A. Pérez-Rodríguez, J. Appl. Phys. **114**, 193514 (2013).
[19]N. B. M. Amiri and A. Postnikov, Phys. Rev. B **82**, 205204 (2010).
[20]L. S. Price, I. P. Parkin, A. M. E. Hardy, R. J. H. Clark, T. G. Hibbert, and K. C. Molloy, Chem. Mater. **11**, 1792 (1999).
[21]T. Fukunaga, S. Sugai, T. Kinosada, and K. Murase, Solid State Commun. **38**, 1049 (1981).
[22]A. Nagoya, R. Asahi, R. Wahl, and G. Kresse, Phys. Rev. B **81**, 113202 (2010).
[23]M. Ishii, K. Shibata, and H. Nozaki, J. Solid State Chem. **105**, 504 (1993).
[24]M. Dimitrievska, A. Fairbrother, A. Pérez-Rodríguez, E. Saucedo, and V. Izquierdo-Roca, Acta Mater. **70**, 272 (2014).

# Chapter 3

## *Defect dynamics in kesterites: Classification, detection and effect on optoelectronic properties*

The presence of defects in semiconductor materials plays a significant, even dominant role in determining their electronic and optical properties, and as such, identifying and understanding their influence on material properties is of critical importance. Kesterites, as quaternary compounds, have an additional number of elements relative to binary and ternary compounds, thus providing ample opportunities for material design. However, this also results in a higher probability for formation of defects, either in intrinsic form, such as point defects like anti-sites and vacancies, or in the form of secondary phases.

In the case of kesterites, the highest performing devices are made in conditions corresponding to Cu-poor (Cu/(Zn+Sn) < 1) and Zn-rich (Zn/Sn > 1) compositions. Such conditions have been shown both theoretically and experimentally to enhance the formation of Zn(S,Se), while suppressing formation of Cu-(S,Se) and Cu-Sn-(S,Se) secondary phases.[27,28] Regarding defect formation, the more energetically favorable defect clusters have been calculated to be [$Cu_{Zn}$ + $Zn_{Cu}$], [$V_{Cu}$ + $Zn_{Cu}$], [$2Zn_{Cu}$ + $Zn_{Sn}$], and [$2Cu_{Zn}$ + $Sn_{Zn}$].[29] Aside from their formation, the impact of secondary phases and especially of defects on optoelectronic properties of solar cells is not fully understood. Secondary phases such as binary and ternary Cu-, Zn-, and Sn- sulfides and selenides in the absorbers can reduce the carrier transport and lead to an increased recombination, which in general have detrimental effects on the optoelectronic properties.[30] The influence of point defects is thus far estimated by theoretical studies to affect charge transport properties and modify the band alignment with the n-type buffer layer, which is an important factor in determining the current and voltage which can be extracted from a device. Studying the effect of defects on the optoelectronic properties is of uppermost importance for the optimization of the production process in order to obtain high efficiency working devices.[28,29]

Raman spectroscopy has proven to be an effective technique for detecting and identifying different types of defects in various materials.[31,32] This is due to the Raman spectra being extremely sensitive to structural disorder, which is defined as any kind of modification of the crystalline structure of the material. This includes point defects, such as vacancies, interstitials and anti-sites, and also other crystalline defects, like dislocations or grain interfaces. Presence of defects in the material can lead to several kinds of changes in the Raman spectra, depending on their type and concentration. The main effects are expected to be observed in the changes of frequency, half-with and intensity of the modes.

The main objective of this chapter is to present Raman spectroscopy as a potential experimental method for detection of defects in kesterites. Additionally,

influence of deferent defects types on the optoelectronic properties of kesterite based solar cells will be described and explained.

The effects of defects on the Raman spectra could be divided in two groups. In the first group, the general effect of defects, regardless of their type, on the Raman features will be considered. This is explained by taking into account phonon confinement effects. In contrast, in the second group, the influence of specific types of defect clusters on the Raman spectra will be evaluated, leading to a methodology for the identification of certain types of defects using Raman spectroscopy.

Phonon confinement effects are arising as a consequence of the loss of translational symmetry in the crystal caused by high density of defects.[33] An illustrative explanation of the phonon confinement and its effect on the Raman peaks is presented in Figure 3.1. In the case of an ideal crystal, the wave function of the phonon is delocalized in space, which according to the uncertainty principle leads to conservation of the crystalline momentum law. This means that only phonons centered at the Γ point of the Brillouin zone will contribute to the Raman signal, which will result in the narrow and symmetric Raman peaks in the spectra. On the other side, in real crystals, due to either point or extended defects, the phonon remains confined in space. This leads to an uncertainty in the phonon momentum and, consequently, to the relaxation of the momentum conservation rule, which results in the activation of the non-center phonons. These effects create a characteristic change in the shape of the main peaks in the Raman spectra, with the appearance of asymmetric broadening at the side of peaks. Depending on the slope of the phonon dispersion of the Raman mode, the Raman peak will become asymmetric and broadens towards the high energy side (positive slope) or towards the low energy side (negative slope). The resulting shape can be modeled assuming the correlation length model, from which a quantitative estimation of the degree of the disorder in the crystals can be obtained.[32]

Phonon confinement effects in case of kesterites are investigated on a set of CZTS samples with different crystal quality. Difference in crystal quality was obtained by changing the annealing time during the preparation process. Variation in the frequency and shape of the two main Raman peaks at 287 and 338 $cm^{-1}$ assigned both to A symmetry modes has been observed. Simultaneous fitting of the two peaks according to the phonon confinement model is used to determine both the correlation length and stress induced shift components, that have been correlated with the grain size and crystalline quality assessed by complementary techniques (XRD and SEM). The estimated correlation length is shown to be a suitable quantitative indicator of the crystal quality for these materials (Figure 3.2). Based on these results, a simple experimental methodology is proposed for the structural assessment of these films. This

methodology is compatible with micro-scale analysis configurations and can also be extended to CZTSe compounds.

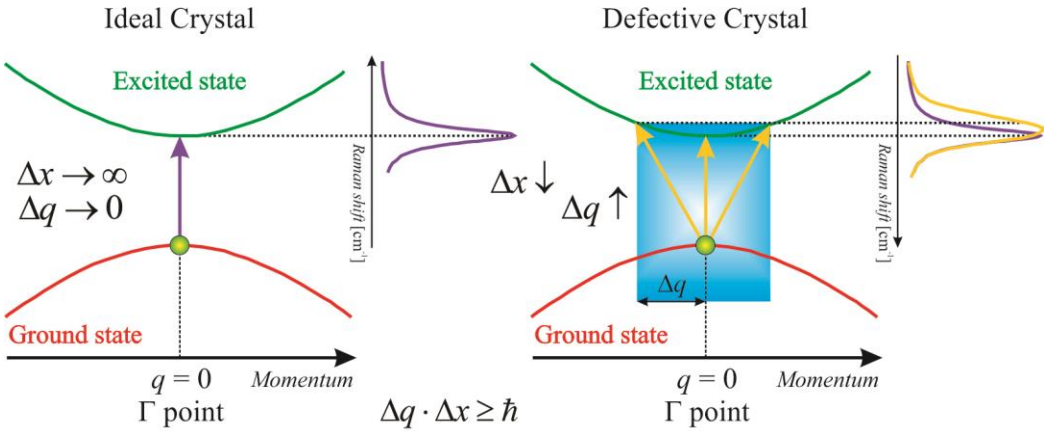


Figure 3.1 Schematic explanations of the phonon confinement and its effect on the Raman spectra.

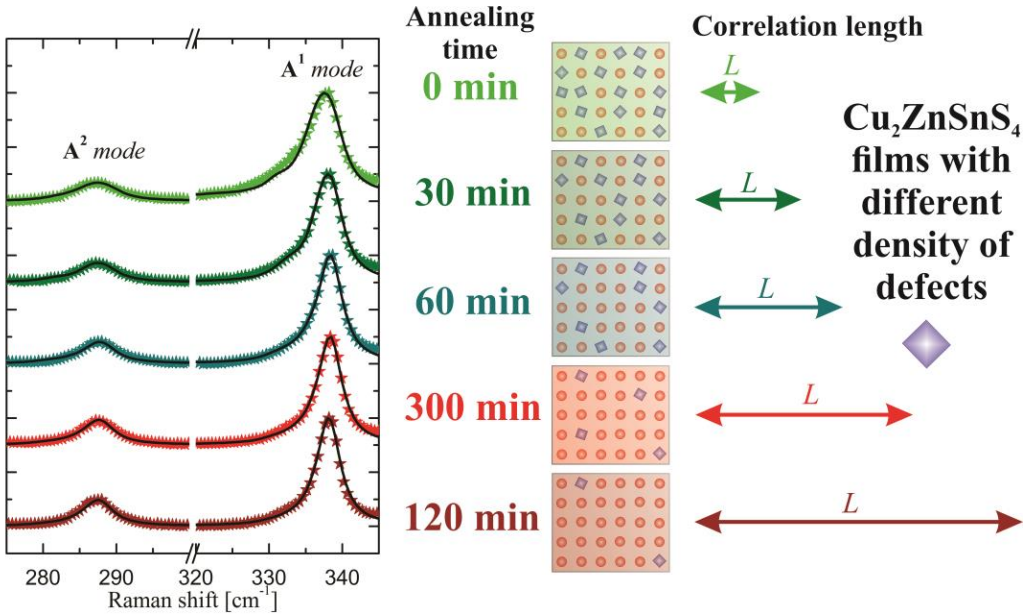


Figure 3.2 Phonon confinement effects in Raman spectra of CZTSe samples with various crystal quality achieved by different annealing times.

On the other side, presence of the small amount of defects usually does not induce significant changes in the Raman spectra, especially in polycrystalline materials.

As the crystal symmetry is mostly preserved in this case, Raman selection rules are also maintained, meaning that no significant changes in the frequencies of the Raman modes are expected. In regard with this kind of behavior, three possible changes can occur in the Raman spectra due to the presence of defects:

(1) In some cases the occurrence of defects in a crystalline material may cause local vibrational modes, which lead to the presence of additional, usually rather small features in the Raman spectra. Introduction of impurities in the crystal could lead to these effects.[34]

(2) Presence of defects leads to a reduction of the phonon lifetime. This leads to a symmetric broadening of the Raman peaks, as the phonon lifetime is inversely proportional to the natural line-width of the Raman peaks.[35,36]

(3) Changes in the intensity of the Raman peaks can occur because of the changes in the chemical bonds among the atoms in the material. In some cases defects could induce braking of the certain bonds, while in others they can lead to formation of new ones. This implies changes in the values of the elements of the polarizability tensors related to the vibrational modes involving these bonds, which in turns leads to changes in the intensity of the corresponding peaks.[37]

In order to investigate the effect of different types of defects on the Raman spectra, as well as on the optoelectronic properties, CZTSe thin films with lateral compositional gradients have been prepared and used for the fabrication of a high number of solar cells (~200) with different absorber composition.[38,39] This permits a detailed combinatorial study of these films using a methodology readily applicable to other multinary compound systems, with the aim of narrowing the compositional range to produce higher performance devices as well as to study fundamental properties of the materials.

Metallic (Cu-Zn-Sn) precursor thin films with lateral compositional gradients were synthesized by DC-magnetron sputtering deposition. After thermal treatment in a selenium containing atmosphere at 550 $^{o}$C, 5 x 5 cm$^2$ compositionally graded samples are formed with Cu/(Zn+Sn) and Zn/Sn ratios between 0.55 - 1.20 and 0.70 - 1.90, respectively. CZTSe films were made into solar cell devices using a CdS buffer layer, and a ZnO/ZnO:Al window layer. The samples were mechanically scribed to form cells 3 x 3 mm$^2$ in size (around 200 solar cells per sample), thus isolating each solar cell device and dividing the graded film into small regions of relatively constant composition with which to correlate material and device properties. Compositional mapping (Cu/Zn and Cu/Sn) of a representative combinatorial CZTSe sample is shown

in Figure 3.3. The selected compositional range includes the Cu-poor and Zn-rich region frequently reported for high efficiency kesterite-based devices, as well as overlap into stoichiometric and Cu-rich and Zn-poor regions.

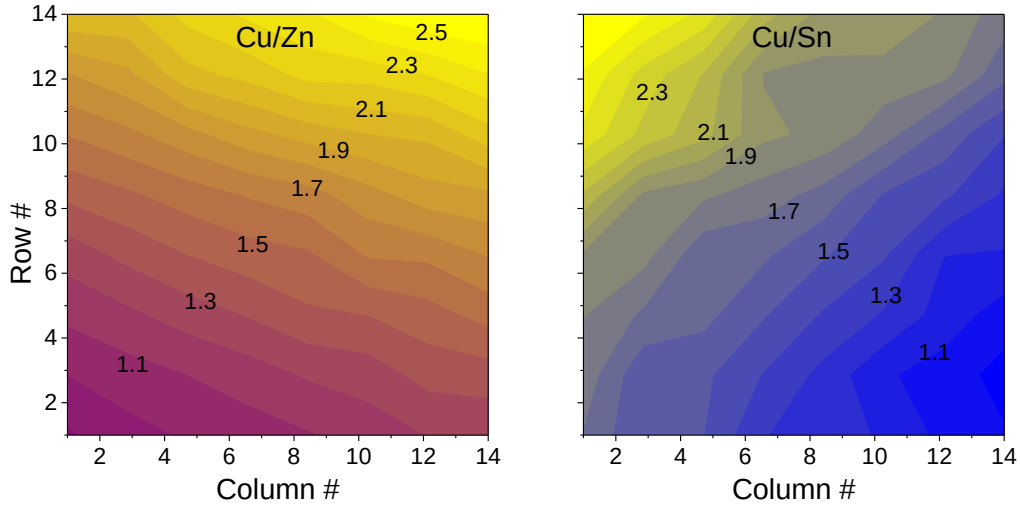


Figure 3.3 Compositional mapping of the ratios Cu/Zn (left) and Cu/Sn (right) of a 5x5 $cm^2$ graded kesterite film; each [column,row] corresponds to one 3x3 $mm^2$ cell.

Figure 3.4 presents pseudo-ternary phase diagrams of $Cu_2Se$-ZnSe-$SnSe_2$ with around 200 points showing device efficiency, open-circuit voltage ($V_{OC}$) and short-circuit current ($J_{sc}$) with dependence on composition (fill factor (FF) follows a similar trend as $V_{OC}$). In the figure, solid lines indicate the most expected secondary phases ($Cu_2Se$, ZnSe, and $SnSe_2$) and the different kinds (A, B, C, D, E and F) of charge compensated point defect clusters.[40,41] The stoichiometric composition point is given by the intersection of all these lines. This means that for a composition between two of the secondary phase lines, a mixture of CZTSe and these two secondary phases would be expected, as well as different point defects and defect clusters.

A maximum device efficiency of 6.9% is obtained, together with a highest open circuit voltage ($V_{OC}$) values of 411 mV for the devices analyzed in this work. The maximum values of the optoelectronic properties are achieved for a very narrow interval of compositions around Cu/(Zn+Sn) ≈ 0.7, Zn/Sn ≈ 1.2, Cu/Zn ≈ 1.4, and Cu/Sn ≈ 1.6, which is in agreement with previously reported results for high efficiency CZTSe-based solar cells. Furthermore, a deterioration in optoelectronic properties is observed for regions corresponding to compositions Cu/(Zn+Sn) > 0.95 or Zn/Sn < 1.00. In addition, distinct compositional regions corresponding to the maximum open circuit voltage (Figure 3.4(b)) and short circuit current values (Figure 3.4(c)) have been identified. These regions appear in the phase diagram corresponding to Cu-poor and

Zn-rich compositions, where occurrence of $V_{Cu}$, $Zn_{Cu}$ and $Zn_{Sn}$ point defects is expected. It is also concluded that Cu/Sn is a better indicator of device performance than the typically reported ratios of Zn/Sn and Cu/(Zn+Sn), because of a narrow range for high efficiency devices (Cu/Sn is in the interval of 1.6-1.7 for the best devices in this study).

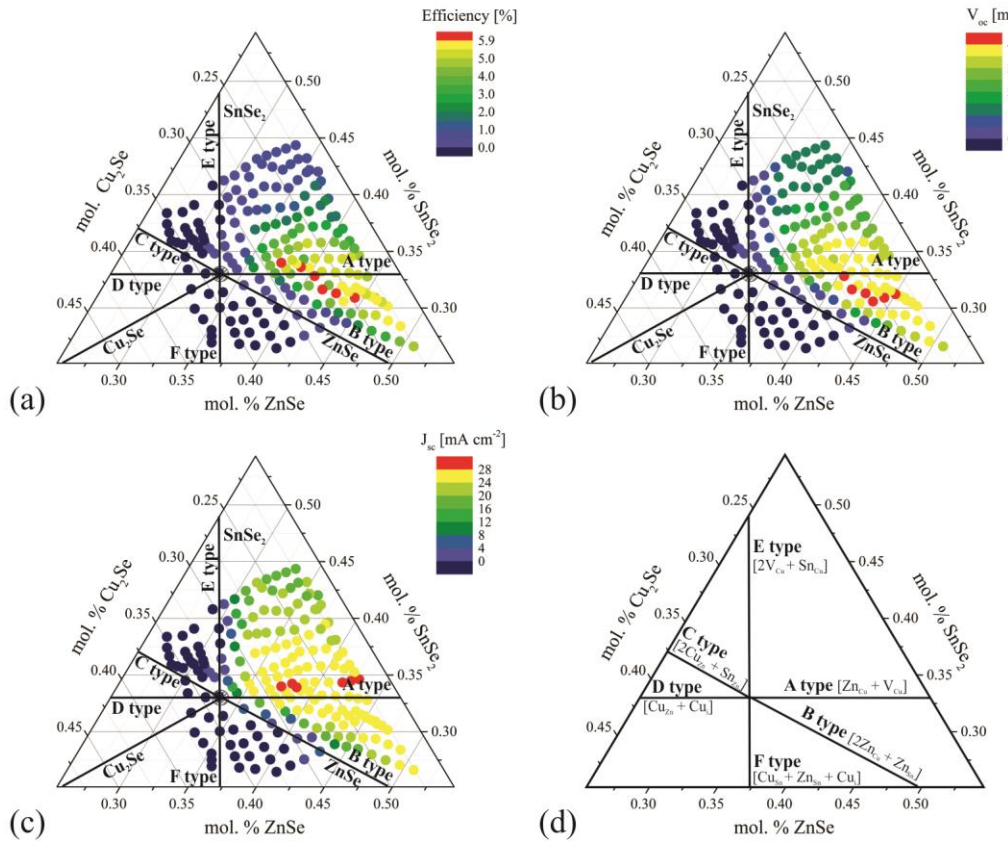


Figure 3.4. Compositional dependence of device (a) efficiency, (b) $V_{OC}$ and (c) $J_{SC}$ shown in a pseudo-ternary phase diagram of $Cu_2Se$-ZnSe-$SnSe_2$ for compositionally graded CZTSe solar cells; lines indicate expected secondary phases or defect clusters for a given region. (d) Pseudo-ternary phase diagram of $Cu_2Se$-ZnSe-$SnSe_2$ with lines indicating different defect clusters.

In order to obtain a deeper understanding of absorber composition related effects on optoelectronic properties, a systematic study of the appearance of secondary phases has been performed using two characterization techniques: XRD and multi-wavelength excitation Raman spectroscopy. The combination of both techniques enables differentiation in the location of secondary phase formation, either on the surface (s) or in the bulk (b) of the absorber (Figure 3.5).

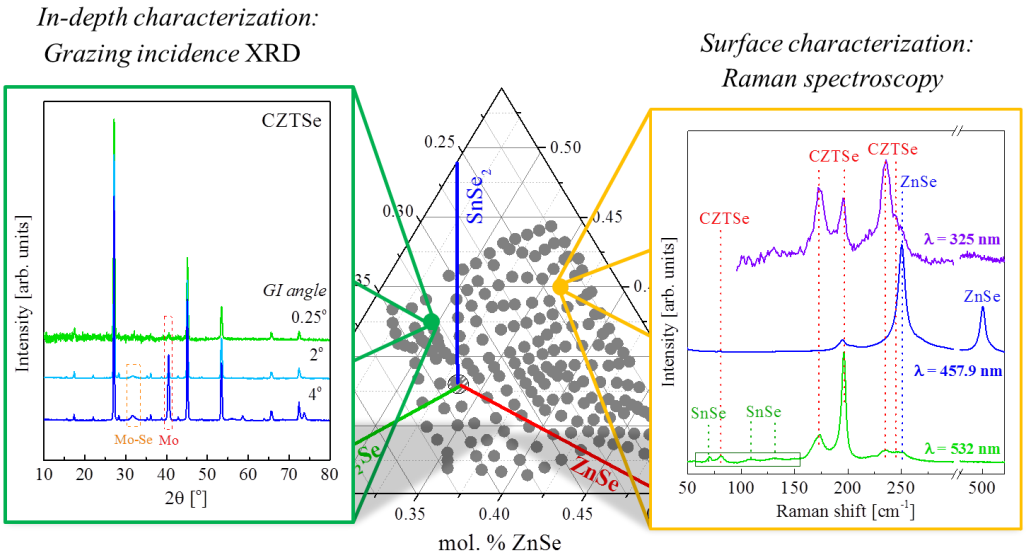


Figure 3.5 Systematic characterizations of secondary phases in the combinatorial samples using XRD and multi-wavelength Raman spectroscopy.

Figure 3.6 shows a pseudo-ternary phase diagram of the detected secondary phases (Cu-Se, ZnSe, and Sn-Se) with dependence on the composition of the solar cells. Cu-Se phases are not detected on the surface for any composition, though there are found in the bulk of the absorber for almost all cells with the composition Cu/(Zn+Sn) < 1.00. Sn-Se secondary phases are usually present in the bulk of the absorber for compositions Zn/Sn < 1.20. Very Sn-rich conditions, Zn/Sn < 1.00, give rise to the appearance of Sn-Se secondary phases on the surface of the absorbers. Zn-rich conditions are in most cases followed by the appearance of the surface ZnSe secondary phase. The presence of ZnSe in the bulk is expected to increase with higher Zn content, but this is undetectable with the bulk characterization method utilized in this work (XRD). It is interesting to note that within the sensitivity limits of the techniques utilized, no secondary phases are detected in the compositional region around the stoichiometric point (labeled as "none" in Figure 3.6).

The appearance of secondary phases can be correlated with the performance of the devices, as shown in Figure 3.6 which presents the dependence of the optoelectronic properties from the presence of the detected phases. Secondary phases have the strongest effect on the maximum achievable $V_{oc}$ and FF, and consequently the efficiency of devices. The effects on $J_{sc}$ are much weaker, except when Cu-Se phases are detected.

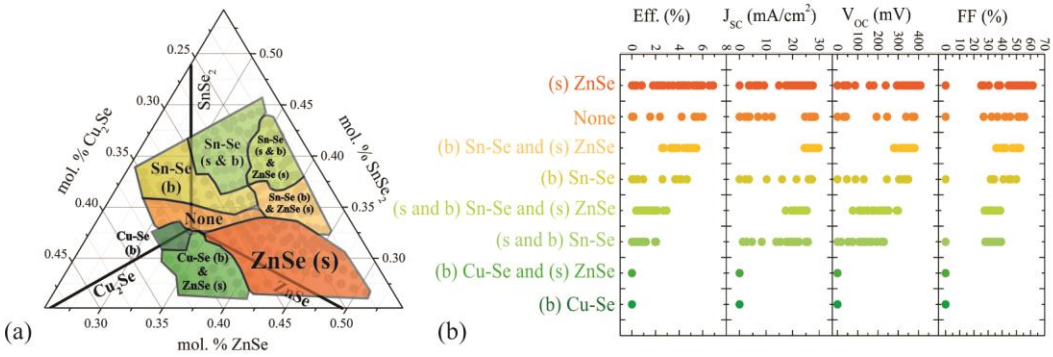


Figure 3.6 (a) Compositional dependence of detected secondary phases – Cu-Se, ZnSe, and Sn-Se – in surface (s) and bulk (b) absorber regions shown in a psuedo-ternary phase diagram (lines indicate theoretically expected secondary phases). (b) Influence of secondary phases on the optoelectronic properties (efficiency, $J_{SC}$, $V_{OC}$ and FF).

In all cases the presence of Cu-Se phases result in a non-performing solar cell device.[42] This is expected because of the high conductivity of this phase, which effectively shunts the device. The presence of other secondary phases (ZnSe and Sn-Se) does not a priori result in non-functioning devices, and they have a more nuanced effect on the device performance.[43,44] Sn-Se phases on the surface of absorber have more detrimental effect on all optoelectronic properties than when they are present only in the bulk of the absorber. The reduction in the performance of solar cells in the case of surface Sn-Se is mostly due to the structural and lattice mismatch between the CZTSe and Sn-Se, which creates an interface with high density of defects. Additionally, these facts are also confirmed by numerical simulations of optoelectronic properties.[45] In contrast, an enhancement in the maximum optoelectronic performance is observed for the cells in which ZnSe was detected on the surface of the absorber, when compared to ones without any detected ZnSe. This is mainly due to the small amount of ZnSe present in the surface, and partly due to the beneficial optoelectronic defects present in this compositional region.

In order to closely investigate the effect of different defect clusters on the optoelectronic properties, first the influence of defects on the Raman modes has to be explored. This is done by the systematic Raman study on the samples corresponding to A, B and C type of defects (Figure 3.7).[31] It is important to note that, all Raman peaks observed in the spectra shown in Figure 3.7 are attributed to the kesterite CZTSe phase, with peak positions in agreement with the previously reported data.[26,31,46] The following impact of $V_{Cu}$, $Zn_{Cu}$, $Zn_{Sn}$, $Cu_{Zn}$ and $Sn_{Zn}$ point defects is observed:

(1) Presence of $V_{Cu}$ and $Zn_{Cu}$ point defects induce a decrease in intensity of the B symmetry modes around 170 $cm^{-1}$ related to the vibrations of Cu/Zn and Cu/Sn planes (i.e. a decrease of Cu/Zn and Cu/Sn vibrational units).

(2) Presence of $Zn_{Sn}$ point defects lead to appearance of an additional ZnSe-like contribution at 250 $cm^{-1}$ and conversion from E symmetry modes at the 220 $cm^{-1}$ spectral region to B symmetry modes at the 250 $cm^{-1}$ spectral region.

(3) Presence of $Cu_{Zn}$ point defects lead to appearance of an additional CuSe-like contribution at the 250 $cm^{-1}$ frequency region.

(4) Presence of $Sn_{Zn}$ point defects lead to appearance of an additional SnSe-like contribution around the 185 $cm^{-1}$ frequency region and to conversion of B symmetry vibrational modes at the 250 $cm^{-1}$ spectral region into E symmetry vibrational modes at the 220 $cm^{-1}$ frequency region.

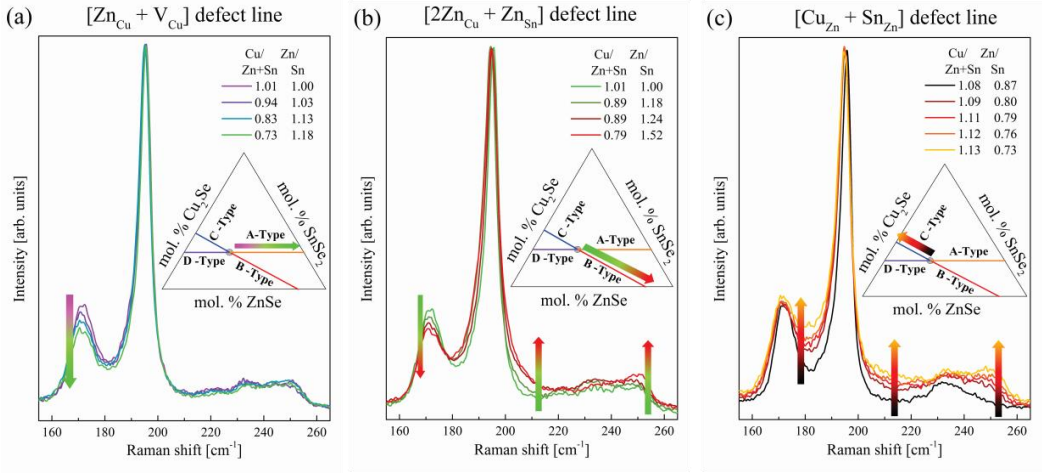


Figure 3.7 Comparison of Raman spectra measured from samples with compositions corresponding to different defect lines: (a) A-type, (b) B-type and (c) C-type. All Raman spectra are measured with 532 nm excitation wavelength. The arrows indicate changes in the intensity of the modes with the change in the composition in the directions shown on the ternary diagram.

Theoretical calculations have revealed that non-stoichiometry conditions in kesterites result in facile formation of self-compensated defect clusters, from which a high population of A type defect clusters ($[V_{Cu} + Zn_{Cu}]$) has shown to be especially beneficial to the performance of solar cells, since they enhance the electron-hole separation in the absorber layer.[29] This is why special focus is put on investigation of this type of defect on the optoelectronic properties.

According to the previously mentioned results, the decrease in the relative intensity of the band at around 170 $cm^{-1}$ is associated with the increase in concentration of the [$V_{Cu}$ + $Zn_{Cu}$] defect clusters. In that sense, changes in the concentration of [$V_{Cu}$ + $Zn_{Cu}$] defect clusters present in the material can be assessed by analyzing the integral intensity ratio of the defect sensitive band at 170 $cm^{-1}$ ($I_2$) and the peak at 196 $cm^{-1}$ ($I_1$), which is not significantly affected by this type of defect (Figure 3.8(a)). Dependence of the optoelectronic parameters (energy band gap ($E_g$), $V_{OC}$, and $V_{OC}$ deficit (defined as $E_g$ - $V_{OC}$)) on the variations in the intensity ratio $I_2 / (I_1 + I_2)$, related to changes of the concentration of [$V_{Cu}$ + $Zn_{Cu}$] defect clusters, is presented in Figure 3.8(b). It is observed that the $V_{OC}$ follows the trend of the band gap up to a certain concentration of [$V_{Cu}$ + $Zn_{Cu}$], when it is maximized, and after which it starts to decrease even for the still increasing band gap. The steady decrease in the $V_{OC}$ for the higher concentrations of [$V_{Cu}$ + $Zn_{Cu}$] is probably due to the increased number of recombinations caused by the large number of defects, and/or increased p-type doping of the absorber due to the large amount of $V_{Cu}$ expected at very Cu-poor conditions. These results demonstrate that the $V_{OC}$ can be tuned by modifying the amount of Cu substitutional defects in the absorber layer. To further demonstrate that this is an intrinsic property of the CZTSe material, and not a consequence of the preparation method, the same analysis of the Raman spectra was performed on different sets of absorbers prepared by various methods.[47,48] These results have also confirmed the possibility of $V_{OC}$ tuning through the changes in the concentration of [$V_{Cu}$ + $Zn_{Cu}$] defects clusters.

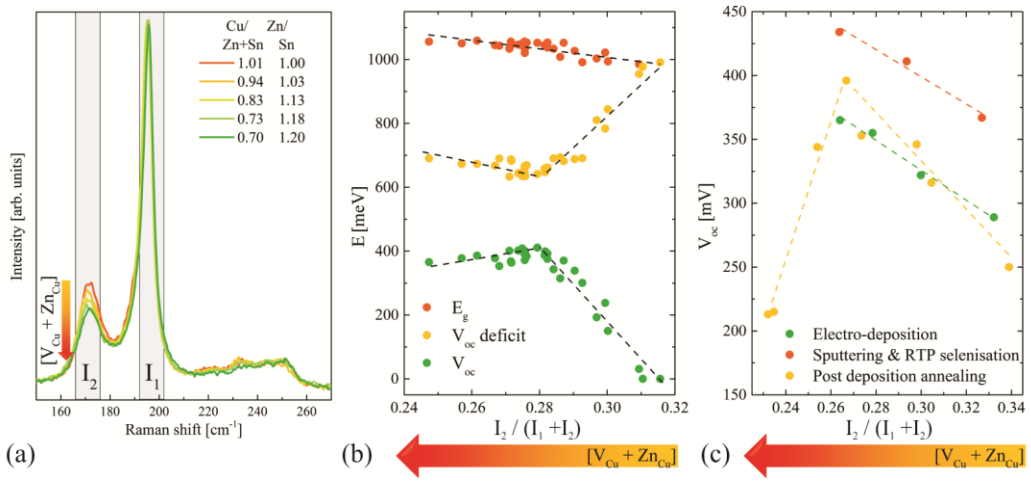


Figure 3.8 (a) Comparison of Raman spectra for absorbers with different composition. Dependence of the optoelectronic parameters: energy band gap ($E_g$), $V_{OC}$, and $V_{OC}$ deficit from Raman intensity ratio $I_2 / (I_1 + I_2)$ correlated with the concentration of [$V_{Cu}$ + $Zn_{Cu}$] defect clusters obtained from the samples prepared from (b) combinatorial studies (c) various methods.

In conclusion, this chapter presents a detailed study of the defects dynamics in kesterite materials. Successful experimental identification of defects was achieved by application of Raman spectroscopy on combinatorial samples. This investigation has also enabled exploring the effect of different type of defects, either in intrinsic form or as secondary phases on the optoelectronic properties of devices based on kesterite absorbers. It is concluded that the $V_{OC}$ values could be tuned by modifying the amount of the [$V_{Cu}$ + $Zn_{Cu}$] defect clusters, either by adjusting the composition or altering the production process. These results should provide a crucial step in solving the $V_{OC}$-deficit problem in kesterites. Furthermore, a methodology for the general assessment of crystal quality is presented based on the phonon confinement effects.

This chapter concludes with four publications: "Raman scattering crystalline assessment of polycrystalline $Cu_2ZnSnS_4$ thin films for sustainable photovoltaic technologies: Phonon confinement model", "Compositional paradigms in multinary compound systems: A case study of kesterites", "Influence of compositionally induced defects on the vibrational properties of device grade $Cu_2ZnSnSe_4$ absorbers for kesterite based solar cells" and "Secondary phase and Cu substitutional defect dynamics in kesterite solar cells: impact on optoelectronic properties" in which detailed information about the presented results is given.

Available online at www.sciencedirect.com

ScienceDirect

Acta Materialia 70 (2014) 272–280

Acta MATERIALIA

www.elsevier.com/locate/actamat

# Raman scattering crystalline assessment of polycrystalline $Cu_2ZnSnS_4$ thin films for sustainable photovoltaic technologies: Phonon confinement model

M. Dimitrievska [a], A. Fairbrother [a], A. Pérez-Rodríguez [a,b], E. Saucedo [a], V. Izquierdo-Roca [a,*]

[a] *Catalonia Institute for Energy Research (IREC), C. Jardins de les Dones de Negre 1, 08930 Sant Adrià del Besos, Barcelona, Spain*
[b] *IN²UB, Departament d'Electrònica, Universitat de Barcelona, C. Martí i Franquès 1, 08028 Barcelona, Spain*

Received 31 December 2013; received in revised form 14 February 2014; accepted 18 February 2014

**Abstract**

Phonon confinement effects in the Raman scattering spectra from polycrystalline $Cu_2ZnSnS_4$ thin films synthesized with different crystalline qualities – including photovoltaic grade layers – are investigated in terms of a phonon confinement model. Interpretation of the experimentally obtained spectra required the development of a modified model that includes additional features such as lattice strain. The model has been systematically applied for the simultaneous fitting of the two main A symmetry Raman peaks in the experimental spectra. The experimental data show that the line shape of the Raman peaks is determined mainly by phonon confinement effects, while their frequency is also sensitive to the presence of strain in the lattice. Simultaneous modeling of the A dominant peaks allows a quantitative estimation of the frequency strain shift that has been correlated with the strain measured by X-ray diffraction. Estimation of the correlation length also provides a quantitative indicator of the crystalline quality of the films that is found to correlate with the grain size assessed by scanning electron microscopy. Based on this model, a general and simple methodology for the assessment of the crystalline quality of $Cu_2ZnSnS_4$ samples independently of the experimental measurement conditions is proposed through the use of an asymmetry parameter.


*Keywords:* Kesterite; Raman spectroscopy; Defects; Nanoconfinement; Lattice strains

## 1. Introduction

Copper zinc tin sulfide ($Cu_2ZnSnS_4$ or CZTS) has sparked tremendous research interest due to its significant potential for photovoltaic (PV) applications. CZTS is a quaternary compound p-type semiconductor with the kesterite crystal structure, a high absorption coefficient on the order of $10^4$ $cm^{-1}$ and direct band gap of ~1.5 eV, which make it a highly suitable material as an absorber layer for low-cost thin-film solar PV cells [1–3]. In contrast to more mature PV chalcogenide technologies, such as those based on $Cu(In,Ga)(S,Se)_2$ (CIS), CZTS comprises only elements that exist in abundance, which makes this material more suited to sustainable mass deployment. This has motivated the strong interest in research into this material for the development of absorbers in thin film solar cells, with a current record in efficiency of 9.2% [3]. Even if higher efficiencies can be achieved with the use of selenide $Cu_2ZnSnSe_4$ compounds or Se-rich $Cu_2ZnSn(S,Se)_4$ alloys, the higher abundance of S in relation to Se, and the lower toxicity of S related compounds, have created additional

* Corresponding author.
*E-mail address:* vizquierdo@irec.cat (V. Izquierdo-Roca).

http://dx.doi.org/10.1016/j.actamat.2014.02.035
1359-6454/

interest in the development of absorbers based on the pure sulfide kesterite.

Numerous studies done on optoelectronic properties of CZTS-based solar cells have shown that they are strongly dependent on the structural properties, crystalline quality and presence of secondary phases in the absorber layers [4–6]. Therefore, in order to achieve better device performance it is necessary to study the influence of all physical parameters which have a major impact on the characteristics of solar cells. This also implies the need to develop characterization methodologies suitable for the crystalline assessment of the films, and if possible at a quantitative level and using optical non-destructive techniques.

Thus far theoretical calculations on band structure, optical properties and intrinsic defects of CZTS have been made [7–10], as well as experimental determination of all active Raman scattering vibrational modes [11–13]. Raman scattering has also been used as an effective approach to probe the crystalline structure and quality of different kinds of semiconductor thin films, since the presence of defects in the material strongly influences the position and shape of Raman peaks [14]. Raman scattering also appears to be a more suitable technique than X-ray diffraction (XRD) for detection of secondary phases [11,15,16], because XRD is compromised by the high level of overlapping between the main peaks in the diffractograms corresponding to some of the expected phases in the Cu–Zn–Sn–S material system.

In this framework, this work investigates the development of a Raman scattering based methodology for the analysis of the crystalline quality of CZTS thin films for photovoltaic applications. This has included modeling of the spectral features of the main A symmetry CZTS Raman peaks using a phonon confinement model. Phonon confinement effects are especially notable in nanostructural materials [17], and a brief analysis of phonon confinement for CZTS nanocrystals was done in Ref. [18].

The aim of this work is to obtain a deeper physical insight into numerous issues related to phonon confinement effects in the CZTS thin films by combining the structural analysis by Raman scattering spectroscopic techniques and XRD. Quantitative estimation of the presence of disorder effects in Raman spectra of CZTS thin films grown for PV application was done for a series of films with different crystalline quality, starting from highly defective layers to device-grade high quality polycrystalline films. Based on the obtained results, a methodology independent of the experimental measuring conditions has been proposed for the quantitative estimation of the correlation length, which constitutes a physical parameter directly related to the crystalline quality of the layers.

## 2. Phonon confinement model

Richter et al. were the first to develop phonon confinement model (PCM I) for silicon thin films [19]. According to this model, the $\vec{q} = 0$ selection rule for the optical phonon can be applied only to infinite crystals. In nano-sized crystallites the phonon remains confined in space, which leads to an uncertainty in the phonon momentum and, consequently, to the relaxation of the momentum conservation rule. As a result there is a contribution of phonons to the Raman signal which are not located at the Γ point of the Brillouin zone (BZ). Depending on the slope of the phonon dispersion curve $\omega(\vec{q})$ of the Raman mode, the Raman peak will become asymmetric and broadens towards the high energy side (positive slope) or towards the low energy side (negative slope).

According to the PCM I, the Raman phonon line intensity $I(\omega)$ is calculated by superimposing Lorentzian lines centered each at the wave vector value $\omega(\vec{q})$ and weighted by the uncertainty in $\omega(\vec{q})$ due to confinement:

$$I(\omega) \propto \iiint_{BZ} \frac{|\Omega(0,\vec{q})|^2}{\left[\omega - \omega(\vec{q})\right]^2 + \frac{\Gamma^2}{4}} \mathrm{d}\vec{q} \tag{1}$$

where Γ is the natural linewidth of the Raman mode, $\omega(\vec{q})$ is the phonon dispersion curve and $|\Omega(0,\vec{q})|^2$ is a spectral weighting function.

The PCM I assume the uncertainty in $\omega(\vec{q})$ to be Gaussian, which leads to a spectral weighting function defined as:

$$|\Omega(0,\vec{q})|^2 = \left|\exp\left(-\frac{L^2}{4\kappa}\vec{q}^2\right)\right|^2 \tag{2}$$

where $L$ is defined as the phonon confinement correlation length, and $\kappa$ is a parameter which determines how fast the contribution of the $\vec{q}$ vectors decreases with increasing $|\vec{q}|$. There is no physical reason to choose a certain value for parameter $\kappa$ in the PCM I and various authors have proposed different values [17,19].

A more realistic model that describes the influence of the confinement of phonons without the need for the introduction of the $\kappa$ parameter was proposed by Nemanich et al. (PCM II) [20]. The PCM II suggests that the influence of the confinement of phonons could be expressed as a structure factor in form of a spherical Bessel function $j_1$ (Eq. (3)).

$$|\Omega(0,\vec{q})|^2 = \frac{9 j_1^2\left(\frac{L}{2}\vec{q}\right)}{\left(\frac{L}{2}\vec{q}\right)^2} \tag{3}$$

Even though these models were first derived from the analysis of the spectra from nanocrystalline materials, the presence of structural defects – including extended or point defects – in the crystal lattice determines also the presence of disorder effects in the spectra that can be modeled with the correlation length model [14,21]. In general, the correlation length parameter $L$ corresponds to the characteristic distance where translational crystal symmetry holds, and this is related to the average distance between defects in the lattice. Estimation of the correlation length allows a quantitative estimation of the degree of disorder in the crystals related to the presence of the structural defects.

## 3. Experimental

CZTS thin films were prepared by the thermal treatment of metallic precursors at 550 °C for 0, 30, 60, 120, and 300 min in a sulfur and tin containing atmosphere. The Sn/Cu/Zn precursor stacks were made by DC-magnetron sputtering deposition onto soda-lime glass/Mo substrates. More details about precursor deposition and thermal processing can be found in Ref. [22]. Compositional ratios of the annealed films were approximately $Cu/(Zn + Sn) = 0.79$ and $Zn/Sn = 1.30$, near values used for higher efficiency CZTS-based devices (the best efficiency achieved using the particular process described here is 5.5% [22,23]).

After annealing the samples were subjected to a chemical etching in an HCl-based solution developed for the selective removal of ZnS [24]. The Cu-poor and Zn-rich conditions, in addition to this etching, ensure a surface free of secondary phases, as confirmed by Raman scattering measurements with 325 and 532 nm excitation wavelengths.

Raman scattering measurements were performed in backscattering configuration with a LabRam HR800-UV Horiba-Jobin Yvon spectrometer coupled to an Olympus metallographic microscope. A diode-pumped solid state laser with a wavelength of 532 nm and power of 0.5 mW was used for excitation. A 50× microscope objective (numerical aperture of 0.75) was used, which yields a focused spot diameter of ~1 μm, and when used in conjunction with the DuoScan™ accessory allowed measurements to be taken over an raster area of $\sim 30 \times 30\ \mu m^2$. Under these experimental measurement conditions, no thermal effects are observed in the spectra. This has been corroborated by the analysis of spectra measured with different excitation powers. The penetration depth of the laser wavelength used is estimated to be below 100 nm in CZTS. The first-order Raman spectrum of monocrystalline silicon was measured as a reference before and after acquisition of each Raman spectrum, and the spectra were corrected with respect to the silicon peak position at 520 $cm^{-1}$.

The synthesized films were imaged by scanning electron microscopy (SEM) using a ZEISS Series Auriga microscope with 20 kV acceleration voltage. To measure the structural properties of the films, XRD diffraction patterns were measured with θ–2θ configuration using a Siemens D500 diffractometer with monochromatic Cu $K_\alpha$ radiation.

## 4. Results and discussion

### 4.1. XRD and SEM characterization

To analyze the potential presence of strain in the layers a detailed analysis of the lattice parameters was done from the XRD characterization. Refinements of the lattice constant values were carried out by Le Bail analysis using the FullProf program with Thompson–Cox–Hastings pseudo-Voigt convoluted with axial divergence asymmetry profile function [25,26]. Thus the lattice parameters *a* and *c* were determined. Dependence of the lattice parameters *a* and *c* for all five CZTS thin film samples on the annealing time are represented in Fig. 1. Horizontal dashed lines in this figure correspond to the lattice parameter values reported for bulk, strain-free CZTS kesterite [27]. These data show the existence of a compressive strain in the crystals in the directions corresponding to the *a* crystalline axes, which tends to decrease as annealing time increases. On the other hand, the data obtained for the *c* lattice constant agree for all the samples with the value reported for a strain-free CZTS kesterite lattice.

As shown in Fig. 1, the structural relaxation of the compressive strain in the *a* lattice constant takes place up to the annealing time of 120 min. The data obtained in the 120 min annealed sample show in this case the absence of a detectable strain. A further increase of annealing time leads again to the detection of a small compressive strain in the *a* lattice constant.

The average grain size in the films was estimated by SEM. Fig. 2 shows the surface SEM micrographs from the different films. These images show that the grain size increases with annealing times, except in the case of the film annealed during 300 min. For the 300 min annealed film it is observed that the grain size is smaller than the one for the 120 min annealed film. This behavior has been attributed to a partial decomposition of the kesterite phase because of increased loss of Sn in the samples exposed to very long annealing times [28].

These results are also in accord with the XRD measurements, in which a slight decrease in the value of the *a* lattice parameter in the 300 min annealed film in comparison to that annealed during 120 min is observed. As shown in Fig. 3, the average *a* lattice strain, $\varepsilon_a$ correlates with the average grain size estimated by SEM from the films annealed during different times. This points out a direct relationship between the improvement of the crystalline quality of the layers and the relaxation of the compressive average strain detected in the *a* crystalline directions.

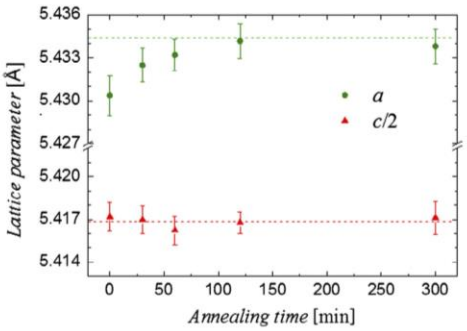


Fig. 1. Lattice parameter dependence on annealing time for CZTS thin films. The dashed lines represent the values of lattice parameters from bulk, strain-free CZTS [27].

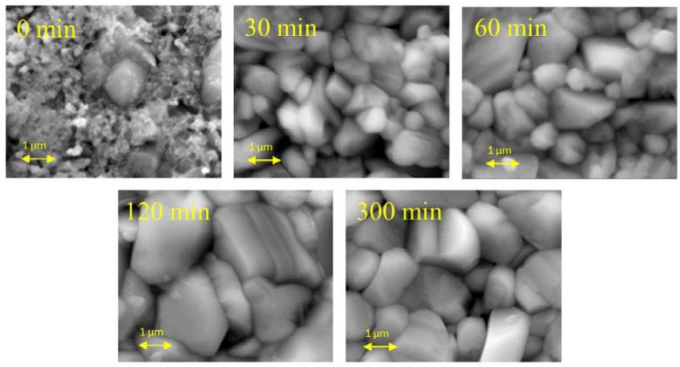


Fig. 2. Surface SEM images of the annealed CZTS thin films.

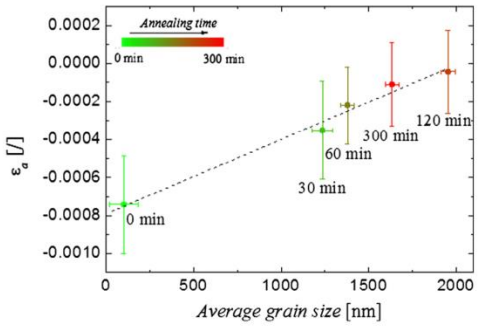


Fig. 3. Relation between average a crystalline lattice strain and grain size for CZTS thin films.

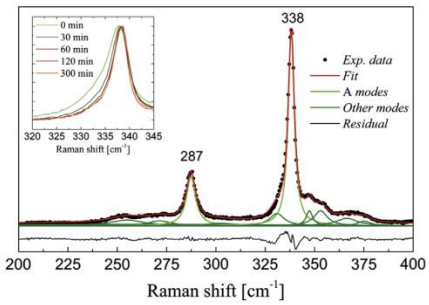


Fig. 4. Raman spectrum of a device grade CZTS thin film (sample annealed for 120 min). Inset shows the presence of a low frequency asymmetry in the main A peak at 338 cm$^{-1}$ that increases for the films annealed with shorter durations.

Similar relation between the strain and grain size was observed in CIS materials [29].

### 4.2. Raman scattering and phonon confinement model

The zone center phonon representation of the optical modes of the kesterite structure with the space group $I\bar{4}$ can be written as $\Gamma = 3A \oplus 6B \oplus 6E$, where all modes are Raman active [30,31]. Fig. 4 shows the Raman spectrum measured from a device grade CZTS sample (corresponding to the film annealed for 120 min), together with the fitting of peaks with Lorentzian curves. The spectrum shows two dominant peaks at 287 cm$^{-1}$ and 338 cm$^{-1}$ which are identified with the dominant A symmetry modes [11]. In addition, the spectrum also shows weaker contributions at 252, 265, 273, 305, 317, 332, 347, 353, 366 and 373 cm$^{-1}$, which are attributed to E and B symmetry modes. The positions of all these peaks agree with the experimental results presented in Refs. [11–13,32], and their symmetry assignment is consistent with the theoretical first principles calculations reported in Refs. [30,31].

The spectrum in Fig. 4 also shows a lower frequency asymmetry between 320 cm$^{-1}$ and the most intense A mode at 338 cm$^{-1}$. This contribution is shown in the plot of the residue signal corresponding to the difference between the experimental spectrum and its fitting with Lorentzian symmetric peaks (black line in Fig. 4). This contribution is higher for the films processed under conditions leading to smaller grain size and higher compressive strain, as shown in the inset in Fig. 4.

This contribution could be explained by the presence of E/B symmetry modes that are reported in this spectral region [30,31], or it could be caused by the presence of a stannite-like ($I\bar{4}$ symmetry group) secondary phase that appears because of the existence of a disordered distribution of Zn and Cu atoms in the cation sublattice [33,34]. This phase is referred to in the literature as the disordered kesterite phase and is characterized by a dominant $A_1$ symmetry Raman peak at 332 cm$^{-1}$. The effect of this phase on the Raman spectra of kesterite is detailed in Ref. [35]. However, in this work fitting of the spectra with an additional Lorentzian peak in this spectral region does not lead to a satisfactory fitting of this asymmetric contribution. It is also important to remark that a similar asymmetric contribution is also observed in the low frequency side of the A

symmetry peak at 287 $cm^{-1}$. Taking this into account, the asymmetry has been explained as due to the phonon confinement effect, similarly to Refs. [18,36–41]. A similar behavior was observed for the main $A_1$ mode of the polycrystalline CIS thin films, and it was shown that this asymmetry could be directly correlated with the deterioration of the photovoltaic performance of CIS based solar cells [21,42]. Observation of these effects in the main A symmetry CZTS peaks ($A^1$ at 338 $cm^{-1}$ and $A^2$ at 287 $cm^{-1}$) is facilitated by the fact that these are the most intense peaks in the experimental spectra and they are also the ones with lowest overlapping with other features in the experimental Raman spectra, while the weaker peaks have a higher degree of overlapping between them (Fig. 4). Accordingly, effects inducing changes in the spectral features of the Raman peaks are much easier to be observed in these peaks.

In order to perform curve fits for the two main A modes according to the PCM II, the phonon dispersion curves along the high symmetry points ($Z-\Gamma-N-X'-\Gamma-X$) were taken from Khare et al. [31]. Since the lengths of all branches are different in the reciprocal space, an approximation was included, where the BZ is replaced by the sphere of a radius that corresponds to the shortest branch ($\Gamma N$) of the phonon dispersion. Inside this sphere the averaged phonon dispersion is assumed to be isotropic.

Using this approximation, the three-dimensional integration over the whole BZ in Eq. (1) could be reduced to only one dimension, and it can be presented in form of Eq. (4).

$$I(\omega)=\int_0^{\Gamma N}\frac{9j_1^2(Lq/2)/(Lq/2)^2}{[\omega-\omega(q)]^2+\frac{\Gamma^2}{4}}4\pi q^2\mathrm{d}q \tag{4}$$

The calculated PCM II predictions for the main A modes using Khare's phonon dispersion curves, with decreasing correlation lengths, are presented in Fig. 5a and b. As can be seen, in both cases the Raman peaks downshift and broaden asymmetrically to lower frequencies with decreasing correlation length.

In Fig. 6 Raman spectra of the CZTS samples with different crystalline quality are shown. Simultaneous fittings of the two A modes which were done according to the PCM II model are presented as blue solid lines in Fig. 6. These fittings have allowed reproduction of the changes observed in the line shape of the experimental peaks, using the same value of correlation length for both peaks in each of the spectra. However, the model does not allow explaining the changes observed in the frequency of the peaks. One reason for this disagreement is the existence of discrepancy in the frequency of these modes between experimental and calculated data. The origin of this discrepancy is attributed to requirement of using approximations in the first-principles simulations for calculating the phonon dispersion curves, Ref. [31].

In order to obtain better fittings with the experimental results the PCM II model was modified (mPCM II). First

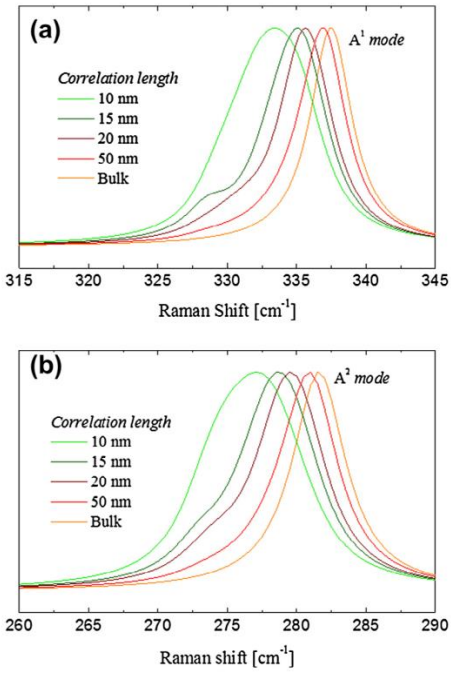


Fig. 5. Calculated Raman line shapes for different correlation lengths as predicted by the PCM II for the $A^1$ (a) and $A^2$ (b) Raman peaks.

modification included correcting the theoretical Raman peak positions of the A modes theoretically calculated in Ref. [31] to the corresponding experimental positions obtained for high crystalline quality stoichiometric CZTS [13]. On the other side, strain-induced effects can also modify the frequency of the peaks [13]. In accord with this, a second modification was introduced in the PCM II model, including an additional parameter that would be related to the strain-induced frequency shift, in agreement with the XRD measurements. The Raman scattering intensity in the modified case is given by:

$$I(\omega)=\int_0^{\Gamma N}\frac{9j_1^2(Lq/2)/(Lq/2)^2}{[\omega-(\omega(q)+\Delta\omega_c+\Delta\omega_s)]^2+\frac{\Gamma^2}{4}}4\pi q^2\mathrm{d}q \tag{5}$$

where $\Delta\omega_c$ is the difference between the theoretical [31] and experimental [13] peak position of the A modes and $\Delta\omega_s$ is the strain-induced frequency shift. The mPCM II described in Eq. (5) now gives the combined effect of average strain and phonon confinement effects.

The simultaneous fittings of both A modes done according to the mPCM II model leads to much better correlation with experimental results (black solid lines shown in Fig. 6). In this case the shape and frequency of both $A^1$ and $A^2$ Raman peaks are satisfactorily fitted. Furthermore, it is important to mention that in all the spectra the $A^1$ peaks were fitted assuming the same value of the natural linewidth $\Gamma(A^1)$, and the $A^2$ peaks were fitted assuming

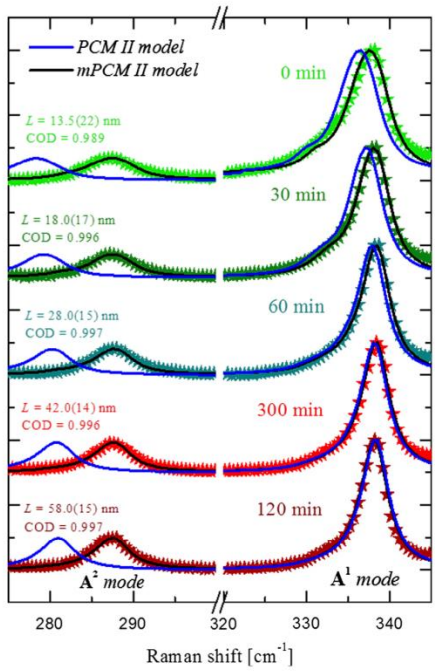


Fig. 6. Raman spectra showing the evolution of the main A modes with confinement. The dots represent the experimental data and solid lines represent the fits done according to PCM II (blue lines) and mPCM II model (black lines). (For interpretation of the references to color in this figure legend, the reader is referred to the web version of this article.)

the same value of the natural linewidth $\Gamma(A^2)$. The best fits were obtained for $\Gamma(A^1) = 3.65\ cm^{-1}$ and $\Gamma(A^2) = 4.65\ cm^{-1}$. Different values for the natural linewidths of the two A symmetry modes are to be expected, since they depend on the decay mechanism of phonons which in principle is different for the different modes [43]. On the other hand, the values obtained are also similar to the natural linewidth observed from reference single crystal Si, which is measured to be $3.6\ cm^{-1}$ for the experimental conditions. The parameters obtained from the best fitting of each sample are indicated above the corresponding spectrum. As shown, in almost all cases the fitting shows values of the correlation coefficient (COD) that are indicative of a good agreement between both experimental and theoretical spectra. Only in the case of the spectra from the sample annealed with the shortest duration time (0 min nominal annealing time) is there a small disagreement in the fit and the experimental data. This sample is the one with the lowest crystalline quality and highest compressive strain. Lower agreement between the theoretical and experimental spectra could be due to the existence in this case of a certain distribution of correlation lengths and/or strain gradients in the scattering volume.

Fig. 7a plots the correlation length $L$ calculated from Raman spectra using the mPCM II model vs. the grain size estimated from the SEM micrographs. As shown, there is a significant correlation between both parameters: samples processed under conditions leading to smaller grain sizes are characterized by Raman spectra with shorter correlation lengths, which points out the presence of a higher density of structural defects in these films. Furthermore, again it is observed that the 300 min annealed sample has a smaller correlation length than the 120 min annealed sample, in accord with the other characterization techniques. These data support the validity in the use of the correlation length as a quantitative estimation of the crystalline quality of the processed samples.

On the other side, the comparison between the strain-induced shifts $\Delta\omega_s$ determined from the fitting of the Raman spectra with the mPCM II model and the average $a$ lattice strain $\varepsilon_a$ measured by XRD is shown in Fig. 7b. The existence of a blue-induced shift (towards higher wavenumbers) agrees with the compressive characteristic of the measured strain. Physically, compressive strain likely arises from crystal surface reconstruction effects induced by surface tension, which is the reason why it is more pronounced in samples with smaller grains. It should be noted that in the case CZTS thin films annealed for more than 30 min, there is a linear relationship between $\Delta\omega_s$ and $\varepsilon_a$, in agreement with the behavior expected at small strain and/or

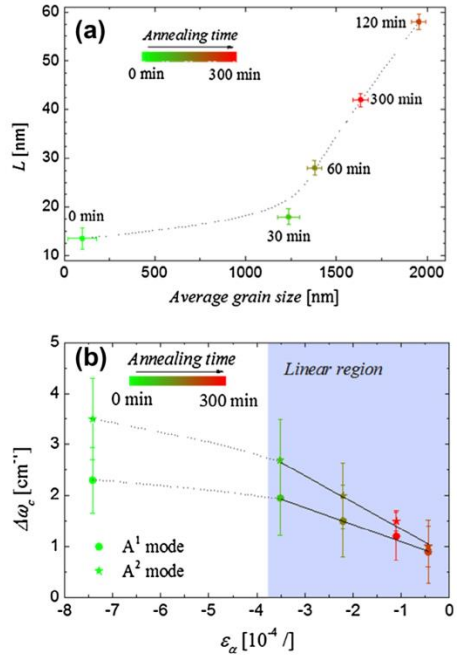


Fig. 7. (a) Relation between correlation length and average grain size calculated from Raman spectra and SEM measurements. (b) Strain induced frequency shift obtained from fitting of Raman spectra with mPCM II model vs. average lattice strain calculated from XRD measurements. Dashed lines are included as a visual guide.

stress levels [14]. Fitting of these data gives a value of the linear slopes of $-3.3(3) \times 10^3\ cm^{-1}$ and $-5.4(6) \times 10^3\ cm^{-1}$ for $A^1$ and $A^2$ peaks, respectively. The differences in the obtained values of the slope are due to the different vibrations physically involved in each of the modes. In the end it can be concluded that the shapes of the peaks depend only on the correlation length, and the frequency of the peak is determined by both correlation length and strain effects.

To compare the model proposed in this work with experiments that are reported in the literature, it is useful to employ a parameter defining the line shape of the Raman peaks which is independent of the experimental conditions used in the measurements (and, therefore, of the measuring spectral resolution). A possibility to do this is by the use of a phenomenological asymmetry parameter α, which measures the asymmetry of the line shape of the Raman peak, as commonly used in liquid chromatography [44]. In this case, the peak asymmetry α is defined as the ratio of the widths (Δω) at 10% of maximum intensity measured relative to the peak maximum (Fig. 8):

$$\alpha = \frac{\Delta\omega_L}{\Delta\omega_R} = \frac{\omega_m - \omega_-}{\omega_+ - \omega_m} \tag{6}$$

where the subscripts $L$ and $R$ refer to 10% linewidth measured to the left and right of the peak maximum, respectively. The frequencies $\omega_-$ and $\omega_+$ locate the positions at 10% intensity on the low and high frequency sides of the peak maximum located at $\omega_m$. This particular definition for α is also used because it is a sensitive probe of subtle changes in the Raman peak asymmetry. $\alpha = 1$ corresponds to a symmetric line shape, as that of a Lorentzian curve.

The values of α in relation to $L$ are calculated from simulated Raman spectra for $A^1$ and $A^2$ modes. Fig. 9 represents the calculated asymmetry factor for $A^1$ mode in relation to the correlation length. Similar behavior was observed for the $A^2$ mode. This figure also includes the asymmetry factor estimated for the $A^1$ mode from Raman spectra reported in the literature for CZTS nanocrystals with different size [36–41,45]. As shown in this figure, estimation of the correlation length using the model

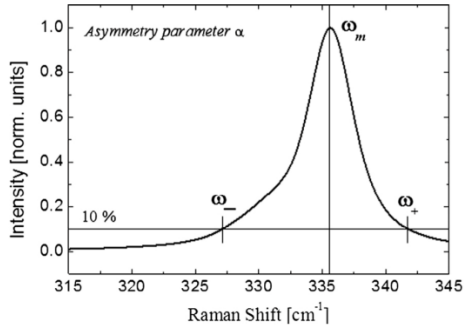


Fig. 8. Definition of the asymmetry parameter (Eq. (6)) used in the analysis.

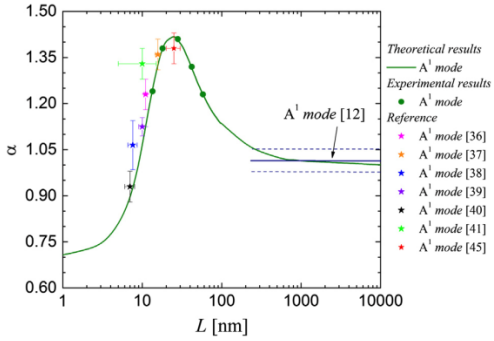


Fig. 9. Asymmetry parameter α vs. correlation length from fitting of $A^1$ CZTS Raman peak.

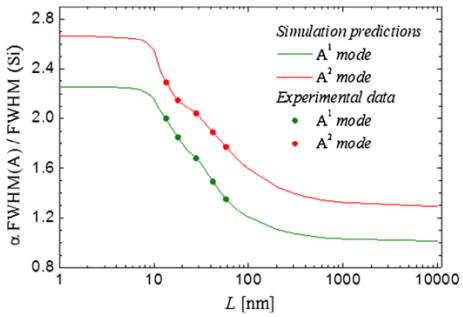


Fig. 10. Prediction curves generated from plot of asymmetry factor multiplied by relative FWHM of experimental Raman peaks vs. correlation length estimated from the mPCM II model.

developed in this work gives a value that has a good agreement with that of the reported nanocrystal size. This gives strong support to the validity of the developed model. The figure also shows the values obtained from the spectra from single crystalline CZTS [12] (asymmetry factor around 1). These values correspond to the asymptotic behavior predicted by the correlation length model for L . Taking into account the experimental uncertainty in the determination of this parameter, this asymptotic behavior is achieved for $L > 200$ nm. This indicates that from the point of view of phonon confinement effects, CZTS nanocrystal domains larger than this size are equivalent to a single crystal kesterite structure.

Using these results, a methodology for the estimation of the correlation length in the samples is proposed. This is based on the plot of the product of the asymmetry parameter α with the relative full width at half maximum (FWHM) of the $A^1$ or $A^2$ peaks in relation to that of the reference Si Raman line ($\alpha \cdot \mathrm{FWHM}(A^{1,2})/\mathrm{FWHM}(Si)$). This methodology gives general prediction curves that are independent of the experimental conditions which are used. The generated prediction curves for both $A^1$ and $A^2$ Raman modes are shown in Fig. 10. This gives a fast,

simple and non-destructive methodology for the assessment of the crystalline quality of the CZTS layers.

## 5. Conclusion

Phonon confinement effects were studied in the Raman spectra of semiconductor CZTS thin films synthesized by DC-magnetron sputtering deposition and annealed in a sulfur and tin containing atmosphere for different periods of time. Notable low frequency asymmetry of both A modes was clearly observed in the Raman spectra from films annealed in conditions leading to lower crystalline quality, and has been interpreted in terms of phonon confinement effects. On the other hand, the observed peak shifts were found to result from a balance between phonon confinement effects and lattice contraction due to compressive strain in the *a* crystalline directions. A combined theoretical model (mPCM II) considering both effects on the two main A modes of CZTS thin films was presented and adopted for the detailed systematic simulation of the experimental data. Quantitative estimation of the correlation length correlates with the crystalline quality of the films as reflected in the behavior of the average grain size. Correlation of Raman spectral modeling with detailed XRD analysis has also allowed quantitative determination of the strain-induced dependence of the frequency of the $A^1$ and $A^2$ Raman peaks. The model has also been successfully applied to Raman spectra reported in the literature from nanocrystalline samples, which gives additional support to its validity. Based on this model, a simple methodology independent of measuring conditions is proposed for the quantitative estimation of the correlation length.

## Acknowledgements

The research leading to these results has received funding from the People Program (Marie Curie Actions) of the European Union's Seventh Framework Program FP7/2007-2013/ under Research Executive Agency Grant agreement no. 316488 (KESTCELLS), and from project KEST-PV (ref. ENE2010-121541-C03-1) from the Spanish "Ministerio de Economia y Competitividad". Authors from IREC and $IN^2UB$ belong to the M-2E (Electronic Materials for Energy) Consolidated Research Group and the XaRMAE Network of Excellence on Materials for Energy of the "Generalitat de Catalunya". A.F. thanks the Spanish Ministry of Economy and Competitiveness (MINECO) for the FPU Fellowship (FPU12/05508), V.I. for the "Juan de la Cierva" Fellowship (JCI-2011-10782), and E.S. for the "Ramon y Cajal" Fellowship (RYC-2011-09212).

## References

[1] Wolden CA, Kurtin J, Baxter JB, Repins I, Shaheen SE, Torvik JT, et al. J Vac Sci Technol A 2011;29:030801.
[2] Katagiri H. Thin Solid Films 2005;480–481:426.
[3] Kato T, Hiroi H, Sakai N, Muraoka S, Sugimoto H. 27th European PV Solar Energy Conf and Exhibition; 2013. p. 2236.
[4] Schorr S. Sol Energy Mater Sol Cells 2011;95:1482.
[5] Redinger A, Berg DM, Dale PJ, Siebentritt S. J Am Chem Soc 2011;133:3320.
[6] Chen S, Gong XG, Walsh A, Wei S-H. Appl Phys Lett 2010;96:021902.
[7] Chen S, Gong XG, Wals A, Wei SH. Phys Rev B 2009;79:165211.
[8] Persson C. J Appl Phys 2010;107:053710.
[9] Nagoya A, Asahi R, Wahl R, Kresse G. Phys Rev B 2010;81:113202.
[10] Chen S, Yang JH, Gong XG, Walsh A, Wei SH. Phys Rev B 2010;81:245204.
[11] Fontane X, Izquerdo-Roca V, Saucedo E, Schorr S, Yukhymchuk VO, Valakh MY, et al. J Alloys Compd 2012;539:190.
[12] Dumcenco D, Huang YS. Opt Mater 2013;35:419.
[13] Dimitrievska M, Fairbrother A, Fontané X, Jawhari T, Izquierdo-Roca V, Saucedo E, et al. Appl Phys Lett 2014;104:021901.
[14] Álvarez-García J, Izquierdo-Roca V, Pérez-Rodríguez A. In: Rau U, Abou-Ras D, Kirchatz T, editors. Handbook on advanced characterization techniques for thin film solar cells. Weinheim: Wiley-VCH; 2011.
[15] Fernandes PA, Salomé MP, da Cunha AF. Semicond Sci Technol 2009;24:105013.
[16] Cheng AJ, Manno M, Khare A, Leighton C, Campbell SA, Aydil ES. J Vac Sci Technol A 2011;29:051203.
[17] Irmer G. J Raman Spectrosc 2007;38:634.
[18] Khare A, Wills AW, Ammerman LM, Norris DJ, Aydil ES. Chem Commun 2011;47:11721.
[19] Richter H, Wang ZP, Ley L. Solid State Commun 1981;39:625.
[20] Nemanich RJ, Solin SA, Martin RM. Phys Rev B 1981;23:6348.
[21] Camus C, Rudigier E, Abou-Ras D, Allsop NA, Unold T, Tomm Y, et al. Appl Phys Lett 2008;92:101922.
[22] Fairbrother A, Fontané X, Izquierdo-Roca V, Espíndola-Rodríguez M, López S, Placidi M, et al. Sol Energy Mater Sol Cells 2013;112:97.
[23] Mitzi DB, Gunawan O, Todorov TK, Wang K, Guha S. Sol Energy Mater Sol Cells 2011;95:1421.
[24] Fairbrother A, Gracia-Hemme E, Izquierdo-Roca V, Fontane X, Pulgarin-Agudelo FA, Vigil-Gala O, et al. J Am Chem Soc 2012;134:8018.
[25] Rodriguez-Carvajal J, Roisnel T. <www.ill.eu/sites/fullprof/> [accessed 23.12.13].
[26] Finger LW, Cox DE, Jephcoat AP. J Appl Cryst 1994;27:892.
[27] Choubrac L, Lafond A, Guillot-Deudon C, Moelo Y, Jobic S. Inorg Chem 2012;51:3346.
[28] Scragg JJ, Ericson T, Kubart T, Edoff M, Platzer-Bjorkman C. Chem Mater 2011;23:4625.
[29] Abou-Ras D, Caballero R, Kaufmann CA, Nichterwitz M, Sakurai K, Schorr S, et al. Phys Stat Sol (RRL) 2008;3(2):135.
[30] Gurel T, Sevik C, Cagin T. Phys Rev B 2011;84:205201.
[31] Khare A, Himmetoglu B, Cococcioni M, Aydil ES. J Appl Phys 2012;111:123704.
[32] Himmrich M, Haeuseler H. Spectrochim Acta A 1991;47:933.
[33] Choubrac L, Lafond A, Guillot-Deudon C, Rocquefelte X, Jobic S. Phys Chem Chem Phys 2013;15:10722.
[34] Valakh MY, Kolomys OF, Ponoaryov SS, Yukhymcuk VO, Babichuk IS, Izquierdo-Roca V, et al. Phys Status Solidi RRL 2013;1.
[35] Caballero R, Garcia-Llamas E, Merino JM, Leon M, Babichuk I, Dzhagan V, et al. Acta Mater 2014;65:412.
[36] Singh A, Geaney H, Laffir F, Ryan KM. J Am Chem Soc 2012;134:2910.
[37] Zou C, Zhang L, Lin D, Yang Y. Cryst Eng Commun 2011;13:3310.
[38] Flynn B, Wang W, Chang C, Hermen GS. Phys Status Solidi A 2012;1.
[39] Shavel A, Cadavid D, Ibanez M, Carrete A, Cabot A. J Am Chem Soc 2012;134:1438.
[40] Saravana Kumar R, Deul Ryu B, Chandramohan S, Kyung Seol J, Lee S, Hong C. Mater Lett 2012;86:174.
[41] Sarswat PK, Free ML. J Cryst Growth 2013;372:87.

[42] Scheer R, Pérez-Rodríguez A, Metzger WK. Prog Photovolt Res Appl 2010;18:467.
[43] Kuzmany H. Solid state spectroscopy. 2nd ed. Berlin: Springer Verlag; 2009.
[44] Kirkland JJ, Yau WW, Stoklosa HJ, Dilks CH. J Chromatogr Sci 1977;15:303.
[45] Carrete A, Shavel A, Fontane X, Montserrat J, Fan J, Ibanez M, et al. J Am Chem Soc 2013;135:15982.

Journal of Materials Chemistry A

COMMUNICATION

View Article Online
View Journal | View Issue

Cite this: *J. Mater. Chem. A*, 2015, **3**, 9451

Received 18th March 2015
Accepted 8th April 2015

DOI: 10.1039/c5ta02000j

www.rsc.org/MaterialsA

# Compositional paradigms in multinary compound systems for photovoltaic applications: a case study of kesterites†

Andrew Fairbrother,[a] Mirjana Dimitrievska,[a] Yudania Sánchez,[a] Victor Izquierdo-Roca,[a] Alejandro Pérez-Rodríguez[ab] and Edgardo Saucedo*[a]

Utilizing a combinatorial approach, two distinct compositions for optimizing optoelectronic properties are found for $Cu_2ZnSnSe_4$-based solar cells, due to formation of different defect clusters, secondary phases, and potentially other composition related effects. One of the highest open circuit voltages for this compound is reported, as well as a narrower compositional range for high efficiency devices.

Off-stoichiometry compositions are characteristic of many multinary compounds used in diverse applications, especially in electronics and optoelectronics. In many of these classes of compounds, such as perovskites ($A^{2+}B^{4+}X_3^{2-}$),[1] spinels ($A^{2+}B_2^{3+}X_4^{2-}$),[2] and chalcopyrites ($A^{+}B^{2+}X_2^{2-}$),[3] deviations from stoichiometry often give rise to beneficial properties in the material for a given application, such as changes in doping from point defect formation, phase stabilization, or inhibited formation of deleterious secondary phases.[4–6] As such, numerous compositional and combinatorial studies are necessary to determine the optimum composition of a compound for diverse applications.[7] Kesterite compounds, especially $Cu_2ZnSnS_4$, $Cu_2ZnSnSe_4$, and $Cu_2ZnSn(S,Se)_4$, are under development as a light absorbing layer in thin film solar cells, and are closely related to chalcopyrite-based ($Cu(In,Ga)Se_2$) technologies. In fact, they are a potential replacement for these technologies in the mid- to long-term, due to their virtue of being composed of earth-abundant elements. To date the highest device performances – 9.2% ($Cu_2ZnSnS_4$),[8] 11.6% ($Cu_2ZnSnSe_4$),[9] and 12.7% ($Cu_2ZnSn(S,Se)_4$)[10] – are achieved in kesterites prepared under Cu-poor and Zn-rich conditions, with the ideal range of compositions commonly reported in the cationic ratios of Cu/(Zn + Sn) and Zn/Sn. Nevertheless, there is uncertainty about the optimal compositional range, and a rather broad range of values for Cu/(Zn + Sn) (0.7 to 0.9) and Zn/Sn (1.1 to 1.4) are often reported for high efficiency devices.[8–13]

In this communication the ratio of Cu/Sn is shown to be a much stronger predictor of device performance than those ratios. Even more critically, a compositional paradigm associated with the complex nature of these multinary compounds when applied as an absorber layer for photovoltaic applications is illustrated. Depending on the composition the open circuit voltage ($V_{OC}$), short circuit current ($J_{SC}$), and fill factor (FF) of devices are maximized in distinct regions of the compositional phase diagram, correlating with the expected formation of different secondary phases and point defects.

To demonstrate this, $Cu_2ZnSnSe_4$ (CZTSe) thin films with lateral compositional gradients have been prepared and used for the fabrication of a high number of solar cells (~200) with different absorber composition. This permits a detailed combinatorial study of these films using a methodology readily applicable to other multinary compound systems, with the aim of narrowing the compositional range to produce higher performance devices as well as study fundamental properties of the materials.[14–17] A maximum device efficiency of 6.9% is obtained, together with one of the highest reported values of open circuit voltage (411 mV) for this compound (compare for example with 394 and 377 mV for recent record devices of 10.4% and 9.2%, respectively).[11,12] This is an especially crucial result because of the high $V_{OC}$-deficit (the difference between theoretical maximum $V_{OC}$ and measured $V_{OC}$) of this class of materials, which is the area where greatest improvement can be made.[9,18] The latest record (11.6%) surpasses previous record efficiency devices in $V_{OC}$ (423 mV),[9] but there are reports of higher $V_{OC}$ devices (432 and 443 mV),[11,17] albeit with lower overall efficiencies.

Optoelectronic properties ($V_{OC}$, $J_{SC}$, and FF) are found to be optimized under distinct compositional regimes, corresponding to areas in which different point defects and secondary phases are expected to form. The estimated bandgap of the

[a]*Catalonia Institute for Energy Research (IREC), Jardins de les Dones de Negre 1, 08930 Sant Adrià de Besòs, Spain. E-mail: esaucedo@irec.cat*

[b]*IN2UB, Universitat de Barcelona, C. Martí Franquès 1, 08028 Barcelona, Spain*

† Electronic supplementary information (ESI) available: Experimental details, compositional maps of Cu/(Zn + Sn) and Zn/Sn, dependence of optoelectronic properties on these ratios, and dependence of properties on bandgap. See DOI: 10.1039/c5ta02000j

devices also varies with composition, though not in a way which strongly correlates to the optoelectronic properties. The ratio of Cu/Sn is shown to be a more critical ratio in correlating the properties of solar cell devices than those which are commonly reported (Cu/(Zn + Sn) and Zn/Sn).[19] For the highest efficiency devices in this work, the optimum ratio of Cu/Sn is ~1.6–1.7, while Cu/Zn should be below 1.7, Zn/Sn above 1.1, and Cu/(Zn + Sn) below 0.9. Additionally, preliminary Raman scattering characterization shows a strong dependence on composition, with spectral features which can be correlated to structural and point defects in the material.[20,21] These results demonstrate a narrower compositional range for photovoltaic-grade kesterites, and provide insights to improving the $V_{OC}$ of kesterite-based devices. They also provide a deeper fundamental understanding of this class of materials.

Compositionally graded CZTSe films were prepared from graded metallic (Cu–Zn–Sn) precursors films deposited by DC-magnetron sputtering onto Mo-coated soda-lime glass substrates,[13,22,23] using processes described in more detail in the ESI.† Briefly, the sputtering system (Alliance Ac450) is constructed with three off-center targets, and typically the substrate is rotated during deposition to form uniform films. However, to form gradient films the substrates were not rotated, resulting in deposition of graded films. The result is a Cu–Zn–Sn precursor film with approximately a 100–500 nm layer of each metal deposited. After a two-step thermal treatment in a selenium containing atmosphere (450 °C under low pressure, and 550 °C at high pressure) CZTSe films are formed with a typical compositional mapping (Cu/Zn and Cu/Sn) shown in Fig. 1. The selected range includes the Cu-poor and Zn-rich region frequently reported for high efficiency kesterite-based devices,[8–13] as well as overlap into stoichiometric and Cu-rich and Zn-poor regions (compositional maps for Cu/(Zn + Sn) and Zn/Sn are shown in Fig. S1†).

A CZTSe film was made into solar cell devices using a CdS buffer layer from chemical bath deposition, and a ZnO/ZnO:Al window layer from pulsed DC-magnetron sputtering deposition (Alliance CT100). The 5 × 5 $cm^2$ samples were mechanically scribed to form cells 3 × 3 $mm^2$ in size, thus isolating each solar cell device and dividing the graded film into regions of relatively constant composition with which to correlate material and device properties. X-Ray fluorescence spectroscopy (Fischerschope XVD) was used to measure the composition in each cell, with mapping measurements made in the center of each cell of the films. Illuminated *J–V* characteristics were measured under AM1.5 standard conditions (ABET3000 Solar Simulator), and external quantum efficiency was measured from 300–1500 nm (Bentham PVE300 characterization system). Raman scattering spectroscopy has been used to characterize not only the CZTSe phase, but also detect secondary phases. This was done using a Horiba Jobin Yvon systems LabRam HR800 and T64000 systems under 532 nm and 458 nm excitation conditions respectively.

The composition of kesterite thin films is commonly given in the form of cationic ratios, especially Cu/(Zn + Sn) and Zn/Sn, and less commonly Cu/Zn and Cu/Sn and other combinations thereof. This work confirms results aggregated from several other reports, namely that the broad range of Cu/(Zn + Sn) = 0.7–0.9 and Zn/Sn = 1.1–1.4 is ideal for high efficiency devices (see Fig. S3†). In contrast, Cu/Sn is shown to be a stronger indicator of device performance (efficiency, $V_{OC}$, and FF) than the typically reported ratios because of a narrow range for high efficiency devices (Cu/Sn from 1.6–1.7 for the best devices in this study). $J_{SC}$ is the only main property which is not strongly correlated to Cu/Sn, and in this case Zn/Sn is the ratio with the smallest range for high value devices in this work (Zn/Sn from 1.1 to 1.3). Device efficiency, $V_{OC}$, and $J_{SC}$ of nearly 200 cells with dependence on Cu/Zn and Cu/Sn are plotted in Fig. 2 (FF follows a similar trend as $V_{OC}$, and is plotted in Fig. S2†). In the

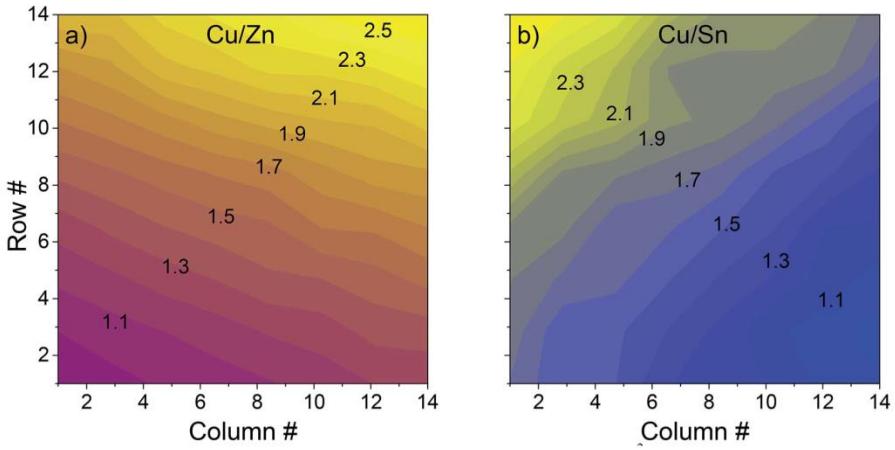


Fig. 1 Compositional mapping of the ratios Cu/Zn (left) and Cu/Sn (right) of a 5 × 5 $cm^2$ graded kesterite film; each [column, row] corresponds to one 3 × 3 $mm^2$ cell.

 

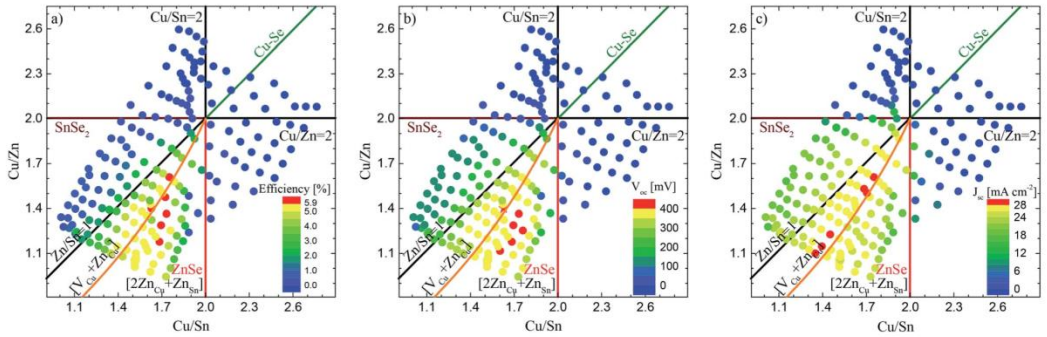


Fig. 2 Dependence of optoelectronic properties on composition – efficiency (a), $V_{OC}$ (b), and $J_{SC}$ (c) – for Cu/Zn *vs.* Cu/Sn for a compositionally graded CZTSe-based solar cell; lines indicate expected secondary phases or defect clusters for a given region, and stoichiometric ratios.

figure, lines indicate stoichiometric cation ratios, the most expected secondary phases (Cu–Se, ZnSe, and $SnSe_2$),[24] and charge compensated point defect clusters ($[V_{Cu} + Zn_{Cu}]$ and $[2Zn_{Cu} + Zn_{Sn}]$)[4,21,25] for a composition deviating from the stoichiometric point, which is at the intersection of all of the lines. In other words, for a composition between two of the secondary phase lines, a mixture of CZTSe and these two secondary phases might be expected, as well as different point defects and defect clusters (note that other secondary phases and defect types may form, though outside of the area of interest for the high efficiency devices presented here). In fact, secondary phases (Cu–Se binaries, ZnSe, and $SnSe_2$) are detected by X-ray diffraction and Raman scattering measurements, corresponding to the expected areas in the phase diagram. The defect cluster lines are based on previous work by Lafond *et al.* in which phase pure kesterite was formed with deviations from stoichiometry.[25] Assuming charge neutrality in the crystal, and based on theoretical calculations for defect formation energy, they propose the creation of different defect types for a given off-stoichiometric composition. Other defects may form, but due to the low formation energy of the proposed defects, they are the most expected. The position of these defect lines has been confirmed by Raman spectroscopy for thin film CZTSe by Dimitrievska *et al.*[21] Large deviations from stoichiometry may result in the formation of secondary phases in addition to point defects, therefore both are presented in the diagram. And finally, other compositional effects such as grain boundary chemistry (including sodium incorporation from the substrate) may also give rise to changes in film and device properties. Film thickness is relatively constant ($2.14 \pm 0.09$ μm), and Raman scattering measurements indicate minimal variation in the CdS and ZnO/ZnO:Al layers,[26] so changes in device performance can be linked mostly to film composition, as opposed to other factors. The device properties demonstrate a very strong dependence on the cell composition, with a much greater sensitivity to compositional changes than piecemeal approaches to optimizing film composition (*i.e.* comparison of a smaller number of samples with different composition).[13,19] An abrupt decrease in device performance occurs in the cells where Cu–Se phases are expected to form (*i.e.* Cu-rich). This observation is in line with behavior of the $Cu(In,Ga)Se_2$-based photovoltaic technologies, in which Cu-rich conditions are typically detrimental to the device efficiency, mainly due to the formation of highly conductive Cu–Se secondary phases inside the film.[3] Efficiency and $V_{OC}$ gradually degrade as the composition shifts from Zn-rich (Zn/Sn > 1) to Sn-rich (Zn/Sn < 1). However, the most remarkable feature is the occurrence of maxima in $V_{OC}$ and $J_{SC}$ under distinct compositional regimes. The composition of the high $J_{SC}$ cells sits slightly above and along the $[V_{Cu} + Zn_{Cu}]$ defect line with a maximum value of 29.9 mA $cm^{-2}$ (six cells with $J_{SC}$ > 28.0 mA $cm^{-2}$, $V_{OCmax}$ = 379 mV and $\eta_{max}$ = 6.0%). This corresponds to an almost constant Sn composition close to the stoichiometric value for CZTSe (~33 mol% $SnSe_2$).

On the other hand, the high $V_{OC}$ cells (and FF, see Fig. S2†) are found in between the $[V_{Cu} + Zn_{Cu}]$ and $[2Zn_{Cu} + Zn_{Sn}]$ defect lines, corresponding to a slightly Sn-poor composition (~31–32 mol% $SnSe_2$), with a maximum of 411 mV (six cells with $V_{OC}$ > 400 mV, $J_{SCmax} = 27.2$ mA $cm^{-2}$ and $\eta_{max} = 6.9\%$). This suggests that in both cases secondary phases and defects related to the Sn composition have a significant impact on the deterioration of these optoelectronic parameters:[21] maximum $J_{SC}$ is achieved with close to the stoichiometric Sn composition while maximum $V_{OC}$ requires a slight Sn deficiency in the absorbers. In relation to the maximum value achieved for $V_{OC}$, it is especially noteworthy that this is one of the highest open circuit voltages reported for this compound, even more than record devices produced by Oueslati *et al.* ($\eta = 10.4\%$ and $V_{OC} = 394$ mV) and Repins *et al.* ($\eta = 9.2\%$ $V_{OC} = 377$ mV).[11,12] It should be noted that in contrast with these record efficiency devices, this device was prepared without an anti-reflective coating or metallic grid, which leads to non-negligible losses in $J_{SC}$ by comparison. It is also interesting to note that there is prior indirect evidence of two optimum compositions for maximizing $V_{OC}$ and $J_{SC}$ in previous work. For example, Collord *et al.* and Brammertz *et al.* report high $V_{OC}$ devices (443 and 432 mV respectively), with lower $J_{SC}$ than the record devices (31.2 and 30.5 mA $cm^{-2}$).[17,27] Whereas Shin *et al.* and Oueslati *et al.* report high $J_{SC}$ devices (42.6 and 39.7 mA $cm^{-2}$ respectively), with

significantly lower $V_{OC}$ (385 and 394 mV).[11,28] Lee *et al.* have produced the current highest efficiency CZTSe-based device which progresses beyond previous record efficiency devices and has very high $V_{OC}$ and $J_{SC}$ (423 mV and 40.6 mA cm$^{-2}$ respectively),[9] but still has lower $V_{OC}$ than devices produced by Collord *et al.* and Brammertz *et al.* [Note that comparison between devices in different works should be made with reservations because of the different production processes used, including deposition of anti-reflection coatings.] The maximum efficiency device (6.9%) is also the cell with the highest $V_{OC}$, and the higher efficiency devices are found near the convergence of the high $V_{OC}$ and high $J_{SC}$ lines.

The fabrication of one of the highest $V_{OC}$ CZTSe-based devices is a remarkable result, because the so-called $V_{OC}$-deficit is a major challenge for improvement of kesterite-based technologies.[9,18] This is essentially the difference between the Shockley–Queisser limit based on the material bandgap and the measured $V_{OC}$. For the highest efficiency CZTSe-based device this is 580 mV,[9] compared to about 410 mV for higher performing Cu(In,Ga)$Se_2$-based devices.[18] $J_{SC}$ is also lagging in kesterite-based devices, though considerably less than the $V_{OC}$ which is clearly the area in which the greatest efficiency gains can be made with these technologies. Both parameters depend strongly on the bandgap of the absorber material, as exemplified in $Cu_2ZnSn(S,Se)_4$ solid-solutions with varying anion composition in which low bandgap selenium-rich devices have low $V_{OC}$ and high $J_{SC}$ compared to the high bandgap sulfur-rich devices.[10] In the devices presented here there are indeed variations in the bandgap due to variations in the cation composition,[19] though on a much smaller scale, and in the high efficiency region they do not correlate strongly with either the $V_{OC}$ or $J_{SC}$ (see ESI, Fig. S4†). In addition to bandgap, two principle limitations on these properties are expected to be interface or bulk charge carrier recombination.[12,18,29] These are both intimately tied to secondary phase and defect formation, and the reason for optimization of optoelectronic properties in two distinct compositional regimes is likely to be related to these as well. To date defect studies in kesterite materials have been rather limited, and mostly based on density functional theory calculations.[4,5] The highest density defects and defect clusters are calculated to be [$Cu_{Zn}$ + $Zn_{Cu}$], [$V_{Cu}$ + $Zn_{Cu}$], [2$Zn_{Cu}$ + $Zn_{Sn}$], and [2$Cu_{Zn}$ + $Sn_{Zn}$]. The first is rather shallow and expected at near stoichiometric compositions, while the next two are also rather shallow, and expected in the Cu-poor and Zn-rich conditions used for high efficiency devices. The latter is expected to occur in Zn-poor conditions, is much deeper than the others, and thus can act as a trap for charge carriers. A principle challenge is the precise calculation of defect levels, which is crucial because defects influence the band structure of the material, and thus maximum $V_{OC}$ and $J_{SC}$.[29]

In addition to device optimization, compositionally graded films are especially useful for studying the fundamental properties of multinary compounds, because further experimental characterization of the defect types and levels is necessary to determine how they depend on film composition and influence device performance. As seen in Fig. 2, secondary phases and point defects play a significant role in material properties, which is the reason off-stoichiometry studies of multinary compounds are of high impact. A first detailed analysis of the impact of the different compositional defects in the Raman spectra from these kinds of absorbers in a combinatorial study is reported by Dimitrievska *et al.*[21]

In conclusion, a methodology for studying stoichiometry effects in multinary compound systems has been presented, with a case study of the kesterite compound $Cu_2ZnSnSe_4$. One of the highest $V_{OC}$ CZTSe-based devices is reported (411 mV), and these results indicate that critical device parameters – $V_{OC}$, $J_{SC}$, and FF – are optimized under unique compositional regimes. This presents a new paradigm in kesterite-based technologies, in which device parameters may not be maximized simultaneously, and which provides insight into overcoming the $V_{OC}$-deficit of this class of materials. A stricter range of compositions for higher efficiency kesterite-based solar cell devices has also been reported. The cationic ratio of Cu/Sn is found to be a stronger predictor of device performance, in particular of efficiency, $V_{OC}$ and FF, than the commonly reported ratios of Cu/(Zn + Sn) and Zn/Sn. Specifically, device parameters were maximized for Cu/Sn from 1.6–1.7, with Cu/Zn < 1.7, Cu/(Zn + Sn) < 0.9, and Zn/Sn > 1.1.

## Acknowledgements

The research leading to these results has received funding from the People Program (Marie Curie Actions) of the European Union's Seventh Framework Program FP7/2007–2013/under REA grant agreement no. 316488 (KESTCELLS), and from project KEST-PV (ref. ENE2010-121541-C03-1) from the Spanish "Ministerio de Economia y Competitividad". Authors from IREC and IN2UB belong to the M-2E (Electronic Materials for Energy) Consolidated Research Group and the XaRMAE Network of Excellence on Materials for Energy of the "Generalitat de Catalunya". A.F. thanks the Spanish Ministry of Economy and Competitiveness (MINECO) for the FPU Fellowship (FPU12/05508), V.I. for the "Juan de la Cierva" Fellowship (JCI-2011-10782), and E.S. for the "Ramon y Cajal" Fellowship (RYC-2011-09212).

## Notes and references

1 R. Wendelbo, D. E. Akporiaye, A. Karlsson, M. Plassen and A. Olafsen, *J. Eur. Ceram. Soc.*, 2006, **26**, 849–859.
2 C. Masquelier, M. Tabuchi, K. Ado, R. Kanno, Y. Kobayashi, Y. Maki, O. Nakamura and J. B. Goodenough, *J. Solid State Chem.*, 1996, **123**, 255–266.
3 T.-P. Hsieh, C.-C. Chuang, C.-S. Wu, J.-C. Chang, J.-W. Guo and W.-C. Chen, *Solid-State Electron.*, 2011, **56**, 175–178.
4 S. Chen, A. Walsh, X.-G. Gong and S.-H. Wei, *Adv. Mater.*, 2013, **25**, 1522–1539.
5 S. Chen, L.-W. Wang, A. Walsh, X. G. Gong and S.-H. Wei, *Appl. Phys. Lett.*, 2012, **101**, 223901.
6 A. J. Jackson and A. Walsh, *J. Mater. Chem. A*, 2014, **2**, 7829–7836.
7 B. Jandeleit, D. J. Schaefer, T. S. Powers, H. W. Turner and W. H. Weinberg, *Angew. Chem., Int. Ed.*, 1999, **38**, 2494–2532.

 

8 T. Kato, H. Hiroi, N. Sakai, S. Muraoka and H. Sugimoto, *Proc. 27th Eur. Photovolt. Sol. Energy Conf. Exhib.*, 2012, pp. 2236–2239.

9 Y. S. Lee, T. Gershon, O. Gunawan, T. K. Todorov, T. Gokmen, Y. Virgus and S. Guha, *Adv. Energy Mater.*, 2015, **5**, DOI: 10.1002/aenm.201401372.

10 J. Kim, H. Hiroi, T. K. Todorov, O. Gunawan, M. Kuwahara, T. Gokmen, D. Nair, M. Hopstaken, B. Shin, Y. S. Lee, W. Wang, H. Sugimoto and D. B. Mitzi, *Adv. Mater.*, 2014, **26**, 7427–7431.

11 S. Oueslati, G. Brammertz, M. Buffière, H. ElAnzeery, O. Touayar, C. Köble, J. Bekaert, M. Meuris and J. Poortmans, *Thin Solid Films*, 2015, **582**, 224–228.

12 I. Repins, C. Beall, N. Vora, C. DeHart, D. Kuciauskas, P. Dippo, B. To, J. Mann, W.-C. Hsu, A. Goodrich and R. Noufi, *Sol. Energy Mater. Sol. Cells*, 2012, **101**, 154–159.

13 A. Fairbrother, X. Fontané, V. Izquierdo-Roca, M. Placidi, D. Sylla, M. Espindola-Rodriguez, S. López-Mariño, F. A. Pulgarín, O. Vigil-Galán, A. Pérez-Rodríguez and E. Saucedo, *Prog. Photovoltaics Res. Appl.*, 2014, **22**, 479–487.

14 G. Teeter, H. Du, J. E. Leisch, M. Young, F. Yan, S. W. Johnston, P. Dippo, D. Kuciauskas, M. J. Romero, P. Newhouse, S. E. Asher and D. S. Ginley, in *2010 35th IEEE Photovoltaic Specialists Conference (PVSC)*, 2010, pp. 000650–000655.

15 H. Du, F. Yan, M. Young, B. To, C.-S. Jiang, P. Dippo, D. Kuciauskas, Z. Chi, E. A. Lund, C. Hancock, W. M. H. Oo, M. A. Scarpulla and G. Teeter, *J. Appl. Phys.*, 2014, **115**, 173502.

16 E. A. Lund, H. Du, W. M. H. Oo, G. Teeter and M. A. Scarpulla, *J. Appl. Phys.*, 2014, **115**, 173503.

17 A. D. Collord, H. Xin and H. W. Hillhouse, *IEEE Journal of Photovoltaics*, 2014, 1–11.

18 W. Wang, M. T. Winkler, O. Gunawan, T. Gokmen, T. K. Todorov, Y. Zhu and D. B. Mitzi, *Adv. Energy Mater.*, 2014, **4**, 1301465.

19 H. Sugimoto, C. Liao, H. Hiroi, N. Sakai and T. Kato, in *Photovoltaic Specialists Conference (PVSC), 2013 IEEE 39th*, 2013, pp. 3208–3211.

20 M. Dimitrievska, A. Fairbrother, A. Pérez-Rodríguez, E. Saucedo and V. Izquierdo-Roca, *Acta Mater.*, 2014, **70**, 272–280.

21 M. Dimitrievska, A. Fairbrother, E. Saucedo, A. Perez-Rodriguez and V. Izquierdo-Roca, *Appl. Phys. Lett.*, 2015, **106**, 073903.

22 M. Dimitrievska, A. Fairbrother, V. Izquierdo-Roca, A. Perez-Rodriguez and E. Saucedo, in *Photovoltaic Specialist Conference (PVSC), 2014 IEEE 40th*, 2014, pp. 2307–2309.

23 M. Neuschitzer, Y. Sanchez, S. López-Marino, H. Xie, A. Fairbrother, M. Placidi, S. Haass, V. Izquierdo-Roca, A. Pérez-Rodríguez and E. Saucedo, *Prog. Photovoltaics Res. Appl.*, 2015, DOI: 10.1002/pip.2589.

24 I. D. Olekseyuk, I. V. Dudchak and L. V. Piskach, *J. Alloys Compd.*, 2004, **368**, 135–143.

25 A. Lafond, L. Choubrac, C. Guillot-Deudon, P. Deniard and S. Jobic, *Z. Anorg. Allg. Chem.*, 2012, **638**, 2571–2577.

26 C. Insignares-Cuello, X. Fontané, Y. Sánchez-González, M. Placidi, C. Broussillou, J. López-García, E. Saucedo, V. Bermúdez, A. Pérez-Rodríguez and V. Izquierdo-Roca, *Phys. Status Solidi A*, 2014, **212**, 56–60.

27 G. Brammertz, M. Buffière, Y. Mevel, Y. Ren, A. E. Zaghi, N. Lenaers, Y. Mols, C. Koeble, J. Vleugels, M. Meuris and J. Poortmans, *Appl. Phys. Lett.*, 2013, **102**, 013902.

28 B. Shin, Y. Zhu, N. A. Bojarczuk, S. Jay Chey and S. Guha, *Appl. Phys. Lett.*, 2012, **101**, 053903.

29 S. Siebentritt, *Thin Solid Films*, 2013, **535**, 1–4.

# Electronic Supplementary Information

## Compositional paradigms in multinary compound systems for photovoltaic applications: A case study of kesterites

Andrew Fairbrother, Mirjana Dimitrievska, Yudania Sánchez, Victor Izquierdo-Roca, Alejandro Pérez-Rodríguez, Edgardo Saucedo*

This Electronic Supplementary Information contains additional data about the experimental methods, composition, bandgap, and compositional dependence of optoelectronic properties in $Cu_2ZnSnSe_4$-based solar cells presented in the main text. Specifically, additional compositional maps and the dependence of optoelectronic properties on the commonly reported cationic ratios of Cu/(Zn+Sn) and Zn/Sn is shown. Even though these ratios are more commonly used in describing the composition of kesterite materials, they are less useful in predicting the device performance of devices presented in this work. Because of their common usage they are included here as supplemental information. Some of the figures are directly complementary to Figures 1 and 2 in the main text.

Compositionally graded CZTSe films were prepared by selenization of metallic stack precursors. The DC-magnetron sputtering system (Alliance Ac450) has three off-center sputtering targets, and the substrate is typically rotated during deposition in order to deposit a uniform film. However, to prepare the compositionally graded films, the substrate (10x10 $cm^2$ Mo-coated soda-lime glass) was not rotated during the sequential deposition of Sn, Cu, and Zn. The resulting Sn/Cu/Zn precursor stack contains a 100-500 nm layer of each metal, depending on the distance of each part of the substrate from the sputter target during deposition, and is then cut into a 5x5 $cm^2$ sample, taking into account the compositional range of interest. For this study Cu-poor (Cu/(Zn+Sn)<1) and Zn-rich (Zn/Sn>1) compositions were of greatest interest because they correspond to conditions hereto required for the highest efficiency devices, though overlap into stoichiometric, Cu-rich and Zn-poor regions were also investigated. The precursor film is then placed into a graphite box containing elemental Sn (5 mg) and Se (200 mg). The tin acts to minimize Sn-loss from the film during annealing (in the form of $SnSe_2$), and the selenium is to convert the Cu-Zn-Sn stack into $Cu_2ZnSnSe_4$. The graphite box is a semi-closed system which maintains a uniform atmosphere and temperature inside of the container. Annealing took place in a tubular furnace in a two-step process, first for 30 minutes at 450 °C under flowing Ar with a background pressure of 1 mbar, and then for 15 minutes at 550 °C under a constant 1 bar Ar pressure.

Devices were made out of the graded CZTSe film by formation of a CdS buffer layer by chemical bath deposition, and then pulsed DC-magnetron sputtering deposition (Alliance CT100) of a ZnO and ZnO:Al transparent conducting oxide layer. The completed sample (5x5 $cm^2$) was then mechanically scribed into nearly 200 cells with an area of 3x3 $mm^2$. In this way, the cells were isolated into regions of relatively constant composition with which to correlate the optoelectronic properties. The sample was then submitted to a soft thermal annealing at 200 °C in air before measuring optoelectronic properties [ref. 23 in main paper]. While data for only one 5x5 $cm^2$ solar cell sample is presented, another has been prepared, showing the same compositional dependence of optoelectronic properties.

X-ray fluorescence spectroscopy (Fischerscope XVD) mapping measurements were used to determine the composition of the sample before and after annealing, and was previously calibrated to standard samples measured by inductively coupled plasma optical emission spectroscopy (ICP-OES). Raman scattering spectroscopy was used to characterize not only the CZTSe phase, but also detect secondary phases. This was done using a Horiba Jobin Yvon systems LabRam HR800 and T64000 systems under 532 nm and 458 nm excitation conditions respectively. Illuminated AM1.5 current-voltage characteristics were measured for each cell (ABET3000 Solar Simulator), as was external quantum efficiency (Bentham PVE300 characterization system).

In Figure S1 the compositional map of the graded kesterite film with ratios Cu/(Zn+Sn) and Zn/Sn is shown, this is the same sample presented in Figure 1 of the main text which shows the ratios of Cu/Zn and Cu/Sn.

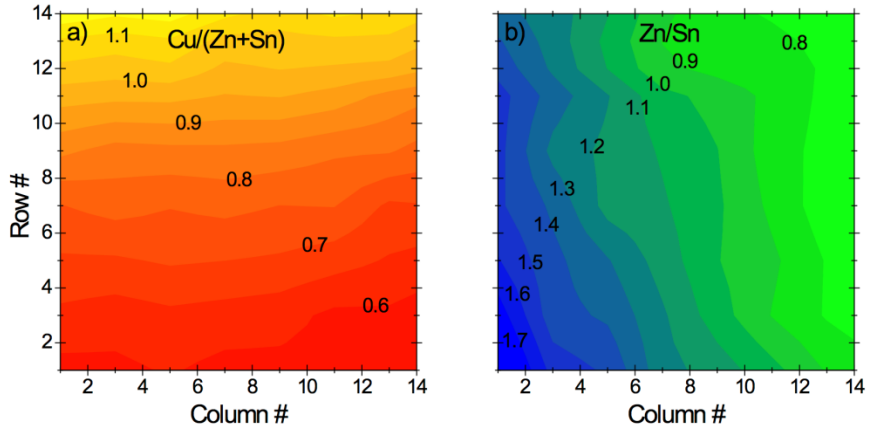


Figure S1. Compositional mapping of the ratios Cu/(Zn+Sn) (left) and Zn/Sn (right) of a 5x5 $cm^2$ graded kesterite film; each [column,row] corresponds to one 3x3 $mm^2$ cell.

In addition to power conversion efficiency, open circuit voltage, and short circuit current, another important optoelectronic property is the fill factor (FF), which it is found to have a similar dependence on the cation composition as the $V_{OC}$. This is shown in Figure S2, presented with dependence on Cu/Zn and Cu/Sn as in Figure 2 in the main text, and has a maximum value of 62%, which is also the highest efficiency and $V_{OC}$ cell.

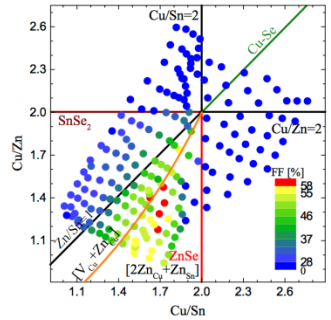


Figure S2. Dependence of FF on Cu/Zn and Cu/Sn for a compositionally graded CZTSe solar cell; lines indicate expected secondary phases or defect clusters for a given region, and stoichiometric cation ratios.

Figure S3 shows the same data as presented in Figure 2 in the main text, but with different cation ratios. It shows the dependence of optoelectronic properties (efficiency, $V_{OC}$, $J_{SC}$, and FF) on the ratios of Cu/(Zn+Sn) and Zn/Sn. The trends correspond well with reports on the high efficiency device, namely that the range of Cu/(Zn+Sn) = 0.7-0.9 and Zn/Sn = 1.1-1.4 is ideal for high efficiency devices. However, Cu/Sn is found to be a much stronger indicator of device properties (specifically efficiency, $V_{OC}$ and FF), as discussed in the main text. $J_{SC}$ is the only main property which does correlate strongly with the ratio of Cu/Sn, and in this case the ratio of Zn/Sn has the narrowest range for the highest values (1.1-1.3).

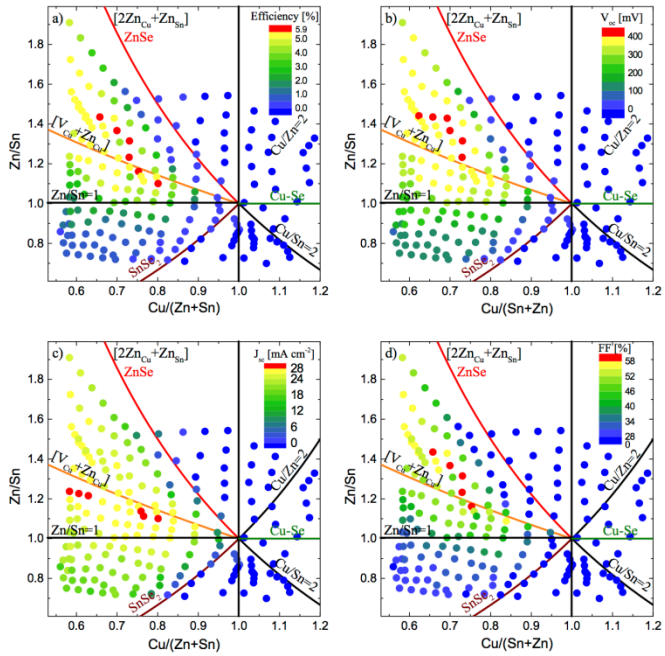


Figure S3. Dependence of optoelectronic properties on composition – efficiency (a), $V_{OC}$ (b), $J_{SC}$ (c), and FF (d) – for Cu/(Zn+Sn) vs. Zn/Sn for a compositionally graded CZTSe solar cell; lines indicate expected secondary phases or defect clusters for a given region, and stoichiometric ratios.

External quantum efficiency was measured in order to estimate the bandgap of each cell by extrapolation of the high wavelength cut-off region. Absorber bandgap has a strong influence on the optoelectronic properties of a device, as exemplified by changes in anion composition of $Cu_2ZnSn(S,Se)_4$ solid-solutions as light absorbers for solar cells. For these materials low bandgap selenium-rich devices have substantially lower $V_{OC}$ and higher $J_{SC}$ compared to high bandgap sulfur-rich devices. Changes in the cation composition have also been shown to influence the bandgap of kesterite compounds, though on a smaller scale, thus one may expect changes in the bandgap from differences in the cation composition to play a similar role. In fact, this is not found to be the case, as shown in Figure S4 which shows the dependence of the estimated bandgap on $V_{OC}$ and $J_{SC}$. The majority of the high efficiency (>5%) cells have bandgaps in the range of 0.88-0.92 eV. There is a spread of bandgap values in the high $V_{OC}$ and high $J_{SC}$ regions, and it is clear that the highest bandgap cells do not necessarily have the highest $V_{OC}$, nor do the lowest bandgap cells have the highest $J_{SC}$. Thus it can be said that changes in the bandgap alone are not responsible for the optimization of these parameters under different compositions, but secondary phases and defect clusters must also be taken into account.

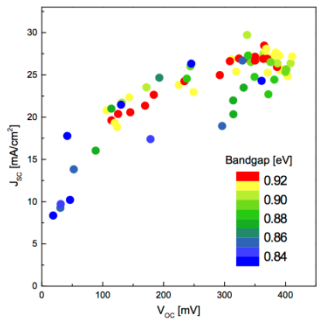


Figure S4. Influence of EQE estimated bandgap on $V_{OC}$ and $J_{SC}$; contrary to expectation, the highest bandgap cells do not have the highest $V_{OC}$, nor do the lower bandgap cells have the highest $J_{SC}$.

APPLIED PHYSICS LETTERS **106**, 073903 (2015)

# Influence of compositionally induced defects on the vibrational properties of device grade $Cu_2ZnSnSe_4$ absorbers for kesterite based solar cells

Mirjana Dimitrievska,[1] Andrew Fairbrother,[1] Edgardo Saucedo,[1] Alejandro Pérez-Rodríguez,[1,2] and Victor Izquierdo-Roca[1,a)]
[1]*Catalonia Institute for Energy Research (IREC), Jardins de les Dones de Negre 1, 08930 Sant Adrià de Besòs, Spain*
[2]*IN2UB, Universitat de Barcelona, C. Martí Franquès 1, 08028 Barcelona, Spain*

(Received 11 January 2015; accepted 9 February 2015; published online 17 February 2015)

This work presents a detailed analysis of the impact of compositionally induced defects on the vibrational properties of $Cu_2ZnSnSe_4$ absorbers for kesterite based solar cells. Systematic changes in the intensity of the E and B modes located around the 170, 220, and 250 $cm^{-1}$ frequency regions, which involve mostly cation vibrations, were observed and analyzed in relation to the occurrence of different kinds of defect clusters involving $V_{Cu}$, $Zn_{Cu}$, $Zn_{Sn}$, $Cu_{Zn}$, and $Sn_{Zn}$ point defects. Additional changes are also interpreted in terms of the appearance of SnSe, ZnSe, and CuSe-like contributions at the 185 and 250 $cm^{-1}$ spectral regions, respectively. The sensitivity of the Raman measurements to the presence of these kinds of defects corroborates the potential of Raman scattering for point defect assessment in these systems. © *2015 AIP Publishing LLC*.
[http://dx.doi.org/10.1063/1.4913262]

Kesterite semiconductors such as $Cu_2ZnSnSe_4$ (CZTSe) are drawing attention because of their ideal optical properties for photovoltaic applications, especially as light-absorbers constituted of earth-abundant elements for development of sustainable thin film photovoltaic technologies. Though relatively high energy conversion efficiencies have already been reached for these materials,[1] still little is known about the nature of defects in these compounds. Kesterites, as quaternary compounds, provide ample opportunities for material design; however, this also results in a higher probability for formation of intrinsic defects. Defect concentration is expected to influence the optoelectronic properties of these materials, therefore a better understanding is crucial for improvement of CZTSe-based solar cells. Because of the limited knowledge about defects, many experimental observations on behavior of these materials cannot be fully understood. For example, why the highest efficiency CZTSe solar cells are produced within a narrow interval of Cu-poor and Zn-rich compositions,[2] or why stoichiometric films have better *p*-type conductivity than non-stoichiometric ones.[3]

Theoretical simulations through first principle calculations[3–5] have given much needed insights on phase stability and defect formation in these materials, but experimental confirmation of these results and identification of different types of defects is still notably lacking. One possible technique that can help in resolving this issue is Raman spectroscopy, which is extremely sensitive to structural disorder, in this case defined as any kind of modification of the crystalline structure of the material. This includes point defects, such as vacancies, interstitials, and anti-sites, and other crystalline defects, like dislocations or grain boundaries. Presence of defects can lead to several types of changes in the Raman spectra, depending on their type and concentration.

a)Email: vizquierdo@irec.cat

Effects in the Raman spectra caused by presence of a high concentration of defects are usually related to changes in frequency, shape, and intensity of the main Raman active vibrational modes. For example, in kesterite $Cu_2ZnSnS_4$, asymmetry in the shape of the low frequency region of the main A modes has been observed, which is attributed to phonon confinement effects arising from loss of translational symmetry in the crystal caused by a high density of defects.[6] The extreme of this situation is an amorphous material, where lack of long-range order leads to a Raman spectrum that reflects the phonon density of states and wave vector selection rules no longer apply. In both cases, changes in the Raman spectra could be explained by activation of non-center phonons due to relaxation of the quasicrystalline momentum conversion law, which is caused when translational symmetry of the crystal lattice is broken.

In contrast, the presence of a small amount of defects usually does not induce big changes in the Raman spectra.[7] Since crystal symmetry is mostly preserved in this case, Raman selection rules are also preserved, meaning that no changes in the frequencies of Raman active modes are expected. For this kind of behavior, three possible changes can occur in Raman spectra due to defects:

(1) Occurrence of defects in a crystalline material may cause local vibrational modes, which lead to the presence of additional, usually rather small features in the Raman spectra. Impurities could lead to these effects.[8]
(2) Presence of defects leads to a reduction of phonon lifetime, leading to a symmetric broadening of the Raman peaks, as phonon lifetime is inversely proportional to the natural line-width of the Raman peaks.[9,10]
(3) Changes in the intensity of the Raman peaks can occur because of changes in the chemical bonds among the atoms in the material. In some cases, defects could lead to breakage of certain bonds, while in others they can induce formation of new ones. This implies changes in

 

the values of elements of the polarizability tensors related to vibrational modes involving these bonds, which in turn leads to changes in intensity of the corresponding peaks.[11]

In this framework, this work presents a detailed analysis of the impact of different kinds of compositionally induced defects in the Raman spectra from device-grade CZTSe absorbers (maximum efficiency 6.9%). Presence of different defect types is induced by changes in the processing composition of the CZTSe film in a sample with about 200 solar cells, each cell with an incremental change in the absorber composition. Analysis of the optoelectronic properties of the solar cells corroborates the strong impact of these defects on the device performance. The evaluation of vibrational properties of the absorbers in the cells has led to the observation of a correlation among the intensity ratio of different Raman bands and different types of defects. This analysis achieves a deeper understanding of the nature of the vibrations involved in the different peaks from CZTSe Raman spectra and provides experimental procedures for Raman scattering assessment of the presence of different kinds of defects with strong impact on the optoelectronic properties of these solar cell absorbers.

For the present study, a CZTSe thin film with a lateral composition gradient (Cu/(Zn + Sn) from 0.55 to 1.20 and Zn/Sn from 0.70 to 1.90) was prepared by selenization of a Cu-Zn-Sn precursor film deposited by DC-magnetron sputtering.[12] The film was made into solar cell devices with a CdS/ZnO/ZnO:Al window layer and then mechanically scribed to form ~200 cells $3 \times 3\,mm^2$ in size, isolating each solar cell and dividing the graded film into small regions of relatively constant composition with which to correlate material and device properties. J-V characterization was made with an AAA Abet 3000 Solar Simulator, while compositional characterization of film was done by X-ray fluorescence spectroscopy (Fischerscope XVD). Raman scattering measurements were performed with 532.0 nm excitation using a LabRam HR800-UV and 457.9 nm excitation a with T64000 Horiba-Jobin Yvon spectrometers.[13] All Raman spectra were acquired after the fabrication of the solar cell devices from which the CdS/ZnO/ZnO:Al window layer was removed using a dilute HCl solution.

Figure 1 shows a pseudo-ternary phase diagram of $Cu_2Se$-ZnSe-$SnSe_2$ showing device efficiency with dependence on composition. Solid lines indicate the most expected secondary phases ($Cu_2Se$, ZnSe, and $SnSe_2$) and charge compensated point defect clusters: the A-type line corresponds to $[Zn_{Cu} + V_{Cu}]$ defect complexes, the B-type line to $[2Zn_{Cu} + Zn_{Sn}]$, the C-type line to $[2Cu_{Zn} + Sn_{Zn}]$, and the D-type line to $[Cu_{Zn} + Cu_i]$.[14] The stoichiometric point is given by the intersection of these lines. For a composition between two secondary phase lines, a mixture of CZTSe and these two secondary phases would be expected, as well as different point defects and defect clusters. Note that D-type defect clusters were not investigated in this work due to lack of cells corresponding to that composition.

A maximum device efficiency of 6.9% is obtained, together with one of the highest reported open circuit voltage values (411 mV) for this compound.[15,16] The maximum values

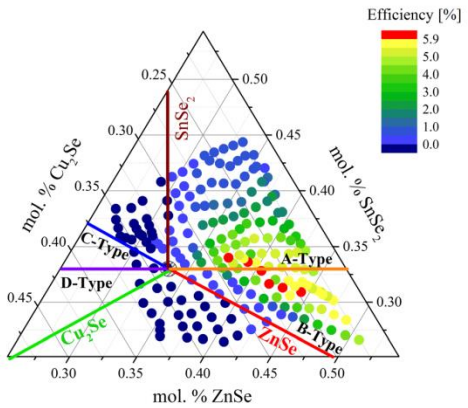


FIG. 1. Compositional dependence of device efficiency shown in a pseudo-ternary $Cu_2Se$-ZnSe-$SnSe_2$ phase diagram for CZTSe solar cells; colored lines indicate expected secondary phases or defect clusters for a given region.

of the optoelectronic properties are achieved for a very narrow interval of compositions around Cu/(Zn + Sn) ≈ 0.74 and Zn/Sn ≈ 1.23, which agree with previously reported results.[2] More detailed investigation of the optoelectronic properties with composition is presented elsewhere.[12]

In order to compare the influence of different defect clusters on the Raman modes, identification of peak positions and their symmetry assignment are necessary. Identification of peak positions of the stoichiometric CZTSe cell (Cu/(Zn + Sn) = 1.01 and Zn/Sn = 1.00) was done by simultaneous fitting of the Raman spectra with Lorentzian curves. The position of each Raman peak with the symmetry assignment is presented in Table I, which also contains theoretical calculations[17] and previously reported experimental data.[18] The symmetry assignment of Raman modes was done by

TABLE I. Frequency (in $cm^{-1}$) of peaks from simultaneous fitting of Raman spectra of the stoichiometric CZTSe thin film and proposed mode symmetry assignment. These are compared with theoretical predictions[17] and reported experimental data.[18]

| This work | | Theoretical predictions | Experimentally reported |
|---|---|---|---|
| RS[a] ($cm^{-1}$) | Sym[b] | RS[c] ($cm^{-1}$) | RS[d] ($cm^{-1}$) |
| 156.9 | B | 156.7 B(TO)/157.3 B(LO) | 157 B(TO/LO) |
| 171.9 | A | 162.8 A | 170 A |
| 174.5 | A | 166.5 A | 174 A |
| 177.4 | B | 175.3 B(TO)/178.7 B(LO) | 178 B(TO/LO) |
| 192.0 | E | 179.0 E(TO)/180.5 E(LO) | 189 E(TO/LO) |
| 196.8 | A | 186.3 A | 196 A |
| 220.6 | E | 199.8 E(TO) | 224 E(TO) |
| 231.9 | E | 202.8 E(LO) | 231E(LO) |
| 234.2 | B | 204.2 B(TO) | 235 B(TO) |
| 239.7 | B | 205.4 B(LO) | 239B(LO) |
| 248.3 | B | 227.1 B(TO) | 245B(TO) |
| 250.8 | B | 228.8 B(LO) | 250 B(LO) |

[a]RS is the Raman shift from this work.
[b]Sym is the symmetry proposed in this work.
[c]RS is the Raman shift reported in Ref. 17.
[d]RS is the Raman shift reported in Ref. 18.

comparing the experimentally obtained frequencies with the reported references as well as applying the rules[13] for the mode behavior to polarization measurements preformed on this sample. It can be concluded that peak positions in Table I are in good agreement with the previous work.

Figures 2(a)–2(c) show the Raman spectra measured on samples that were selected with compositions following the lines corresponding to the A-, B-, and C-type of defect clusters. All Raman peaks observed in the spectra shown in these figures are attributed to the kesterite CZTSe phase, with peak positions in agreement with Table I. Raman characterization of these samples shows that formation of surface Sn-Se secondary phases takes place only in the region corresponding to $Cu/(Zn + Sn) < 0.80$ and $Zn/Sn < 0.95$ and has not been observed on the surface of any of the samples presented in Figure 2. In addition, Cu-Se binary phases have not been observed on the surface of any of the cells in this work. On the other hand, formation of ZnSe surface secondary phases has been observed, mainly in Zn-rich cells, detected with measurements with 457.9 nm excitation, which correspond to resonant excitation conditions for this compound.[19] Nevertheless, comparison of Raman spectra measured with 532 nm excitation from cells with and without ZnSe secondary phases indicates the absence of its Raman contribution in the 250 $cm^{-1}$ spectral region. The low sensitivity of the Raman scattering measurements performed with 532 nm excitation to the presence of ZnSe secondary phases is related to low optical absorption of green photons in this compound, in contrast with very high optical absorption of CZTSe. This is also an indication of the low overall amount of ZnSe formed on the surface of the samples investigated. Accordingly, changes in this spectral region of the Raman spectra measured with 532 nm excitation from samples with different compositions cannot be attributed to the presence of ZnSe, in agreement with the previous work showing Raman analysis before and after ZnSe etching.[20]

Figure 2(a) presents a comparison of Raman spectra for samples corresponding to different compositions when moving along the A-type defect line ($[Zn_{Cu} + V_{Cu}]$) in the direction away from the stoichiometric point. Frequencies of the modes are not affected with this kind of compositional change, which implies that the concentration of defects in this region is not so high as to cause a notable overall distortion of the crystalline lattice. Additionally, no significant changes in the main A mode centered at 196 $cm^{-1}$ are observed. Since this mode is attributed to only anion vibrations,[21] changes in its frequency and peak shape are usually correlated to the crystal quality of the absorber,[6] again confirming that no significant degradation of overall crystal quality of CZTSe is expected for this compositional interval. However, a systematic decrease in relative intensity of peaks around the 170 $cm^{-1}$ spectral region is observed. This region corresponds to two A symmetry modes and two B symmetry modes. Since the A modes correspond to only Se vibrations, no changes in their intensity are expected with changes in cation composition. On the other side, theoretical simulations[21] indicate that B modes in this region correspond mostly to cation vibrations, in particular, to vibrations of Cu/Zn and Cu/Sn atomic planes. Considering that along the A-type defect compositional line, formation of $[Zn_{Cu} + V_{Cu}]$ defect clusters is promoted, it can be concluded that Cu/Zn and Cu/Sn atomic planes are going to be affected: with an increase in concentration of $[Zn_{Cu} + V_{Cu}]$ defects clusters, there will be a decrease in the number of Cu/Zn and Cu/Sn vibration units. This is consistent with a decrease in overall relative intensity of the B modes, in agreement with the experimental observations. This is also consistent with the fitting of the spectra that can be done keeping a constant Lorentzian contribution for the A modes in this spectral region.

Figure 2(b) shows a comparison of Raman spectra measured for samples along the B-type defect line ($[2Zn_{Cu} +$

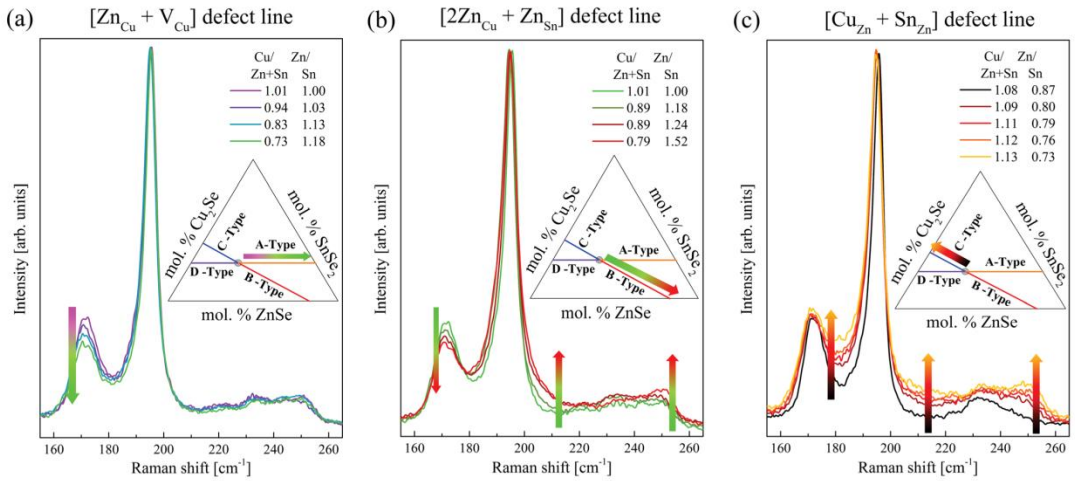


FIG. 2. Comparison of Raman spectra measured from samples with compositions corresponding to different defect lines: (a) A-type, (b) B-type, and (c) C-type. All Raman spectra are measured with 532 nm excitation wavelength. The arrows indicate changes in the intensity of the modes with the change in the composition in the directions shown on the ternary diagram.

$Zn_{Sn}$]), again moving away from the stoichiometric point. As in the previous case, the frequency of the main A modes is not affected by this kind of compositional change. There are, however, strong changes in the relative intensity of the peaks around the 170, 215, and 250 $cm^{-1}$ frequency regions. Two defect types, $Zn_{Cu}$ and $Zn_{Sn}$, are expected in this compositional range. A decrease in Cu content and increase in Zn content, which promotes $Zn_{Cu}$ defect formation, are likely responsible for the decrease in relative intensity of the B symmetry modes around 170 $cm^{-1}$, as explained in the previous case of A-type defects clusters. Additionally, increase in Zn content is also accompanied by an increase in the relative intensity of the spectral contribution at the 250 $cm^{-1}$ frequency region. This can be explained by taking into account the increase in density of $Zn_{Cu}$ anti-sites, which leads to an increase in the number of Zn-Se bonds and, consequently, to an enrichment in the amount of Zn atoms surrounding Se anions in the lattice. This likely leads to the appearance of a ZnSe-like contribution that is expected at 250 $cm^{-1}$.[22] An additional contribution to the intensity increase of this region can also be related to the increase in density of $Zn_{Sn}$ anti-sites, which leads to transformation of the -Sn-Se-Cu-Se-Sn- vibrational chains into -$Zn_{Sn}$-Se-Cu-Se-$Zn_{Sn}$-, for which vibrations are also expected in the 250 $cm^{-1}$ region,[21] experimentally identified as a B mode. According to the theoretical analysis,[21] -Sn-Se-Cu-Se-Sn- vibrations are expected at a frequency of 211 $cm^{-1}$. The proximity of this value with that of the E symmetry CZTSe mode experimentally observed at 220 $cm^{-1}$ leads to the identification of this mode with the vibrations of the -Sn-Se-Cu-Se-Sn- chains. The expected decrease in the relative intensity of this peak with the increase of $Zn_{Sn}$ anti-sites is likely compensated by symmetric broadening of the main A mode at 196 $cm^{-1}$, due to reduction in the phonon lifetime occurring at higher defect densities. This would lead to an overall increase in the relative intensity of this spectral contribution, in agreement with experimental observations shown in Figure 2(b).

Figure 2(c) presents the comparison of the Raman spectra measured from samples with compositions corresponding to the C-type defect line ([$2Cu_{Zn}$ + $Sn_{Zn}$]) when moving away from the stoichiometric point. As in the other cases, the frequency of the main A modes is unaffected by this compositional change. The most pronounced changes in the relative intensity of modes are observed in the frequency regions around 185, 220, and 250 $cm^{-1}$. As this is a compositional region with a high probability of formation of [$2Cu_{Zn}$ + $Sn_{Zn}$] defect clusters, increase in the relative intensity of the spectral contributions around the 185 and 220 $cm^{-1}$ regions could be related to the increase in density of $Sn_{Zn}$ anti-sites. Increase in the density of $Sn_{Zn}$ anti-sites would lead to an exchange of Zn by Sn in the -Cu-Se-Zn-Se-Cu- vibrational chains, equivalent to the -Zn-Se-Cu-Se-Zn-chains with vibrations identified as B symmetry mode at 250 $cm^{-1}$, thus becoming -Cu-Se-$Sn_{Zn}$-Se-Cu-, that are equivalent to the -Sn-Se-Cu-Se-Sn- chains with vibrations identified as E mode at the 220 $cm^{-1}$ frequency region. This would explain the increase in the contribution at 220 $cm^{-1}$. In addition, the changes of the spectra around the 185 $cm^{-1}$ frequency region can also be explained by taking into account the expected increase in the number of Sn-Se bonds, which would lead to the appearance of a SnSe-like peak reported to be in this region.[23] On the other hand, the decrease expected in the 250 $cm^{-1}$ region because of the conversion of the B symmetry mode vibrations to the E symmetry one at 220 $cm^{-1}$ is likely compensated by the increase in density of $Cu_{Zn}$ anti-sites. This would lead to a corresponding increase of Cu-Se bonds, with a subsequent enrichment of the amount of Cu atoms surrounding the Se anions in the lattice. This likely leads to the appearance of a CuSe-like contribution, as CuSe has a main vibrational peak at 260 $cm^{-1}$.[24] However, differences in the local masses around the Se atoms likely lead to a red shift in the observed frequency of this contribution to the 250 $cm^{-1}$ spectral region. Finally, it is interesting to remark that the absence of changes in the spectral region around 170 $cm^{-1}$ in Figure 2(c) agrees with the assignment of the changes observed in this spectral region in Figures 2(a) and 2(b) to the occurrence of $Zn_{Cu}$ and $V_{Cu}$ defects, because the formation of these defects is inhibited for C-type absorbers.

In conclusion, changes observed in Raman spectra from samples grown with varied compositions which favor the formation of different kinds of defects can be explained by the following impact of $V_{Cu}$, $Zn_{Cu}$, $Zn_{Sn}$, $Cu_{Zn}$, and $Sn_{Zn}$ point defects:

(1) Presence of $V_{Cu}$ and $Zn_{Cu}$ point defects induces a decrease in intensity of the B symmetry modes around 170 $cm^{-1}$ related to the vibrations in Cu/Zn and Cu/Sn planes (i.e., a decrease of Cu/Zn and Cu/Sn vibrational units).
(2) Presence of $Zn_{Sn}$ point defects lead to appearance of an additional ZnSe-like contribution at 250 $cm^{-1}$ and conversion from E symmetry modes at the 220 $cm^{-1}$ spectral region to B symmetry modes at the 250 $cm^{-1}$ spectral region.
(3) Presence of $Cu_{Zn}$ point defects lead to appearance of an additional CuSe-like contribution at the 250 $cm^{-1}$ frequency region.
(4) Presence of $Sn_{Zn}$ point defects lead to appearance of an additional SnSe-like contribution around the 185 $cm^{-1}$ frequency region and to conversion of B symmetry vibrational modes at the 250 $cm^{-1}$ spectral region into E symmetry vibrational modes at the 220 $cm^{-1}$ frequency region.

These results confirm the potential of Raman scattering for advanced characterization of absorbers in kesterite-based solar cells and corroborate the sensitivity of the Raman spectra from CZTSe device grade layers to the different kinds of point defects that are relevant for performance of solar cells. Systematic analysis of different spectral regions related to vibration of the different cations in the crystal gives a way for analysis of the processes in terms of point defect formation, which is especially relevant for further optimization of these technologies.

The research leading to these results has received funding from the People Program (Marie Curie Actions) of the European Union's Seventh Framework Program FP7/2007-2013/under REA Grant Agreement No. 316488 (KESTCELLS). Authors from IREC and $IN^2UB$ belong to

the M-2E (Electronic Materials for Energy) Consolidated Research Group and the XaRMAE Network of Excellence on Materials for Energy of the "Generalitat de Catalunya." E.S. thanks the Government of Spain for the "Ramon y Cajal" fellowship (RYC-2011-09212) and V.I.-R. for the "Juan de la Cierva" fellowship (JCI-2011-10782) and A.F. thanks the Spanish Government for the FPU Fellowship (FPU12/05508).

[1]W. Wang, M. T. Winkler, O. Gunawan, T. Gokmen, T. K. Todorov, Y. Zhu, and D. B. Mitzi, Adv. Energy Mater. **4**, 1301465 (2014).
[2]H. Katagiri, Thin Solid Films **480–481**, 426 (2005).
[3]S. Chen, A. Walsh, X.-G. Gong, and S.-H. Wei, Adv. Mater. **25**, 1522 (2013).
[4]S. Chen, X. G. Gong, A. Walsh, and S.-H. Wei, Appl. Phys. Lett. **96**, 021902 (2010).
[5]S. Chen, J.-H. Yang, X. G. Gong, A. Walsh, and S.-H. Wei, Phys. Rev. B **81**, 245204 (2010).
[6]M. Dimitrievska, A. Fairbrother, A. Pérez-Rodríguez, E. Saucedo, and V. Izquierdo-Roca, Acta Mater. **70**, 272 (2014).
[7]U. Rau, D. Abou-Ras, and T. Kirchartz, *Advanced Characterization Techniques for Thin Film Solar Cells* (John Wiley & Sons, 2011).
[8]P. Panpech, S. Vijarnwannaluk, S. Sanorpim, W. Ono, F. Nakajima, R. Katayama, and K. Onabe, J. Cryst. Growth **298**, 107 (2007).
[9]N. Kazemi-Zanjani, E. Kergrene, L. Liu, T.-K. Sham, and F. Lagugné-Labarthet, Sensors **13**, 12744 (2013).
[10]T. B. Ivetić, M. R. Dimitrievska, N. L. Finčur, L. R. Đačanin, I. O. Gúth, B. F. Abramović, and S. R. Lukić-Petrović, Ceram. Int. **40**, 1545 (2014).
[11]L. G. Canc¸ado, A. Jorio, E. H. M. Ferreira, F. Stavale, C. A. Achete, R. B. Capaz, M. V. O. Moutinho, A. Lombardo, T. S. Kulmala, and A. C. Ferrari, Nano Lett. **11**, 3190 (2011).
[12]M. Dimitrievska, A. Fairbrother, V. Izquierdo-Roca, A. Perez-Rodriguez, and E. Saucedo, in *40th IEEE Photovoltaic Specialist Conference (PVSC)* (2014), pp. 2307–2309.
[13]M. Dimitrievska, A. Fairbrother, X. Fontané, T. Jawhari, V. Izquierdo-Roca, E. Saucedo, and A. Pérez-Rodríguez, Appl. Phys. Lett. **104**, 021901 (2014).
[14]A. Lafond, L. Choubrac, C. Guillot-Deudon, P. Deniard, and S. Jobic, Z. Anorg. Allg. Chem. **638**, 2571 (2012).
[15]Y. Sanchez, M. Neuschitzer, M. Dimitrievska, M. Espindola-Rodriguez, J. Lopez-Garcia, V. Izquierdo-Roca, O. Vigil-Galan, and E. Saucedo, in *40th IEEE Photovoltaic Specialist Conference* (*PVSC*) (2014), pp. 0417–0420.
[16]Y. S. Lee, T. Gershon, O. Gunawan, T. K. Todorov, T. Gokmen, Y. Virgus, and S. Guha, "$Cu_2ZnSnSe_4$ thin-film solar cells by thermal co-evaporation with 11.6% efficiency and improved minority carrier diffusion length," Adv. Energy Mater. (published online, 2014).
[17]A. Khare, B. Himmetoglu, M. Cococcioni, and E. S. Aydil, J. Appl. Phys. **111**, 123704 (2012).
[18]M. Guc, S. Levcenko, V. Izquierdo-Roca, X. Fontané, E. Arushanov, and A. Pérez-Rodríguez, J. Appl. Phys. **114**, 193514 (2013).
[19]A. Fairbrother, X. Fontané, V. Izquierdo-Roca, M. Placidi, D. Sylla, M. Espindola-Rodriguez, S. López-Mariño, F. A. Pulgarín, O. Vigil-Galán, A. Pérez-Rodríguez, and E. Saucedo, Prog. Photovoltaics **22**, 479 (2014).
[20]S. López-Marino, Y. Sánchez, M. Placidi, A. Fairbrother, M. Espindola-Rodríguez, X. Fontané, V. Izquierdo-Roca, J. López-García, L. Calvo-Barrio, A. Pérez-Rodríguez, and E. Saucedo, Chem. - Eur. J. **19**, 14814 (2013).
[21]N. B. Mortazavi Amiri and A. Postnikov, Phys. Rev. B **82**, 205204 (2010).
[22]A. Redinger, K. Hönes, X. Fontané, V. Izquierdo-Roca, E. Saucedo, N. Valle, A. Pérez-Rodríguez, and S. Siebentritt, Appl. Phys. Lett. **98**, 101907 (2011).
[23]T. Fukunaga, S. Sugai, T. Kinosada, and K. Murase, Solid State Commun. **38**, 1049 (1981).
[24]M. Ishii, K. Shibata, and H. Nozaki, J. Solid State Chem. **105**, 504 (1993).

# Secondary phase and Cu substitutional defect dynamics in kesterite $Cu_2ZnSnSe_4$ solar cells: impact on optoelectronic properties

Mirjana Dimitrievska[1], Andrew Fairbrother[1], Edgardo Saucedo[1], Alejandro Pérez-Rodríguez[1,2], and Victor Izquierdo-Roca[1*]

1 – Catalonia Institute for Energy Research (IREC), Jardins de les Dones de Negre 1, 08930 Sant Adrià de Besòs, Spain

2 – IN2UB, Universitat de Barcelona, C. Martí Franquès 1, 08028 Barcelona, Spain

* contact email: vizquierdo@irec.cat

**Abstract**

Low open circuit voltage ($V_{OC}$) has been recognized as one of the principle limitations in the current generation of kesterite based solar cells. In order to investigate the origin and possible solution for this problem, the influence of point defects and secondary phases on the performance of $Cu_2ZnSnSe_4$ (CZTSe) devices is explored. Compositionally graded CZTSe films have been prepared with nearly 200 solar cells, each with minute changes in cation composition. Systematic structural characterization of these absorbers with Raman spectroscopy and X-ray diffraction is used to detect secondary phases and defect clusters, and their relative concentration is correlated to device properties. The presented results show the experimental evidence of the effect of the Cu-substitutional defects, in particular [$V_{Cu}$ + $Zn_{Cu}$], on the optoelectronic properties, especially $V_{OC}$. It is shown that $V_{OC}$ can be tuned by adjusting composition, and consequently the amount of the [$V_{Cu}$ + $Zn_{Cu}$] defect clusters. Secondary phases are also found to influence device properties, and their effects are dependent on whether they are present in the bulk or surface of the absorber.

**Keywords:** kesterite, defects, secondary phases, $V_{oc}$-deficit, optoelectronic properties, Raman spectroscopy

## 1. Introduction

The presence of point defects in a semiconductor material plays a significant, even dominant role in determining its electronic and optical characteristics, and as such, identifying and understanding their influence on material properties is of critical importance. While monoatomic (Si, Ge) and binary (GaAs, SiC, CdTe) semiconductors have relatively simple and well-known defect structures, both intrinsic and extrinsic,[1–3] there is a growing number of applications for more complex multinary compounds for which these structures are not well understood. Several multinary compounds are being investigated especially for photovoltaic applications, including chalcopyrites[4] $\left(A^{+}B^{3+}X_2^{2-}\right)$ and the related kesterites[5,6] $\left(A_2^{+}B^{2+}C^{4+}X_4^{2-}\right)$, perovskites[7] $\left(A^{2+}B^{4+}X_3^{2-}\right)$, and mohite[8] $\left(A^{2+}B^{4+}X_3^{2-}\right)$. A complicating factor in the application of many of these compounds is the use of off-stoichiometry compositions for the best device performance, which greatly increases the probability of forming secondary phases and point defects.

Kesterite $Cu_2ZnSnSe_4$ (CZTSe) and its related compounds hold particular interest as light absorbers for solar cells due to being composed of earth-abundant elements, with record efficiencies of 11.6%,[9] and even higher (12.6%) for the related $Cu_2ZnSn(S,Se)_4$ material.[10] The highest performing devices are made from kesterites with Cu-poor (Cu/(Zn+Sn) < 1) and Zn-rich (Zn/Sn > 1) compositions. Such conditions have been shown both theoretically and experimentally to enhance the formation of Zn(S,Se), while suppressing formation of Cu-(S,Se) and Cu-Sn-(S,Se) secondary phases.[11,12] Regarding defect formation, the more energetically favorable defect clusters have been calculated to be $[Cu_{Zn} + Zn_{Cu}]$, $[V_{Cu} + Zn_{Cu}]$, $[2Zn_{Cu} + Zn_{Sn}]$, and $[2Cu_{Zn} + Sn_{Zn}]$[13], and the few experimental works on the subject thus far confirm this.[14–16] Aside from their formation, the impact of secondary phases and especially of defects on optoelectronic properties of solar cells is not fully understood. Secondary phases such as binary and ternary Cu-, Zn-, and Sn- sulfides and selenides in the absorbers can reduce the carrier transport and lead to an increased recombination, which in general have detrimental effects on the optoelectronic properties.[6] The influence of point defects is thus far estimated by theoretical studies to affect charge transport properties and modify the band alignment with the n-type buffer layer, which is an important factor in determining the current and voltage which can be extracted from a device.[12,13]

In order to closely examine the influence of point defects and secondary phases on the performance of CZTSe-based solar cells, compositionally graded CZTSe films have been prepared with minute changes in cation composition.[17] Approximately 200 solar cells have been fabricated on a single large sample, each with slight differences in absorber composition covering the range of Cu-poor and Zn-rich compositions used in the highest performance CZTSe-based devices, and extending also to stoichiometric, Cu-rich and Sn-rich compositions. Optoelectronic properties are found to rapidly degrade when moving from the Zn-rich cells to the Cu-rich cells, and in a more gradual trend when moving towards the Sn-rich cells. Systematic structural characterization of the absorbers with Raman spectroscopy and X-ray diffraction (XRD) is used to detect secondary phases and defect clusters, and their relative concentration is correlated to device properties. This has been done by the analysis of the changes of the relative intensity of Raman bands that are sensitive to the presence of these defect clusters.[16] Special emphasis is placed on Cu substitutional defects, namely the charge compensated $[V_{Cu} + Zn_{Cu}]$ cluster, for which a clear effect of the variations in the concentration of this defect cluster on the open circuit voltage ($V_{oc}$) of the devices is observed.

Figure 1 presents pseudo-ternary phase diagrams of $Cu_2Se$-$ZnSe$-$SnSe_2$ with around 200 points showing device efficiency, $V_{OC}$ and short-circuit current ($J_{sc}$) with dependence on composition (fill factor (FF) follows a similar trend as $V_{OC}$, as seen in Figure S1 in Supporting Information). In the figure, solid lines indicate the most expected secondary phases ($Cu_2Se$, $ZnSe$, and $SnSe_2$) and the different kinds (A, B, C, D, E and F) of charge compensated point defect clusters.[16,18] The stoichiometric composition point is given by the intersection of all these lines. This means that for a composition between two of the secondary phase lines, a mixture of CZTSe and these two secondary phases would be expected, as well as different point defects and defect clusters.

A maximum device efficiency of 6.9% is obtained, together with a highest open circuit voltage ($V_{OC}$) values of 411 mV for the devices analyzed in this work.[17] The maximum values of the optoelectronic properties are achieved for a very narrow interval of compositions around Cu/(Zn+Sn) ≈ 0.7, Zn/Sn ≈ 1.2, Cu/Zn ≈ 1.4, and Cu/Sn ≈ 1.6, which is in agreement with previously reported results for high efficiency CZTSe-based solar cells. Furthermore, a deterioration in optoelectronic properties is observed for regions corresponding to compositions Cu/(Zn+Sn) > 0.95 or Zn/Sn < 1.00. In addition, distinct compositional regions corresponding to the maximum open circuit voltage ($V_{oc}$) (Figure 1(b)) and short circuit current ($J_{sc}$) values (Figure 1(c)) have been identified.[17] These regions appear in the phase diagram corresponding to Cu-poor and Zn-rich compositions, where occurrence of $V_{Cu}$, $Zn_{Cu}$ and $Zn_{Sn}$ point defects is expected. A more detailed report about the optoelectronic properties of these devices can be found in Fairbrother et al.[17]

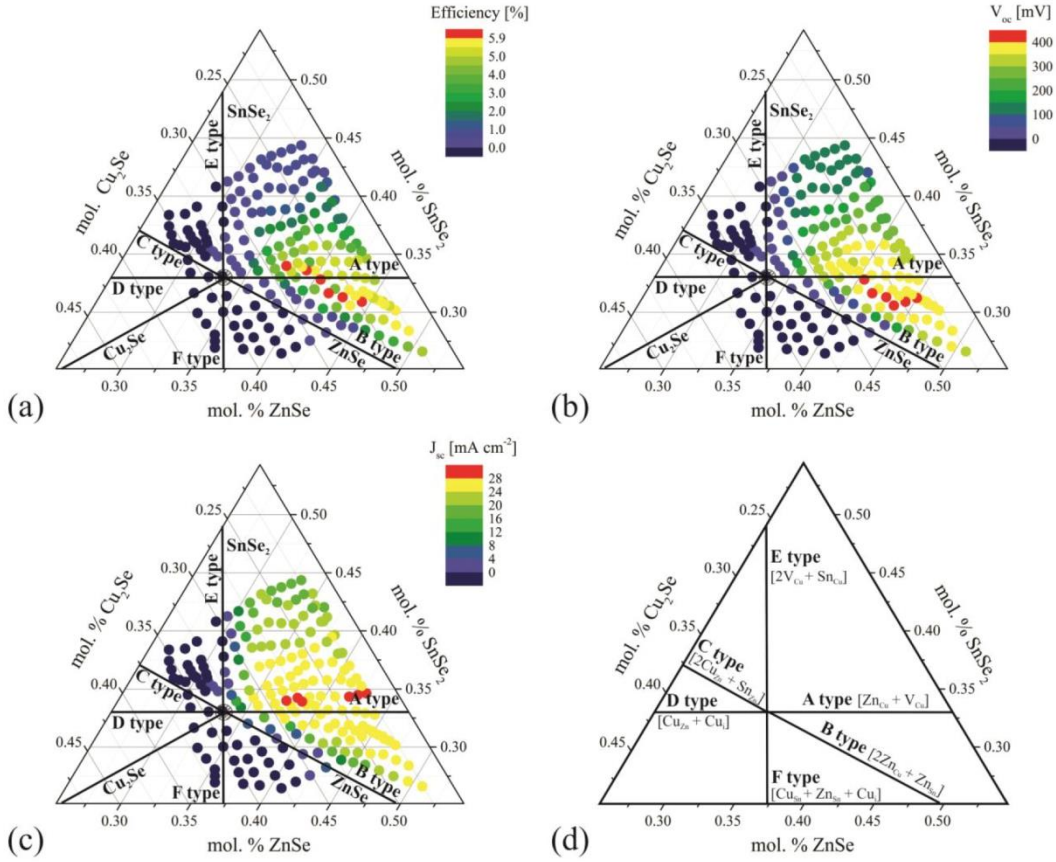


Figure 1. Compositional dependence of device (a) efficiency, (b) $V_{OC}$ and (c) $J_{SC}$ shown in a pseudo-ternary phase diagram of $Cu_2Se$-ZnSe-$SnSe_2$ for compositionally graded CZTSe solar cells; lines indicate expected secondary phases or defect clusters for a given region. (d) Pseudo-ternary phase diagram of $Cu_2Se$-ZnSe-$SnSe_2$ with lines indicating different defect clusters.

In order to obtain a deeper understanding of absorber composition related effects on optoelectronic properties, a systematic study of the appearance of secondary phases and defect clusters has been performed using two characterization techniques: XRD and multi-wavelength excitation Raman spectroscopy. XRD mapping measurements have allowed obtaining a detailed characterization of the absorber layers with the detection of Cu-Se and Sn-Se secondary phases. ZnSe is not readily detectable by this method due to its structural similarities with CZTSe, though it has been shown to form in the bulk of the absorber, especially

for very Zn-rich compositions.[11] Raman spectroscopy mapping measurements with 457.9 nm excitation allowed identification of ZnSe phase on the surface of the samples, while 532.0 nm excitation allowed detection of the surface Cu-Se and Sn-Se phases. The combination of both techniques enables differentiation in the location of secondary phase formation, either on the surface (s) or in the bulk (b) of the absorber.

Figure 2 shows a pseudo-ternary phase diagram of the detected secondary phases (Cu-Se, ZnSe, and Sn-Se) with dependence on the composition of the solar cells. Cu-Se phases are not detected on the surface for any composition, though there are found in the bulk of the absorber for almost all cells with the composition Cu/(Zn+Sn) < 1.00. Sn-Se secondary phases are usually present in the bulk of the absorber for compositions Zn/Sn < 1.20. Very Sn-rich conditions, Zn/Sn < 1.00, give rise to the appearance of Sn-Se secondary phases on the surface of the absorbers. Zn-rich conditions are in most cases followed by the appearance of the surface ZnSe secondary phase. The presence of ZnSe in the bulk is expected to increase with higher Zn content,[11] but this is undetectable with the bulk characterization method utilized in this work (XRD). It is interesting to note that within the sensitivity limits of the techniques utilized, no secondary phases are detected in the compositional region around the stoichiometric point (labeled as "none" in Figure 2).

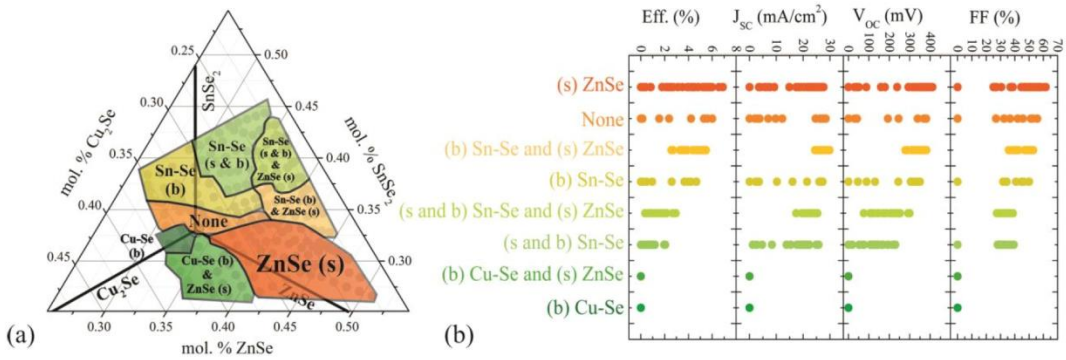


Figure 2. (a) Compositional dependence of detected secondary phases – Cu-Se, ZnSe, and Sn-Se – in surface (s) and bulk (b) absorber regions shown in a psuedo-ternary phase diagram (lines indicate theoretically expected secondary phases). (b) Influence of secondary phases on the optoelectronic properties (efficiency, $J_{SC}$, $V_{OC}$ and FF).

The appearance of secondary phases can be correlated with the performance of the devices, as shown in Figure 2 which presents the dependence of the optoelectronic properties from the presence of the detected phases. Secondary phases have the strongest effect on the maximum achievable $V_{oc}$ and FF, and consequently the efficiency of devices. The effects on $J_{sc}$ are much weaker, except when Cu-Se phases are detected.

For most secondary phases there is a spread of optoelectronic values obtained for the devices, but this analysis will focus on the maximum obtained values for the different secondary phases detected in this work. In all cases the presence of Cu-Se phases result in a non-performing solar cell device. This is expected because of the high conductivity of this phase, which effectively shunts the device.[19] The presence of other secondary phases (ZnSe and Sn-Se) does not a priori result in non-functioning devices, and they have a more nuanced effect on the device performance. Sn-Se phases on the surface of absorber have more detrimental effect on all optoelectronic properties than when they are present only in the bulk of the absorber. This is in agreement with numerical simulations of optoelectronic properties performed by Kanevce et al.[20], which have shown that the impact of the secondary phases is the strongest in the vicinity of the CZTSe/CdS heterointerface, decreases as the secondary phases move away from it, and becomes very low outside of the space charge region. The reduction in the performance of solar cells in the case of surface

Sn-Se is mostly due to the structural and lattice mismatch between the CZTSe and Sn-Se, which creates an interface with high density of defects.[21,22] This then leads to increased recombination at the Sn-Se/CZTSe boundary, which results in the reduction of both the output current and voltage, as observed in Figure 2. These results are further supported by the measurements of the series and shunt resistance (Figure S2 in Supporting Information), which in the case of surface detected Sn-Se, show an abrupt increase and decrease in the values, respectively, when compared to the values of cells with Sn-Se present only in the bulk of the absorber.

In contrast, an enhancement in the maximum optoelectronic performance is observed for the cells in which ZnSe was detected on the surface of the absorber, when compared to ones without any detected ZnSe. Literature reports suggest that ZnSe can have both benign and malignant effects, which explains why there is a spread from 0% to 6.9% devices with the presence of this phase. Typically it is expected that the high band gap, resistive ZnSe phase reduces the performance of the devices by increasing the series resistance and reducing the short circuit current, potentially due to the spike like band gap alignment between the ZnSe and CZTSe phase.[23] On the other side, it has been shown that recombination is suppressed on the ZnSe/CZTSe interface when compared to other heterointerfaces, due to the similar crystal structure and lattice constants of ZnSe and CZTSe.[24] In the case of this study, for the highest performing devices the detrimental effects of ZnSe secondary phase on the optoelectronic properties are suppressed in part due to the small amount of ZnSe present in the surface, and partly due to the beneficial optoelectronic defects present in this compositional region.

Theoretical calculations have revealed that non-stoichiometry conditions in kesterites result in facile formation of self-compensated defect clusters, from which a high population of A type defect clusters ([$V_{Cu}$ + $Zn_{Cu}$]) has shown to be especially beneficial to the performance of solar cells, since they enhance the electron-hole separation in the absorber layer.[13] Experimentally, these facts have yet to be confirmed. In order to better explore the influence of these defects on the optoelectronic properties, a systematic Raman spectroscopy study was performed on the cells in which no secondary phases or only ZnSe was detected using both XRD and Raman spectroscopy techniques (regions labeled as "None" and "ZnSe" in the ternary diagram presented in Figure 2). Raman spectroscopy has shown potential for the defect detection in kesterites as presented in Dimitrievska et al.[16] It is observed that the relative intensity of the broad band at 170 $cm^{-1}$ is inversely proportional to the concentration of [$V_{Cu}$ + $Zn_{Cu}$] defect clusters present in the material.[16,25]

Figure 3(a) shows representative Raman spectra of several kesterite absorbers with different compositions. All Raman peaks present in the spectra are attributed to the kesterite phase, as the ZnSe phase is not detectable with the 532.0 nm laser utilized in the measurements.[16] A clear decrease in the relative intensity of the band at 170 $cm^{-1}$ is observed, and it is associated with the increase in concentration of the [$V_{Cu}$ + $Zn_{Cu}$] defect clusters. Changes in the concentration of [$V_{Cu}$ + $Zn_{Cu}$] defect clusters present in the material can be assessed by analyzing the integral intensity ratio of the defect sensitive band at 170 $cm^{-1}$ ($I_2$) and the peak at 196 $cm^{-1}$ ($I_1$). The Raman peak at 196 $cm^{-1}$ is identified as the dominant A symmetry mode in the kesterite structure, and it corresponds to only Se vibrations in the lattice.[16,25] In general, the only effect that cation defects have on the A mode is the appearance of an asymmetrical broadening at the low frequency side of peak, which is caused by the phonon confinement effects arising from the loss of translational symmetry in the crystal due to the presence of defects.[26] In order to exclude this effect in the analysis of the changes of the defect cluster concentration, the low frequency part of the A mode is excluded in the calculation of the integral intensity $I_1$. In this way, the spectra are normalized, and in principle all changes observed in the intensity ratio $I_2/(I_1 + I_2)$ are mainly due to variations in the concentration of [$V_{Cu}$ + $Zn_{Cu}$] defect clusters.

Dependence of the optoelectronic parameters (energy band gap ($E_g$), $V_{OC}$, and $V_{OC}$ deficit (defined as $E_g$ - $V_{OC}$)) on the variations in the intensity ratio $I_2/(I_1 + I_2)$, related to changes of the concentration of [$V_{Cu}$ + $Zn_{Cu}$] defect clusters, is presented in Figure 3(b). Based on the theoretical calculations performed by Chen et al., it is expected that [$V_{Cu}$ + $Zn_{Cu}$] defect clusters increase the energy band gap, by downshifting the valence band, and upshifting the conduction band.[13] This behavior is experimentally confirmed here, where

a continuous increase in the band gap was observed with the increase in the [$V_{Cu}$ + $Zn_{Cu}$] defect clusters concentration. In contrast, a slightly different behavior than expected is observed for $V_{OC}$. The $V_{OC}$ follows the trend of the band gap up to a certain concentration of [$V_{Cu}$ + $Zn_{Cu}$], when it is maximized, and after which it starts to decrease even for the still increasing band gap. The steady decrease in the $V_{OC}$ for the higher concentrations of [$V_{Cu}$ + $Zn_{Cu}$] is probably due to the increased number of recombinations caused by the large number of defects, and/or increased p-type doping of the absorber due to the large amount of $V_{Cu}$ expected at very Cu-poor conditions. These results demonstrate that the $V_{OC}$ can be tuned by modifying the amount of Cu substitutional defects in the absorber layer.

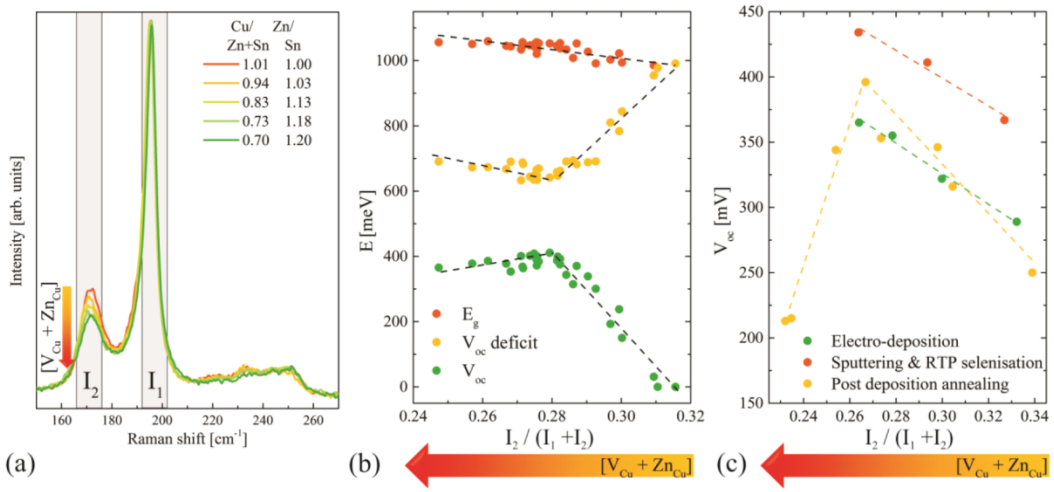


Figure 3. (a) Comparison of Raman spectra for absorbers with different composition. Dependence of the optoelectronic parameters: energy band gap ($E_g$), $V_{OC}$, and $V_{OC}$ deficit from Raman intensity ratio $I_2 / (I_1 + I_2)$ correlated with the concentration of [$V_{Cu}$ + $Zn_{Cu}$] defect clusters obtained from the samples prepared in (b) this work and (c) from the literature [27-29].

To further demonstrate that this is an intrinsic property of the CZTSe material, and not a consequence of the preparation method, the same analysis of the Raman spectra was performed on different sets of absorbers prepared by various methods and reported in the literature. The first set of samples was synthesized by the electro-deposition method with achieved record efficiency of 8.2%,[27] the second set was prepared by sputtering of the metallic precursors after which a rapid thermal selenization process was performed (maximum efficiency of 8.1%),[28] and the last set of samples was synthesized in a process similar to the devices analyzed in this work but including a post-deposition annealing treatment of the devices (maximum efficiency of 8.3%).[29] In all cases, same dependencies of the $V_{OC}$ from the concentration of [$V_{Cu}$ + $Zn_{Cu}$] defects clusters are observed, as shown in Figure 3(c). Additionally, in the case of the post-deposition annealing process, again maximization of the $V_{OC}$ is achieved for a certain concentration of [$V_{Cu}$ + $Zn_{Cu}$] defects clusters, after which these defects start to have detrimental effects, as previously explained. In the first two cases, changes in the concentration of [$V_{Cu}$ + $Zn_{Cu}$] defects clusters are achieved by the variations in the compositions of the samples, while in the last case, it is observed that the post-deposition annealing process is inducing Cu depletion and Zn enrichment of the absorber surface relative to the CZTSe bulk, which in consequence creates [$V_{Cu}$ + $Zn_{Cu}$] defects clusters in the surface.

In conclusion, the presented results show experimental evidence of the effect of the Cu-substitutional defects, namely [$V_{Cu}$ + $Zn_{Cu}$], on the optoelectronic properties, especially $V_{OC}$. It is concluded that the $V_{OC}$ values could be tuned by modifying the amount of the [$V_{Cu}$ + $Zn_{Cu}$] defect clusters, either by adjusting the composition or altering the production process. These results should provide a crucial step in solving the $V_{OC}$-deficit problem in kesterites. Furthermore, the detailed knowledge of the effects of defects on the

optoelectronic properties presented here will be the basis for optimization of the synthesis and post-deposition processes in order to achieve even higher efficiencies with these kinds of absorbers, and may provide insights into improving applications for other multinary compounds.

## Experimental section

Compositionally graded metallic (Cu-Zn-Sn) precursor films were deposited by DC-magnetron sputtering (Alliance Ac450) onto Mo-coated soda-lime glass substrates. During deposition the substrate was not rotated, and due to the positioning of the three off-center targets (Cu, Zn, Sn), a film with gradual lateral composition changes is formed. The precursor films were then subjected to a two-step thermal process in a selenium containing atmosphere to convert it into a CZTSe film, with a composition range of Cu/(Zn+Sn) from 0.55 to 1.20 and Zn/Sn from 0.70 to 1.90.[17] A CZTSe-based device was fabricated by chemical bath deposition of a CdS buffer layer, and DC-magnetron sputtering deposition (Alliance CT100) of a ZnO/ZnO:Al window layer. The device was mechanically scribed into 3x3 $mm^2$ cells, forming approximately 200 individual solar cells with gradual changes in composition with respect to neighboring cells. The composition of each cell was measured by x-ray fluorescence spectroscopy (Fischerscope XVD). AM1.5 illuminated J-V characteristics (ABET3000 Solar Simulator) and external quantum efficiency (Bentham PVE300 characterization system) were measured for each cell. Raman scattering measurements were performed with 532.0 nm excitation using a LabRam HR800-UV spectrometer, and 457.9 nm excitation using a T64000 Horiba-Jobin Yvon spectrometer.[30] XRD diffraction patterns were measured on PANalytical X'pert Pro MPD diffractometer with Cu−Kα -radiation (λ=1.54056 Å).

## Acknowledgements

The research leading to these results has received funding from the People Program (Marie Curie Actions) of the European Union's Seventh Framework Program FP7/2007-2013/ under REA grant agreement n°316488 (KESTCELLS) and by MINECO (Ministerio de Economía y Competitividad de España) under the NASCENT project (ENE2014-56237-C4-1-R). Authors from IREC and $IN^2UB$ belong to the M-2E (Electronic Materials for Energy) Consolidated Research Group and the XaRMAE Network of Excellence on Materials for Energy of the "Generalitat de Catalunya". E.S. thanks the Government of Spain for the "Ramon y Cajal" fellowship (RYC-2011-09212).

## References

(1) Queisser, H. J.; Haller, E. E. Defects in Semiconductors: Some Fatal, Some Vital. *Science* **1998**, *281* (5379), 945–950.

(2) Seebauer, E. G.; Kratzer, M. C. Charged Point Defects in Semiconductors. *Mater. Sci. Eng. R Rep.* **2006**, *55* (3–6), 57–149.

(3) Pantelides, S. T. The Electronic Structure of Impurities and Other Point Defects in Semiconductors. *Rev. Mod. Phys.* **1978**, *50* (4), 797–858.

(4) Siebentritt, S. What Limits the Efficiency of Chalcopyrite Solar Cells? *Sol. Energy Mater. Sol. Cells* **2011**, *95* (6), 1471–1476.

(5) Siebentritt, S.; Schorr, S. Kesterites—a Challenging Material for Solar Cells. *Prog. Photovolt. Res. Appl.* **2012**, *20* (5), 512–519.

(6) Siebentritt, S. Why Are Kesterite Solar Cells Not 20% Efficient? *Thin Solid Films* **2013**, *535*, 1–4.

(7) Niu, G.; Guo, X.; Wang, L. Review of Recent Progress in Chemical Stability of Perovskite Solar Cells. *J. Mater. Chem. A* **2015**, *3* (17), 8970–8980.
(8) Kanai, A.; Araki, H.; Takeuchi, A.; Katagiri, H. Annealing Temperature Dependence of Photovoltaic Properties of Solar Cells Containing Cu2SnS3 Thin Films Produced by Co-Evaporation. *Phys. Status Solidi B* **2015**, *252* (6), 1239–1243.
(9) Lee, Y. S.; Gershon, T.; Gunawan, O.; Todorov, T. K.; Gokmen, T.; Virgus, Y.; Guha, S. $Cu_2ZnSnSe_4$ Thin-Film Solar Cells by Thermal Co-Evaporation with 11.6% Efficiency and Improved Minority Carrier Diffusion Length. *Adv. Energy Mater.* **2014**, *5* (7), 1614-6840.
(10) Wang, W.; Winkler, M. T.; Gunawan, O.; Gokmen, T.; Todorov, T. K.; Zhu, Y.; Mitzi, D. B. Device Characteristics of CZTSSe Thin-Film Solar Cells with 12.6% Efficiency. *Adv. Energy Mater.* **2014**, *4* (7), 1614-6840.
(11) Fairbrother, A.; Fontané, X.; Izquierdo-Roca, V.; Placidi, M.; Sylla, D.; Espindola-Rodriguez, M.; López-Mariño, S.; Pulgarín, F. A.; Vigil-Galán, O.; Pérez-Rodríguez, A.; et al. Secondary Phase Formation in Zn-Rich $Cu_2ZnSnSe_4$-Based Solar Cells Annealed in Low Pressure and Temperature Conditions. *Prog. Photovolt. Res. Appl.* **2014**, *22* (4), 479–487.
(12) Walsh, A.; Chen, S.; Wei, S.-H.; Gong, X.-G. Kesterite Thin-Film Solar Cells: Advances in Materials Modelling of $Cu_2ZnSnS_4$. *Adv. Energy Mater.* **2012**, *2* (4), 400–409.
(13) Chen, S.; Walsh, A.; Gong, X.-G.; Wei, S.-H. Classification of Lattice Defects in the Kesterite $Cu_2ZnSnS_4$ and $Cu_2ZnSnSe_4$ Earth-Abundant Solar Cell Absorbers. *Adv. Mater.* **2013**, *25* (11), 1522–1539.
(14) Yin, L.; Cheng, G.; Feng, Y.; Li, Z.; Yang, C.; Xiao, X. Limitation Factors for the Performance of Kesterite $Cu_2ZnSnS_4$ Thin Film Solar Cells Studied by Defect Characterization. *RSC Adv.* **2015**, *5* (50), 40369–40374.
(15) Choubrac, L.; Lafond, A.; Paris, M.; Guillot-Deudon, C.; Jobic, S. The Stability Domain of the Selenide Kesterite Photovoltaic Materials and NMR Investigation of the Cu/Zn Disorder in $Cu_2ZnSnSe_4$ (CZTSe). *Phys. Chem. Chem. Phys.* **2015**, *17* (23), 15088–15092.
(16) Dimitrievska, M.; Fairbrother, A.; Saucedo, E.; Pérez-Rodríguez, A.; Izquierdo-Roca, V. Influence of Compositionally Induced Defects on the Vibrational Properties of Device Grade $Cu_2ZnSnSe_4$ Absorbers for Kesterite Based Solar Cells. *Appl. Phys. Lett.* **2015**, *106* (7), 073903.
(17) Fairbrother, A.; Dimitrievska, M.; Sánchez, Y.; Izquierdo-Roca, V.; Pérez-Rodríguez, A.; Saucedo, E. Compositional Paradigms in Multinary Compound Systems for Photovoltaic Applications: A Case Study of Kesterites. *J. Mater. Chem. A* **2015**, *3* (18), 9451–9455.
(18) S. Schorr. Point Defect Characteristics in CZTS/Se. In *5th European Kesterite Workshop*; Tallinn, Estonia, 2014.
(19) Saucedo, E.; Izquierdo-Roca, V.; Ruiz, C. M.; Parissi, L.; Broussillou, C.; Grand, P.-P.; Jaime-Ferrer, J. S.; Pérez-Rodríguez, A.; Morante, J. R.; Bermúdez, V. Key Role of Cu–Se Binary Phases in Electrodeposited $CuInSe_2$ Precursors on Final Distribution of Cu–S Phases in $CuIn(S,Se)_2$ Absorbers. *Thin Solid Films* **2009**, *517* (7), 2268–2271.
(20) Kanevce, A.; Repins, I.; Wei, S.-H. Impact of Bulk Properties and Local Secondary Phases on the $Cu_2(Zn,Sn)Se_4$ Solar Cells Open-Circuit Voltage. *Sol. Energy Mater. Sol. Cells* **2015**, *133*, 119–125.
(21) Krämmer, C.; Sachs, J.; Pfaffmann, L.; Musiol, T.; Lang, M.; Gao, C.; Gerthsen, D.; Kalt, H.; Powalla, M.; Hetterich, M. Epitaxial $Cu_2ZnSnSe_4$ Layers by Annealing of Sn/Cu/ZnSe(001) Precursors on GaAs(001). *Thin Solid Films* **2015**, *582*, 158–161.
(22) Wiedemeier, H.; von Schnering, H. G. Refinement of the Structures of GeS, GeSe, SnS and SnSe. *Z. Krist.* **1978**, *148*, 295–303.
(23) Bao, W.; Ichimura, M. Prediction of the Band Offsets at the $CdS/Cu_2ZnSnS_4$ Interface Based on the First-Principles Calculation. *Jpn. J. Appl. Phys.* **2012**, *51*, 10NC31.
(24) Mendis, B. G.; Shannon, M. D.; Goodman, M. C.; Major, J. D.; Claridge, R.; Halliday, D. P.; Durose, K. Direct Observation of Cu, Zn Cation Disorder in $Cu_2ZnSnS_4$ Solar Cell Absorber Material Using Aberration Corrected Scanning Transmission Electron Microscopy. *Prog. Photovolt. Res. Appl.* **2012**, 1–11.

(25) Skelton, J. M.; Jackson, A. J.; Dimitrievska, M.; Wallace, S. K.; Walsh, A. Vibrational Spectra and Lattice Thermal Conductivity of Kesterite-Structured $Cu_2ZnSnS_4$ and $Cu_2ZnSnSe_4$. *APL Mater*. **2015**, *3* (4), 041102.

(26) Dimitrievska, M.; Fairbrother, A.; Pérez-Rodríguez, A.; Saucedo, E.; Izquierdo-Roca, V. Raman Scattering Crystalline Assessment of Polycrystalline $Cu_2ZnSnS_4$ Thin Films for Sustainable Photovoltaic Technologies: Phonon Confinement Model. *Acta Mater*. **2014**, *70*, 272–280.

(27) Vauche, L.; Risch, L.; Sánchez, Y.; Dimitrievska, M.; Pasquinelli, M.; Goislard de Monsabert, T.; Grand, P.-P.; Jaime-Ferrer, S.; Saucedo, E. 8.2% Pure Selenide Kesterite Thin-Film Solar Cells from Large-Area Electrodeposited Precursors. *Prog*. *Photovolt*. *Res*. *Appl*. **2015**, (DOI: 10.1002/pip.2643).

(28) Márquez, J.; Neuschitzer, M.; Dimitrievska, M.; Gunder, R.; Haass, S.; Werner, M.; Romanyuk, Y.; Schorr, S.; Pearsall N.; Forbes, I. Systematic compositional changes and their influence on lattice and optoelectronic properties of $Cu_2ZnSnSe_4$ kesterite solar cells. *Sol*. *Energy Mater*. *Sol*. *Cells* **2015**, *under review*.

(29) Neuschitzer, M.; Sanchez, Y.; Olar, T.; Thersleff, T.; Lopez-Marino, S.; Oliva, F.; Espindola-Rodriguez, M.; Xie, H.; Placidi, M.; Izquierdo-Roca, V.; et al. The Complex Surface Chemistry of Kesterites: Cu/Zn Re-Ordering after Low Temperature Post Deposition Annealing and Its Role in High Performance Devices. *Chem*. *Mater*. **2015**.

(30) Dimitrievska, M.; Fairbrother, A.; Fontané, X.; Jawhari, T.; Izquierdo-Roca, V.; Saucedo, E.; Pérez-Rodríguez, A. Multiwavelength Excitation Raman Scattering Study of Polycrystalline Kesterite $Cu_2ZnSnS_4$ Thin Films. *Appl*. *Phys*. *Lett*. **2014**, *104* (2), 021901.

# Supporting information for:

# Secondary phase and Cu substitutional defect dynamics in kesterite $Cu_2ZnSnSe_4$ solar cells: impact on optoelectronic properties

Mirjana Dimitrievska[1], Andrew Fairbrother[1], Edgardo Saucedo[1], Alejandro Pérez-Rodríguez[1,2], and Victor Izquierdo-Roca[1*]

1 – Catalonia Institute for Energy Research (IREC), Jardins de les Dones de Negre 1, 08930 Sant Adrià de Besòs, Spain

2 – IN2UB, Universitat de Barcelona, C. Martí Franquès 1, 08028 Barcelona, Spain

* contact email: vizquierdo@irec.cat

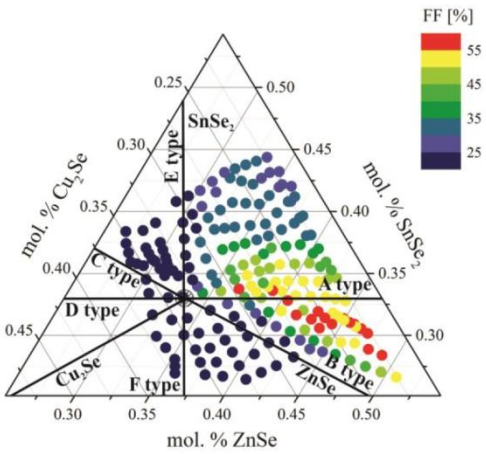


**Figure S1.** Compositional dependence of fill factor (FF) shown in a pseudo-ternary phase diagram of $Cu_2Se$-ZnSe-$SnSe_2$ for compositionally graded CZTSe solar cells; lines indicate expected secondary phases or defect clusters for a given region.

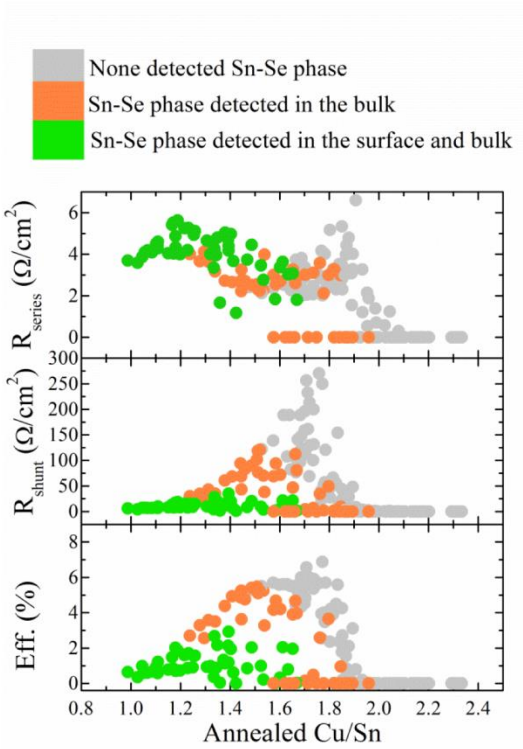


**Figure S2.** Compositional dependence of device efficiency (Eff.), shunt ($R_{shunt}$) and series ($R_{series}$) resistance for compositionally graded CZTSe solar cells, with colors indicating the presence of the detected Sn-Se secondary phase in the bulk and surface of absorber.

# Chapter 4

## *Raman spectroscopy based methodologies for anion compositional assessment of kesterites and sulfo-selenide secondary phases*

The highest efficiency devices based on kesterite materials are achieved with Se-rich CZTSSe solid solution absorbers. In order to obtain even higher increase in the efficiency of these systems, problems involving material and design issues require a very accurate control of the anion composition of the kesterite absorbers, which is a crucial parameter for several functional properties, such as band gap and mobility. The ability to accurately determine anion composition is compulsory to fully exploit properties engineering of these materials. This requires the development of accurate and sensitive analytical methods, which so far is still a challenge. The most common methods for measuring anion composition of kesterite thin film solid solutions are XRD and EQE. Both these methods, though reliable, are not fast, and in the case of EQE require the production of full solar cells, which is not suitable for application in in-line production. Other technique widely used for the chemical assessment of the layers in chalcogenide PV technologies is XRF, which has the advantage of being non-destructive.[49] However, use of XRF for the measurement of the S relative content in these systems is compromised by overlapping of the S and Mo signals, the latter coming from the Mo back contact layer commonly used in these devices. Other techniques, like XPS, EDX or Auger electron spectroscopy (AES) can also be used, but are not simple and require special handling of the samples under vacuum conditions, which compromises their applicability at in-line level.[50–53] On the other side, Raman spectroscopy applied to CZTSSe alloys has demonstrated that it is a very mature and suitable technique for their non-destructive structural and physico-chemical characterization.[54–61] Using suitable optical configurations, Raman scattering measurements can be fast enough to become compatible with their implementation at in-line level.

The first part of this chapter presents a general methodology that has been developed for the quantitative determination of anion composition of CZTSSe solid solutions using Raman spectroscopy. The methodology is based on the analysis of the integral intensity ratio of Raman bands sensitive to anion vibrations with anion composition of CZTSSe solid solutions.

Calibration of parameters used in the methodology was done using a series CZTSSe powders with different anion composition ($0 < [S]/([S]+[Se]) < 1$) which were prepared by a solid state reaction method.[62,63] The chemical composition of the powders was determined by electron microprobe analysis with an accuracy of ±1 atom%. Raman spectra were obtained from all reference samples using 532 nm excitation. From Figure 4.1, it is observed that Raman peaks in the high frequency region, corresponding mostly to S vibrations, are gradually increasing in intensity, while Raman peaks in low and intermediate frequency region, corresponding to mostly Se and S/Se vibrations are gradually decreasing in intensity. Taking into account this behavior, dependence of the

ratio of the integral intensities of the spectra from these two spectral regions on the anion composition of the layers is analyzed.

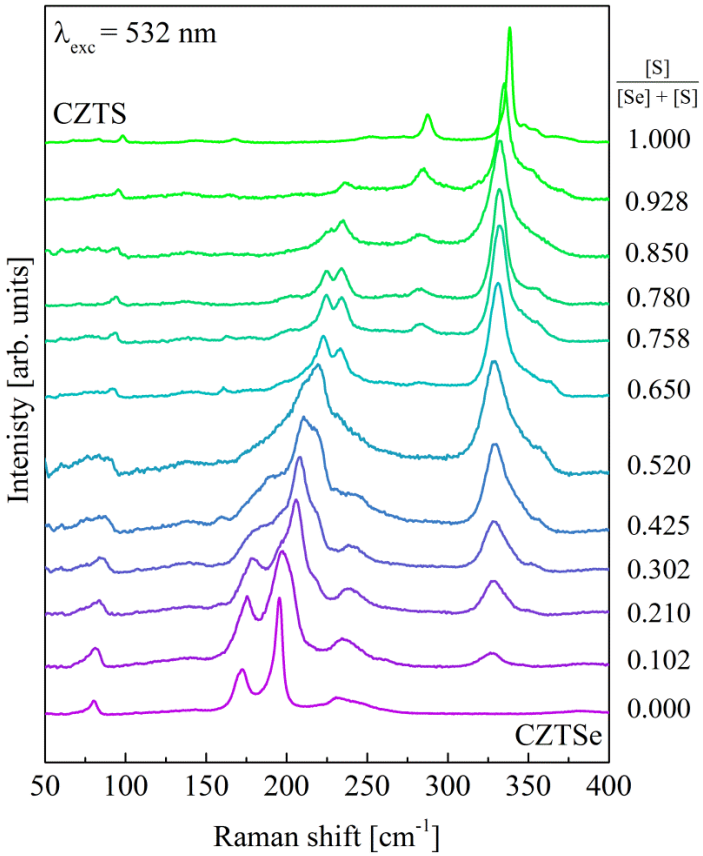


Figure 4.1. Raman spectra of reference polycrystalline CZTSSe solid solution powders measured with 532.0 nm excitation wavelength.

Figure 4.2 shows the plot of the [S]/([S]+[Se]) composition versus the chosen integral ratio calculated for the series of CZTSSe reference powder samples. As can be seen, there is a direct correlation between these parameters and linear fitting of the data has allowed obtaining calibration parameters for the methodology.

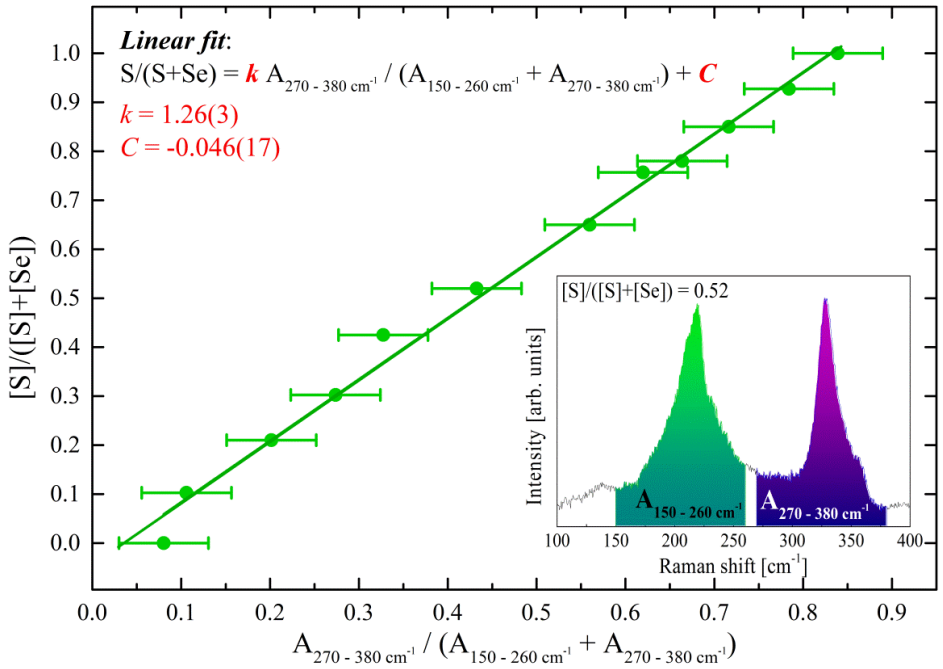


Figure 4.2 [S] /([S] + [Se] ) anion composition in dependence of integral ration of Raman peaks presented in the inset of the Figure. Solid line presents the calibration line according to linear fitting.

In order to test the validity of the proposed methodology, calculated anion compositions from Raman spectra of a set of polycrystalline CZTSSe device grade thin films, are compared with anion compositions obtained from XRD and EQE measurements (Figure 4.3). It should be stressed here that this additional sample set was not part of the sample set used for obtaining the calibration parameters. It is concluded that the results are in good accordance, with the largest deviation among the results always being less than 0.05 of absolute values.

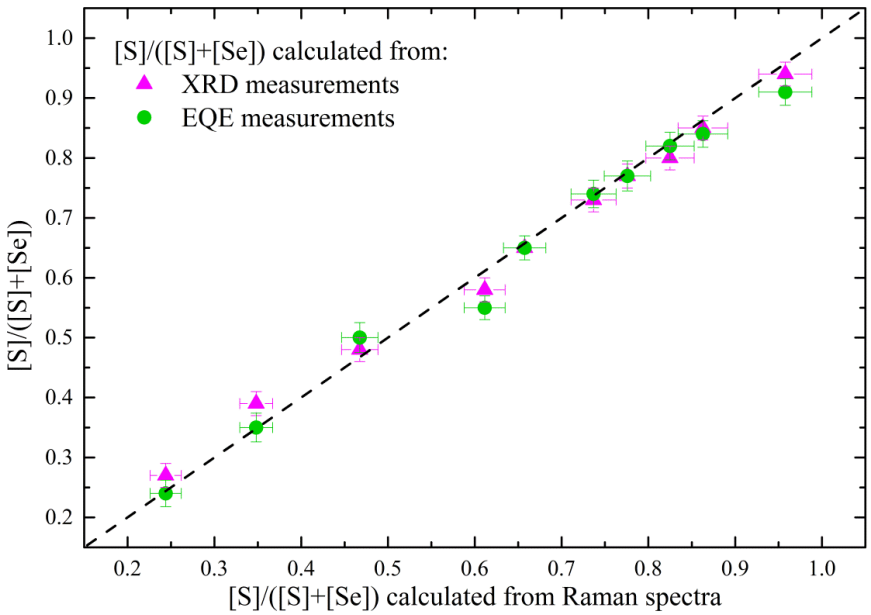


Figure 4.3 Comparison of anion compositions for CZTSSe photovoltaic grade thin films obtained from Raman scattering (dashed line) with values calculated based on XRD (triangles) and EQE (circles) measurements.

Additionally, the validity of the methodology has been tested in different kinds of samples, including layers with different crystalline quality and the same composition. A strong support on the performance of the methodology has been obtained from the analysis of a wide range of CZTSSe samples fabricated by different methods using Raman spectra reported in the literature. The good agreement obtained in the whole range of compositions points out the validity of the proposed methodology for the simple non-destructive assessment of the anion composition of different kinds of CZTSSe samples (thin films, powders, nanocrystals, monograins, etc.) independently on the experimental conditions used for the Raman scattering measurements.

Besides the accurate control of the anion composition in the development of kesterite based technologies, another factor that needs to be controlled is presence of secondary phases. Secondary phases are vital issues related to efficiency limitation in kesterites and are commonly present on the surface, bulk or in the back of the films, due to very narrow single phase existence zone of kesterite, and off-stoichiometry and non-equilibrium thermodynamics conditions used in the synthesis of these materials.[64,65] This is why development of accurate technologies for the detection of secondary phases is necessary. Earlier reports have shown that Raman spectroscopy is extremely useful for the detection of secondary phases on the surface and with a suitable sample

preparation even in the back of absorbers.[16] Additionally, the main advantage of Raman spectroscopy when compared to other methods is the possibility to differentiate phases with the same structure as kesterite, which is not the case with XRD for example.

Since the highest efficiency absorbers are produced in Zn-rich and Cu-poor conditions, the most probable secondary phase present will be ZnS or ZnSe. Furthermore, in the case of CZTSSe solid solutions, presence of both S and Se will likely lead to formation of $ZnS_xSe_{1-x}$ mixtures (ZnSSe), rather than the single ZnS and ZnSe phases.[64] This is confirmed with the Raman measurements performed on the front and back of a series of CZTSSe thin films with different [S] / ([S] + [Se]) compositions (Figure 4.4). From this study it is also observed that the most common secondary phases are ZnSSe and ZnS, while ZnSe was not detected in any of the CZTSSe absorbers, either in the front or in the back region. This work corroborates the need to study the dynamics of ZnSSe solid solutions in more detail, especially using the same Raman spectroscopy techniques which are used for detection of these phases in kesterite absorbers.

The second part of this chapter describes Raman resonance scattering characterization of ZnSSe solid solutions over the whole sulfo-selenide compositional range using 325 and 455 nm excitation wavelengths.[66] Besides providing the reference Raman spectra of the various ZnSSe thin films, with both characteristic wavelengths, which are useful in the detection of these phases in kesterites, this study has also provided an insightful knowledge about the fundamental proprieties of sulfo-selenide compounds in general.

In particular, special focus is put on the Raman scattering intensities of the LO ZnS-like and ZnSe-like phonon modes, corresponding to vibrations of only S and Se atoms, respectively, which proved to be significantly enhanced when excited with 325 nm excitation in the case of S vibrations, and with 455 nm in the case of the Se vibrations. This behavior is explained with the interaction of the excitation photons with the corresponding S or Se electronic states in the conduction band, and further confirmed with first principle simulations.

Additionally, it should be mentioned that the same effect was observed in kesterite solid solutions, where significant enhancement of the S related Raman modes is detected during the 785 nm excitation wavelength.[18] This phenomenon is described in more detail in the article "Multiwavelength excitation Raman scattering of $Cu_2ZnSn(S_xSe_{1-x})_4$ ($0 \leq x \leq 1$) polycrystalline thin films: Vibrational properties of sulfoselenide solid solutions" which is presented in Chapter 2.

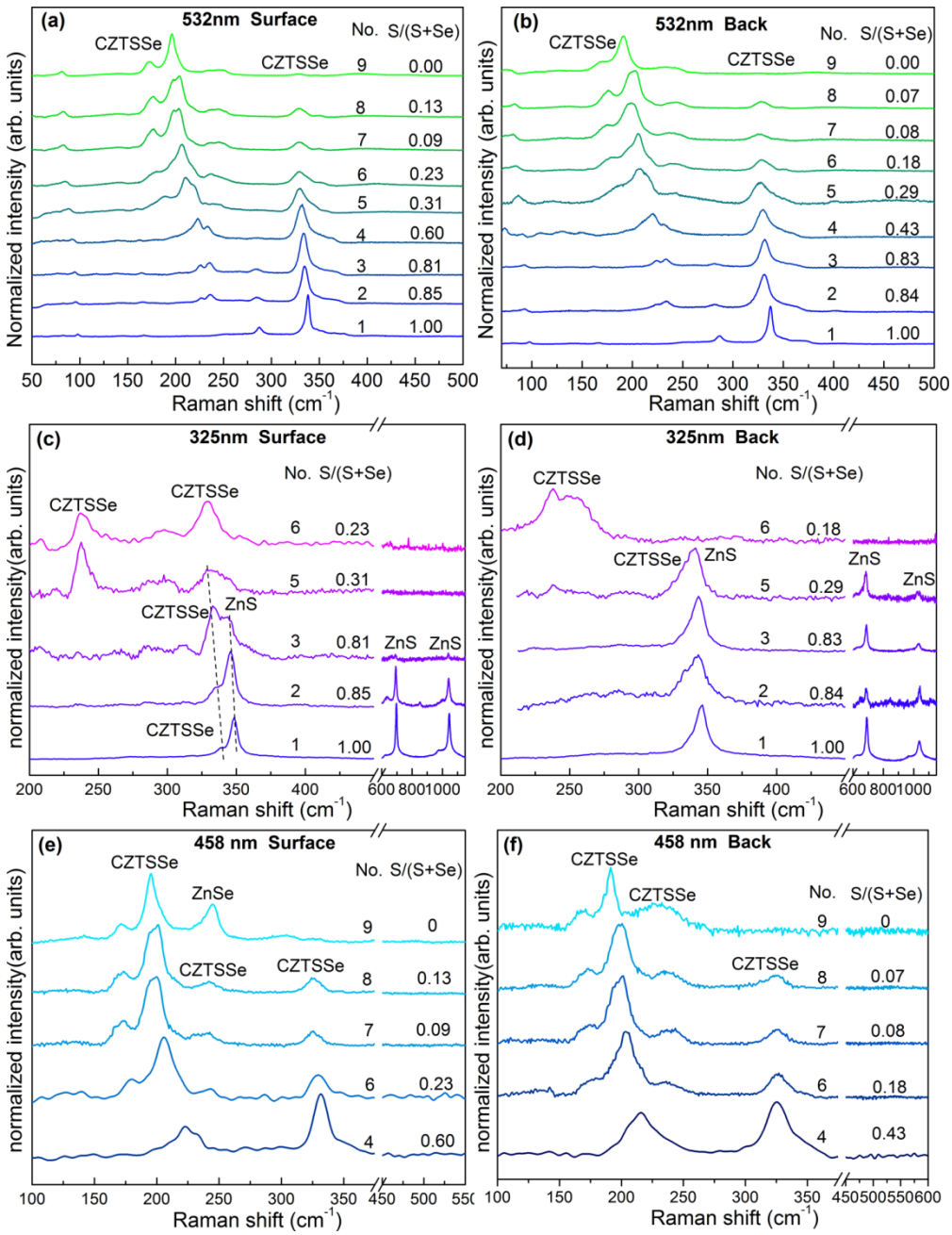


Figure 4.4 Raman spectra measured with 532, 325 and 458 nm excitation wavelengths on the surface (a), (c), (e) respectively; and at the back region (b), (d), (f) of CZTSSe samples with [S] / ([S] + [Se]) ratio varying from 0 to 1. Surface and back region [S] / ([S] + [Se]) ratios shown in the spectra are estimated from the surface (a) and back (b) Raman spectra with excitation wavelength of 532 nm, respectively.

These results advance the fundamental understanding of the coupling between the electronic transitions and photons in the case of Raman resonance effects, and provide inputs for further studies of lattice dynamics, especially in the case of chalcogenide materials.[20] Additionally, the coexistence of modes corresponding to only S vibrations and only Se vibrations in the ZnSSe alloys makes these results applicable for the compositional assessment of ZnSSe compounds.

In conclusion, this chapter describes the usefulness of development of methodologies based on Raman spectroscopy for compositional assessment of not only kesterite but in general sulfo-selenide compounds. Additionally, valuable fundamental insights were obtained regarding photon-matter interaction, which could be useful for further study of lattice dynamics in these materials.

This chapter concludes with two publications: "Raman scattering quantitative analysis of the anion chemical composition in kesterite $Cu_2ZnSn(S_xSe_{1-x})_4$ solid solutions", and "Resonant Raman scattering of $ZnS_xSe_{1-x}$ solid solutions: role of S and Se electronic states" in which detailed information about the mentioned results are presented.

Journal of Alloys and Compounds 628 (2015) 464–470

Contents lists available at ScienceDirect

Journal of Alloys and Compounds

journal homepage: www.elsevier.com/locate/jalcom

# Raman scattering quantitative analysis of the anion chemical composition in kesterite $Cu_2ZnSn(S_xSe_{1-x})_4$ solid solutions

Mirjana Dimitrievska [a], Galina Gurieva [b], Haibing Xie [a], Alex Carrete [a], Andreu Cabot [a,c], Edgardo Saucedo [a], Alejandro Pérez-Rodríguez [a,d], Susan Schorr [b,e], Victor Izquierdo-Roca [a,*]

[a] Catalonia Institute for Energy Research (IREC), Jardins de les Dones de Negre 1 2pl., 08930 Sant Adrià del Besòs, Barcelona, Spain
[b] Helmholtz Centre Berlin for Materials and Energy, Department Crystallography, Hahn-Meitner-Platz 1, 14109 Berlin, Germany
[c] Institució Catalana de Recerca i Estudis Avançats – ICREA, Passeig Lluís Companys 23, 08010 Barcelona, Spain
[d] IN²UB, Departament d'Electrònica, Universitat de Barcelona, C. Martí i Franquès 1, 08028 Barcelona, Spain
[e] Freie Universität Berlin, Institute of Geological Sciences, Malteserstr. 74-100, 12249 Berlin, Germany

ARTICLE INFO

*Article history:*
Received 10 October 2014
Received in revised form 29 November 2014
Accepted 2 December 2014
Available online 3 January 2015

*Keywords:*
Composition fluctuations
Thin films
Nanostructured materials
Inelastic light scattering
Photoconductivity and photovoltaics

ABSTRACT

A simple and non destructive optical methodology for the quantitative measurement of [S]/([S] + [Se]) anion composition in kesterite $Cu_2ZnSn(S_xSe_{1-x})_4$ (CZTSSe) solid solutions by means of Raman spectroscopy in the whole S–Se range of compositions has been developed. This methodology is based on the dependence of the integral intensity ratio of Raman bands sensitive to anion vibrations with the [S]/([S] + [Se]) composition of the kesterite solid solutions. The calibration of the parameters used in this analysis involved the synthesis of a set of CZTSSe powders by solid state reaction method, spanning the range from pure $Cu_2ZnSnS_4$ to pure $Cu_2ZnSnSe_4$. The validity of the methodology has been tested on different sets of independent samples, including also non-stoichiometric device grade CZTSSe layers with different compositions and films that were synthesized by solution based processes with different crystalline quality. In all cases, the comparison of the results obtained from the analysis of the intensity of the Raman bands with independent composition measurements performed by different techniques as X-ray diffraction and external quantum efficiency has confirmed the satisfactory performance of the developed methodology for the quantitative analysis of these compounds, independently on the crystal quality or the method of synthesis. Further strong support on the methodology performance has been obtained from the analysis of a wider range of samples, including nanocrystals, monograins, powders and thin films, which Raman spectra and anion compositions were reported in the literature. The agreement of the values of [S]/([S] + [Se]) obtained from the analysis of the Raman spectra published in the literature with the compositions reported for these samples demonstrate the validity of the developed methodology for the chemical analysis of these compounds, independently of the experimental conditions of the measurements and of the type of samples.



## 1. Introduction

Earth abundant quaternary semiconductors $Cu_2ZnSnS_4$ (CZTS) and $Cu_2ZnSnSe_4$ (CZTSe) and their solid solutions $Cu_2ZnSn(S_xSe_{(1-x)})_4$ (CZTSSe) have been intensively studied because of their desired optoelectronical properties for photovoltaic (PV) applications. Being mainly constituent of naturally abundant elements with low toxicity, CZTSSe kesterites have emerged as promising low cost and high-efficiency materials for thin film solar cell technologies. One of the most important motivations for the growing interest in CZTSSe solid solutions is the possibility of band structure engineering [1–5], which greatly extends their potential application in thin film PV devices, where a defined and controllable band-gap is required. So far, the best devices rely on Se-rich absorbers, with a reported record efficiency of 12.6% [6]. However, this value is still far away from the theoretical predictions for these materials.

In order to achieve an increase in the efficiency of these systems, problems involving material and design issues require for a very accurate control of the anion composition of the kesterite absorbers, which is a crucial parameter for several functional properties, such as band gap and mobility. The ability to accurately determine anion composition is compulsory to fully exploit properties engineering of these materials. This requires the development of accurate and sensitive analytical methods, which so far

* Corresponding author.
*E-mail addresses:* mdimitrievska@irec.cat (M. Dimitrievska), vizquierdo@irec.cat (V. Izquierdo-Roca).

http://dx.doi.org/10.1016/j.jallcom.2014.12.175
0925-8388/

is still a challenge. The contemporary methods for measuring anion composition of kesterite thin film solid solutions are X-ray diffraction (XRD) and external quantum efficiency (EQE) [7]. Though reliable to a reasonable extent, both these methods are time consuming. Moreover, in the case of EQE, it requires the effort of fully producing solar cells prior to characterization, hence, rendering the procedure unsuitable for use in in-line production systems. A complementary technique widely used for the chemical assessment of the layers in chalcogenide PV technologies is X-ray Fluorescence (XRF), which has the advantage of being non-destructive [8]. Unfortunately, XRF cannot be used for the measurement of the S relative content in these systems, due to the existence of the overlapping with the Mo signal coming from the Mo back contact layer used in these devices. Other techniques, like X-ray photoelectron spectroscopy (XPS) [9], energy dispersive X-ray spectroscopy (EDX) [10–12] or Auger electron spectroscopy (AES) can also be used, but are not simple and require special handling of the samples under vacuum conditions, yet another aspect which limits their applicability at an in-line level. On the other side, Raman spectroscopy applied to $Cu(In,Ga)(S,Se)_2$ alloys [13–17] has demonstrated superior suitability as a technique for their non-destructive structural and physico-chemical characterization. Using suitable optical configurations, Raman scattering measurements can be fast enough to become compatible with their implementation at in-line level. In the last years Raman spectroscopy has emerged as a promising and feasible technique for the advanced characterization of the CZTSSe system, because of the strong effect of the solid solution anion composition on optical phonon modes [1,3,7,18–20].

In this framework, this work presents a general methodology that has been developed for the quantitative determination of anion composition of CZTSSe solid solutions using Raman spectroscopy. The methodology is based on the analysis of the integral intensity ratio of Raman bands sensitive to anion vibrations with anion composition of CZTSSe solid solutions. Calibration of parameters used in the methodology was done using a series CZTSSe powders with different anion composition ($0 < [S]/([S] + [Se]) < 1$) which were prepared by solid state reaction method. The chemical composition of the powders was determined by electron microprobe analysis with an accuracy of ±1 atom%. The methodology has also been tested on a series of polycrystalline CZTSSe device grade layers (used for producing solar cells with up to 8.2% efficiency) with different anion compositions which were synthesized by DC magnetron sputtering technique. The obtained anion compositions from the methodology were compared with compositions determined by XRD and EQE methods. Additionally, tests on CZTSSe thin film samples that were synthesized using solution based processes with different crystal quality and same anion composition were performed in order to investigate the effect of crystal quality on the methodology. In the end, the validity of the methodology was also investigated on a very wide range of different types of CZTSSe samples (nanocrystals, monograins, powders and thin films) taken from Refs. [1–3,19–23]. Based on the obtained results, a methodology independent of the experimental measuring conditions has been proposed for the quantitative analysis of anion composition of CZTSSe solid solutions.

## 2. Experimental

CZTSSe powder samples were synthesized from pure elements by solid state reaction in evacuated quartz tubes at 750 °C in duration for 14 days. The homogenization step – grinding in agate mortar and pressing the pellets, was followed by annealing in evacuated and sealed quartz ampoules for 10 days at 750 °C, and repeated twice.

CZTSSe device grade layers have been synthesized onto Mo coated soda lime glass by annealing of Cu/Sn/Cu/Zn metallic multi-stacks, deposited by DC magnetron sputtering technique, under S + Se + Sn atmosphere. Changing the mass of S and Se and the total pressure during the annealing, it was possible to tune the S–Se composition in the whole compositional range [2]. To achieve devices with good efficiency, the layers were synthesized with non-stoichiometric Cu poor and Zn rich compositions, and the cationic ratios, i.e. Cu/(Sn + Zn) and Zn/Sn were kept constant between 0.75–0.80 and 1.16–1.22 respectively. To avoid presence of ZnS(Se) secondary phases that can be formed for these compositions, as grown S-rich samples were submitted to an HCl etching [24] and Se-rich ones to a $KMnO_4/H_2SO_4 + Na_2S$ [25] etching.

Finally, CZTSSe solution processed thin films were prepared from CZTS nanoparticles obtained by colloidal synthesis, which were used as a precursor ink that was sprayed onto a Mo substrate [26]. CZTSSe thin films with different crystal quality were obtained by selenization of CZTS nanocrystal precursor layers under a Se/Sn atmosphere at 475 and 525 °C for 60 min.

In all analyzed samples, the possible presence of ZnS and/or ZnSe secondary phases in the measured surfaces was excluded using Raman scattering measurements with 325.0 and 457.9 nm excitation wavelengths, which correspond to resonant excitation conditions for these compounds [24,25]. Additionally the spectral contributions of Sn–(S,Se) phases which are expected in the 50–220 $cm^{-1}$ interval, have not been detected in the Raman spectra [27]. Finally, no evidences have been found of the presence of Cu–Sn–(S,Se) ternary phases and Cu–(S,Se) binary phases. This agrees with the experimental Zn-rich and Cu-poor conditions under which the device grade non stoichiometric layers were prepared, that are expected to inhibit formation of these phases [28].

Solar cells were fabricated with the device grade layers as described in Ref. [2]. Optoelectronic properties from the devices synthesized in this way, gave efficiencies up to 8.2%. External quantum efficiency (EQE) curves were obtained using a PV300 Photovoltaic characterization system (Bentham Instruments).

Raman scattering measurements were performed in back scattering configuration with a LabRam HR800-UV and T64000 Horiba-Jobin Yvon spectrometers. For the HR800-UV system, diode-pumped solid state lasers with wavelength of 532.0 nm, and gas HeCd laser with wavelength of 325.0 nm were used for excitation. In this system excitation and light collection were made through an Olympus metallographic microscope with a laser spot diameter of the order of 1–2 μm, depending on the excitation wavelength. To avoid effects in the spectra related to potential microscopic inhomogeneities, the spot was rastered over an area of $30 \times 30\ \mu m^2$. Furthermore, the T64000 system works coupled with an ion-Ar + laser, and measurements were made with 457.9 nm excitation line, with a 100 μm diameter spot size on the sample. In all cases, and to avoid the presence of thermal effects in the spectra, the power excitation density on the surface of the samples was around 50 $W/cm^2$. Under these experimental measurement conditions no thermal effects are observed in the spectra. This has been corroborated by the analysis of spectra measured with different excitation powers. The first-order Raman spectrum of monocrystalline Si was measured as a reference before and after acquisition of each Raman spectrum, and the spectra were corrected with respect to the Si line at 520 $cm^{-1}$.

XRD diffraction patterns were measured on PANalytical X'pert Pro MPD diffractometer with Cu Kα-radiation ($\lambda = 1.54056$ Å). Structural characterization of thin films was carried out by grazing incidence X-ray diffraction (GIXRD) with angles of 0.5°, 1°, 2° and 5°. Refinements of the lattice constant values were carried out by Le Bail analysis using the FullProf package [29] with Thompson–Cox–Hastings pseudo-Voigt convoluted with axial divergence asymmetry profile function [30].

To determine the chemical composition of the powder samples, wave length dispersive X-ray measurements (WDX) have been performed using an electron microprobe analysis JEOL-JXA 8200 EMPA system. In order to obtain reliable results from the WDX measurements, the system was calibrated using elemental standards. High accuracy of the composition parameters was achieved by averaging over 20 local measurement points to an integral chemical composition, with an accuracy of ±1 atom%.

The synthesized films have been imaged by scanning electron microscopy (SEM) using a ZEISS Series Auriga microscope with 5 kV acceleration voltage.

## 3. Results and discussion

### 3.1. Methodology for Raman scattering analysis of anion chemical composition: calibration of parameters for quantitative analysis

Kesterite structure with space group $I\bar{4}$ is characterized with irreducible representation $\Gamma = 3A \oplus 6B \oplus 6E$ which leads to theoretical prediction of 27 active Raman modes, from which most have been experimentally detected for the CZTS and CZTSe compounds [31,32]. Usually two dominant Raman peaks have been observed in this system and assigned to *A* symmetry modes involving pure anion vibrations [7].

In difference, CZTSSe solid solutions have a more complex vibrational behavior as reported in Ref. [6]. Raman spectra of CZTSSe solid solutions are characterized by three frequency regions which differ mainly in the vibrations attributed to different

type of anions. In that regard, low frequency region (170–205 $cm^{-1}$) is characterized by the presence of two dominant peaks corresponding to *A* symmetry modes involving pure Se vibrations. Similarly, high frequency region (280–400 $cm^{-1}$) is characterized by the presence of two dominant peaks corresponding to *A* symmetry modes involving pure S vibrations. On the other side, intermediate frequency region (205–280 $cm^{-1}$) is characterized by peaks that have been attributed to vibrational modes which include vibrations from both S and Se atoms in the lattice. Additionally, it is also observed that frequency and intensity of all Raman modes as well as the shape of the Raman spectrum depend on the anion composition. These results indicate that a method for determining [S]/([S] + [Se]) anion composition from Raman spectra could be proposed.

In order to develop and calibrate a methodology for the quantitative determination of the anion composition from Raman spectra, series of reference CZTSSe powder samples with different [S]/([S] + [Se]) compositions were produced.

Fig. 1 presents the Raman spectra measured from the series of CZTSSe powder reference samples with 532 nm excitation wavelength. The exact compositions of CZTSSe powders obtained by electron microprobe analysis are summarized in Table 1. All peaks appearing in the spectra agree with Raman peaks characteristic of the CZTSSe solid solutions, in accordance with previously reported results [1–4,7,19,20,23].

From Fig. 1, it can be observed that with increasing [S]/([S] + [Se]) ratio, Raman peaks in the high frequency region, corresponding mostly to S vibrations, are gradually increasing in intensity, while Raman peaks in low and intermediate frequency region, corresponding to mostly Se and S/Se vibrations are gradually decreasing in intensity. Taking into account this behavior, dependence of the ratio of the integral intensities of the spectra from these two spectral regions on the anion composition of the layers was investigated. This parameter is defined as $A_{270-380\ cm^{-1}}/(A_{150-260\ cm^{-1}} + A_{270-380\ cm^{-1}})$, where $A_{270-380\ cm^{-1}}$ is area of the Raman spectra in the region between 270 and 380 $cm^{-1}$ corresponding to Raman modes which involve mainly vibrations from S atoms, and $A_{150-260\ cm^{-1}}$ is area of the Raman spectra in the region between 150 and 260 $cm^{-1}$ corresponding to vibrational modes which include vibrations from both S and Se atoms in the lattice (illustratively shown on inset in Fig. 2). Fig. 2 shows the

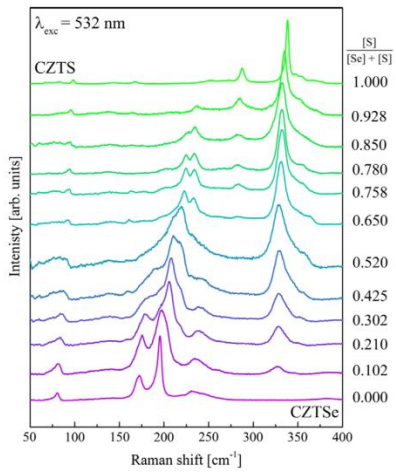


**Fig. 1.** Raman spectra of reference polycrystalline CZTSSe solid solution powders measured with 532.0 nm excitation wavelength.

**Table 1**
Chemical composition and [S]/([S] + [Se]) ratio of the reference $Cu_2ZnSn(S_xSe_{(1-x)})_4$ powder samples.

| Chemical composition determined by EMPA | $\frac{[S]}{[S]+[Se]}$ |
|---|---|
| $Cu_2ZnSnSe_4$ | 0.000(3) |
| $Cu_{1.99}ZnSnS_{0.41}Se_{3.59}$ | 0.102(3) |
| $Cu_2ZnSnS_{0.84}Se_{3.16}$ | 0.210(3) |
| $Cu_{1.99}ZnSn_{1.01}S_{1.21}Se_{2.78}$ | 0.302(3) |
| $Cu_2Zn_{0.98}Sn_{1.02}S_{1.7}Se_{2.3}$ | 0.425(3) |
| $Cu_{2.04}Zn_{0.91}Sn_{1.05}S_{2.08}Se_{1.92}$ | 0.520(3) |
| $Cu_{2.25}Zn_{0.61}Sn_{1.14}S_{2.6}Se_{1.4}$ | 0.650(3) |
| $Cu_{2.03}Zn_{1.09}Sn_{0.88}S_{3.03}Se_{0.97}$ | 0.758(3) |
| $Cu_{2.06}Zn_{1.04}Sn_{0.9}S_{3.12}Se_{0.88}$ | 0.780(3) |
| $Cu_{1.96}Zn_{0.98}Sn_{1.05}S_{3.4}Se_{0.6}$ | 0.850(3) |
| $Cu_{2.28}Zn_{0.77}Sn_{0.95}S_{3.71}Se_{0.29}$ | 0.928(3) |
| $Cu_{1.99}ZnSn_{1.01}S_4$ | 1.000(3) |

plot of the [S]/([S] + [Se]) composition versus $A_{270-380\ cm^{-1}}/(A_{150-260\ cm^{-1}} + A_{270-380\ cm^{-1}})$ calculated for the series of CZTSSe reference powder samples. As can be seen, there is a linear correlation between these data. It can be noticed that in the case of pure CZTSe sample, ratio $A_{270-380\ cm^{-1}}/(A_{150-260\ cm^{-1}} + A_{270-380\ cm^{-1}})$ is slightly different than 0, which is the expected value in case of [S]/([S] + [Se]) = 0. The difference is due to the fact that the area $A_{270-380\ cm^{-1}}$ overlaps with the second order peaks of the CZTSe compound, which are located around 360 $cm^{-1}$. Since the contribution of the second order peaks appears for all samples, regardless of their composition, they should not affect the performance of the methodology.

Linear fitting of the data has allowed obtaining calibration parameters which are summarized in Eq. (1).

$$S/(S+Se) = k \cdot A_{270-380\ cm^{-1}}/(A_{150-260\ cm^{-1}} + A_{270-380\ cm^{-1}}) + C$$
$$k = 1.26(3), \quad C = -0.046(17) \tag{1}$$

This relation is expected to describe the vibrational properties of CZTSSe solid solutions in the entire anion composition range. It should be mentioned that besides the proposed methodology, frequencies of the Raman modes could be also used for the assessment of the anion chemical composition in the case of these materials. As shown in Ref. [6], the most intense modes experience a

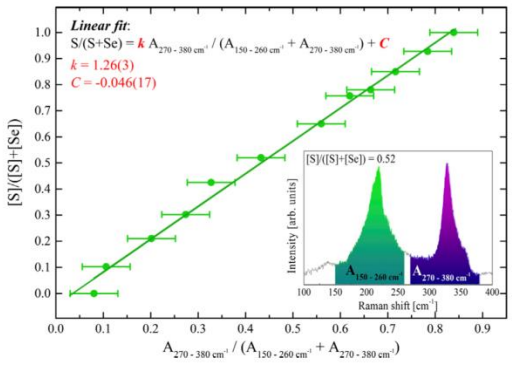


**Fig. 2.** S/(S + Se) anion composition in dependence of $A_{270-380\ cm^{-1}}/(A_{150-260\ cm^{-1}} + A_{270-380\ cm^{-1}})$ calculated from Raman spectra of CZTSSe reference powder samples. Solid line presents the calibration line according to Eq. (1) which was obtained by linear fitting of the data. Inset figure illustratively presents the areas of Raman spectra which were used for calculating the ratio $A_{270-380\ cm^{-1}}/(A_{150-260\ cm^{-1}} + A_{270-380\ cm^{-1}})$.

linear dependence from the anion compositions, meaning that essentially anion composition could be determined based on the frequencies. However, in order to determine correctly the frequencies of the Raman modes, it is necessary to do a deconvolution of the spectra, which is usually time consuming and rather difficult work, especially in the case of overlapping of three or more Raman modes under one broad band, as reported for the modes correlated with the Se and S/Se vibrations around the 200 $cm^{-1}$ frequency region in Ref. [6]. On the other side, calculating the integral intensity of the modes is rather easy and not time expensive, which is the reason why the proposed methodology is based on this principle.

### *3.2. Determination of anion composition by Raman spectroscopy*

#### *3.2.1. Application to device grade CZTSSe thin films*

Hereby, it will be shown that Raman spectra are effective for the quantitative analysis of anion composition using the dependence described by Eq. (1). To exploit this purpose and in order to test the validity of the methodology, calculated anion compositions from Raman spectra of a set of polycrystalline CZTSSe device grade thin films, are compared with anion compositions obtained from XRD and EQE measurements. It should be stressed here that this additional sample set was not part of the sample set used for obtaining Eq. (1).

XRD measurements performed on CZTSSe thin films have revealed the presence of a single and symmetric 112 diffraction peak in all measured diffractograms indicating that all samples are homogeneously alloyed rather than a mixture of CZTSSe phases with different [S]/[S] + [Se] compositions [33] (see Supporting Information Fig. S1). Lattice parameters $a$ and $c$ of the thin films were obtained as result of the Le Bail analysis, where the kesterite structure (space group $I\bar{4}$) was used as starting model for the refinement procedure [34]. Anion compositions of the samples were calculated by applying Vegard's law on the lattice parameters $a$ and $c$ of the CZTSSe thin films in comparison with lattice parameters of pure CZTS and CZTSe compounds.

Similarly, EQE measurements in final devices were also used for calculation of anion compositions of these layers. In this case they were calculated using Vegard's law as explained in Ref. [35], which was applied on the band gap energies. The band gap energies were determined from the EQE curves of solar cell devices based on these films. The energy band gap references used in these calculations are 1.00 and 1.61 eV for pure CZTSe and CZTS samples respectively. Similar calculations of the band gap energies based on optical properties were reported in [36–39].

Fig. 3 presents Raman spectra of the series of CZTSSe thin film samples measured with 532.0 nm excitation wavelengths.

In order to be able to compare anion compositions from Raman scattering, XRD and EQE measurements, the compositional uniformity through the thickness of the CZTSSe thin films has been checked. This is because the penetration depths of the used techniques are different, especially in the case of Raman scattering which is more surface sensitive technique with penetration depth of approximately 100 nm in CZTSSe. Compositional uniformity of the samples was investigated with GIXRD measurements which were performed with 0.5°, 1°, 2° and 5° angles. No significant shift in peak positions of the 112 reflection or in the lattice parameters obtained from the refinements with the change in the grazing incidence angles was observed (see Supporting Information Fig. S2). Additionally, Raman measurements preformed on the front and back surface of the layers do not show changes in the shape and positions of Raman peaks (see Supporting Information Fig. S3). Raman measurements from the back region were made with the laser spot directly focused on the back surface of the layer from layers that were previously mechanically removed from the substrate [40]. This behavior points out the absence of significant changes in the [S]/([S] + [Se]) composition through the thickness of the layers, which allows comparison among the anion compositions measured with the different techniques regardless of their differences in penetration depth.

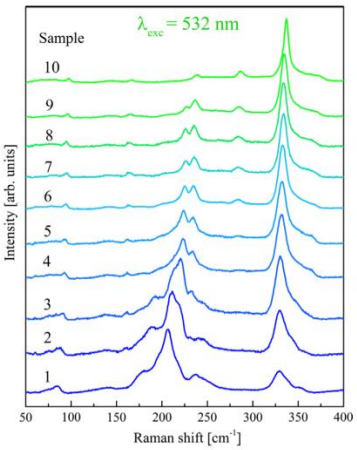


**Fig. 3.** Raman spectra of polycrystalline CZTSSe solid solution thin films measured with 532.0 nm excitation wavelength.

All calculated anion compositions of the CZTSSe thin films using XRD and EQE methods and their comparison with the estimation obtained using the Raman scattering methodology, Eq. (1), are summarized and presented in Table 2 and in Fig. 4. It is observed that anion compositions of the CZTSSe thin films, obtained from Raman spectra and using Eq. (1) are in good accordance with the results calculated from XRD and EQE measurements, with the largest deviation among the results always being less than 0.05 of absolute values. Additionally, it could be concluded that the proposed method for calculating anion compositions based on the Raman spectra is independent of the cation compositions of the CZTSSe, since used thin films are of device grade which correspond to Cu-poor and Zn-rich cation compositions. This could be explained by the fact that, firstly, Raman modes used for calculating anion composition are mostly involving only anion vibrations, and secondly, the usage of intensity ratio of the Raman modes cancels the effect of cation composition. These results strongly indicate that the proposed methodology based on Raman scattering and Eq. (1) could be used for the quantitative analysis of the anion composition in the case of CZTSSe thin film absorbers.

**Table 2**
Comparison of the anion compositions of CZTSSe solid solution thin films obtained from XRD, EQE and Raman scattering measurements.

| Sample | [S]/([S] + [Se]) | | |
|---|---|---|---|
| | XRD | EQE | Raman scattering |
| 1 | 0.26(2) | 0.24(2) | 0.24(2) |
| 2 | 0.38(2) | 0.35(3) | 0.35(2) |
| 3 | 0.48(2) | 0.50(2) | 0.47(2) |
| 4 | 0.58(2) | 0.55(3) | 0.61(2) |
| 5 | 0.65(2) | 0.65(2) | 0.66(2) |
| 6 | 0.73(2) | 0.74(2) | 0.74(2) |
| 7 | 0.77(2) | 0.77(3) | 0.77(3) |
| 8 | 0.80(2) | 0.82(2) | 0.82(3) |
| 9 | 0.85(2) | 0.84(2) | 0.86(3) |
| 10 | 0.94(2) | 0.91(2) | 0.95(3) |

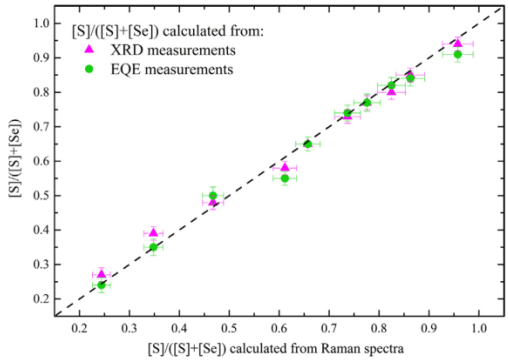


**Fig. 4.** Comparison of anion compositions for CZTSSe photovoltaic grade thin films obtained from Raman scattering and using Eq. (1) (dashed line) with values calculated based on XRD (triangles) and EQE (circles) measurements.

*3.2.2. Effect of crystal quality of the CZTSSe layer*

Raman scattering has also been proposed for the assessment of the crystalline quality of different kinds of semiconductor thin films, since the presence of crystalline defects in the material strongly influences the position and shape of Raman peaks [41]. Because of that, it is mandatory to investigate if the crystal quality of the samples can affect the performance of the proposed Raman scattering methodology for determining the anion composition in the CZTSSe solid solutions.

In order to evaluate this issue, two CZTSSe thin films with different crystal quality and same anion composition, were synthesized by selenization at 475 and 525 °C during 60 min of pure CZTS precursors that were prepared by spray deposition of a solution containing CZTS nanocrystals. Structural characterization of the two CZTSSe samples was done by XRD measurements (see Supporting Information Fig. S4). Again, presence of a single and symmetric 112 diffraction peak in both diffractograms and the absence of changes between Raman spectra obtained in the front and back surfaces indicate the existence of an homogeneous composition of the samples through their thickness, Finally, Le Bail refinements preformed on the diffraction patterns of the samples have revealed no significant difference in the lattice parameters values ($a = 5.655(3)$ Å and $c/2 = 5.652(3)$ Å for the sample annealed at 475 °C, while $a = 5.655(3)$ Å and $c/2 = 5.649(3)$ Å for the sample annealed at 525 °C). These results indicate that both samples have same anion composition.

On the other side, cross sectional SEM images of the two samples have shown noticeable differences in the grain size (Fig. 5), indicating that there is a difference in the crystal quality between the samples annealed at different temperatures. Similar behavior in the crystal quality with annealing at different temperatures was observed for pure CZTS thin films, as reported in Ref. [42].

Fig. 5 presents the Raman spectra of the two samples measured with 532 nm excitation wavelength. Appearance of the broad peak at 325 $cm^{-1}$, indicates the presence of S in the samples, which implies that the films have not been completely selenized, but rather they are CZTSSe solid solutions (in agreement with XRD results). Additionally, there is a noticeable broadening of the main Se-like peak at 196 $cm^{-1}$ in the case of 475 °C annealed sample (as shown in the inset in Fig. 5). This broadening is attributed to phonon confinement effects due to the poorer crystal quality and higher density of defects in this sample [41], in agreement with the SEM observations.

Application of the methodology and Eq. (1) for calculating the anion composition from Raman spectra of these two samples, has led to results of $[S]/([S]+[Se]) = 0.075(17)$ and $[S]/([S]+[Se]) = 0.079(17)$ for the films annealed at 475 and 525 °C respectively. Since the differences in the $[S]/([S]+[Se])$ values are within the experimental error, it is concluded that these two samples have same anion compositions based on the Raman scattering measurements, which is in agreement with XRD results. This confirms the validity of the proposed methodology in spite of the differences in the corresponding Raman spectra determined by the differences in the crystalline quality of the samples.

Based on these results, it can be concluded that the methodology for the quantitative analysis of the anion composition from Raman spectra is not affected by the crystal quality of the samples. This is explained by the fact that disorder effects related to the presence of defects affect all peaks in the Raman spectra (though the changes are usually mostly noticeable in the most intensive peaks). This explains the absence of significant changes in the ratio of intensities of the peaks on which the proposed methodology is based.

*3.2.3. Effect of experimental conditions on the proposed methodology: analysis of data from the literature*

In order to prove the independency of the performance of the proposed methodology from the experimental conditions used

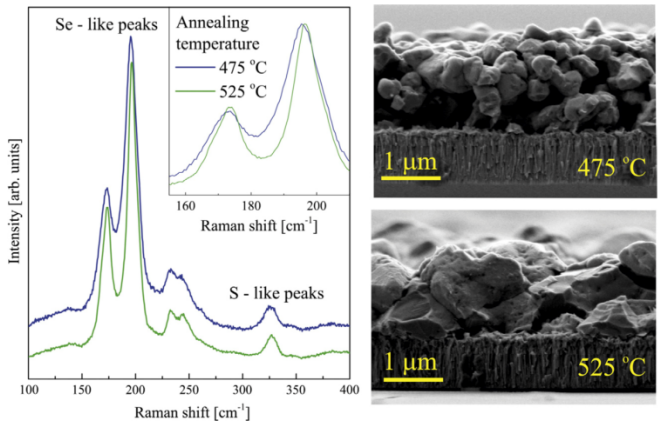


**Fig. 5.** Raman spectra measured with 532.0 nm excitation wavelength and cross sectional SEM images of two polycrystalline CZTSSe thin films annealed at 457 and 525 °C.

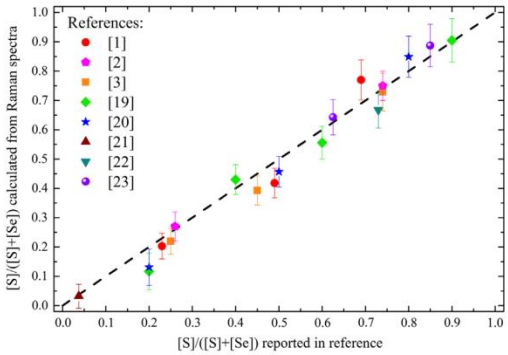


**Fig. 6.** Comparison of the [S]/([S] + [Se]) ratio calculated from the methodology proposed in this work (dashed line) with the values reported in the literature.

for the fabrication of the samples and for the Raman scattering measurements, the methodology has been applied to the analysis of Raman spectra from different types of CZTSSe samples (monograins, nanocrystals, powders and thin films) that have been reported in the literature [1–3,19–23]. Application of Eq. (1) on the Raman spectra reported in these references has allowed calculating the anion compositions of these samples. Fig. 6 presents the comparison of [S]/([S] + [Se]) ratios obtained from the analysis of the Raman spectra with the values reported for each sample in the corresponding reference. As shown in Fig. 6, estimation of the [S]/([S] + [Se]) ratio using the methodology developed in this work gives for all the analyzed cases values that are in good agreement with the reported ones in the literature. This gives a strong support to the validity of the developed methodology that can be applied independently on the experimental conditions used for the measurement of the Raman spectra.

## 4. Conclusions

This work describes a methodology that has been developed for the quantitative determination of the anion composition of CZTSSe solid solutions using Raman spectroscopy. The methodology is based on the analysis of the integral intensity measured in the spectral regions characteristic of only S vibrational modes (between 270 $cm^{-1}$ and 380 $cm^{-1}$) and of vibrational modes involving only Se and also both kinds of anions (between 150 $cm^{-1}$ and 260 $cm^{-1}$). Calibration of the methodology was done using reference CZTSSe powder samples synthesized by solid state reaction method, which compositions were measured by electron micro probe analysis. The validity of the methodology has been tested in different kinds of samples, including photovoltaic grade layers with different compositions (from the whole range of compositions from pure selenide to pure sulfide compounds) and layers with different crystalline quality and same composition. A strong support on the performance of the methodology has been obtained from the analysis of a wide range of CZTSSe samples fabricated by different methods using Raman spectra reported in the literature. The good agreement obtained in the whole range of compositions points out the validity of the proposed methodology for the simple non destructive assessment of the anion composition of different kinds of CZTSSe samples (thin films, powders, nanocrystals, monograins, etc.) independently on the experimental conditions used for the Raman scattering measurements.

## Acknowledgements

The research leading to these results has received funding from the European Union's Seventh Framework Program FP7/2007–2013 under Grant agreement no. 284486 (SCALENANO), the People Programme (Marie Curie Actions) under REA Grant agreement no. 316488 (KESTCELLS) and European Regional Development Founds (ERDF, FEDER Programa Competitivitat de Catalunya 2007–2013). Authors from IREC and Univ. of Barcelona belong to the M-2E (Electronic Materials for Energy) Consolidated Research Group and the XaRMAE Network of Excellence on Materials for Energy of the "Generalitat de Catalunya". V.I. for the "Juan de la Cierva" Fellowship (JCI-2011-10782), E.S. for the "Ramon y Cajal" Fellowship (RYC-2011-09212) and H.X. thanks support from the "China Scholarship Council" fellowship (CSC No. 201206340113).

## Appendix A. Supplementary material

Supplementary data associated with this article can be found, in the online version, at http://dx.doi.org/10.1016/j.jallcom.2014.12.175.

## References

[1] J. He, L. Sun, S. Chen, Y. Chen, P. Yang, J. Chu, J. Alloys Comp. 511 (2012) 129–132.
[2] A. Fairbrother, X. Fontané, V. Izquierdo-Roca, M. Espindola-Rodriguez, S. López-Marino, M. Placidi, J. López-García, A. Pérez-Rodríguez, E. Saucedo, ChemPhysChem 14 (2013) 1836–1843.
[3] M. Grossberg, J. Krustok, J. Raudoja, K. Timmo, M. Altosaar, T. Raadik, Thin Solid Films 519 (2011) 7403–7406.
[4] A. Singh, S. Singh, S. Levcenko, T. Unold, F. Laffir, K.M. Ryan, Angew. Chem., Int. Ed. 52 (2013) 9120–9124.
[5] W. Sun, X. Geng, J.C. Armstrong, J. Cui, T.-P. Chen, in: IEEE 40th Photovolt. Spec. Conf. PVSC 2014, 2014, pp. 0421–0424.
[6] W. Wang, M.T. Winkler, O. Gunawan, T. Gokmen, T.K. Todorov, Y. Zhu, D.B. Mitzi, Adv. Energy Mater. 4 (2014) 1301465.
[7] M. Dimitrievska, H. Xie, A. Fairbrother, X. Fontané, G. Gurieva, E. Saucedo, Al. Pérez-Rodríguez, S. Schorr, V. Izquierdo-Roca, Appl. Phys. Lett. 105 (2014) 031913.
[8] A. Fairbrother, L. Fourdrinier, X. Fontané, V. Izquierdo-Roca, M. Dimitrievska, A. Pérez-Rodríguez, E. Saucedo, J. Phys. Chem. C 118 (2014) 17291–17298.
[9] S. Das, K.C. Mandal, Mater. Res. Bull. 57 (2014) 135–139.
[10] M. Salvador, S.M. Vorpahl, H. Xin, W. Williamson, G. Shao, D.U. Karatay, H.W. Hillhouse, D.S. Ginger, Nano Lett. (2014), http://dx.doi.org/10.1021/nl503068h.
[11] M.I. Amal, S.H. Lee, K.H. Kim, Curr. Appl. Phys. 14 (2014) 916–921.
[12] X. Yin, C. Tang, L. Sun, Z. Shen, H. Gong, Chem. Mater. 26 (2014) 2005–2014.
[13] V. Izquierdo-Roca, R. Caballero, X. Fontané, C.A. Kaufmann, J. Álvarez-García, L. Calvo-Barrio, E. Saucedo, A. Pérez-Rodríguez, J.R. Morante, H.W. Schock, Thin Solid Films 519 (2011) 7300–7303.
[14] Y. Xie, H. Chen, A. Li, X. Zhu, L. Zhang, M. Qin, Y. Wang, Y. Liu, F. Huang, J. Mater. Chem. A 2 (2014) 13237–13240.
[15] C. Insignares-Cuello, C. Broussillou, V. Bermúdez, E. Saucedo, A. Pérez-Rodríguez, V. Izquierdo-Roca, Appl. Phys. Lett. 105 (2014) 021905.
[16] J. Chantana, D. Hironiwa, T. Watanabe, S. Teraji, K. Kawamura, T. Minemoto, Thin Solid Films (2014), http://dx.doi.org/10.1016/j.tsf.2014.10.097.
[17] M. Wang, S.K. Batabyal, H.M. Lim, Z. Li, Y.M. Lam, J. Alloys Comp. 618 (2015) 522–526.
[18] M. Dimitrievska, H. Xie, G. Gurieva, X. Fontane, A. Fairbrother, R. Gunder, E. Saucedo, A. Perez-Rodriguez, S. Schorr, V. Izquierdo-Roca, in: IEEE 40th Photovolt. Spec. Conf. PVSC 2014, 2014, pp. 33–36.
[19] S. Ji, T. Shi, X. Qiu, J. Zhang, G. Xu, C. Chen, Z. Jiang, C. Ye, Sci. Rep. 3 (2013) 2733.
[20] A. Nagaoka, K. Yoshino, H. Taniguchi, T. Taniyama, K. Kakimoto, H. Miyake, J. Cryst. Growth 386 (2014) 204–207.
[21] L. Grenet, S. Bernardi, D. Kohen, C. Lepoittevin, S. Noël, N. Karst, A. Brioude, S. Perraud, H. Mariette, Sol. Energy Mater. Sol. Cells 101 (2012) 11–14.
[22] K. Muska, M. Kauk-Kuusik, M. Grossberg, M. Altosaar, M. Pilvet, T. Varema, T. Varema, K. Timmo, O. Volobujeva, A. Mere, Thin Solid Films 535 (2013) 35–38.
[23] S. Kim, M. Oh, W.K. Kim, Thin Solid Films 549 (2013) 59–64.
[24] A. Fairbrother, E. García-Hemme, V. Izquierdo-Roca, X. Fontané, F.A. Pulgarín-Agudelo, O. Vigil-Galán, A. Pérez-Rodríguez, E. Saucedo, J. Am. Chem. Soc. 134 (2012) 8018–8021.
[25] S. López-Marino, Y. Sánchez, M. Placidi, A. Fairbrother, M. Espindola-Rodríguez, X. Fontané, V. Izquierdo-Roca, J. López-García, L. Calvo-Barrio, A. Pérez-Rodríguez, E. Saucedo, Chem. – Eur. J. 19 (2013) 14814–14822.

[26] A. Carrete, A. Shavel, X. Fontané, J. Montserrat, J. Fan, M. Ibáñez, E. Saucedo, A. Pérez-Rodríguez, A. Cabot, J. Am. Chem. Soc. 135 (2013) 15982–15985.
[27] H. Xie, Y. Sánchez, S. López-Marino, M. Espíndola-Rodríguez, M. Neuschitzer, D. Sylla, A. Fairbrother, V. Izquierdo-Roca, A. Pérez-Rodríguez, E. Saucedo, ACS Appl. Mater. Interfaces 6 (15) (2014) 12744–12751.
[28] A. Nagoya, R. Asahi, R. Wahl, G. Kresse, Phys. Rev. B 81 (2010) 113202.
[29] J. Rodriguez-Carvajal, T. Roisnel, Physica B 192 (1993) 55–69.
[30] L.W. Finger, D.E. Cox, A.P. Jephcoat, J. Appl. Crystallogr. 27 (1994) 892–900.
[31] M. Dimitrievska, A. Fairbrother, X. Fontané, T. Jawhari, V. Izquierdo-Roca, E. Saucedo, A. Pérez-Rodríguez, Appl. Phys. Lett. 104 (2014) 021901.
[32] M. Guc, S. Levcenko, V. Izquierdo-Roca, X. Fontané, E. Arushanov, A. Pérez-Rodríguez, J. Appl. Phys. 114 (2013) 193514.
[33] P.M.P. Salomé, J. Malaquias, P.A. Fernandes, M.S. Ferreira, A.F. da Cunha, J.P. Leitão, J.C. González, F.M. Matinaga, Sol. Energy Mater. Sol. Cells 101 (2012) 147–153.
[34] S. Siebentritt, S. Schorr, Prog. Photovolt. Res. Appl. 20 (2012) 512–519.
[35] A. Khare, B. Himmetoglu, M. Cococcioni, E.S. Aydil, J. Appl. Phys. 111 (2012) 123704.
[36] O. Amiri, M. Salavati-Niasari, M. Sabet, D. Ghanbari, Mater. Sci. Semicond. Process. 16 (2013) 1485–1494.
[37] S.M. Hosseinpour-Mashkani, M. Salavati-Niasari, F. Mohandes, K. Venkateswara-Rao, Mater. Sci. Semicond. Process. 16 (2013) 390–402.
[38] S.M. Hosseinpour-Mashkani, F. Mohandes, M. Salavati-Niasari, K. Venkateswara-Rao, Mater. Res. Bull. 47 (2012) 3148–3159.
[39] M. Sabet, M. Salavati-Niasari, D. Ghanbari, O. Amiri, M. Yousefi, Mater. Sci. Semicond. Process. 16 (2013) 696–704.
[40] S. Lopez-Marino, M. Placidi, A. Perez-Tomas, J. Llobet, V. Izquierdo-Roca, X. Fontane, A. Fairbrother, M. Espíndola-Rodríguez, D. Sylla, A. Pérez-Rodríguez, E. Saucedo, J. Mater. Chem. A 1 (2013) 8338–8343.
[41] M. Dimitrievska, A. Fairbrother, A. Pérez-Rodríguez, E. Saucedo, V. Izquierdo-Roca, Acta Mater. 70 (2014) 272–280.
[42] A. Fairbrother, X. Fontané, V. Izquierdo-Roca, M. Espíndola-Rodríguez, S. López-Marino, M. Placidi, L. Calvo-Barrio, A. Pérez-Rodríguez, E. Saucedo, Sol. Energy Mater. Sol. Cells 112 (2013) 97–105.

# Supporting Information For

# Raman scattering quantitative analysis of the anion chemical composition in kesterite $Cu_2ZnSn(S_xSe_{1-x})_4$ solid solutions

Mirjana Dimitrievska[1], Galina Gurieva[2], Haibing Xie[1], Alex Carrete[1], Andreu Cabot[1, 3], Edgardo Saucedo[1], Alejandro Pérez-Rodríguez[1, 4], Susan Schorr[2, 5] and Victor Izquierdo-Roca[1*]

1. Catalonia Institute for Energy Research (IREC), Jardins de les Dones de Negre 1 2pl., 08930 Sant Adrià del Besòs, Barcelona, Spain.
2. Helmholtz Centre Berlin for Materials and Energy, Department Crystallography, Hahn-Meitner-Platz 1, 14109 Berlin, Germany.
3. Institució Catalana de Recerca i Estudis Avançats - ICREA, Barcelona, Spain
4. IN$^2$UB, Departament d'Electrònica, Universitat de Barcelona, C. Martí i Franquès 1, 08028 Barcelona, Spain.
5. Freie Universität Berlin, Institute of Geological Sciences, Malteserstr. 74-100, 12249 Berlin, Germany.

* Contact email: vizquierdo@irec.cat

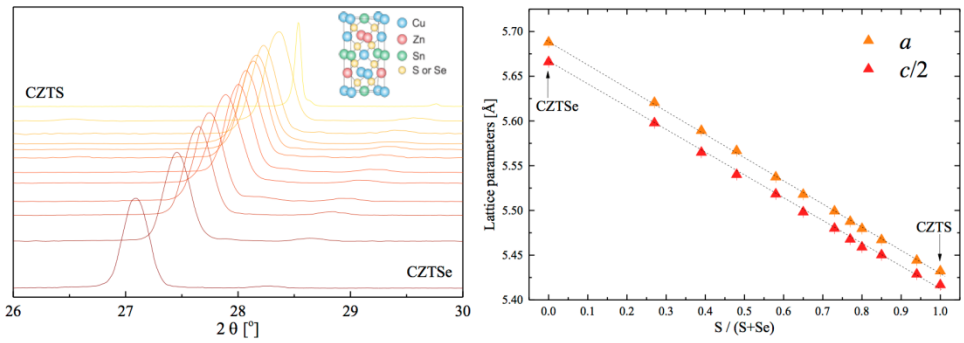


Figure S1. Left: Diffraction patterns centered at the 112 reflection kesterite peak measured for CZTSSe solid solutions. Right: Lattice parameters in dependence of anion S/(S+Se) composition ratio

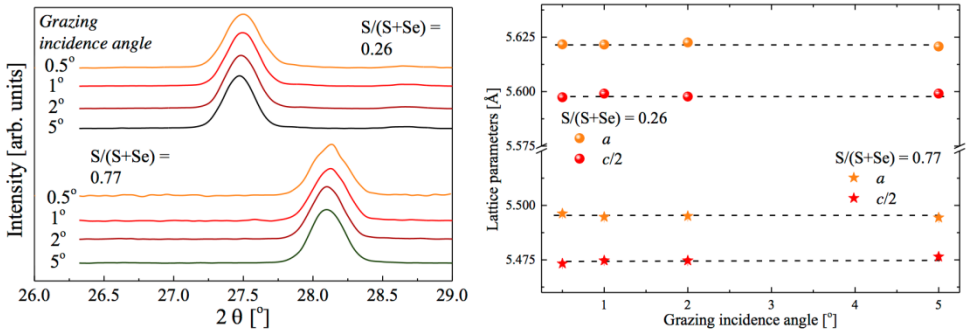


Figure S2. Left: Representative diffraction patterns centered at the 112 reflection kesterite peak measured for CZTSSe solid solutions for different grazing incidence angle. Right: Lattice parameters in dependence of grazing incidence angle calculated by Le Bail refinements. No significant shift in peak position or change in the lattice parameters was detected.

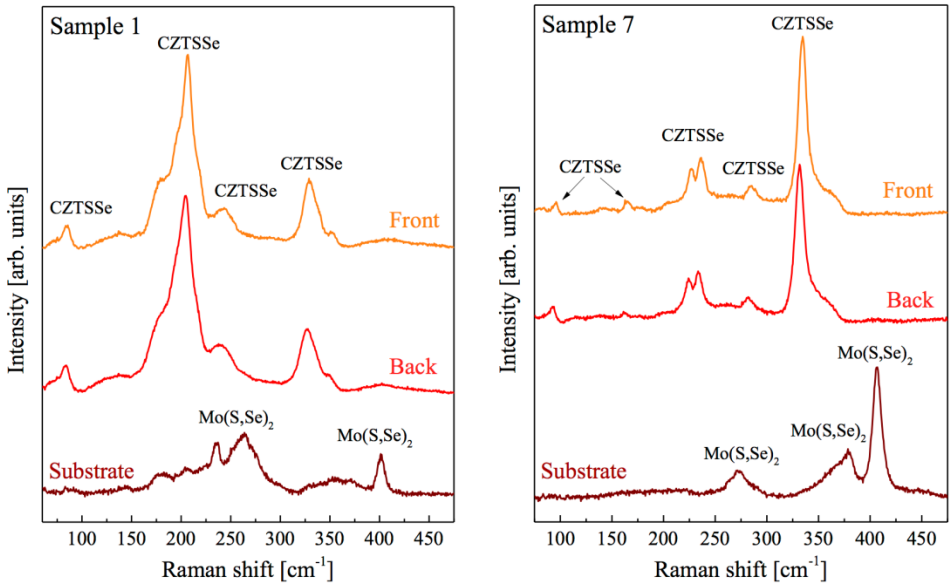


Figure S3. Raman spectra of front, back and substrate surfaces for two representative samples measured with 532 nm excitation wavelength.

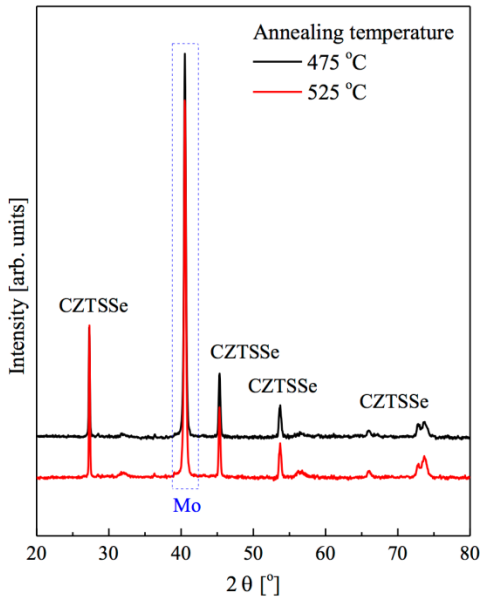


Figure S4. Diffraction patterns of CZTSSe solid solution thin films annealed at 425 and 525 °C for 60 min. No significant shift in peak positions was detected, implying that the anion compositions of the samples are approximately the same.

PCCP

PAPER

View Article Online
View Journal

# Resonant Raman scattering of $ZnS_xSe_{1-x}$ solid solutions: the role of S and Se electronic states

M. Dimitrievska,*[a] H. Xie,[a] A. J. Jackson,[b] X. Fontané,[a] M. Espíndola-Rodríguez,[a] E. Saucedo,[a] A. Pérez-Rodríguez,[ac] A. Walsh[b] and V. Izquierdo-Roca*[a]

Cite this: DOI: 10.1039/c5cp04498g

Received 30th July 2015,
Accepted 27th August 2015

DOI: 10.1039/c5cp04498g

www.rsc.org/pccp

A comprehensive Raman resonance scattering study of $ZnS_xSe_{1-x}$ (ZnSSe) solid solutions over the whole compositional range ($0 \leq x \leq 1$) has been carried out using 325 and 455 nm excitation wavelengths. The Raman scattering intensities of LO ZnS-like and ZnSe-like phonon modes, corresponding to pure S and Se vibrations, respectively, are revealed to be significantly enhanced when excited with 325 nm excitation in the case of S vibrations, and with 455 nm in the case of Se vibrations. This behavior is explained by the interaction of the excitation photons with the corresponding S or Se electronic states in the conduction band, and further confirmed by first principles simulations. These findings advance the fundamental understanding of the coupling between the electronic transitions and photons in the case of Raman resonance effects, and provide inputs for further studies of lattice dynamics, especially in the case of chalcogenide materials. Additionally, the coexistence of modes corresponding to only S vibrations and only Se vibrations in the ZnSSe alloys makes these results applicable for the compositional assessment of ZnSSe compounds.

## Introduction

Wide band gap II–IV semiconductor binaries and their solid solutions have gained considerable attention due to their potential application in electronic and optoelectronic devices. The efficient miscibility of ZnS and ZnSe compounds in the $ZnS_xSe_{1-x}$ (ZnSSe) solid solutions over the whole compositional range, $0 \leq x \leq 1$, enables easy tuning of the band gap energies (ranging from 2.67 eV (ZnSe) to 3.66 eV (ZnS)) and the lattice constants, which additionally enhances the potential application of these materials. ZnSSe compounds have been reported as highly suitable and promising materials for blue lasers, light emitting diodes, light emitters, and wavelength tunable UV photodetectors, due to their wide direct band gap and high photoresistivity.[1–4] Polycrystalline ZnSSe compounds are excellent candidates for window and/or buffer layers in thin film heterojunction solar cells and promising alternatives to the presently explored materials such as CdS, which contain toxic Cd.[5,6] Additionally, because of its low absorption at infrared wavelength and exciton binding energy, ZnSSe is considered as a future material in the production of biomedical labels, output couplers, lenses, and optically controlled switches. Changing the ratio of S to Se of ZnSSe compounds leads to tuning of the electron affinity and electrical properties which greatly enhances the blue response of the material.[7] ZnSSe may also appear as a secondary phase in other multinary compounds, like $Cu_2ZnSn(S,Se)_4$, which have shown promising results for application as thin film absorber layers in solar cells.[8,9] It has been shown that ZnSSe secondary phases, besides having unfavorable effects on the conversion efficiency of solar cells, are also quite challenging for detection using standard characterization techniques such as X-ray diffraction (XRD). For all these reasons, synthesis and characterization of ZnSSe materials is a very attractive topic.

Until now, a wide range of characterization studies on the ZnSSe thin films have been reported, including structural, electrical and optical property variations depending on the S/Se ratio.[2,5,7,10–16] Raman spectroscopy as such has been extensively used for investigating the lattice vibration dynamics in these systems.[12,14,17,18] Raman scattering is a powerful non-destructive method which can provide useful information on the structure, morphology and chemical composition of semiconductor materials, as well as on the photon–electron and electron–phonon interactions occurring in these materials. Although many studies have been devoted to compositional dependence of the optical modes in the ZnSSe systems, most are usually done using standard non-resonant Raman conditions. The main disadvantage of the standard excitation methods is the observation of high number of Raman modes with relatively low intensity, which leads to difficulties in the determination of peak

[a] *Catalonia Institute for Energy Research (IREC), Jardins de les Dones de Negre 1, 08930 Sant Adrià de Besòs, Spain. E-mail: mdimitrievska@irec.cat, vizquierdo@irec.cat*
[b] *Centre for Sustainable Chemical Technologies and Department of Chemistry, University of Bath, Claverton Down, Bath BA2 7AY, UK*
[c] *IN²UB, University of Barcelona, C. Martí Franquès 1, 08028 Barcelona, Spain*

positions and phase identification. This is due to very weak Raman scattering efficiency of ZnSSe compounds caused by weak photon–matter interaction under standard excitations (514 and 532 nm lasers).[19,20] In contrast, resonance Raman methods allow measuring spectra, which are simpler in the sense that the number of observed independent modes is lower and at the same time, with several orders of magnitude higher intensity.[20–22] This allows easier identification of the modes and facilitates their correlation with other properties, such as composition, impurities, defects, crystallinity, and electronic band structure. Additionally, the use of resonant Raman conditions allows the use of shorter integration times, usually of the order of seconds, which is a significant advantage when compared to other characterization methods, especially in the case of nanosystems, where normally long integration times are required for the structural and electrical characterization.

In this work a study of the vibrational properties of ZnSSe solid solutions, over the full range of anion compositions, $0 \leq [S]/([S] + [Se]) \leq 1$, was made using resonance Raman spectroscopy. A special focus is put on the changes in the integral intensity of the Raman modes sensitive to anion vibrations, with the variations in the excitation energy. It is observed that Raman modes corresponding to S vibrations are exhibiting resonance behavior in the case of 325 nm excitation, while Raman modes corresponding to Se vibrations become resonant when probed with 455 nm excitation. This behavior is explained by the interaction of the excitation photons with the corresponding S or Se states in the electronic band structure, and confirmed by first principles calculations. The understanding of this kind of resonance effect could improve fundamental knowledge not only of the ZnSSe compounds, but also other types of mixed chalcogenide materials, including Cd-(S,Se) and Mo-$(S,Se)_2$. Finally, these results can be applied for the development of a simple and non-destructive optical methodology for the quantitative measurement of [S]/([S] + [Se]) anion composition in ZnSSe solid solutions by means of Raman spectroscopy.

## Experimental

### Thin film formation

Zn precursors of 80 nm were deposited by DC-magnetron sputtering (Ac450 Alliance Concepts) using a power density of 1.27 W $cm^{-2}$ onto glass substrates. Binary ZnS thin films were produced by reactive annealing of the Zn precursors under a sulfur atmosphere at 550 °C, 1 bar Ar pressure for 30 min, and using a crucible with 50 mg of sulfur powder (Alfa-Aesar, 99.995%). ZnSe thin films were produced by reactive annealing under a selenium atmosphere at 550 °C for 30 min with the flow of Ar to maintain a pressure of 1 mbar, and with a crucible containing 50 mg of selenium powder (Alfa-Aesar, 99.999%). To form ZnSSe alloy films a single-step sulfo-selenization annealing was used.[8] This process is similar to that used for the pure ZnS or ZnSe films, but varying the ratio of the mixture of sulfur and selenium while maintaining the total weight of the mixture of 50 mg. Two annealing temperature profiles were employed; "one step profile": 550 °C, 30 min, and 1 mbar or 1 bar; and "two step profile": first 200 °C in 1 mbar atmosphere and then 550 °C for 30 min in 1 bar atmosphere, which is proved to be beneficial for obtaining various Se-rich thin films. The heating rate for all thermal treatments was 20 °C $min^{-1}$ and the cooling process was allowed to proceed naturally.

### Characterization

Raman scattering measurements were performed in back scattering configuration using a LabRam HR800-UV and DXR™xi Raman Imaging Microscope. For the HR800-UV system, a gas HeCd laser with a wavelength of 325 nm was used for excitation. In this system excitation and light collection were made using an Olympus metallographic microscope with a laser spot diameter of the order of 1–2 μm. To avoid effects in the spectra related to potential microscopic inhomogeneities, the spot was rastered over an area of 30 × 30 $\mu m^2$. Furthermore, the DXR™xi Raman Imaging Microscope system works coupled with a 455 nm laser, with a 1–2 μm diameter spot size on the sample. In all cases, and to avoid the presence of thermal effects in the spectra, the power excitation density on the surface of the samples was around 50 W $cm^{-2}$. Under these experimental measurement conditions no thermal effects are observed in the spectra. This has been corroborated by the analysis of spectra measured with different excitation powers. The first-order Raman spectrum of monocrystalline Si was measured as a reference before and after acquisition of each Raman spectrum, and the spectra were corrected with respect to the Si line at 520 $cm^{-1}$.

XRD patterns were measured on a Siemens D500 diffractometer with Cu-Kα-radiation ($\lambda$ = 1.54056 Å) in a $\theta$–$2\theta$ configuration. Refinements of the lattice constant values were carried out by Le Bail analysis using the FullProf package.[23]

The band gap energies were determined from the ultraviolet-visible (UV-Vis) spectra which were obtained using a Perkin Elmer Lambda 950 UV/VIS spectrometer.

The composition of the samples was measured using X-ray fluorescence (XRF) spectroscopy performed on a Fisherscope XVD system.

The synthesized films have been imaged by scanning electron microscopy (SEM) using a ZEISS Series Auriga microscope with 5 kV acceleration voltage.

### Theoretical calculations

Electronic structure calculations within density functional theory (DFT) were carried out within periodic boundary conditions as implemented in VASP, a quantum chemistry package using plane-wave basis sets.[24] 8-atom unit cells were formed for ZnS, a ZnSSe alloy with 3:1 S:Se ratio, and ZnSe (Fig. 1). The alloy cell of composition $Zn_4S_3Se$ provides a mixture of Zn–S and Zn–Se interactions for comparison with the binary compounds; however, the effects of long-range disorder are neglected in this work. The initial lattice parameters were $a$ = 5.383 Å for ZnS and the alloy cell, and $a$ = 5.667 Å for ZnSe, based on crystallographic studies;[25,26] these structures were optimized with the PBEsol exchange–correlation functional, using projector-augmented wave (PAW) pseudopotentials optimized for the PBE functional

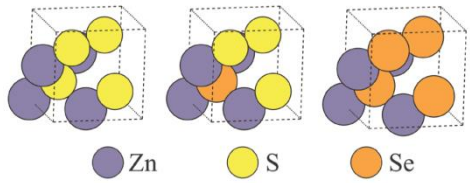


Fig. 1 Unit cells for theoretical calculations. Zn (indigo), S (yellow) and Se (orange) atoms in 8-atom ZnS ($a$ = 5.363 Å), alloy ($a$ = 5.431 Å) and ZnSe ($a$ = 5.642 Å) unit cells.

and including the Zn 3d states as valence electrons. The basis-set energy cutoff was 500 eV and the Brillouin zone was sampled with a 5 × 5 × 5 $\Gamma$-centered $k$-point grid (reduced by symmetry to 10 irreducible points).[27] The ionic positions and lattice parameters were optimized by a succession of conjugate gradient procedures until the difference in total energy between relaxation steps was reduced to below 1 meV. The structures optimized with PBEsol were then used for electronic structure calculations with the non-local screened hybrid HSE06 exchange–correlation functional.[28] The same pseudopotentials and energy cutoff were used for these calculations, while the $k$-point mesh density was increased to 15 × 15 × 15 (reduced by symmetry to 120 points). In these cases the initial electronic structure convergence was achieved by Gaussian smearing ($\sigma$ = 0.05 eV), and the density of states was refined by further SCF iterations using the tetrahedron method with Blöchl corrections.

## Results and discussion

The crystal structure of ZnSSe solid solutions was characterized by XRD measurements from which representative patterns are presented in Fig. 2(a). All main diffraction peaks have been identified for the zinc-blende structure,[29] and no evidence of any other phases or impurities has been found. Furthermore, the presence of a single and symmetric (111) diffraction peak in all measured patterns implies that all samples are homogeneously alloyed rather than a mixture of ZnS and ZnSe phases. The systematic shift in peak positions toward higher angles as the [S]/([S] + [Se]) ratio increases correlates with the replacement of smaller S atoms with larger Se atoms, which in turn leads to a decrease in the lattice constants. The lattice constants of the ZnSSe solid solutions were obtained as a result of the Le Bail analysis, for which the zinc-blende structure was used as a starting model for the refinements. By assuming the validity of Vegard's law and using the lattice constants calculated from the XRD data, the anion compositions [S]/([S] + [Se]) of the ZnSSe thin films were determined and are presented in Fig. 2(b). The obtained results are in agreement with the previously reported data.[13,30–32]

The band gap energies of the ZnSSe compounds have been evaluated from the UV-vis absorption spectra using the Tauc relation:[33]

$$(\alpha h\nu)^n = C(E - E_g) \quad (1)$$

where $\alpha$ is the absorption coefficient, $h$ is Planck's constant, $\nu$ is the frequency, $n$ = 2 for a direct band gap semiconductor material (such as ZnSSe), $C$ is a proportionality constant, $E$ is the energy (equal to $h\nu$), and $E_g$ is the band gap energy. The estimated band gap energies for each anion composition of the ZnSSe alloys are shown in Fig. 2(b). It is observed that the band gap energies can be tuned from 3.66 eV in pure ZnS thin films to 2.67 eV in pure ZnSe thin films, just by changing the anion composition in the samples. The change in the band gap energies with the anion composition $x$ = [S]/([S] + [Se]) shows nonlinear behavior and can be fitted as a quadratic function of $x$:

$$E_g(x) = xE_g(\mathrm{ZnS}) + (1 - x)E_g(\mathrm{ZnS}) - x(1 - x)b \quad (2)$$

where $E_g$(ZnSe), $E_g$(ZnS), and $E_g(x)$ are the band gap energies of ZnS, ZnSe, and their alloy, respectively, while $b$ is the bowing constant, and in this case the best fit was obtained for $b$ = 0.70(6), which is in agreement with the previously reported values.[34]

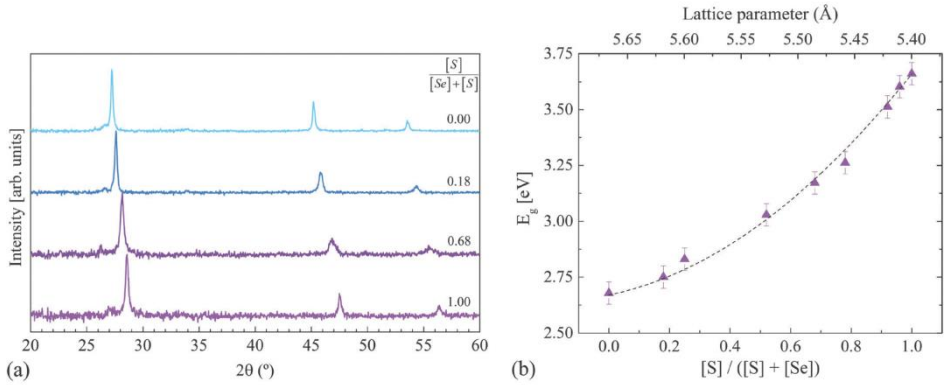


Fig. 2 (a) Representative XRD patterns of ZnSSe solid solutions for different anion compositions and (b) band gap energies depending on [S]/([S] + [Se]) compositions and lattice constants.

The Raman scattering spectra of ZnSSe solid solutions measured under ultra-violet (UV) ($\lambda$ = 325 nm, 3.82 eV) and blue ($\lambda$ = 455 nm, 2.72 eV) excitations are shown in Fig. 3. Raman spectra of the pure ZnS measured under resonant conditions (UV excitation) are characterized by the strongly enhanced longitudinal optical (LO) phonon mode observed at 348 $cm^{-1}$.[20] This mode is attributed to vibrations

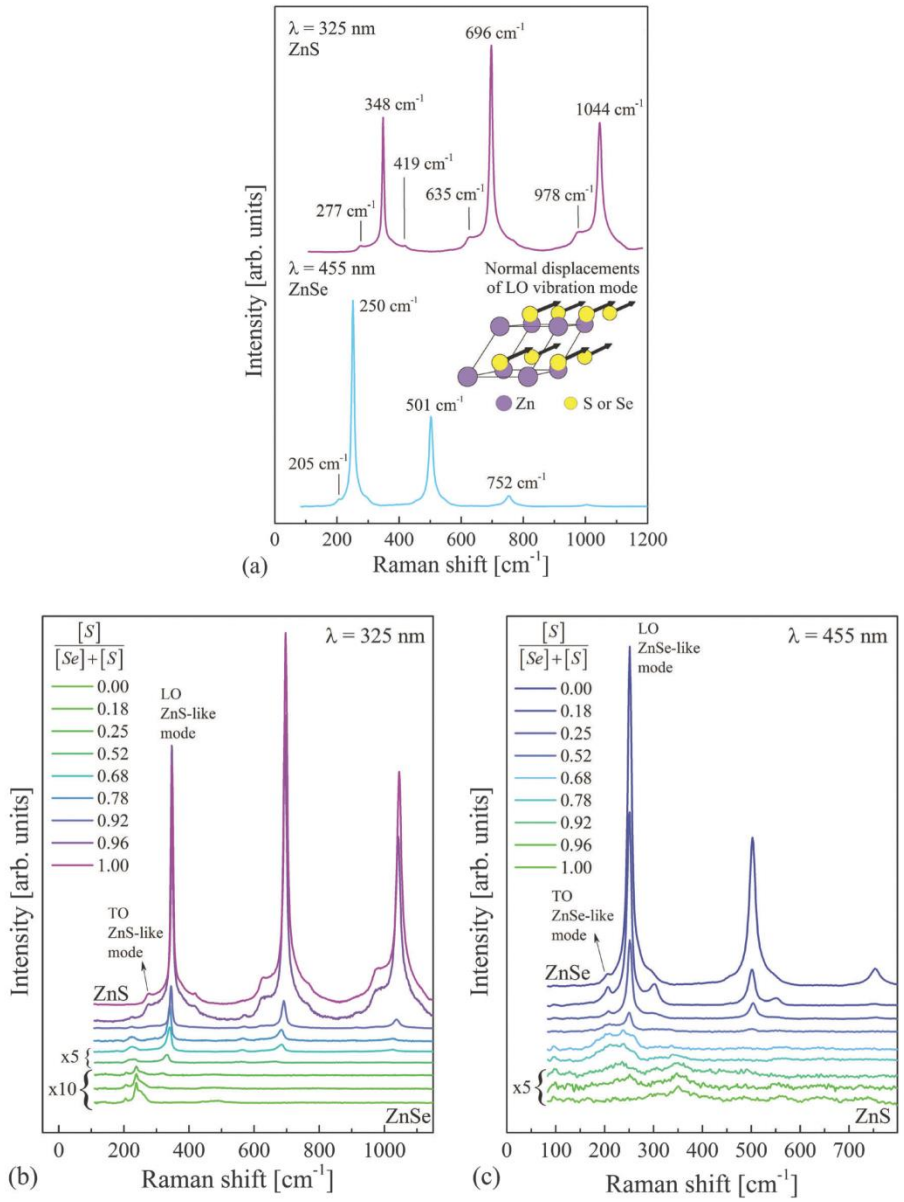


**Fig. 3** (a) Normalized reference Raman spectra of pure ZnS and ZnSe compounds with the identification of modes measured under resonant conditions; the inset shows the normal displacements of the LO phonon mode for pure ZnS or ZnSe, with the arrows indicating the direction of the movement of the atoms; (b) and (c) Raman spectra of ZnSSe solid solutions measured with 325 and 455 nm excitation wavelengths. Some of the low intensity spectra in both cases were multiplied ×5 or ×10 for more details, as labeled in the figure.

 

of only S anions in the lattice. An illustration of the normal displacements of the LO phonon mode, obtained from the first principles simulations, is presented in the inset of Fig. 3(a). Second (LO2) and third (LO3) orders of this mode are also observed at 696 and 1044 $cm^{-1}$ frequencies, respectively. Additionally, a lower intensity peak is observed at 277 $cm^{-1}$, and attributed to the fundamental transverse optical (TO) phonon mode. Bands at 419, 635 and 978 $cm^{-1}$ are attributed to the higher order combination bands of the fundamental modes.[35] In the case of pure ZnSe, a resonance Raman spectrum is measured under the blue excitation, and characterized by the strongly enhanced LO mode at 250 $cm^{-1}$, attributed to vibrations of only Se anions, and a low intensity TO mode observed at 205 $cm^{-1}$.[36] Again, second (LO2) and third (LO3) order peaks are observed at 501 and 752 $cm^{-1}$, respectively. The first order Raman spectra of ZSSe solid solutions are characterized by the presence of two dominant peaks in the frequency region 270–350 $cm^{-1}$, and two dominant peaks in the frequency region 200–270 $cm^{-1}$. The peaks in the higher frequency region are identified as ZnS-like peaks corresponding to TO and LO phonon modes involving S vibrations, and the peaks in the lower frequency region are identified as ZnSe-like peaks corresponding to TO and LO phonon modes involving Se vibrations.[37,38] This agrees with the existence of a two-mode behavior of these peaks, as previously reported.[17,37,39,40]

The optical phonon frequencies vary with the changes in composition. With the increase in S composition, the LO ZnSe-like peak shifts downward in frequency, while the TO ZnSe-like peak monotonically moves upward. For the very S-rich samples, these two modes almost overlap, and then finally disappear for $x = 1$. Similar behavior is observed for the LO and TO ZnS-like peaks with the increase in the Se composition. The compositional dependence of LO and TO frequencies for both ZnS-like and ZnSe-like peaks is shown in Fig. 4. Solid lines in Fig. 4 present the calculated phonon frequencies of the modes using the modified-random-element-isodisplacement (MREI) model.[17] Additional information about the MREI model, as well as the explanation of the calculation process and the parameter values used for obtaining results presented in Fig. 4, is given in ref. 17. The experimental data presented in Fig. 4 are in good agreement with the model predictions and as well as the previously reported results.[39,40]

Asymmetrical broadening in the low frequency side of the LO ZnS-like peak can be observed with the decrease in the S composition in the Raman spectra measured with 325 nm excitation. Similarly, asymmetrical broadening in a low frequency side of the LO ZnSe-like peak is noticeable in the Raman spectra measured with 455 nm excitation, with the decrease in Se composition. This phenomenon is attributed to the phonon confinement effects arising from the loss of translational symmetry in the crystal caused by the alloy disorder.[39–41]

An interesting phenomenon, which was not previously observed in the ZnSSe systems, is the intensity dependence of the LO ZnS-like and LO ZnSe-like modes with the excitation energy. Fig. 5(a) and (b) present the changes in the intensity of the LO ZnS-like and ZnSe-like modes with respect to the

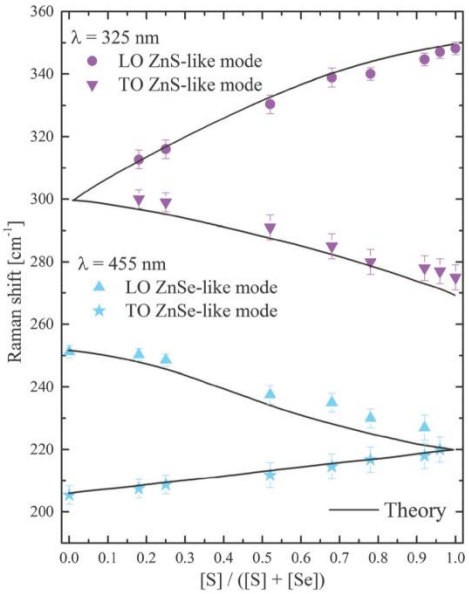


Fig. 4 The optical phonon frequencies of the ZnSe-like and ZnS-like modes as a function of the anion composition [S]/([S] + [Se]). The ZnSe-like and ZnS-like mode frequencies were determined from the resonance Raman spectra measured with 455 and 325 nm excitation wavelength, respectively. The solid lines represent the theoretical frequencies obtained by the modified random-element-isodisplacement model.

difference between the energy band gap and the excitation energy.

Three kinds of resonance behaviors can be observed from the results presented in Fig. 5. In the case of S-rich ZnSSe samples, only LO ZnS-like peaks are enhanced when measured with UV excitation; while LO ZnSe-like peaks do not exhibit resonance behavior for any of the used excitation wavelengths. A reverse situation is observed for the Se-rich ZnSSe samples, where LO ZnSe-peaks are enhanced in the Raman spectra measured with blue excitation; while LO ZnS-like peaks show non-resonance behavior for any of the used excitation wavelengths. Lastly, for the case of intermediate anion compositions, the LO ZnS-like peaks become resonant when using the UV excitation and the LO ZnSe-like peaks become resonant when probed using the blue excitation.

According to these experimental results, UV excitation only enhances modes correlated with vibrations of S anions, while blue excitation only induces resonance effects in modes attributed to vibrations of Se anions. This behavior suggests that UV photons mostly interact with S electronic states, while blue photons interact with Se states. Further explanation of these results can be made by taking into account the electronic band structure of ZnSSe compounds and working principles of the resonance Raman effect.

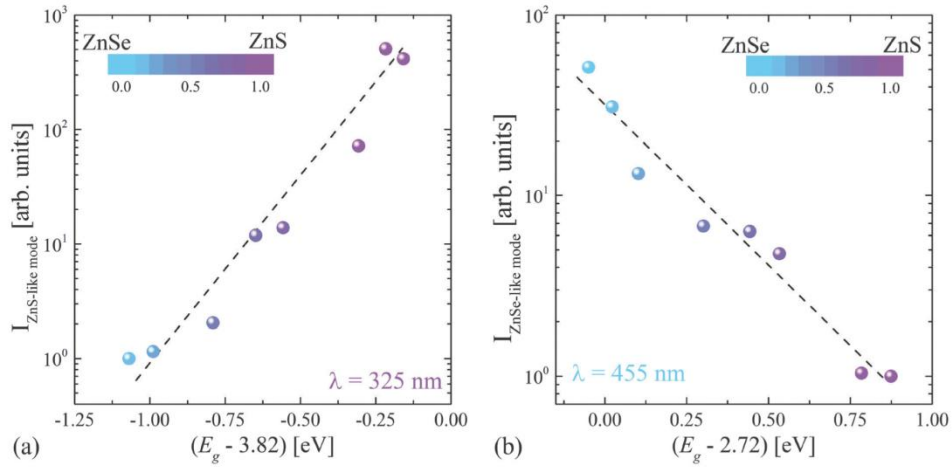


**Fig. 5** Enhancement in the intensity of the (a) LO ZnS-like mode and (b) LO ZnSe-like mode depending on the difference between the band gap energy of the ZnSSe thin films and the excitation energy. Dashed lines are a guide to the eye.

In general, Raman scattering intensity can be defined as:[42,43]

$$I(\omega_i) \propto \omega_s{}^4 |\hat{e}_s \cdot R \cdot \hat{e}_i|^2 \left| \sum_{\alpha\beta} \frac{1}{(E_\alpha - \hbar\omega_i - i\Gamma_\alpha)(E_\beta - \hbar\omega_s - i\Gamma_\beta)} \right|^2 \quad (3)$$

where $\omega_s$ and $\omega_i$ are the scattered and the incoming photon frequencies, respectively; $E_\alpha$ and $E_\beta$ are the energies of the intermediate crystal states, $R$ is the Raman tensor, $\hat{e}_s$ and $\hat{e}_i$ are the scattered and the incident polarization vectors, and $\Gamma_\alpha$ and $\Gamma_\beta$ are damping constants. The first term in eqn (3) represents the dipole transition radiation; the second term represents the Raman selection rules, which is dependent on the crystal symmetry, while the last term represents the resonance effects. As the incident excitation energy is tuned to the energy of the intermediate state, the denominator in eqn (3) becomes smaller, which then leads to the enhancement in the Raman intensity, and thus the resonance effects. Raman resonance effects in semiconductors may be achieved if the excitation energy approaches the band-gap energy, or *via* the interaction of the incident photon with the exciton states or the impurity states.

For the pure ZnS and ZnSe compounds, the energies of the above-gap S and Se states are close to the energy band gap, which are 3.66 and 2.82 eV, respectively.[44] As the energy of the S states is close to the energy of the UV photons (3.82 eV or 325 nm), the interaction between them will result in a decrease in the denominator value in eqn (3), which will then lead to the increase in intensity of the Raman mode associated with this interaction (LO mode). This is why only LO modes will be enhanced in the Raman spectra of ZnS when measured with UV excitation. A similar situation is expected in the case of LO mode in pure ZnSe when probed with blue excitation (2.72 eV or 455 nm).

Previous studies of the electronic structure of Zn chalcogenides identified an increase in the valence band energy of ~0.5 eV between ZnS and ZnSe,[45,46] arising from the lower binding energy of the Se 4p states compared to S 3p. There is a comparable drop in the conduction band energy, due to the larger Zn–Se bond length compared to Zn–S, leading to an overall difference in $E_g$ of ~1.0 eV. In the case of ZnSSe mixtures, both S and Se states are involved. Depending on the anion composition of the solid solution, the electronic density of states is expected to interpolate smoothly between those of the binary compounds.

For crystals with intermediate composition, changes in the S and Se electronic states are low enough to allow the preservation of the resonance excitation behavior of the LO ZnS-like and ZnSe-like modes with the UV and blue excitations, respectively. However, for S-rich or Se-rich alloys this is not the case. As an example of the last situation, Fig. 6 shows the full and species-projected density of states for ZnS, $ZnS_{0.75}Se_{0.25}$ and ZnSe. As can be seen in the case of $ZnS_{0.75}Se_{0.25}$, the above-gap S states are shifted slightly closer to the Fermi level in comparison to the pure ZnS compound, while the above-gap Se states are shifted considerably further from the Fermi level relative to the pure ZnSe compound.

This means that for S-rich ZnSSe samples, interaction between S states and UV photons is expected, due to their similar energies, while no interaction will occur between Se states and blue photons, because of their energy mismatch. This should then lead to resonance behavior of the LO ZnS-like modes, when probed with UV excitation, and non-resonance behavior of LO ZnSe-like modes when probed with blue excitation, which is experimentally observed. An opposite situation is expected in the case of Se-rich samples. Similar resonance effects were also observed in the case of kesterite solid solutions $Cu_2ZnSnS_xSe_{1-x}$.[47]

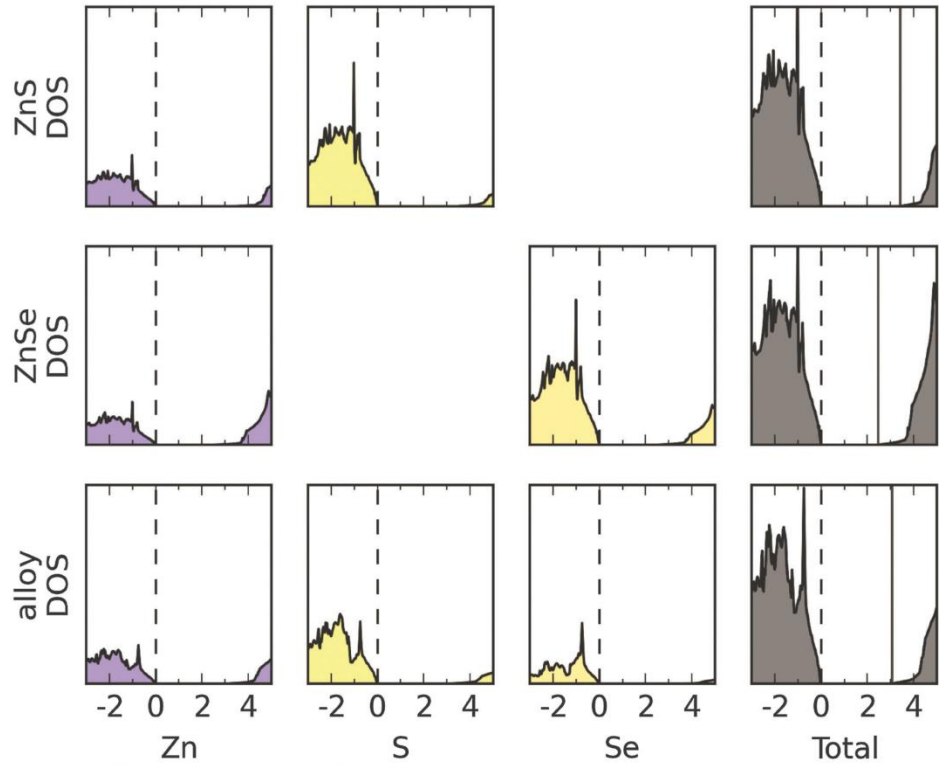


Fig. 6 Partial and total density of states (DOS) for ZnS, ZnSe and $ZnS_{0.75}Se_{0.25}$ alloys obtained from hybrid DFT calculations. Horizontal axes give energy relative to the Fermi level (indicated with a dashed line) in eV. The right-most column represents total DOS; the vertical solid line indicates the conduction band minimum (CBM).

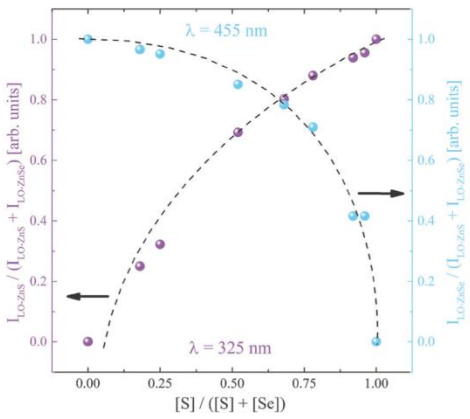


Fig. 7 Anion composition depending on the integral intensity ratio of LO ZnS-like and LO ZnSe-like peaks calculated from Raman spectra measured with 325 and 455 nm excitation.

Finally, these results can be applied for the development of a simple and non-destructive optical methodology for the quantitative measurement of [S]/([S] + [Se]) anion composition in ZnSSe solid solutions by means of Raman spectroscopy, similar to the study presented in ref. 48. Since the intensity of LO ZnS-like and ZnSe-like modes is proportional to the concentration of S and Se in the material, respectively, plotting the integral intensity ratio of these two bands *versus* the anion composition should give the calibration curves which can be later used for the estimation of anion composition in unknown ZnSSe samples. An example of this kind of plot is given in Fig. 7. As shown in the figure, for S-poor compositions changes in the relative intensity of the ZnS-like peak are very sensitive to changes in the alloy composition, while for S-rich compositions changes in the relative intensity of the ZnSe-like peak are very sensitive to changes in the alloy composition. In general, this methodology is completely independent of the experimental conditions of the measurements and of the type of sample, which is another advantage of using Raman spectroscopy for the estimation of the anion composition in this kind of material.

## Conclusions

This work describes joint experimental and theoretical investigation of the Raman resonance effects in ZnSSe solid solutions. Resonance behavior is observed in the Raman modes corresponding to the anion vibrations, when changing the excitation energy from UV (325 nm) to blue (455 nm). Significant enhancement in the Raman intensity of the LO ZnS-like modes, corresponding to pure S vibrations, is observed in cases of S-rich and intermediate compositions when excited with UV energy. On the other side, LO ZnSe-like modes attributed to pure Se vibrations are enhanced in the case of blue excitation for samples with Se-rich and intermediate compositions. This enhancement of only certain Raman modes in the spectra is explained by interaction of the excitation photon with the corresponding S or Se states in the electronic band structure, and confirmed by the first principles calculations. Raman resonance effects in this case are achieved due to the tuning of the excitation energy with the energy of the S or Se electronic states in the conduction band. These findings advance the fundamental understanding of the coupling between the electronic transitions and photons in the case of Raman resonance effects, and provide inputs for further studies of lattice dynamics, especially in the case of chalcogenide materials. Additionally, the application of Raman resonant conditions in the case of this kind of material can be used for developing a simple and non-destructive optical methodology for the quantitative measurement of [S]/([S] + [Se]) anion composition. They should also enable easier characterization of the ZnSSe system, like reducing the integration time of the Raman measurements, which is extremely important in the case of nanosystems.

## Acknowledgements

The research leading to these results has received funding from the People Program (Marie Curie Actions) of the European Union's Seventh Framework Program FP7/2007-2013/under REA grant agreement no. 316488 (KESTCELLS). The authors from IREC and IN$^2$UB belong to the M-2E (Electronic Materials for Energy) Consolidated Research Group and the XaRMAE Network of Excellence on Materials for Energy of the "Generalitat de Catalunya". E.S. thanks the Government of Spain for the "Ramon y Cajal" fellowship (RYC-2011-09212) and H. X. thanks support from the "China Scholarship Council" fellowship (CSC No. 201206340113). A.J.J. is funded by the EPSRC Doctoral Training Centre in Sustainable Chemical Technologies (EP/G03768X/1). A.W. acknowledges support from the Royal Society and the ERC (grant no. 277757). DFT calculations made use of UK national facility ARCHER, *via* A.J.J. and A.W.'s membership of the UK's HPC Materials Chemistry Consortium which is funded by EPSRC grant EP/L000202, and of the University of Bath's HPC facilities.

## References

1 D. S. Patil and D. K. Gautam, *Phys. B*, 2004, **344**, 140–146.
2 S. A.-B. Nasrallah, S. B. Afia, H. Belmabrouk and M. Said, *Eur. Phys. J. B*, 2005, **43**, 3–9.
3 Y. Ichimura, K. Kishino, M. Satake, M. Kuramoto and A. Yoshida, *J. Cryst. Growth*, 1995, **150**(Part 2), 812–816.
4 H. Okuyama, E. Kato, S. Itoh, N. Nakayama, T. Ohata and A. Ishibashi, *Appl. Phys. Lett.*, 1995, **66**, 656–658.
5 Y. P. V. Subbaiah, P. Prathap, K. T. R. Reddy, D. Mangalaraj, K. Kim and J. Yi, *J. Phys. D: Appl. Phys.*, 2007, **40**, 3683.
6 S. V. Sorokin, S. V. Gronin, E. A. Evropeytsev, I. V. Sedova, A. A. Toropov and S. V. Ivanov, *J. Cryst. Growth*, 2015, **425**, 212–215, DOI: 10.1016/j.jcrysgro.2015.02.007.
7 S. Fridjine, S. Touihri, K. Boubaker and M. Amlouk, *J. Cryst. Growth*, 2010, **312**, 202–208.
8 H. Xie, M. Dimitrievska, X. Fontané, Y. Sánchez, S. López-Marino, V. Izquierdo-Roca, V. Bermúdez, A. Pérez-Rodríguez and E. Saucedo, *Sol. Energy Mater. Sol. Cells*, 2015, **140**, 289–298.
9 A. Fairbrother, L. Fourdrinier, X. Fontané, V. Izquierdo-Roca, M. Dimitrievska, A. Pérez-Rodríguez and E. Saucedo, *J. Phys. Chem. C*, 2014, **118**, 17291–17298.
10 P. Kannappan, K. Asokan, J. B. M. Krishna and R. Dhanasekaran, *J. Alloys Compd.*, 2013, **580**, 284–289.
11 P. Kannappan and R. Dhanasekaran, *J. Cryst. Growth*, 2014, **401**, 691–696.
12 L.-J. Chen, C.-R. Lee, Y.-J. Chuang, Z.-H. Wu and C. Chen, *CrystEngComm*, 2015, **17**, 4434–4438.
13 R. G. Valeev, E. A. Romanov, V. L. Vorobiev, V. V. Mukhgalin, V. V. Kriventsov, A. I. Chukavin and B. V. Robouch, *Mater. Res. Express*, 2015, **2**, 025006.
14 T. Basak, M. N. Rao, S. L. Chaplot, N. Salke, R. Rao, R. Dhanasekaran, A. K. Rajarajan, S. Rols, R. Mittal, V. B. Jayakrishnan and P. U. Sastry, *Phys. B*, 2014, **433**, 149–156.
15 G. L. Agawane, S. W. Shin, S. A. Vanalakar, A. V. Moholkar, K. V. Gurav, M. P. Suryawanshi, J. Y. Lee, J. H. Yun and J. H. Kim, *Mater. Res. Bull.*, 2014, **55**, 106–113.
16 H. K. Sadekar, A. V. Ghule and R. Sharma, *J. Alloys Compd.*, 2011, **509**, 5525–5531.
17 I. F. Chang and S. S. Mitra, *Phys. Rev.*, 1968, **172**, 924–933.
18 J. F. Scott, T. C. Damen, W. T. Silfvast, R. C. C. Leite and L. E. Cheesman, *Opt. Commun.*, 1970, **1**, 397–399.
19 S. S. Kumar, M. A. Khadar, K. G. M. Nair, S. Dhara and P. Magudapathy, *J. Raman Spectrosc.*, 2008, **39**, 1900–1906.
20 A. Fairbrother, V. Izquierdo-Roca, X. Fontané, M. Ibáñez, A. Cabot, E. Saucedo and A. Pérez-Rodríguez, *CrystEngComm*, 2014, **16**, 4120–4125.
21 M. Dimitrievska, A. Fairbrother, X. Fontané, T. Jawhari, V. Izquierdo-Roca, E. Saucedo and A. Pérez-Rodríguez, *Appl. Phys. Lett.*, 2014, **104**, 021901.
22 M. Placidi, M. Dimitrievska, V. Izquierdo-Roca, X. Fontané, A. Castellanos-Gomez, A. Pérez-Tomás, N. Mestres, M. Espindola-Rodriguez, S. López-Marino, M. Neuschitzer, V. Bermudez, A. Yaremko and A. Pérez-Rodríguez, *2D Mater.*, 2015, **2**, 035006.
23 J. Rodríguez-Carvajal, *Phys. B*, 1993, **192**, 55–69.
24 G. Kresse and J. Hafner, *Phys. Rev. B: Condens. Matter Mater. Phys.*, 1993, **47**, 558–561.
25 J. C. Jamieson and H. H. Demarest Jr., *J. Phys. Chem. Solids*, 1980, **41**, 963–964.

 

26 P. D. O. Madelung, *Semiconductors: Data Handbook*, Springer, Berlin Heidelberg, 2004, pp. 173–244.
27 J. P. Perdew, A. Ruzsinszky, G. I. Csonka, O. A. Vydrov, G. E. Scuseria, L. A. Constantin, X. Zhou and K. Burke, *Phys. Rev. Lett.*, 2008, **100**, 136406.
28 A. V. Krukau, O. A. Vydrov, A. F. Izmaylov and G. E. Scuseria, *J. Chem. Phys.*, 2006, **125**, 224106.
29 J. Baars and G. Brandt, *J. Phys. Chem. Solids*, 1973, **34**, 905–909.
30 Y. Matsushima, K. Yoshino, Y. Yamamoto, S. R. Tiong and M. Hiramatsu, *J. Cryst. Growth*, 1992, **117**, 328–330.
31 O. Senthil Kumar, S. Soundeswaran and R. Dhanasekaran, *Mater. Chem. Phys.*, 2004, **87**, 75–80.
32 O. Senthil Kumar, S. Soundeswaran, D. Kabiraj, D. K. Avasthi and R. Dhanasekaran, *J. Cryst. Growth*, 2005, **275**, e567–e570.
33 J. Tauc and A. Menth, *J. Non-Cryst. Solids*, 1972, **8–10**, 569–585.
34 S. Park, H. Kim, C. Jin and C. Lee, *Curr. Appl. Phys.*, 2012, **12**, 499–503.
35 W. G. Nilsen, *Phys. Rev.*, 1969, **182**, 838–850.
36 W. Taylor, *Phys. Lett. A*, 1967, **24**, 556–558.
37 E. A. Vinogradov, B. N. Mavrin, N. N. Novikova, V. A. Yakovlev and D. M. Popova, *Laser Phys.*, 2009, **19**, 162–170.
38 M. Dimitrievska, A. Fairbrother, E. Saucedo, A. Pérez-Rodríguez and V. Izquierdo-Roca, *Appl. Phys. Lett.*, 2015, **106**, 073903.
39 K. Hayashi, N. Sawaki and I. Akasaki, *Jpn. J. Appl. Phys.*, 1991, **30**, 501.
40 J. Lu, H. Liu, C. Sun, M. Zheng, M. Nripan, G. S. Chen, G. M. Subodh, X. Zhang and C. H. Sow, *Nanoscale*, 2012, **4**, 976–981.
41 M. Dimitrievska, A. Fairbrother, A. Pérez-Rodríguez, E. Saucedo and V. Izquierdo-Roca, *Acta Mater.*, 2014, **70**, 272–280.
42 *Raman Scattering in Materials Science*, ed. W. H. Weber and R. Merlin, Springer Berlin Heidelberg, Berlin, Heidelberg, 2000, vol. 42.
43 P. Yu and M. Cardona, *Fundamentals of Semiconductors: Physics and Materials Properties*, Springer Science & Business Media, 2010.
44 J. E. Bernard and A. Zunger, *Phys. Rev. B: Condens. Matter Mater. Phys.*, 1987, **36**, 3199–3228.
45 S.-H. Wei and A. Zunger, *J. Appl. Phys.*, 1995, **78**, 3846–3856.
46 Y.-H. Li, A. Walsh, S. Chen, W.-J. Yin, J.-H. Yang, J. Li, J. L. F. D. Silva, X. G. Gong and S.-H. Wei, *Appl. Phys. Lett.*, 2009, **94**, 212109.
47 M. Dimitrievska, H. Xie, A. Fairbrother, X. Fontané, G. Gurieva, E. Saucedo, A. Pérez-Rodríguez, S. Schorr and V. Izquierdo-Roca, *Appl. Phys. Lett.*, 2014, **105**, 031913.
48 M. Dimitrievska, G. Gurieva, H. Xie, A. Carrete, A. Cabot, E. Saucedo, A. Pérez-Rodríguez, S. Schorr and V. Izquierdo-Roca, *J. Alloys Compd.*, 2015, **628**, 464–470.

# Chapter 5

*Conclusions*

The main objective of this thesis is to deepen the knowledge of fundamental properties of kesterite CZTS, CZTSe and CZTSSe materials. This principally included full characterization of structural and vibrational properties mainly using various Raman spectroscopy techniques. Special focus is also put on the investigation of defect dynamics in kesterites, especially on the experimental identification of defects and their effect on the optoelectronic properties of kesterite absorbers and thus the performance of solar cells devices. Additionally, among the objectives of the thesis was development of Raman based methodologies for the compositional assessment of these materials, as well as obtaining more information regarding the fundamental properties of ZnSSe secondary phase. The results were shown in the series of articles which have been published in high impact peer-review journals.

In the first part of the thesis, a complete analysis of all Raman active modes of the stoichiometric CZTS and CZTSe compounds was made using six different excitation wavelengths from near infrared to ultraviolet. Simulations fitting of the spectra allowed identification of 18 and 17 peaks which were attributed to all optical modes theoretically expected for the crystalline structure of CZTS and CZTSe, respectively. Based on the first principle simulations, normal displacements of each Raman mode were calculated and provided insightful knowledge about the involvement of atoms in vibrations corresponding to different modes. Furthermore, evaluation of crystal structure and phonon modes of CZTSSe materials was made using Raman spectroscopy and XRD, which led to complete characterization of their vibrational and structural properties. In contrast with previous reports on the existence of a two-mode behavior for CZTSSe, a more complex behavior of the most intense peaks with the change in anion composition has been observed. The Raman spectra of CZTSSe solid solutions show dominant CZTS-like peaks in the high frequency region (280–400 $cm^{-1}$), dominant CZTSe-like peaks in the low frequency region (170–205 $cm^{-1}$), and additional peaks related to vibrations of both S and Se anions in the intermediate frequency region (205–280 $cm^{-1}$). In all cases, polarization measurements were used for the symmetry assignment of the peaks. This work also demonstrated the utility of using multiwavelength Raman technologies, including resonance conditions, for easier identification of vibrational modes.

In the next part of the thesis, defect dynamics in kesterite materials was explored. Asymmetry in the shape of the low frequency region of the A symmetry modes has been observed for CZTS samples with different crystal quality. This has been attributed to phonon confinement effects which are arising from the loss of translational symmetry in the crystal caused by a high density of defects. On the other hand, changes in the frequency of the peaks were also observed and found to result from a balance between phonon confinement effects and lattice contraction due to

compressive strain. A combined theoretical model considering both effects was developed. Simultaneous fitting of the two dominant peaks in the spectra was used to determine the correlation length, for which it was shown to correlate well with the grain size, thus indicating a quantitative parameter for estimation of crystal quality. Based on this model, a simple methodology independent of measuring conditions is proposed for the quantitative assessment of crystal quality through the correlation length. After this, the effect of specific defect clusters on the Raman spectra and optoelectronic properties was investigated. Combinatorial CZTSe thin films with lateral compositional gradients were synthesized and made into solar cell devices (around 200 cells per sample), in order to study the correlation between the optoelectronic properties and absorber composition. A maximum device efficiency of 6.9% was obtained, together with a highest open circuit voltage value of 411 mV for the devices analyzed in this work. In addition, distinct compositional regions corresponding to the maximum open circuit voltage and short circuit current values were identified. It was concluded that these regions appear in the phase diagram corresponding to Cu-poor and Zn-rich compositions, where occurrence of $V_{Cu}$, $Zn_{Cu}$ and $Zn_{Sn}$ point defects is expected. Furthermore, detailed analysis of the Raman spectra has allowed investigation of systematic changes in the intensity of the E and B modes located around 170, 220 and 250 $cm^{-1}$ frequency regions, which involve mostly cation vibrations. Changes in the relative intensity of these peaks were systematically analyzed in relation to the occurrence of different kinds of defect clusters involving $V_{Cu}$, $Zn_{Cu}$, $Zn_{Sn}$, $Cu_{Zn}$ and $Sn_{Zn}$ point defects. Finally, the influence of point defects and secondary phases on the performance of CZTSe devices was presented. The results showed experimental evidence of the effect of the Cu-substitutional defects, in particular $[V_{Cu} + Zn_{Cu}]$, on the optoelectronic properties, especially $V_{OC}$. It was shown that $V_{OC}$ can be tuned by adjusting composition, and consequently the amount of the $[V_{Cu} + Zn_{Cu}]$ defect clusters. Furthermore, this proved to be intrinsic property of the CZTSe material, independent of the synthesis and post-deposition processes used for the preparation of samples. Secondary phases are also found to influence device properties, and their effects were dependent on whether they were present in the bulk or surface of the absorber. These results should provide a crucial step in solving the $V_{OC}$-deficit problem in kesterites. Furthermore, the detailed knowledge of the effects of defects on the optoelectronic properties presented here will be the basis for optimization of the synthesis and post-deposition processes in order to achieve even higher efficiencies with these kinds of absorbers, and may provide insights into improving applications for other multinary compounds.

Last part of the thesis was dedicated to development of a methodology for the quantitative determination of the anion composition of CZTSSe solid solutions using

Raman spectroscopy. The methodology is based on the analysis of the integral intensity ratio of Raman bands sensitive to anion vibrations with anion composition of CZTSSe solid solutions. Calibration of the methodology was done using reference CZTSSe powder samples synthesized by solid state reaction method, which compositions were measured by electron micro probe analysis. The validity of the methodology has been tested in different kinds of samples, including photovoltaic grade layers with different compositions and layers with different crystalline quality and same composition. A strong support on the performance of the methodology has been obtained from the analysis of a wide range of CZTSSe samples fabricated by different methods using Raman spectra reported in the literature. The good agreement obtained in the whole range of compositions points out the validity of the proposed methodology for the simple non-destructive assessment of the anion composition of different kinds of CZTSSe samples (thin films, powders, nanocrystals, monograins and etc.) independently on the experimental conditions used for the Raman scattering measurements.

Finally, a fundamental study, based on experimental and theoretical investigation, of the Raman resonance effects in ZnSSe solid solutions was presnted. Resonance behavior is observed in the Raman modes corresponding to the anion vibrations, when changing the excitation energy from UV (325 nm) to blue (455 nm). Significant enhancement in the Raman intensity of the LO ZnS-like modes, corresponding to vibrations of only S ions, is observed in cases of S-rich and intermediate compositions when excited with UV energy. On the other side, LO ZnSe-like modes attributed to vibrations of only Se ions, are enhanced in the case of blue excitation for samples with Se-rich and intermediate compositions. This enhancement of only certain Raman modes in the spectra was explained by interaction of the excitation photon with the corresponding S or Se states in the electronic band structure, and confirmed by the first principle calculations. Raman resonant effects in this case are achieved due to the tuning of the excitation energy with the energy of the S or Se electronic states in the conduction band. These findings advance the fundamental understanding of the coupling between the electronic transitions and photons in the case of Raman resonance effects, and provide inputs for further studies of lattice dynamics, especially in the case of chalcogenide materials. Additionally, application of Raman resonant conditions in the case of this kind of materials can be used for development of simple and non-destructive optical methodology for the quantitative measurement of [S] / ([S] + [Se]) anion composition. They should also enable easier characterization of the ZnSSe system, like reducing the integration time of the Raman measurements, which is extremely important in the case of nanosystems.

In conclusion, the works presented in this thesis are a significant contribution to the study of fundamental properties of materials in general, and kesterites materials in particular. Additionally, due to the unique approach of utilizing Raman spectroscopy with other characterization techniques, these methods could prove to be very successful in structure/function studies of other multinary compounds which are gaining increasing interest for electronic applications. In the end, the presented results give significant contribution to thin film photovoltaic field and should bring kesterites materials one step closer to commercial application.

# References

[1] Solar Power Europe (SPE), formerly known as EPIA – European Photovoltaic Industry Association, *Global Market Outlook for Solar Power 2015-2019* (2015).

[2] D.S. Ginley and D. Cahen, editors , *Fundamentals of Materials for Energy and Environmental Sustainability* (Cambridge University Press, Cambridge, 2011).

[3] M.A. Green, Phys. E Low-Dimens. Syst. Nanostructures **14**, 11 (2002).

[4] M.A. Green, K. Emery, Y. Hishikawa, W. Warta, and E.D. Dunlop, Prog. Photovolt. Res. Appl. **23**, 1 (2015).

[5] A. Zuser and H. Rechberger, Resour. Conserv. Recycl. **56**, 56 (2011).

[6] C. Candelise, J.F. Speirs, and R.J.K. Gross, Renew. Sustain. Energy Rev. **15**, 4972 (2011).

[7] W. Wang, M.T. Winkler, O. Gunawan, T. Gokmen, T.K. Todorov, Y. Zhu, and D.B. Mitzi, Adv. Energy Mater. **4**, n/a (2014).

[8] O. Gunawan, T. Gokmen, and D.B. Mitzi, J. Appl. Phys. **116**, 084504 (2014).

[9] T. Gokmen, O. Gunawan, and D.B. Mitzi, Appl. Phys. Lett. **105**, 033903 (2014).

[10] P. YU and M. Cardona, *Fundamentals of Semiconductors: Physics and Materials Properties* (Springer Science & Business Media, 2010).

[11] S. Chen, X.G. Gong, A. Walsh, and S.-H. Wei, Phys. Rev. B **79**, 165211 (2009).

[12] J.J.S. Scragg, L. Choubrac, A. Lafond, T. Ericson, and C. Platzer-Björkman, Appl. Phys. Lett. **104**, 041911 (2014).

[13] F.J. Espinosa-Faller, D.R. Conradson, S.C. Riha, M.B. Martucci, S.J. Fredrick, S. Vogel, A.L. Prieto, and S.D. Conradson, J. Phys. Chem. C **118**, 26292 (2014).

[14] G. Rey, A. Redinger, J. Sendler, T.P. Weiss, M. Thevenin, M. Guennou, B.E. Adib, and S. Siebentritt, Appl. Phys. Lett. **105**, 112106 (2014).

[15] Y.-T. Zhai, S. Chen, J.-H. Yang, H.-J. Xiang, X.-G. Gong, A. Walsh, J. Kang, and S.-H. Wei, Phys. Rev. B **84**, 075213 (2011).

[16] X. Fontané, L. Calvo-Barrio, V. Izquierdo-Roca, E. Saucedo, A. Pérez-Rodriguez, J.R. Morante, D.M. Berg, P.J. Dale, and S. Siebentritt, Appl. Phys. Lett. **98**, 181905 (2011).

[17] M. Dimitrievska, A. Fairbrother, X. Fontané, T. Jawhari, V. Izquierdo-Roca, E. Saucedo, and A. Pérez-Rodríguez, Appl. Phys. Lett. **104**, 021901 (2014).

[18] M. Dimitrievska, H. Xie, A. Fairbrother, X. Fontané, G. Gurieva, E. Saucedo, A. Pérez-Rodríguez, S. Schorr, and V. Izquierdo-Roca, Appl. Phys. Lett. **105**, 031913 (2014).

[19] A. Fairbrother, V. Izquierdo-Roca, X. Fontané, M. Ibáñez, A. Cabot, E. Saucedo, and A. Pérez-Rodríguez, CrystEngComm **16**, 4120 (2014).

[20] M. Placidi, M. Dimitrievska, V. Izquierdo-Roca, X. Fontané, A. Castellanos-Gomez, A. Pérez-Tomás, N. Mestres, M. Espindola-Rodriguez, S. López-Marino, M.

Neuschitzer, V. Bermudez, A. Yaremko, and A. Pérez-Rodríguez, 2D Mater. **2**, 035006 (2015).

[21] A. Fairbrother, E. García-Hemme, V. Izquierdo-Roca, X. Fontané, F.A. Pulgarín-Agudelo, O. Vigil-Galán, A. Pérez-Rodríguez, and E. Saucedo, J. Am. Chem. Soc. **134**, 8018 (2012).

[22] S. López-Marino, Y. Sánchez, M. Placidi, A. Fairbrother, M. Espindola-Rodríguez, X. Fontané, V. Izquierdo-Roca, J. López-García, L. Calvo-Barrio, A. Pérez-Rodríguez, and E. Saucedo, Chem. – Eur. J. **19**, 14814 (2013).

[23] J.M. Skelton, A.J. Jackson, M. Dimitrievska, S.K. Wallace, and A. Walsh, APL Mater. **3**, 041102 (2015).

[24] M. Kumar and C. Persson, Int J Theor Appl Sci **5**, 1 (2013).

[25] M. Dimitrievska, H. Xie, G. Gurieva, X. Fontane, A. Fairbrother, R. Gunder, E. Saucedo, A. Perez-Rodriguez, S. Schorr, and V. Izquierdo-Roca, in *Photovolt. Spec. Conf. PVSC 2014 IEEE 40th* (2014), pp. 0033–0036.

[26] A. Khare, B. Himmetoglu, M. Cococcioni, and E.S. Aydil, J. Appl. Phys. **111**, 123704 (2012).

[27] A. Fairbrother, X. Fontané, V. Izquierdo-Roca, M. Placidi, D. Sylla, M. Espindola-Rodriguez, S. López-Mariño, F.A. Pulgarín, O. Vigil-Galán, A. Pérez-Rodríguez, and E. Saucedo, Prog. Photovolt. Res. Appl. **22**, 479 (2014).

[28] A. Walsh, S. Chen, S.-H. Wei, and X.-G. Gong, Adv. Energy Mater. **2**, 400 (2012).

[29] S. Chen, A. Walsh, X.-G. Gong, and S.-H. Wei, Adv. Mater. **25**, 1522 (2013).

[30] S. Siebentritt, Thin Solid Films **535**, 1 (2013).

[31] M. Dimitrievska, A. Fairbrother, E. Saucedo, A. Pérez-Rodríguez, and V. Izquierdo-Roca, Appl. Phys. Lett. **106**, 073903 (2015).

[32] M. Dimitrievska, A. Fairbrother, A. Pérez-Rodríguez, E. Saucedo, and V. Izquierdo-Roca, Acta Mater. **70**, 272 (2014).

[33] H. Richter, Z.P. Wang, and L. Ley, Solid State Commun. **39**, 625 (1981).

[34] P. Panpech, S. Vijarnwannaluk, S. Sanorpim, W. Ono, F. Nakajima, R. Katayama, and K. Onabe, J. Cryst. Growth **298**, 107 (2007).

[35] N. Kazemi-Zanjani, E. Kergrene, L. Liu, T.-K. Sham, and F. Lagugné-Labarthet, Sensors **13**, 12744 (2013).

[36] T.B. Ivetić, M.R. Dimitrievska, N.L. Finčur, L.R. Đačanin, I.O. Gúth, B.F. Abramović, and S.R. Lukić-Petrović, Ceram. Int. **40**, 1545 (2014).

[37] L.G. Cançado, A. Jorio, E.H.M. Ferreira, F. Stavale, C.A. Achete, R.B. Capaz, M.V.O. Moutinho, A. Lombardo, T.S. Kulmala, and A.C. Ferrari, Nano Lett. **11**, 3190 (2011).

[38] A. Fairbrother, M. Dimitrievska, Y. Sánchez, V. Izquierdo-Roca, A. Pérez-Rodríguez, and E. Saucedo, J. Mater. Chem. A **3**, 9451 (2015).

[39] M. Dimitrievska, A. Fairbrother, V. Izquierdo-Roca, A. Perez-Rodriguez, and E. Saucedo, in *Photovolt. Spec. Conf. PVSC 2014 IEEE 40th* (2014), pp. 2307–2309.

[40] A. Lafond, L. Choubrac, C. Guillot-Deudon, P. Deniard, and S. Jobic, Z. Für Anorg. Allg. Chem. **638**, 2571 (2012).

[41] S. Schorr, in *5th Eur. Kesterite Workshop* (Tallinn, Estonia, 2014).

[42] E. Saucedo, V. Izquierdo-Roca, C.M. Ruiz, L. Parissi, C. Broussillou, P.-P. Grand, J.S. Jaime-Ferrer, A. Pérez-Rodríguez, J.R. Morante, and V. Bermúdez, Thin Solid Films **517**, 2268 (2009).

[43] C. Krämmer, J. Sachs, L. Pfaffmann, T. Musiol, M. Lang, C. Gao, D. Gerthsen, H. Kalt, M. Powalla, and M. Hetterich, Thin Solid Films **582**, 158 (2015).

[44] H. Wiedemeier and H.G. von Schnering, Z. Krist. **148**, 295 (1978).

[45] A. Kanevce, I. Repins, and S.-H. Wei, Sol. Energy Mater. Sol. Cells **133**, 119 (2015).

[46] M. Guc, S. Levcenko, V. Izquierdo-Roca, X. Fontané, E. Arushanov, and A. Pérez-Rodríguez, J. Appl. Phys. **114**, (2013).

[47] M. Neuschitzer, Y. Sanchez, T. Olar, T. Thersleff, S. Lopez-Marino, F. Oliva, M. Espindola-Rodriguez, H. Xie, M. Placidi, V. Izquierdo-Roca, I. Lauermann, K. Leifer, A. Pérez-Rodríguez, and E. Saucedo, Chem. Mater. (2015).

[48] L. Vauche, L. Risch, Y. Sánchez, M. Dimitrievska, M. Pasquinelli, T. Goislard de Monsabert, P.-P. Grand, S. Jaime-Ferrer, and E. Saucedo, Prog. Photovolt. Res. Appl. n/a (2015).

[49] A. Fairbrother, L. Fourdrinier, X. Fontané, V. Izquierdo-Roca, M. Dimitrievska, A. Pérez-Rodríguez, and E. Saucedo, J. Phys. Chem. C **118**, 17291 (2014).

[50] S. Das and K.C. Mandal, Mater. Res. Bull. **57**, 135 (2014).

[51] M. Salvador, S.M. Vorpahl, H. Xin, W. Williamson, G. Shao, D.U. Karatay, H.W. Hillhouse, and D.S. Ginger, Nano Lett. (2014).

[52] M.I. Amal, S.H. Lee, and K.H. Kim, Curr. Appl. Phys. **14**, 916 (2014).

[53] X. Yin, C. Tang, L. Sun, Z. Shen, and H. Gong, Chem. Mater. **26**, 2005 (2014).

[54] J. He, L. Sun, S. Chen, Y. Chen, P. Yang, and J. Chu, J. Alloys Compd. **511**, 129 (2012).

[55] A. Fairbrother, X. Fontané, V. Izquierdo-Roca, M. Espindola-Rodriguez, S. López-Marino, M. Placidi, J. López-García, A. Pérez-Rodríguez, and E. Saucedo, ChemPhysChem **14**, 1836 (2013).

[56] M. Grossberg, J. Krustok, J. Raudoja, K. Timmo, M. Altosaar, and T. Raadik, Thin Solid Films **519**, 7403 (2011).

[57] S. Ji, T. Shi, X. Qiu, J. Zhang, G. Xu, C. Chen, Z. Jiang, and C. Ye, Sci. Rep. **3**, (2013).

[58] A. Nagaoka, K. Yoshino, H. Taniguchi, T. Taniyama, K. Kakimoto, and H. Miyake, J. Cryst. Growth **386**, 204 (2014).

[59] L. Grenet, S. Bernardi, D. Kohen, C. Lepoittevin, S. Noël, N. Karst, A. Brioude, S. Perraud, and H. Mariette, Sol. Energy Mater. Sol. Cells **101**, 11 (2012).

[60] K. Muska, M. Kauk-Kuusik, M. Grossberg, M. Altosaar, M. Pilvet, T. Varema, K. Timmo, O. Volobujeva, and A. Mere, Thin Solid Films **535**, 35 (2013).

[61] S. Kim, M. Oh, and W.K. Kim, Thin Solid Films **549**, 59 (2013).

[62] G. Gurieva, M. Dimitrievska, S. Zander, A. Pérez-Rodríguez, V. Izquierdo-Roca, and S. Schorr, Phys. Status Solidi C **12**, 588 (2015).

[63] M. Dimitrievska, G. Gurieva, H. Xie, A. Carrete, A. Cabot, E. Saucedo, A. Pérez-Rodríguez, S. Schorr, and V. Izquierdo-Roca, J. Alloys Compd. **628**, 464 (2015).

[64] H. Xie, M. Dimitrievska, X. Fontané, Y. Sánchez, S. López-Marino, V. Izquierdo-Roca, V. Bermúdez, A. Pérez-Rodríguez, and E. Saucedo, Sol. Energy Mater. Sol. Cells **140**, 289 (2015).

[65] H. Xie, Y. Sánchez, S. López-Marino, M. Espíndola-Rodríguez, M. Neuschitzer, D. Sylla, A. Fairbrother, V. Izquierdo-Roca, A. Pérez-Rodríguez, and E. Saucedo, ACS Appl. Mater. Interfaces (2014).

[66] M. Dimitrievska, H. Xie, A.J. Jackson, X. Fontané, M. Espíndola-Rodríguez, E. Saucedo, A. Pérez-Rodríguez, A. Walsh, and V. Izquierdo-Roca, Phys. Chem. Chem. Phys. (2015).

# Appendix

"**Raman scattering crystalline assessment of polycrystalline $Cu_2ZnSnS_4$ thin films for sustainable photovoltaic technologies: Phonon confinement model**"

M. Dimitrievska, A. Fairbrother, A. Pérez-Rodríguez, E. Saucedo, and V. Izquierdo-Roca,

**Acta Mater.**, vol. 70, pp. 272 – 280, (2014).

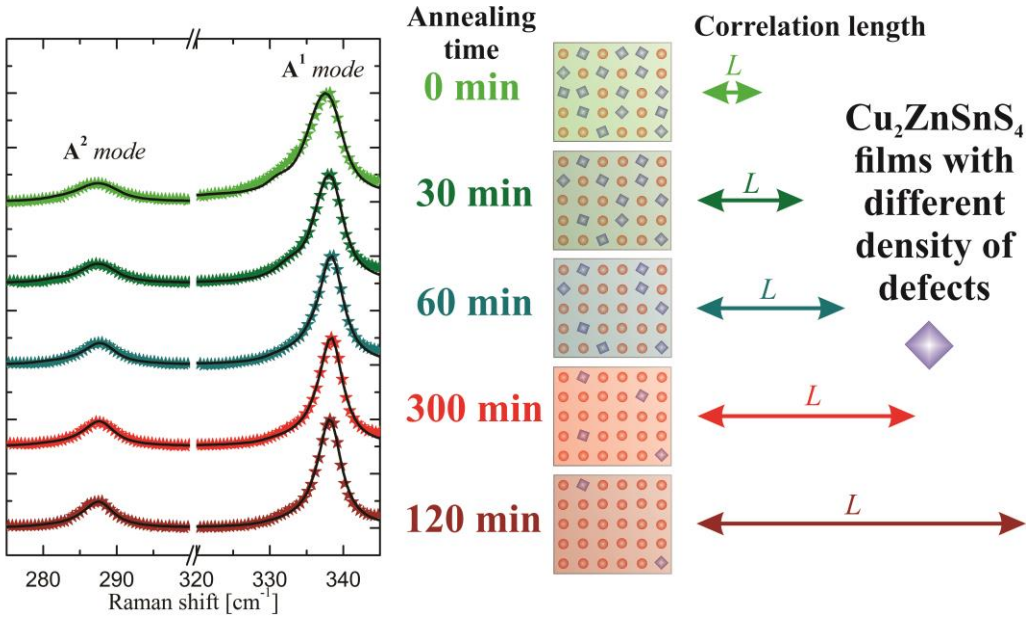

**"Compositional paradigms in multinary compound systems: A case study of kesterites"**

A. Fairbrother, M. Dimitrievska, V. Izquierdo-Roca, A. Pérez-Rodríguez, and E. Saucedo

**J. Mat. Chem. A**, vol. 3, no. 18, p. 9451 (2015)

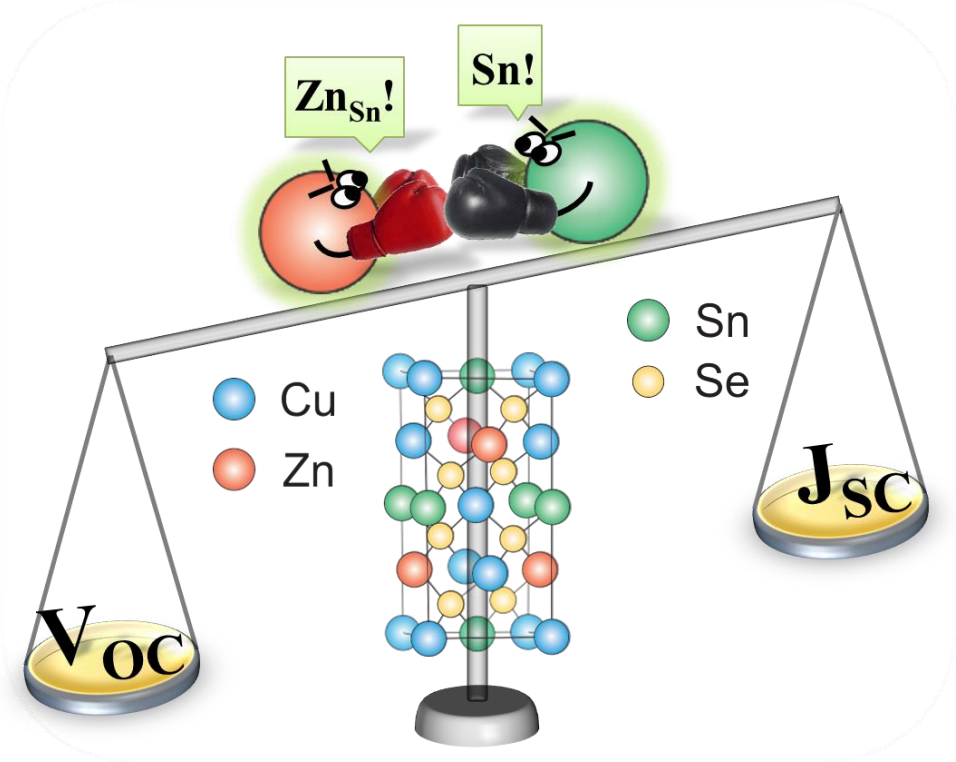

**"Influence of compositionally induced defects on the vibrational properties of device grade $Cu_2ZnSnSe_4$ absorbers for kesterite based solar cells"**

M. Dimitrievska, A. Fairbrother, E. Saucedo, A. Pérez-Rodríguez, and V. Izquierdo-Roca

**Appl. Phys. Lett**., vol. 106, no. 7, p. 073903 (2015)

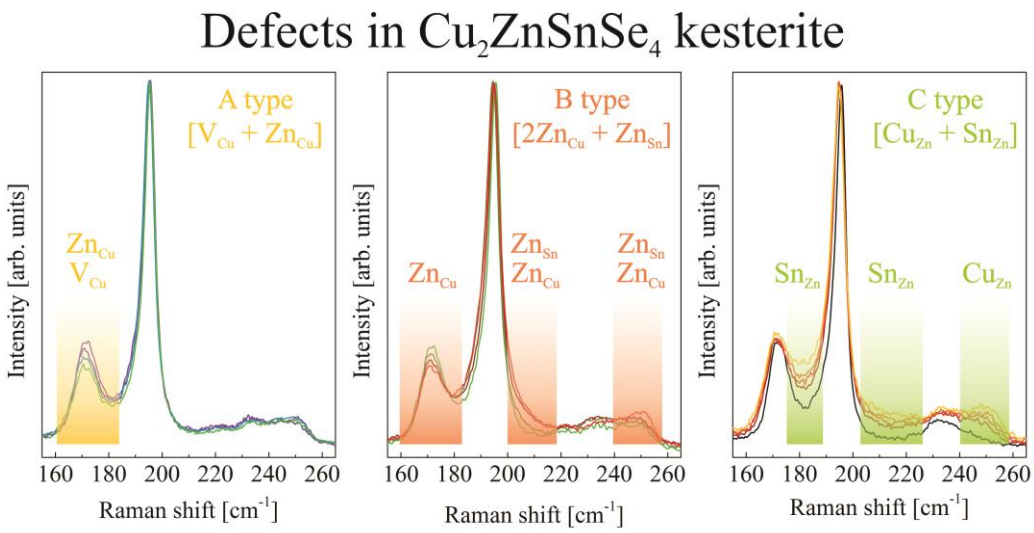

**"Secondary phase and Cu substitutional defect dynamics in kesterite solar cells: impact on optoelectronic properties"**

M. Dimitrievska, A. Fairbrother, E. Saucedo, A. Pérez-Rodríguez, and V. Izquierdo-Roca

**Sol. Energ. Mat. Sol. C.**, accepted (2015)

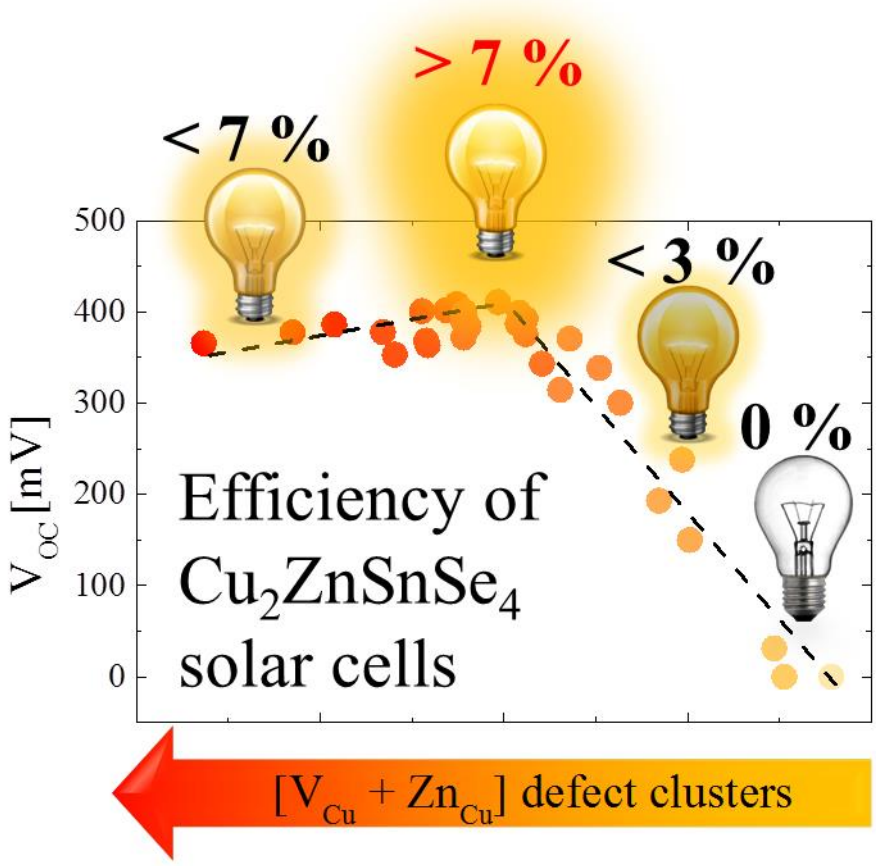

**"Raman scattering quantitative analysis of the anion chemical composition in kesterite $Cu_2ZnSn(S_xSe_{1-x})_4$ solid solutions"**

M. Dimitrievska, G. Gurieva, H. Xie, A. Carrete, A. Cabot, E. Saucedo, A. Pérez-Rodríguez, S. Schorr, and V. Izquierdo-Roca,

**J. Alloys Compd.**, vol. 628, pp. 464 – 470, (2015)

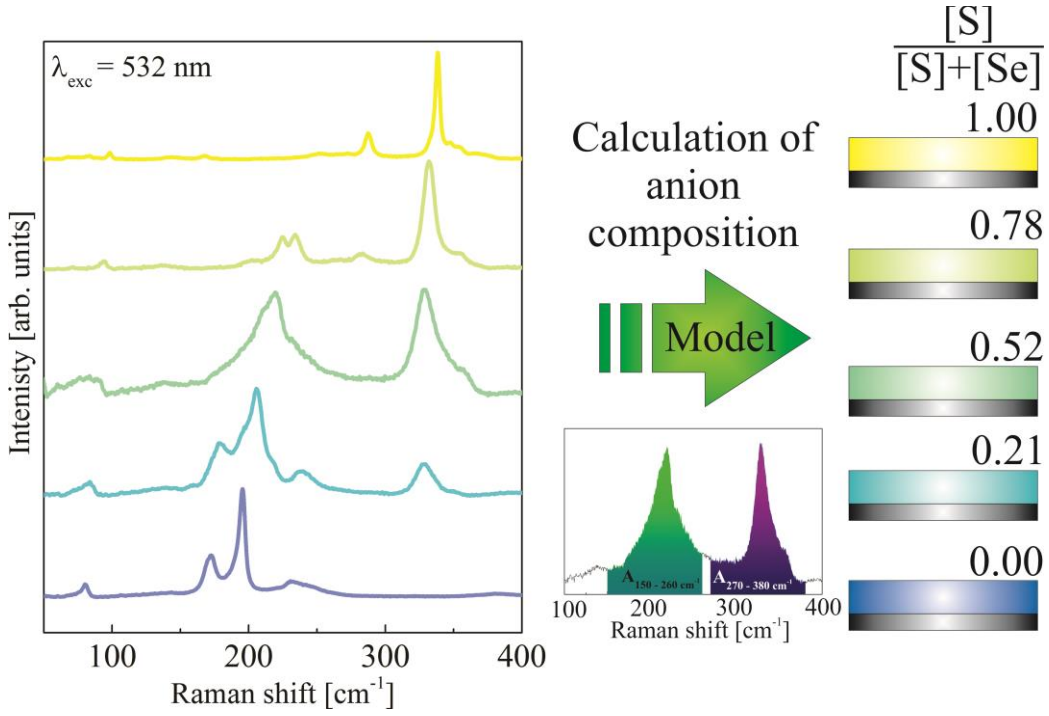

## "Resonant Raman scattering of $ZnS_xSe_{1-x}$ solid solutions: role of S and Se electronic states"

M. Dimitrievska, H. Xie, A. J. Jackson, X. Fontané, M. Espindola-Rodriguez, E. Saucedo, A. Pérez-Rodríguez, A. Walsh and V. Izquierdo-Roca

**Phys. Chem. Chem. Phys**, in press (2015)